Modelgebaseerde kwantificatie
van de systolische en diastolische linker ventrikelmechanica

Model-Based Quantification
of Systolic and Diastolic Left Ventricular Mechanics

Tom Claessens

Promotoren: prof. dr. ir. P. Verdonck, prof. dr. ir. P. Segers
Proefschrift ingediend tot het behalen van de graad van
Doctor in de Ingenieurswetenschappen

Vakgroep Civiele Techniek
Voorzitter: prof. dr. ir. P. Verdonck
Faculteit Ingenieurswetenschappen
Academiejaar 2006 - 2007

UNIVERSITEIT
GENT

ISBN-10 90-8578-124-8
ISBN-13 978-90-8578-124-0
NUR 910, 870
Wettelijk depot: D/2006/10.500/82

Supervisors:

Prof. dr. ir. Pascal Verdonck and Prof. dr. ir. Patrick Segers
Hydraulics Laboratory
Department of Civil Engineering (IR15)
Faculty of Engineering
Ghent University
Sint-Pietersnieuwstraat 41
B-9000 Gent

Members of the exam committee:

Prof. dr. ir. Ronny Verhoeven	(chairman, Faculty of Engineering, UGent)
Prof. dr. ir. Jan Vierendeels	(secretary, Faculty of Engineering, UGent)
dr. Damien Coisne	(Centre Hospitalier Universitaire de Poitiers, France)
Prof. dr. Johan De Sutter	(Faculty of Medicine and Health Sciences, UGent)
Prof. dr. ir. Joris Degrieck	(Faculty of Engineering, UGent)
Prof. dr. Thierry Gillebert	(Faculty of Medicine and Health Sciences, UGent)
Prof. dr. Jan Poelaert	(Faculty of Medicine and Health Sciences, UGent)
Prof. dr. ir. Patrick Segers	(supervisor, Faculty of Engineering, UGent)
Prof. dr. Stanislas Sys	(Faculty of Veterinary Medicine, UGent)
Prof. dr. ir. Pascal Verdonck	(supervisor, Faculty of Engineering, UGent)

This research has been made possible by a specialization grant of the Institute for the Promotion of Innovation by Science and Technology in Flanders (**IWT 023228**).

Acknowledgements

The work that I have been doing in the Hydraulics lab in the last four years has been a challenging, inspiring and interesting experience. It would not have been possible without the help, support and encouragement of a number of people I would like to acknowledge at this point.

I had the privilege to be supervised by two great people, Prof. Pascal Verdonck and Prof. Patrick Segers. I'm grateful for their advice and helpful guidance from the very early stage of this research. Thanks to them, I had the chance to participate in various interesting research projects and attend several international conferences. Their supervision was invaluable in completing most of this work. I really appreciated the help of Patrick, for always being present for discussions and interactions, for proofreading all my abstracts, proceedings and papers. His constructive comments had a direct impact on the final form and quality of this thesis. I'm also very appreciative of all the efforts of Pascal in helping me with my future career. I hope to keep up our collaboration in the future.

I am thankful to Prof. Ronny Verhoeven, Prof. Johan De Sutter, Prof. Thierry Gillebert, Prof. Stanislas Sys, Prof. Joris Degrieck, Prof. Jan Poelaert, Prof. Jan Vierendeels and Prof. Damien Coisne because they accepted to be members of the exam committee in the midst of all their activity. Thank you also for all the insightful conversations about fluid mechanics, structural mechanics, cardiac physiology and ultrasound.

I would also like to thank my former colleagues (in random order) Ilse, Koen, Dirk, Kris, Stijn, Kathy, Fadi and Evelyn, my current colleagues Guy, Wim, Lieve, Daniel, Peter T and Peter VR, Sebastian, Dries, Dimitri, Sunny, Liesbet, Matthieu, Rado, Robert, Veerle and Edawi, and the newbies Koen, Jan, Frederic and Frederik, Binod, Peter, Abigail, Benjamin and Denis for their companionship, for the comic relief and fun times. I wish them all the best for their own research. I appreciated very much the presence of our foreign post-doc visitors, in particular Masanori Nakamura and Stein-Inge Rabben. I gratefully thank Sunny, Wim, Abigail, Frederik, Sebastian, Lieve and Peter, who all volunteered to proofread parts of my thesis drafts. I had a great time working with you all. I'll remember that.

I am glad that I have had several opportunities to get to know some very experienced scientists from other departments and institutes. I would like to acknowledge the work from Dimitrios Georgakopoulos who provided me with murine pressure and volume data. My sincere thanks also goes to Marina Afanasyeva and Nico Westerhof for their very to-the-point answers to all my questions. I greatly benefited from dr. Ernst Rietzschel's lifework, the Asklepios Study database, as it enabled me to write chapter 4 in my thesis. Thanks to the valuable comments and the constructive criticism of Ernst, Marc De Buyzere and Dirk De Bacquer, the manuscript has only

improved. In particular I would like to thank the ultrasound experts Jan, Stian and Piet, for showing me what we can still expect from ultrasound in the near future. I also truly enjoyed working with many more very talented people. Thank you, Paul, Nico, Marc, Pieter and Ruggero for your enthusiasm and endless creativity.

Thank you very much, Jurgen, Stefaan, Marcel and Martin. Without your help, the development of the experimental models would simply not have been possible. I am also grateful to Manuella for the assistance with my administrative tasks, and to Ivo for his unique computer problem solving skills.

The financial support from the Institute for the Promotion of Innovation through Science and Technology in Flanders (IWT-Vlaanderen) was greatly appreciated.

I wish to thank my partner Inge for her continuous support and encouragement and for her unfailing patience. Don't worry, I'll spend more time with you in the very near future. Finally, I would also like to express my gratitude to my family and parents for the constant support and care taking during the past years.

Thanks to all of you who may not have been directly involved in this work, but were curious to know how this thesis advanced.

Gent, December 2006

Tom Claessens

Table of Contents

Nederlandse Samenvatting

Hoofdstuk 1
Het Cardiovasculaire Systeem

Het *cardiovasculaire systeem* bestaat uit het hart en het bloedvatenstelsel en heeft als belangrijkste taken de aanvoer van zuurstof en voedingsstoffen naar de organen en de afvoer van afvalstoffen en koolstofdioxide. Het hart, een holle spier bestaande uit vier hartkamers, is het centrale orgaan van het cardiovasculaire systeem. De meest gespierde kamer, het *linker ventrikel* (LV), zorgt ervoor dat het zuurstofrijke bloed afkomstig van de longen doorheen het lichaam gepompt wordt. De energie (zuurstof) nodig om zijn pompfunctie uit te oefenen wordt gehaald uit het bloed geleverd door de *kransslagaders*. Het middelste deel van de LV-wand wordt het *myocardium* genoemd en bestaat voornamelijk uit *hartspiercellen* (cardiomyocyten), omgeven door een matrix van *extracellulair weefsel*. Deze twee componenten bepalen in belangrijke mate de *actieve* en *passieve* mechanische kenmerken van het myocardium.

De hartcyclus is het gevolg van de periodieke contractie en relaxatie van de hartspiercellen en wordt klassiek opgedeeld in twee fasen, de systole en de diastole. Tijdens de *systole* wordt er in het LV snel druk opgebouwd (*isovolumetrische contractie*), waarna het bloed onder hoge druk in het arteriële systeem wordt gepompt (*ejectie*). Tijdens de *diastole* ontspannen de hartspiercellen zich waardoor de druk in het LV snel daalt (*isovolumetrische relaxatie*); vervolgens wordt het LV in twee fasen gevuld met bloed vanuit het linker atrium (*vulling*).

De *performantie* van het LV wordt in grote mate bepaald door de *contractiliteit* van het LV, maar ook door het *hartritme*, de *voorbelasting* (rek van hartspiercellen op het einde van de vullingsfase) en de *nabelasting* (belasting waaraan de hartspiercellen worden onderworpen tijdens de ejectiefase).

In dit proefschrift worden concepten en modellen behandeld die in het onderzoeksdomein en/of in de klinische praktijk gebruikt worden om de *tijdsvariabele systolische en diastolische mechanische eigenschappen* van het LV te begroten. Het onderliggende verband met *hartspiercelmechanica* wordt daarbij niet uit het oog verloren. Ten slotte wordt het mechanische effect van de hartspierwand op de stroming in de kransslagaders behandeld.

Hoofdstuk 2
Invasieve Bepaling van de Mechanica van het Linker Ventrikel

Om de tijdsvariabele *mechanische eigenschappen* van het linker ventrikel te begroten wordt voor onderzoeksdoeleinden vaak gebruik gemaakt van druk- en conductantiecatheters. Een drukcatheter laat toe om invasief en accuraat de *druk* in het LV meten. De conductantiecatheter meet indirect het *volume* door de geleidbaarheid van het bloedvolume in de hartkamer te meten.

Vaak maakt men gebruik van *druk-volumelussen* (druksignaal in functie van het volumesignaal) om de performantie van het LV te evalueren. Deze lussen laten toe om eenvoudig het *eind-diastolische* en *eind-systolische* volume, het *slagvolume* en de

slagarbeid af te lezen. Door het LV te belasten met gradueel variërende voor- en/of nabelastingen wordt een reeks druk-volumelussen verkregen. De eind-systolische druk-volume relatie (ESPVR) die de linker bovenhoeken van deze lussen met elkaar verbindt, verschaft informatie over de *actieve eigenschappen* van het LV. De druk-volume koppels rechts onder vormen de eind-diastolische druk-volume relatie (EDPVR). De EDPVR beschrijft voornamelijk de *passieve eigenschappen* van het LV.

Het *lineair tijdsvariabele elastantieconcept* is een vrij populair model om het cardiovasculaire systeem te modelleren. Wanneer (i) alle isochronen (i.e., de lijnen die alle druk-volume koppels die voorkomen op eenzelfde tijdstip na de aanvang van de systole met elkaar verbinden) *lineair* zijn, en (ii) alle isochronen de volume-as *in eenzelfde punt* (V_0) snijden, kan de elastantiefunctie zinvol gedefinieerd worden als $E(t) = P(t)/(V(t)-V_0)$. Deze functie beschrijft dan de variabele elastantie (de stijfheid) van het LV *tijdens* de contractie- en relaxatiefase.

Aangezien bij muizen de ESPVR vaak niet lineair is, zelfs niet in basale omstandigheden, kan de toepasbaarheid van dit model bij muizen terecht in vraag gesteld worden. Daarom werd nagegaan of aan beide bovenvermelde voorwaarden van het lineaire elastantiemodel voldaan is. In 13 muizen werden druk en volume gemeten met een *geminiaturiseerd druk-conductantie systeem*, waarna de ischronen gefit werden met lineaire, kwadratische en logaritmische functies, zowel met een constant als een tijdsvariabel snijpunt met de volume-as. De analyses toonden aan dat:

- De opgemeten isochronen een *tijdsvariabele curvilineariteit* vertonen, voornamelijk tijdens de isovolumetrische contractiefase, de ejectiefase en de isovolumetrische relaxatiefase.
- De vorm van de ischronen het best wordt beschreven door een *niet-lineaire* functie (logaritmische of kwadratische) met een tijdsvariabel snijpunt met de volume-as. Een lineaire functie voldoet niet om de isochronen te beschrijven, voornamelijk tijdens de isovolumetrische relaxatiefase en de vroege vulling.
- De *logaritmische* functie het best voldoet om het snijpunt V_0 te bepalen. Bovendien is deze waarde altijd positief en dus fysiologisch realistisch.
- In de isovolumetrische contractiefase en de ejectiefase de tijdsvariabele snijpunten van de ischronen van elkaar *verschillen* naargelang de manier waarop de isochronen werden gefit.

Bij muizen is er dus *niet* voldaan aan de veronderstellingen waarop het lineaire elastantiemodel gebaseerd is. Hoewel de functie E(t) altijd kan berekend worden indien druk-volume data beschikbaar zijn, wordt ze beter niet aangewend om de tijdsvariabele stijfheid van het ventrikel te begroten. Complexere modellen die het verband aangeven tussen tijd, druk en volume zullen dus nog moeten onderzocht worden.

Hoofdstuk 3

Niet-invasieve Bepaling van de Linker Ventrikelfunctie met behulp van Echocardiografie

Grijswaarden *echocardiografie* is een *niet-invasieve* op ultrageluid gebaseerde beeldvormingsmodaliteit waarmee de structuur van het hart in beeld kan worden gebracht. *Doppler-echocardiografie* laat bovendien toe om de snelheden van bloed en van hartweefsel te meten. De laatste jaren wordt er veel aandacht geschonken aan het meten van *rekken* en *reksnelheden* (met behulp van strain rate imaging), omdat deze grootheden vanuit fysisch standpunt beter de actieve vervormingen weergeven, en aldus beter de LV-contractiliteit kunnen begroten. Alle bovengenoemde beeldmodaliteiten berusten op het verwerken van de gereflecteerde signalen (de RF signalen) afkomstig van de rode bloedcellen en/of het hartweefsel. Alle Doppler-gebaseerde applicaties hebben eenzelfde nadeel: ze zijn intrinsiek *hoek-afhankelijk*, dit wil zeggen dat enkel de component van de opgemeten grootheid (snelheid, rek en/of reksnelheid) *in de richting van de scanlijn* van de ultrageluidprobe kan worden geregistreerd.

Recent is er een nieuwe *hoek-onafhankelijke* methode ontwikkeld die toelaat om tweedimensionale rekken te bepalen. In dit algoritme wordt eerst het tweedimensionale snelheidsveld van het weefsel bepaald door het traceren van RF patronen in opeenvolgende beeldscans. Op basis van het snelheidsveld reconstrueert men vervolgens de *verplaatsingen* en berekent men de *rekken*. De nieuwe techniek werd gevalideerd in een periodiek vervormend cilindrisch *fantoom* door de ultrageluid-gebaseerde rekken te vergelijken met referentierekken afkomstig van *sonomicrometrie* metingen. Sonomicrometrie is een meettechniek waarbij men continu de afstand (en dus ook de rek) registreert tussen een aantal *ultrageluidkristallen* die strategisch worden vastgemaakt op een fantoom of op hartspierweefsel.

De resultaten toonden een algemeen goede correlatie tussen beide meettechnieken. De nauwkeurigheid was echter hoger in de richting van de probe dan in de richting loodrecht daarop. Later werd dit algoritme toegepast om de longitudinale en de radiale rekken te meten in het LV van vijf varkens. Ook hier bleken beide technieken heel goed met elkaar overeen te stemmen.

Mogelijks zal door de ontwikkeling van deze tweedimensionale nieuwe methode de *toepasbaarheid* van rek- en reksnelheidsmetingen in de klinische praktijk *versneld* worden.

Hoofdstuk 4

Niet-invasieve Bepaling van Ventrikulaire en Myocardiale Contractiliteit

De *performantie* van het LV wordt bepaald door zijn *intrinsieke contractiliteit*, maar wordt tegelijkertijd beïnvloed door de aanwezige *voor-* en *nabelasting*. Studies hebben uitgewezen dat de grootheid E_{es} (i.e., de helling van de lineair veronderstelde ESPVR) gevoelig is voor veranderingen in LV-contractiliteit, maar vrijwel

onafhankelijk is van voor- en nabelasting. Daarom wordt in onderzoeksomgevingen E_{es} vaak gebruikt als *gouden standaard* voor het begroten van LV-contractiliteit. Omdat E_{es} een verhouding is van druk en volume is deze index echter intrinsiek afhankelijk van de *grootte* van het ventrikel. *Normalisatie* of schaling van E_{es} is dus nodig om op een zinvolle manier de intrinsieke of *myocardiale* contractiliteit te kunnen vergelijken in verschillende personen onderling.

In 2524 deelnemers van de Asklepiosstudie werd E_{es} met een reeds eerder gevalideerde niet-invasieve methode bepaald (op basis van echocardiografie en bloeddrukmetingen op de bovenarm). De Asklepiosstudie is een cross-sectionele en longitudinale bevolkingsstudie (leeftijd tussen 35 en 55 jaar bij aanvang van de studie) naar het samenspel tussen veroudering, cardiovasculaire hemodynamica en ontstekingsmechanismen in hart- en vaatziekten. Een *drietal bestaande* en een vierde, *populatiespecifieke* methode werden gebruikt om de *myocardiale contractiliteit* te berekenen:

- Vermenigvuldiging met LVM: $E_{es} \cdot LVM$
- Vermenigvuldiging met EDV: $E_{es} \cdot EDV$
- Elastantie index: $0.433 \cdot E_{es} \cdot LVM / RWT$
- Populatiespecifieke methode: $0.0941 \cdot E_{es} \cdot LVM^{0.455} / RWT^{0.159}$

met LVM de massa van de linker ventrikelwand, EDV het eind-diastolische volume en RWT de verhouding van de wanddikte ten opzichte van de interne diameter. Er werd vervolgens onderzocht hoe de myocardiale contractiliteit varieert naargelang de leeftijd en het geslacht van de Asklepios deelnemers.

Het onderzoek wees uit dat er aanzienlijke *verschillen* optraden tussen de verschillende normalisatiemethoden, te wijten aan de verschillende specifieke *veronderstellingen* die voor elk van deze methoden gemaakt zijn. Desondanks leken alle methoden aan te tonen dat er een *blijvende stijging* van de myocardiale contractiliteit was in vrouwen, terwijl bij de mannen de contractiliteit een *plateauwaarde* vertoonde vanaf de leeftijd van 50 jaar. De oorzaak van dit merkwaardige verschil is tot op heden onbekend en dient verder te worden bestudeerd.

Hoofdstuk 5
Niet-invasieve Evaluatie van de Diastolische Linker Ventrikelfunctie

In de *klinische praktijk* wordt de *diastole* beschouwd als de periode tussen het sluiten van de aortaklep (i.e., het einde van de ejectiefase) en het sluiten van de mitraalklep (i.e., het einde van de vullingsfase). Ze is het gevolg van de hartspierrelaxatie (inactivatie) die eigenlijk al aanvangt tijdens de ejectiefase. Een *goede diastolische functie* houdt in dat het LV snel kan *relaxeren* en gemakkelijk kan gevuld wordt onder een *lage druk*.

Tegenwoordig bestaan er heel wat op Doppler-echocardiografie gebaseerde beeldvormingsmodaliteiten om de diastolische functie niet-invasief te evalueren. Soms zijn de opgemeten diastolische *bloedsnelheden* en *wandbewegingen* echter

moeilijk te interpreteren omdat ze het gevolg zijn van een aantal interagerende factoren. Om meer inzicht te krijgen in de verschillende factoren die de vroege diastolische fase (potentieel) beïnvloeden, werd een dikwandig hydraulisch model van het LV ontwikkeld, bestaande uit een echogeen medium (polyvinylalcohol). Een analyse van de drukken in het LV tijdens de isovolumetrische relaxatiefase toonde aan dat de maximale snelheid waarmee de druk daalt (i.e., een maat voor *relaxatiecapaciteit*) toeneemt met toenemende inactivatiesnelheid, eind-systolische druk en passieve stijfheid van het LV. De relaxatiesnelheid bleek echter voornamelijk bepaald te worden door de eind-systolische druk en in mindere mate door de passieve stijfheid en de inactivatiesnelheid.

In het tweede deel van dit hoofdstuk werd een uitgebreid literatuuroverzicht gegeven over de recente hoogtechnologische echocardiografische technieken om diastolische functie te evalueren. Deze technieken laten toe om een aantal specifieke eigenschappen van de bloedsnelheden en intraventrikulaire drukken, en van de wandbewegingen op te meten. De analyse van de *golfvoortplantingssnelheid* en de intraventrikulaire *drukgradiënten* met behulp van kleuren M-mode Doppler beelden werd uitvoerig beschreven. Ook de *longitudinale* bewegingen van de *mitraalklepring* en de *torsiebewegingen* van de wand, beide opgemeten met weefsel-Doppler technieken, werden uitvoerig behandeld. Het analyseren van de drukgradiënten en de snelle torsiebeweging van het ventrikel bleek in de klinische praktijk nog relatief onbekend terrein dat verder onderzocht dient te worden.

Hoofdstuk 6

Model van de Myocardiale Weerstand: Implicaties voor het Bepalen van de Fractionele Stromingsreserve (FFR)

De energie die het hart gebruikt om zijn pompfunctie te kunnen uitoefenen wordt geleverd via de *kransslagaders* (coronaire arteriën of coronairen) die het zuurstofrijke bloed naar de hartspier brengen. De bloedstroming naar het ventrikel kan echter ernstig beperkt worden wanneer er in één of meerdere kransslagaders een lokale vernauwing (*coronaire stenose*) ontstaat.

Om de *hemodynamische impact* van een coronaire stenose op de bloedstroming naar het hart te bepalen wordt vaak gebruik gemaakt van de functionele index FFR (Fractional Flow Reserve). Deze index wordt gedefinieerd als de verhouding van het *werkelijke* maximale coronair debiet (Q_S) tot het maximale coronair debiet in het *hypothetische* geval zonder stenose (Q_N). In de veronderstelling dat (i) de afwaartse druk in de coronaire circulatie gelijk gesteld mag worden aan de (verwaarloosbare) *veneuze druk*, en (ii) de myocardiale weerstand *lineair* is, kan FFR ook berekend worden als de verhouding van twee drukken: $FFR = P_{dis}/P_{ao}$. P_{dis} is de gemiddelde distale (afwaarts van de stenose) druk en P_{ao} is de gemiddelde aortadruk, beide opgemeten tijdens een toestand van hyperemie (maximale dilatatie van de weerstandvaten). In tegenstelling tot de debietgebaseerde Q_S/Q_N, kan de drukgebaseerde FFR relatief gemakkelijk en snel opgemeten worden in een catheterisatielaboratorium. Indien $FFR < 0.75$, is een interventie (bijvoorbeeld het plaatsen van een stent) aangewezen.

De afwaartse druk (veneuze druk) die in dit model gebruikt wordt is echter vatbaar voor discussie. Theoretisch gezien zou het correcter zijn om in de formule voor FFR rekening te houden met een *zero-flow druk* (P_{zf}), die waarschijnlijk het gevolg is van de weefseldruk op de intramyocardiale bloedvaten, en die aanzienlijk groter kan worden dan de veneuze druk. Indien men FFR accuraat wil bepalen op basis van drukmetingen, moet die weefseldruk in rekening gebracht worden: $FFR_C = (P_{dis}-P_{zf})/(P_{ao}-P_{zf})$.

In een vereenvoudigd *hydraulisch model van de coronaire circulatie* (coronaire arterie en myocardweerstand), aangesloten op een linkerhartmodel, werd de invloed van een verhoogde P_{zf} op FFR bepaald. Het effect van P_{zf} werd gemodelleerd door het creëren van een *hydraulische waterval*. Tevens werd de impact van een variabele P_{ao} onderzocht.

De resultaten toonden aan dat de conventioneel berekende drukgebaseerde FFR de debietgebaseerde (referentie-) waarde Q_S/Q_N steeds overschat. De overschatting neemt toe met toenemende P_{zf} en afnemende P_{ao} en kan tot 50% bedragen in een extreem geval (P_{zf} = 30 mmHg en P_{ao} = 70 mmHg). Verder werd aangetoond dat zowel FFR als FFR_C afhankelijk zijn van het coronair debiet en dus ook van P_{ao}, omdat de weerstand over een stenose functie is van het debiet.

English Summary

Chapter 1
The Cardiovascular System

The *cardiovascular system* consists of the *heart* and the *circulatory system*. Its most important tasks are to deliver oxygen and nutrients to the body organs and to remove waste products from the tissue cells. The heart, a hollow muscular pump with four chambers, is the central organ of the cardiovascular system. The most powerful heart chamber, the *left ventricle* (LV), transports the oxygen-rich blood coming from the lungs into the arterial circulation. The energy required to fulfil its pump function is supplied by blood flow from the *coronary arteries*. The middle layer of the LV wall, called the *myocardium*, consists mainly of cardiac muscle cells (or *cardiomyocytes*), embedded in a matrix of extracellular tissue. These two components determine the *active* and *passive* mechanical properties of the myocardium.

The cardiac cycle is a direct consequence of the periodic contraction and relaxation of cardiomyocytes, and is commonly divided in two phases, *systole* and *diastole*. During systole, LV pressure increases rapidly (*isovolumic contraction*), after which blood is ejected under high pressure in the arterial system (*ejection*). During diastole, pressure decreases rapidly due to cardiomyocyte relaxation (*isovolumic relaxation*). When LV pressure falls below left atrial pressure, the LV starts to fill with blood coming from the left atrium (*filling*).

The performance of the LV is determined by the *contractile state*, the *heart rate*, the *preload* (stretch of the cardiomyocytes prior to isovolumic contraction) and the *afterload* (load to which the cardiomyocytes are subjected during ejection).

In this thesis, we critically evaluate a number of concepts and models that are used in research and in clinical practice to quantify the *time-varying systolic and diastolic mechanical properties* of the LV. The link with underlying *cardiomyocyte mechanics* is provided where necessary. The influence of systolic and diastolic wall mechanics upon coronary blood flow is also discussed.

Chapter 2
Invasive Assessment of Global Left Ventricular Mechanics

In cardiac research, pressure and conductance catheters are often used to quantify the time-varying *mechanical properties* of the LV. A pressure catheter allows for accurate recording of LV *pressure*. The conductance catheter indirectly measures LV *volume* by measuring the conductivity of the blood pool in the LV.

Pressure-volume (P-V) *loops*, obtained by plotting the pressure signal as a function of the volume signal, are frequently used to evaluate the pump function of the LV. P-V loops allow to easily derive the *end-diastolic* and *end-systolic volume*, the *stroke volume* and the *stroke work*. When loading the LV with transient changes in preload and/or afterload, a family of P-V loops is obtained. The *end-systolic pressure-volume relationship* (ESPVR), which connects the upper left corners of these P-V loops, provides information about the *active* properties of the LV. The P-V couples in the

lower right corners make up the *end-diastolic pressure-volume relationship* (EDPVR), which describes the *passive* properties of the LV.

The *linear time-varying elastance concept* is a relatively popular model for modelling the cardiovascular system. When (i) all isochrones (i.e., lines that connect the P-V couples occurring at the same time instant after the onset of systole) are *linear*, and (ii) all isochrones have a *common intercept* (V_0) with the volume-axis, the elastance function can be defined as $E(t) = P(t)/(V(t)-V_0)$. This function is then used to describe the *time-varying elastance* (stiffness) of the LV during the contraction and relaxation phase.

The applicability of this model in *mice* can be rightfully questioned, given the considerable non-linear shape of the ESVPR, even in basal conditions. The underlying assumptions of the linear elastance model have been critically investigated in this species. In 13 mice P-V data were acquired with a miniaturized pressure-conductance system, after which the isochrones were fitted using *linear*, *quadratic* and *logarithmic* functions, either with a fixed or time-varying volume intercept. The analyses showed that:

- the isochrones measured in a mouse LV show a time-varying curvilinearity during isovolumic contraction, ejection and isovolumic relaxation;
- the shape of the isochrones is best described using a non-linear function (quadratic or logarithmic) with a time-varying volume intercept, while the linear approximation with a fixed volume intercept yields the poorest results, particularly during isovolumic relaxation and early filling;
- the logarithmic fitting appears superior in estimating the fixed volume intercept of the ESPVR and, moreover, yields a physiological (i.e., positive) value;
- the intercepts of the linear, quadratic and logarithmic regression functions vary with time and differ from each other during isovolumic contraction and ejection.

The assumptions of the linear time-varying elastance model are *not* met in mouse ventricles. Even though the elastance function E(t) can *always* be calculated when P-V data are available, it should not be used for describing the time-varying stiffness of the mouse LV. More *complex models* incorporating pressure, volume and time need therefore to be investigated.

Chapter 3
Echocardiography as a Non-invasive Tool for Assessing Left Ventricular Function

Greyscale echocardiography is a non-invasive ultrasound-based imaging modality capable of displaying the structure of the heart. Doppler-echocardiography, moreover, allows to measure velocities of blood and tissue. In recent years, much interest has arisen in measuring strain and strain rate (using *strain rate imaging*), because these quantities better reflect the active deformation (and thus contractility)

of cardiac tissue from a physical point of view. All of the abovementioned imaging modalities rely on processing the RF signals reflected by the red blood cells and/or cardiac tissue. All Doppler-applications have a common limitation: they are intrinsically *angle-dependent*, which means that only the velocity/deformation component in the direction of the ultrasound beam can be registered.

A novel *angle-independent* method has recently been developed that permits to assess *two-dimensional* strains. In this algorithm, the two-dimensional velocity field is determined by tracing the displacement of a specific RF pattern from one frame to the other. When the velocity field as a function of time is found, the displacement and the strain of the underlying tissue can be calculated. This new technique has been validated in a cyclically deforming cylindrical *phantom* by comparing the ultrasound-derived strains with reference strains obtained from *sonomicrometry* measurements. Sonomicrometry is a measurement technique in which the distance and, hence, strain between two or more *ultrasound crystals* is continuously measured. These crystals are strategically placed on the phantom or sutured on cardiac tissue.

The results showed an overall *good correlation* between both measurement techniques. The accuracy in the direction of the probe was higher than in the lateral (i.e., perpendicular) direction. The same approach has later been applied to find the longitudinal and radial strains in the LV of five pigs. That study also showed a high agreement between both methods.

It is to be expected that this new technology, by solving the angle dependence, will *accelerate* the clinical acceptance of deformation imaging in cardiology.

Chapter 4
Non-invasive Assessment of Ventricular and Myocardial Contractility

The performance of the LV is determined by its intrinsic *contractility*, but also by the governing preload and afterload. Studies have shown that E_{es} (i.e., the slope of the linear assumed ESPVR) is sensitive for changes in LV contractility, but virtually independent of changes in pre- and afterload. As a consequence, E_{es} is considered the *gold standard* for assessing LV contractility in the research environment. However, because E_{es} is a ratio of pressure and volume, it is intrinsically dependent on the *size* of the LV. *Normalization* or *scaling* of E_{es} is thus required to make meaningful comparisons about *intrinsic* or *myocardial contractility* between different individuals.

In 2524 participants of the Asklepios Study, E_{es} was measured with a previously validated non-invasive method (based on echocardiography and blood pressure measurements on the upper arm). The Asklepios Study is a cross-sectional and longitudinal population study (age of the participating subjects between 35 and 55 at study initiation) focusing on the interplay between ageing, cardiovascular haemodynamics and inflammation in (preclinical) cardiovascular disease. Three *existing* and a fourth *population-specific* method were used to determine myocardial contractility:

- Multiplication with LVM: $E_{es} \cdot LVM$
- Multiplication with EDV: $E_{es} \cdot EDV$
- Elastance index: $0.433 \cdot E_{es} \cdot LVM / RWT$
- Population-specific method: $0.0941 \cdot E_{es} \cdot LVM^{0.455} / RWT^{0.159}$

with LVM the LV mass, EDV the end-diastolic volume and RWT the ratio between the LV wall thickness and the internal diameter. Afterwards, it was investigated how myocardial contractility varied with age and gender.

The results showed that E_{es} as such *cannot* be used to compare myocardial contractility between men and women of various ages. Normalization is required to cancel out the effect of geometry. Due to the differences in their underlying assumptions, the various myocardial contractility indices do *not* provide *consistent* information with respect to gender differences. Despite these discrepancies, it was found that myocardial contractility appears to monotonically rise in women, while this value in men tends to stagnate between the age of 45 to 55. This finding at the population level could have potentially important *clinical implications* that require further investigation.

Chapter 5
Non-invasive Assessment of Left Ventricular Diastolic Function

In *clinical practice* diastole is defined as the period between the closure of the aortic valve (end of ejection phase) and the closure of the mitral valve (end of filling phase). It is the manifestation of the myocardial *relaxation process*, which already starts during ejection. Diastolic function is considered *normal* when the capability of the LV to relax and to fill with a blood volume is sufficient to maintain a normal stroke volume while maintaining normal diastolic pressures at rest and during exercise.

Presently, a number of *Doppler-echocardiography-based* imaging modalities exist that allow for non-invasive assessment of diastolic function. Unfortunately, the measured blood and/or tissue velocities are sometimes difficult to *interpret* because they are influenced by several interacting factors. In order to gain more insight in the (relative) impact that some factors may have upon early diastolic function, a *thick-walled hydraulic LV model*, consisting of an echogeneous medium (polyvinylalcohol) has been developed. Analysis of LV pressure during isovolumic relaxation showed that the *maximum rate of LV pressure decay* (i.e., a measure of relaxation capacity) increases with increasing *end-systolic pressure*, *rate of inactivation* and *passive stiffness*. The model furthermore demonstrated that changes in end-systolic pressure had the largest impact on relaxation rate, followed by LV stiffness and inactivation rate.

In the second part of this chapter, a *comprehensive* and *original overview* was provided about the novel and highly technological echocardiographic imaging modalities. These techniques allow to visualize specific properties of *blood velocity*, *intraventricular pressure* and *wall motion* and *deformation*. The principles of wave propagation velocity and intraventricular pressure gradients were extensively

discussed. The longitudinal motion of the mitral annulus and the rapid untwisting during early relaxation, both measured with tissue Doppler imaging, have been elaborated upon. Assessment of pressure gradients and untwisting are two relatively unexplored techniques that definitely require further investigation.

Chapter 6

Modelling Myocardial Resistance: Implications for the Assessment of Fractional Flow Reserve

The energy required by the heart to fulfil its pump function is provided by the *coronary arteries*, which transport oxygen rich blood to the myocardium. Blood flow to the heart can be considerably limited in case of a *local narrowing* (coronary *stenosis*) in one or more of the coronary arteries. A stenosis is considered functionally *significant* if it limits maximum achievable blood flow to such a degree that ischaemia (imbalance between oxygen demand and oxygen supply) can be induced if the patient is sufficiently stressed.

To assess the *haemodynamic impact* of such a coronary artery stenosis on blood flow, the functional index FFR (*Fractional Flow Reserve*) is often used. It is defined as the ratio of the maximum coronary flow in the stenosed artery (Q_S) to the hypothetical maximum flow in case no stenosis would be present (Q_N). Assuming that (i) the back-pressure in the coronary circulation equals the (negligible) venous pressure, and that (ii) the myocardial resistance is linear, FFR can also be calculated as a ratio between *two pressures*: FFR = P_{dis}/P_{ao}. P_{dis} represents the mean pressure distal to the stenosis and P_{ao} is the mean aortic pressure, both measured during hyperaemia (maximum dilation of the resistance vessels). In contrast to the flow-based Q_S/Q_N, the pressure-based FFR can be readily measured in the cath lab. In patients with a FFR < 0.75 an *intervention* of the target segment is commonly performed.

Nevertheless, the *back-pressure* opposing coronary flow that is used in the formula for FFR remains subject of debate. If venous pressure is the actual back-pressure in the coronary circulation, it can indeed be neglected. However, it has been argued that a so-called *zero-flow pressure* (P_{zf}), which is considerably higher than venous pressure and which is possibly the result of tissue pressures inside the myocardium, should be accounted for. When P_{zf} is the back-pressure opposing coronary flow, the *corrected* FFR should be calculated as $FFR_C = (P_{dis}-P_{zf})/(P_{ao}-P_{zf})$.

In a *simplified hydraulic model* of the coronary circulation (coronary artery and myocardial resistance), connected to a model of the left heart, we measured the influence of P_{zf} on FFR. The effect of an elevated P_{zf} was modelled by creating a *hydraulic waterfall*. We also investigated the effect of varying P_{ao}. The results showed that the conventional pressure-based FFR consistently *overestimates* the true value Q_S/Q_N. The degree of overestimation increases with increasing P_{zf} and decreasing P_{ao} and may amount to more than 50% in an extreme condition (P_{zf} = 30 mmHg and P_{ao} = 70 mmHg). We also showed that FFR as well as FFR_C are dependent on the level of *coronary flow* and, hence, also of P_{ao}, because stenosis resistance is a function of coronary flow.

1

Chapter 1

The Cardiovascular System

1.1 Introduction

This introductory chapter provides a brief overview of the anatomy and physiology of the cardiovascular system for readers not familiar with the terminology. Additional information can be found in a number of reference works about anatomy, physiology, biophysics and biomechanics and a series of extensive review articles [38, 45, 159, 171, 193, 296, 303].

The cardiovascular system consists of the heart, a hollow muscular pump, and the circulatory system, which transports blood throughout the body. It is an elaborate network that performs two major tasks: it delivers oxygen and nutrients to the body organs and removes waste products of metabolism from tissue cells.

1.2 The circulatory system

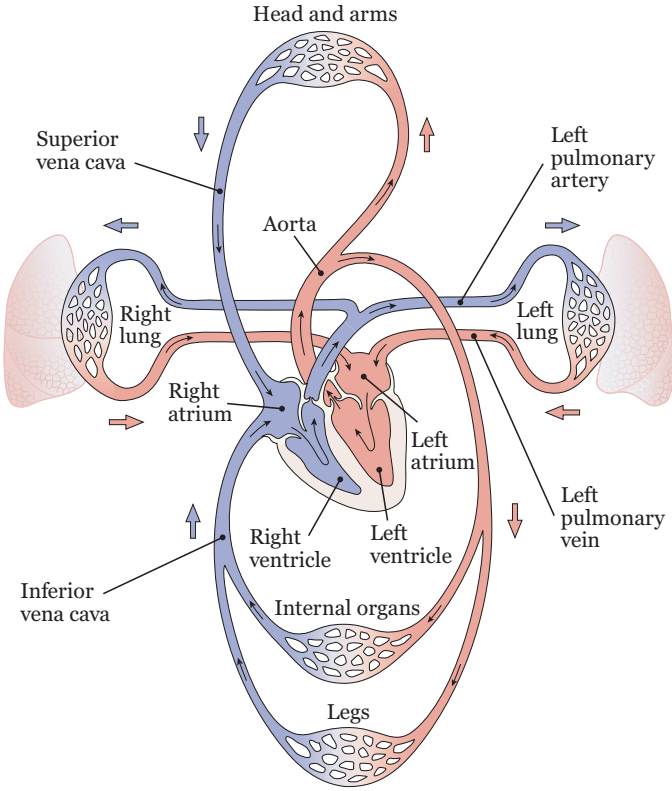

Figure 1-1: Overview of the cardiovascular system. The heart pumps blood through the high pressure systemic and the low pressure pulmonary circulation (adapted from [59]).

The *circulatory system* is composed of two circuits that are connected in series. Each of these circuits begins and ends at the heart (figure 1-1). The part of this intricate vessel network that delivers oxygen-rich blood to all parts of the body (head, arms,

legs and internals organs) is called the *systemic circulation*, while blood flow through the lungs is referred to as the *pulmonary circulation*. Blood flows through these circuits at the same rate, which is about 5.5 l/min in resting conditions.

The systemic circulation is maintained by the *left side of the heart*. The *left ventricle* (LV), the major pumping chamber of the heart, ejects the blood through the *aorta* into the systemic circulation. The aorta, the main trunk of the arterial part of the circulation, branches off in numerous *arteries*. These arteries are further subdivided into smaller tubes, called *arterioles*, which in turn branch off in the smallest vessels, the *capillaries*. The thin capillary walls allow rapid exchanges of oxygen, carbon dioxide, substrates, hormones, and other molecules and, for this reason, are called *exchange vessels*. The capillaries containing blood with lower oxygen content collect and form *venules*, which in turn converge into *larger veins*. The *right atrium* (RA) receives the venous blood through two major vessels: the *superior* and the *inferior venae cavae*. The walls of the veins are considerably thinner than the arterial walls because the blood pressure is lower.

The blood collected in the RA is then pumped into the *right ventricle* (RV). The RA and RV together constitute the *right side of the heart*. Venous blood with low oxygen content is ejected by the RV in the *pulmonary arteries* towards the lungs. The gas exchange between the air and the blood takes place in the *pulmonary capillaries*, the walls of which are thin enough to permit gas exchange. The oxygen-rich blood then returns to the left atrium (LA) through four *pulmonary veins,* where after it is again passed to the LV.

1.3 The heart

1.3.1 Gross anatomy

The *heart* is the central organ in the *cardiovascular system*. It is located in the anterior portion of the mediastinum, i.e., the space between the lungs in the thoracic cavity. A typical adult heart measures approximately 12.5 cm from the *base* (superior end of the heart) to the *apex* (inferior end), and weighs about 300 g. To execute its pumping function and maintain the systemic and pulmonary circulation, the human heart is divided into *four chambers*. The left and right parts of the heart (i.e., the LA and LV, and the RA and RV, respectively) are separated from each other by the *septum* (figure 1-2).

The ventricles are arguably the most important chambers of the heart since they are responsible for pumping blood around the body. The muscular wall of the LV is considerably thicker than that of the RV, because of the higher physiological pressure its needs to develop to propel the blood into the high resistance systemic circulation. The atria, which sequentially function as blood reservoirs, conduits of blood to the ventricles and booster pumps, have relatively thin walls and are highly distensible.

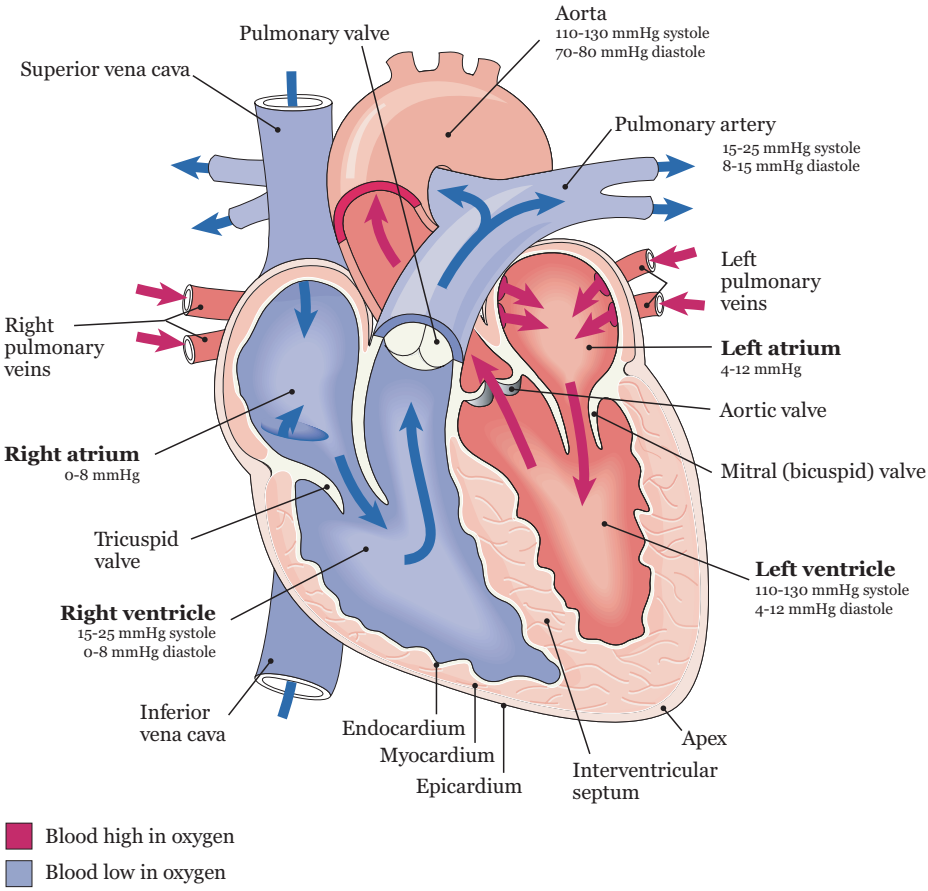

Figure 1-2: Interior view of the heart. Arrows indicate intracardiac unidirectional blood flow. Maximum and minimum governing pressures are displayed for each of the chambers and the large arteries (adapted from [59]).

Within the heart, blood is kept flowing in a forward direction by a system of *four unidirectional valves*, each closing and opening at the appropriate time in the cardiac cycle (see paragraph 1.5). They are embedded in a fibrous disk, which mechanically and electrically isolates the ventricles from the atria. The two valves that separate the ventricles from the circulatory system are called the *semilunar valves*. Both the *pulmonary valve* (separating the RV from the pulmonary artery) and the *aortic valve* (separating the LV from the aorta) have three cusps. Cusps are flexible flaps of connective tissue, covered by endothelium. The ventricles are separated from the atria by the *mitral valve* (in the left heart) and the *tricuspid valve* (in the right heart). The mitral valve only has two cusps, while the tricuspid valve, as its name implies, has three. The atrioventricular valves have, in addition to the cusps, thin and strong chords of fibrous tissue, called *chordae tendineae*. When the ventricles contract, small muscles in their walls (*papillary muscles*), pull these chords and help to prevent the valves from inverting into the atrium (not shown in figure 1-2).

1.3.2 The cardiac wall

On the outside, the heart is encased in a two-layered fibrous sac, the *pericardium*. The inner layer, the *visceral pericardium*, is the *epicardium* that covers the outer surface of the heart. The outer layer, or *parietal pericardium*, holds the heart firmly in place. Both layers are separated from each other by a film of thin lubricating fluid that allows the heart to move freely within this fibrous sac. The inner surfaces of the ventricles and atria, including those of the heart valves, are covered by the *endocardium*, a protective layer of endothelial cells. In addition, the ventricular endocardial surfaces include a complex network of cardiac cells that are arranged in discrete bundles, called *trabeculae*.

The *myocardium*, or middle layer, is the large mass of cardiac muscle between the epicardium and the endocardium. Cardiac muscle cells (or cardiomyocytes), embedded in an extracellular matrix (ECM), constitute the major volume of the myocardium. The rhythmic contraction and relaxation under the stimulation of electrical currents is what ultimately makes the heart to function as a pump. The structure and function of the myocardium and the cardiomyocytes are explained later in paragraph 1.6.

1.3.3 The coronary circulation

Because the heart continuously requires energy to fulfil its pump function, it is nourished by blood through a network of vessels, known as the *coronary circulation* (figure 1-3).

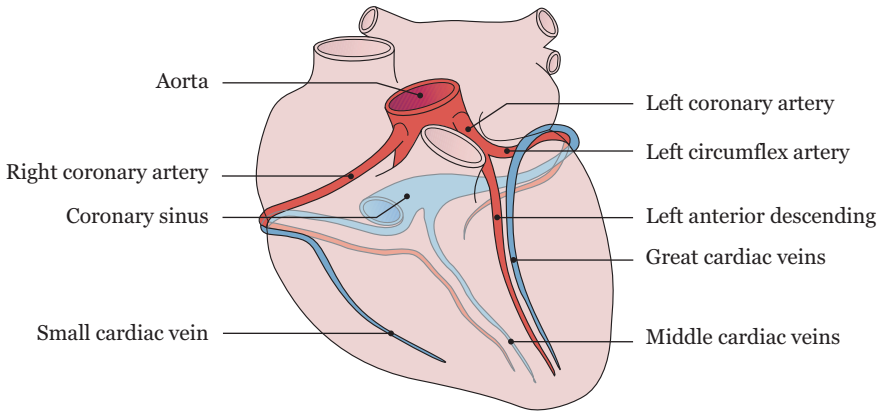

Figure 1-3: The epicardial coronary arteries: the left (LCA) and right coronary artery (RCA), and the left anterior descending (LAD) and left circumflex artery (LCX). Most of the veins of the heart (e.g., great, middle and small cardiac veins) open into the coronary sinus (adapted from [88]).

The coronary circulation consists of two main vessels, the *left* (LCA) and *right coronary arteries* (RCA). The LCA splits into the *left anterior descending* (LAD) and the *left circumflex artery* (LCX). The coronary vessels and their immediate branches course over the outer surface of the heart, and are therefore called the *epicardial*

coronary arteries. Yet, the actual blood flow reaches the myocardium by way of vessels that penetrate the walls of the ventricles, called the *intramyocardial* vessels. The veins collect most of the blood in the small, middle, and great cardiac veins, which collect in the coronary sinus and drain into the RA. A smaller portion of the LV venous flow, and much of that derived from the RV reaches the RA via the *anterior cardiac veins*. A minor fraction flows directly into the ventricular cavities by way of the *thebesian veins* (not shown in figure 1-3).

Coronary artery haemodynamics (i.e., dynamics of blood flow) is a very complex topic because blood flow is impeded by ventricular contraction. It will be further explained in chapter 6.

1.4 Blood

Blood is a life-sustaining circulating fluid which provides a constant supply of *nutrients* (oxygen and glucose) and removes the *waste products* (carbon dioxide and lactic acid) from the tissues. It consists of cells (red blood cells, white blood cells and platelets) suspended in *plasma,* a yellowish fluid consisting of 90% water. In an average adult, the blood volume amounts to approximately 5 l.

The *red blood cells* (*erythrocytes*) constitute the majority of the blood cells and take care of the transportation of oxygen. They are red only because they contain haemoglobin which is bright red in colour. Haemoglobin is a complex protein that carries the oxygen from within the lungs and releases it where needed by the tissue's cells. The *white blood cells* (*leukocytes*) are a part of the immune system and defend the body against a wide variety of invading organisms. Lastly, the *platelets* are the plate-shaped disks that trigger blood-clotting and prevent an uncontrollable loss of blood when the vessels are damaged.

1.5 The cardiac cycle

1.5.1 Electrical activation and conduction

The sequence of mechanical events during the cardiac cycle, i.e., the period between the start of a heartbeat and the beginning of the next, is a direct consequence of the contraction and relaxation of the cardiomyocytes. The generation and conduction of the electrical impulses that excite the cardiomyocytes, is taken care of by the heart's *conduction system* (figure 1-4).

Activation of the heart normally begins in the *pacemaker cells* of the *sinoatrial node* (SA node), located in the wall of the RA between the orifice of the superior and inferior venae cavae. The electrical currents travel rapidly through a network of specialized fibres, including the *internodal pathways*, which distribute the stimulus from the SA node to the *atrioventricular node (*AV node*)*, the *Bundle of His*, the *left and right bundle branches* and the *Purkinje fibres*, which distribute the stimulus to the ventricular myocardium.

It should be realized that the actual mechanical contraction lags behind the passage of the electrical impulses, because *excitation-contraction coupling* and *cross-bridge cycling* occurs (see paragraph 1.6.2)

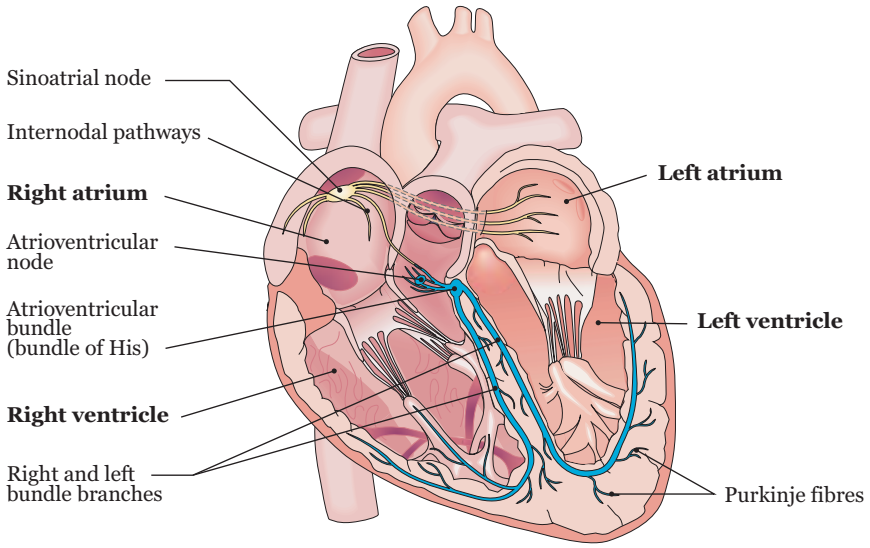

Figure 1-4: The major components of the conduction system of the heart, permitting initiation and conduction of action potentials throughout the atria and ventricles (adapted from [59]).

The sequence of excitation and conduction of action potentials is finely tuned to obtain a highly efficient pump function. The atria contract within 60 to 90 ms, while the bulk of the ventricular myocardium contracts within 70 ms. The delay of the propagation of the action potential through the AV node by 80 to 100 ms allows the atria to complete contraction before the ventricles start to contract.

1.5.2 Electrocardiogram

The electrical currents that are generated during *activation* (depolarization) and *deactivation* (repolarization) spread not only within the heart, but also throughout the body. The signal that represents the heart's electrical activity can be measured with a number of electrodes placed on the body surface, and is called an *electrocardiogram* (ECG). A typical ECG signal is shown in figure 1-5. The different waves that comprise the ECG represent the sequence of depolarization and repolarization waves and thus determine the timings of contraction and relaxation of the atria and ventricles, as explained in paragraph 1.5.3.

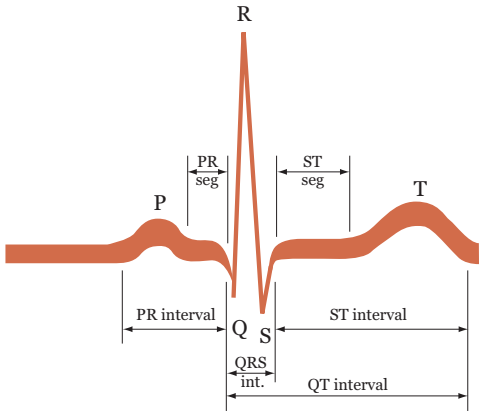

Figure 1-5: Typical ECG signal from a person in sinus rhythm. P-wave: atrial activation; QRS-complex: ventricular activation; T-wave: ventricular deactivation (adapted from [59]).

In clinical electrocardiography, the ECG signal is used to monitor the electrical activity of the heart and to diagnose cardiac disease. An ECG signal is also commonly used as a time reference for many haemodynamic and/or mechanical measurements.

1.5.3 Mechanical events of the cardiac cycle

Figure 1-6 displays the time course of *aortic pressure* (P_{ao}) and *flow* (Q_{ao}), *transmitral flow* (Q_{tm}), *left ventricular pressure* (LVP) and *volume* (LVV) and *left atrial pressure* (LAP) during an entire cardiac cycle, along with the corresponding *heart sounds* and the *ECG*. The information below focuses on the left side of the heart. On the right side, the exact same phases occur, but at lower pressure levels.

It is convenient to divide the cardiac cycle into seven phases. The first phase begins with the P-wave in the ECG, representing LA activation. The last phase of the cardiac cycle ends with the appearance of the next P-wave.

Atrial systole: When the LV is filled with about 70% of its capacity, the LA contracts and pushes an additional 30% of the total volume into the LV. The blood volume in the LV cavity at the end of LA systole is referred to as the *end-diastolic volume* (EDV) and typically amounts to 120 ml. The corresponding LV *end-diastolic pressure* (EDP) equals 8-12 mmHg.

Isovolumic contraction: At end-diastole, the LV is stimulated to contract as a result of the QRS-complex. Cardiomyocyte contraction leads to a rapid increase in LVP. No volume changes occur in this interval because the mitral and aortic valves are closed. The LV is said to *contract isovolumically* until LVP equals P_{ao}.

Rapid ejection: The aortic valve does not open until LVP exceeds P_{ao}. During the rapid ejection phase, the cardiomyocytes begin to shorten, thereby reducing the volume of the LV. Aortic flow increases rapidly until LVP reaches *maximum systolic pressure* (120 mmHg). At that moment, P_{ao} also reaches its maximum value, P_s.

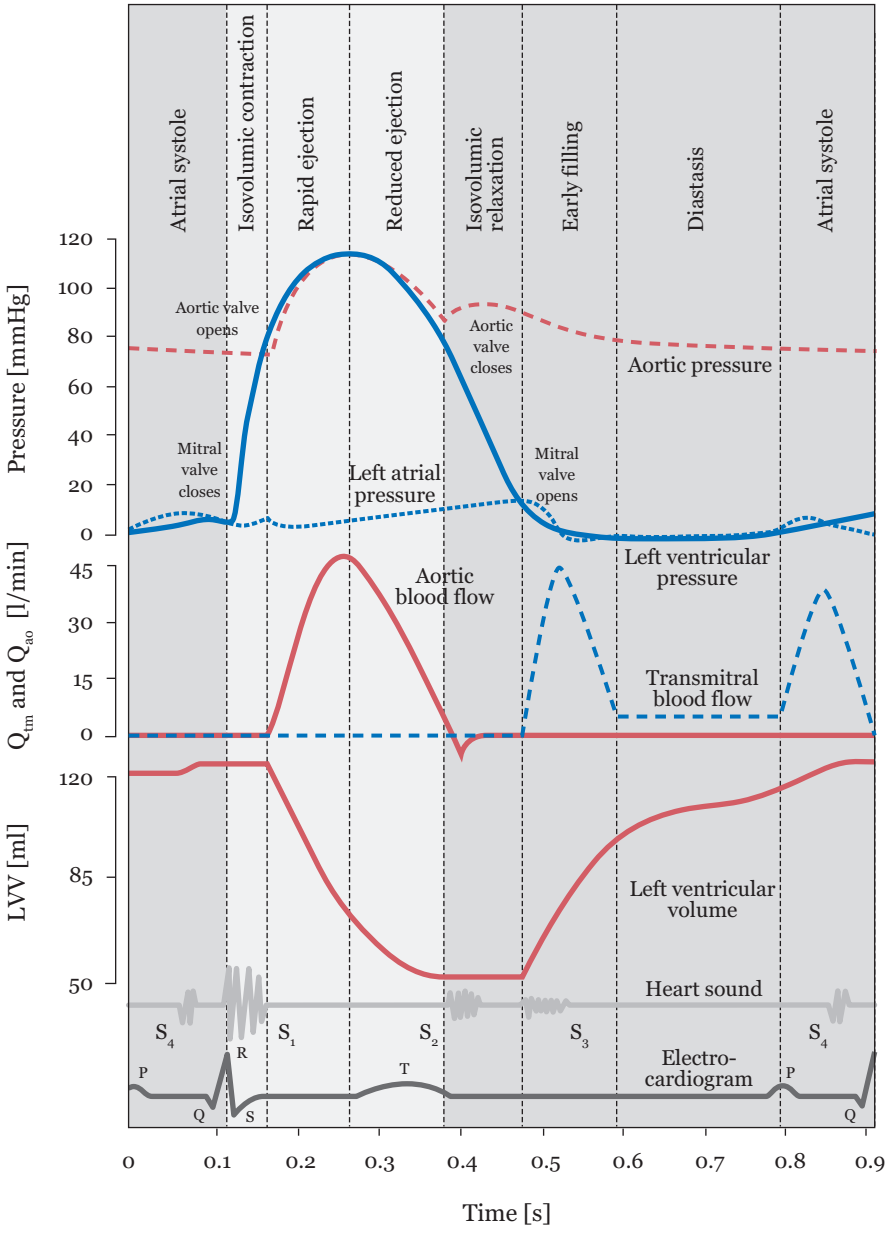

Figure 1-6: Time course of left ventricular pressure (LVP) and volume (LVV), left atrial pressure (LAP), aortic pressure (P_{ao}) and flow (Q_{ao}), and transmitral flow (Q_{tm}) during the cardiac cycle. Timing of opening and closing of the valves is also shown. Ventricular systole (clinical definition) is represented in a light shade of grey. Diastole is shown in the darker shade of grey (adapted from [263]).

Reduced ejection: During the reduced ejection phase, active tension starts to decrease, the rate of ejection declines, and LVP falls slightly below P_{ao}. However,

aortic flow continues due to kinetic (or inertial) energy of the blood. As LVP keeps falling, a point is reached when the total energy of blood within the LV is less than the energy of blood in the aorta. At this point, aortic blood starts to flow back towards the LV, causing the aortic valve to close abruptly. The volume of blood that remains in the LV at the end of the reduced ejection phase is called the *end-systolic volume* (ESV) and is typically 50 ml. The ejected blood volume is referred to as the *stroke volume* (SV), which is about 120 – 50 = 70 ml.

Isovolumic relaxation: After closure of the aortic valve, the LV continues to relax. As long as LVP remains higher than LAP, the closed mitral valve prevents blood flow from the LA into the LV; this is the period of *isovolumic relaxation*.

Early filling: When LVP falls below LAP, the mitral valve opens, allowing the blood accumulated in the LA during systole to flow rapidly into the LV; this is the *early filling phase*. The LV continues to relax despite the inflow.

Diastasis: As the LV continues to fill with blood and expand, it become less compliant. Filling slows down considerably as LVP and LAP converge. Diastasis ends when the LV is filled with about 70% of the SV, after which the LA starts to contract again.

In clinical practice, *ventricular systole* (lighter shade of grey in figure 1-6) is generally seen as the isovolumic contraction and ejection phase, whereas *diastole* (darker shade of grey) then refers to the remainder of the cardiac cycle, i.e., the isovolumic relaxation and filling phase. Diastole is the longer phase which takes up about two thirds of the cardiac cycle. However, when considering the heart as an integrated muscle-pump system, where contraction and relaxation are regarded as two phases of systole in the same way as they constitute two essential phases of an active twitch, Brutsaert and Sys' definition of systole and diastole would be more appropriate [45]. This is further elaborated upon in chapter 5.

1.6 Myocardial structure and function

1.6.1 Cardiomyocyte structure

To fulfil its pumping function, the left ventricular myocardium is largely made of *cardiomyocytes*, joined end-to-end by *intercalated disks* (figure 1-7A and B). These intercalated disks contain gap junctions, which provide electrical continuity between cells, so that excitation can easily reach every cell.

A cardiomyocyte a an elongated, branched, cylindrical cell with a diameter of about 12-20 μm and length of about 50-100 μm (figure 1-7B). Within the cell, *myofibrils* run parallel to the long-axis of the cardiomyocyte (figure 1-7C). Lighter and darker striations can be observed in myofibrils. The darker parts are called A-bands, while the lighter striations are known as I-bands. The I-bands are bisected by dark Z-lines that delimit the fundamental contractile unit of striated cardiac muscle, i.e., the *sarcomere* (figure 1-7D). The length of one sarcomere is about 1.8-2 μm in resting conditions.

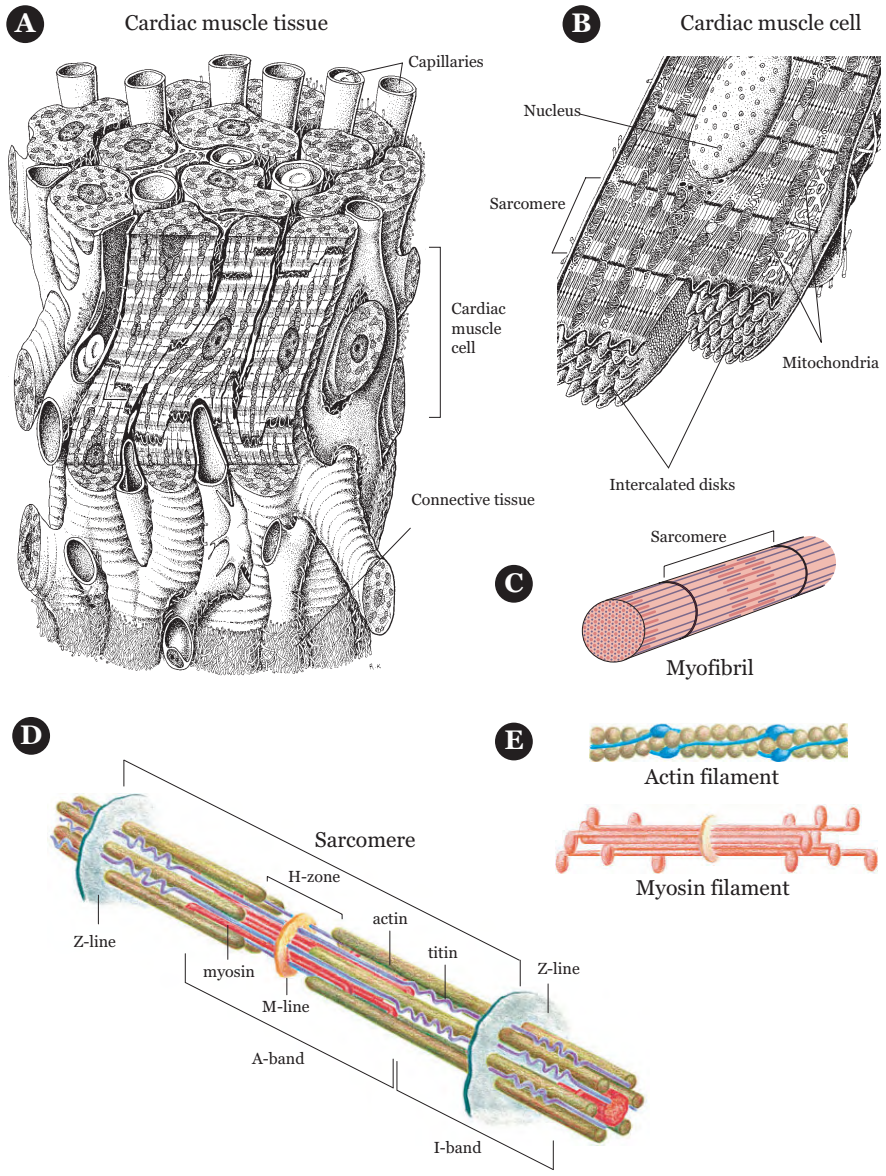

Figure 1-7: Organization of cardiac muscle tissue. A: A small cardiac muscle tissue sample; B: Cardiac muscle cell (or cardiomyocyte), showing the striated structure of the myofibrils (C), which in turn consist of sarcomeres; D: Schematic representation of one sarcomere; E: Schematic representation of an actin and myosin filament (adapted from [76, 263]).

A single sarcomere consists of *thick filaments*, which are composed largely of *myosin*. The myosin filaments are confined to the A-band. The I-band, on the other hand, is characterized by the presence of *thin filaments* that run from the Z-lines towards the centre of the sarcomere (M-line), and are composed mainly of *actin* and *the troponin-tropomyosin complex* (figure 1-7E). It is due to the *interaction* between the

thick and thin filaments that *active tension development* and *shortening* of the cardiomyocytes can occur.

1.6.2 Cardiomyocyte contraction and relaxation

The primary role of the cardiomyocyte is to develop active tension and to relax. The underlying processes of active tension development can be divided in *excitation-contraction coupling (ECC)*, *cross-bridge cycling* and *ATP production*.

Excitation-contraction coupling is the process by which *depolarization* at the cell surface initiates interaction between actin and myosin so that cardiomyocytes can produce tension and shorten.

The contractile machinery of the cardiomyocyte is directly influenced by the presence of *cytosolic calcium* (Ca^{2+}). When a cardiomyocyte is activated by an action potential, Ca^{2+} enters the cell through Ca^{2+} channels located on the cardiac cell membrane (*sarcolemma*). This triggers a subsequent release of Ca^{2+} stored in the *sarcoplasmic reticulum* (*"calcium-induced calcium release"*).

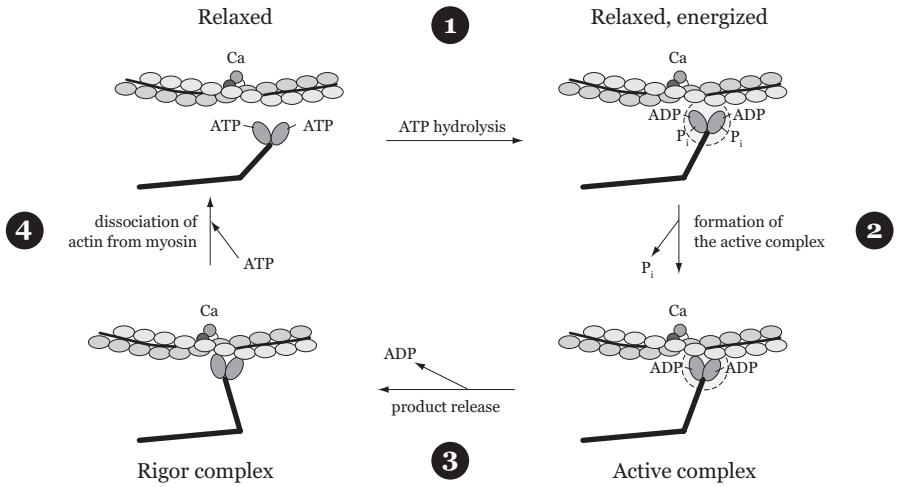

Figure 1-8: Four steps in the cross-bridge cycle. The cycle starts when ATP binding to myosin has caused the muscle to relax. Step 1: Hydrolysis of ATP brings the cross-bridge into a relaxed, but energized state (indicated with a circle). Step 2: Attachment of myosin to actin forms the active complex. Energy from ATP is still associated with the cross-bridge. Step 3: Release of ADP leads to a low-energy rigor bond. Expenditure of energy allows the cross-bridge to perform mechanical work (power stroke). Step 4: ATP binds to the rigor complex, which dissociates the myosin cross-bridge from actin. The muscle returns to its resting state (ATP: adenosine triphosphate, ADP: adenosine diphosphate, P_i: inorganic phosphate) (adapted from [159]).

When Ca^{2+} is diffused in the cytoplasm, it causes a conformational change in the *troponin-tropomyosin complex*, allowing for a cyclic interaction between actin and myosin by means of *cross-bridges*. This *cross-bridge cycling*, depicted in four steps in figure 1-8, continues as long as the Ca^{2+} concentration remains elevated and results in a "*rowing*" movement between the myosin heads and the actin, so that the actin

and myosin filaments can slide past each other and the sarcomere is able to shorten and to develop force. This phenomenon is referred to as the *sliding filament theory*. The number of cross-bridges that are formed, and therefore the force of contraction, depends on the concentration of Ca^{2+} within the cardiomyocyte. During relaxation, the intensity of cross-bridge cycling starts to decrease because the cytoplasmic Ca^{2+} concentration is rapidly lowered through several pathways, which in turn again induces a conformational change in the troponin-tropomyosin complex.

The energy for cross-bridge cycling is supplied by adenosine triphosphate (ATP), which is broken down into phosphate (P) and adenosine diphosphate (ADP) during the cycle (figure 1-8). ATP is produced in the mitochondria (figure 1-7B) by oxidative phosphorylation, for which oxygen is obligatory. This explains why cardiac function is directly dependent on *coronary blood flow*.

1.6.3 Micro- and macrostructure of the myocardium

1.6.3.1 Relation between structure and function

The myocardium is a *heterogeneous structure* consisting of cardiomyocytes, an extracellular matrix (ECM, often referred to as the connective tissue), blood vessels, nerves and interstitial fluid. Its mechanical properties are assumed *non-linear*, *anisotropic*, *time-varying* and, moreover, *spatially inhomogeneous* [296].

Detailed and accurate knowledge of myocardial structure is necessary to understand how *uniaxial* force generation at the cellular level is converted to *three-dimensional* deformation of the ventricular walls during systole and diastole. Few will debate that the *microstructure* as well as the *fibre organization* of the myocardium are two major determinants of ventricular macroscopic pump function. Despite many investigations in the last 500 years, myocardial fibre organization and the resulting force transmission pathways are still not fully understood. The relation between cardiomyocyte mechanics, fibre organization and ventricular mechanics therefore remain the subject of many interesting studies at the moment [171].

Two *opposing schools* currently exist that aim to provide a detailed description of myocardial *macrostructure*. The majority claims that the ventricular mass is arranged on the basis of an *interweaving network* of myocardial fibres within a network of fibrous tissue [202, 280], while a smaller minority continues to argue that the myocardium is arranged in the form of a "*ventricular myocardial band*" [334, 335]. Neither school, however, questions the anisotropy of the myocardium at the *microscopic* level.

1.6.3.2 Interweaving network

Over the years, it has become accepted that the myocardium is a complex three-dimensional network of myocardial fibres, functioning as an electrical and mechanical functional unit (i.e., a functional *syncytium)*. The 'sponge-like' ECM in which the fibres are embedded, has a complex and extensive structure of its own. It consists of an intricate network of non-contractile filaments (i.e., endomysium, perimysium and epimysium) orientated both transversely and parallel to the long-axis of the cardiomyocytes [296].

Recent studies concerning the mean fibre orientation [280] entirely support the classic observations of Streeter et al. [304]. They described the myocardium as a *continuum* in which myofibre orientation varied smoothly across the myocardial wall, like an opened-up Japanese fan. In the midwall, halfway between the epicardium and endocardium, the fibres lie in the circumferential plane. In the 10% of wall thickness closest to the endocardial surface, fibres are lying upward to the right, about +60° oblique to the circumferential plane. In the 10% of wall thickness closest to the epicardial surface, the fibre angle is downward to the right, averaging –60° oblique to the circumferential plane, thus overlapping the endocardial fibres at a 120° angle. At the endocardial and epicardial surfaces, fibres are almost vertical in some areas, i.e., parallel to the long-axis of the LV (figure 1-9).

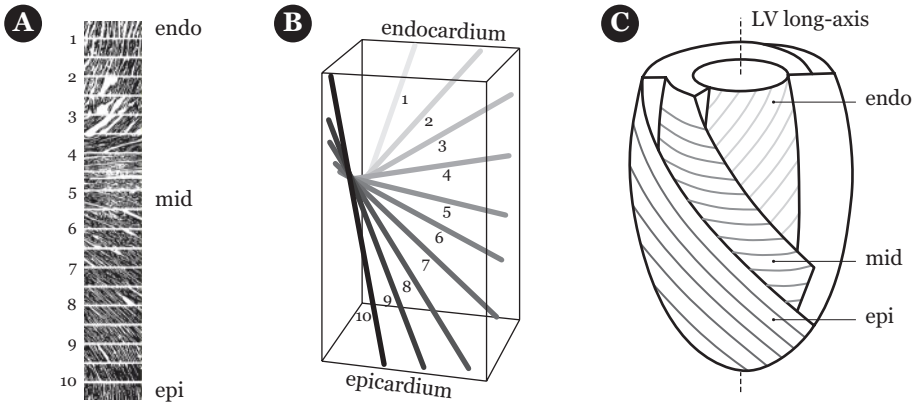

Figure 1-9: A: Fibre angles in successive sections taken from a heart. All sections are parallel to the epicardial plane; B: Idealized representation of fibre orientation; C: Idealized fibre organization in the ventricular wall (endo: endocardial wall, mid: mid-wall, epi: epicardial wall) (adapted from [303, 304]).

Based on a number of quantitative studies on cardiac structure in the dog, Legrice et al. [188] found increasing evidence that there are some *discontinuities* in the myocardial architecture. They showed that the myocardium is composed of discrete myocardial *sheets* or *laminae*, four to six cardiomyocytes thick, and separated from adjacent laminae by an extracellular collagen network. The cardiomyocytes within such a layer are tightly coupled by *endomysial collagen*, whereas the adjacent myocardial laminae are loosely coupled by *perimysial collagen* (figure 1-10) [187]. The laminae are oriented predominantly in planes spanned by the cardiomyocyte axis and the radial direction, and were found to run from the subendocardium toward the subepicardium. The latter observation, however, was contestated by Criscione et al. [63], who described the myolaminae as highly discontinuous structures, which begin and end many times between the inner- and outer wall. The spaces between the laminae give rise to *cleavage planes*, which permit the rearrangement of muscle fibre bundles when wall thickness changes [60, 187, 188]. In a numerical model, Costa et al. [60] showed that the myocardial laminae are deforming structures which represent the *dominant* source of *radial wall thickening* during contraction.

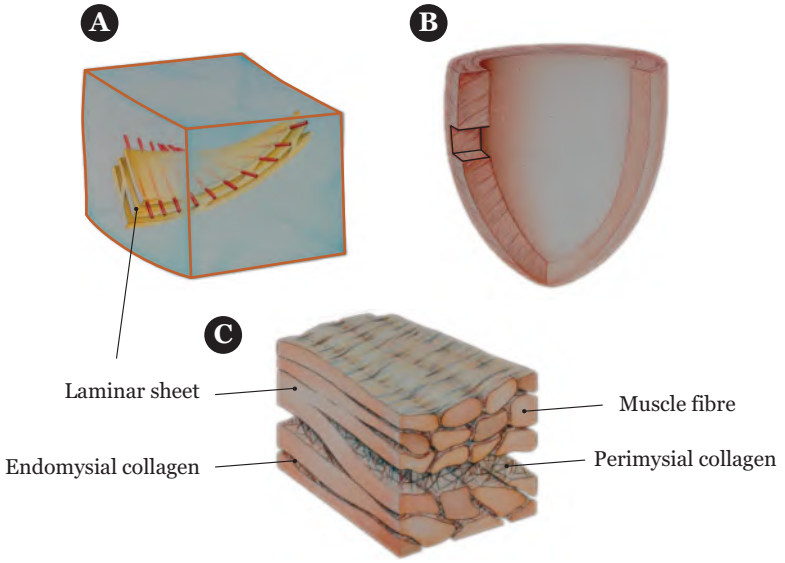

Figure 1-10: Cardiac microstructure according to Legrice et al. A: Transmural segment of the ventricular myocardial wall (B) containing sheets of tightly coupled cardiomyocytes. The sheets run in an approximately radial direction; C: Cellular arrangement in a tissue block: the fine lines represent the different components of the extracellular collagen matrix (adapted from [188]).

1.6.3.3 Ventricular myocardial band

Based on experimental research on more than 1000 meticulously dissected hearts belonging to different species, Torrent-Guasp et al. [171, 335, 336] proposed an alternative, yet very controversial concept regarding myocardial macrostructure. He basically argued that the abovementioned, more conventional description of architecture was merely sufficient to explain the microscopic structure of the myocardium within arbitrarily chosen "*tissue blocks*", but fails to describe the overall force transmission pathways in the myocardial wall. He advocated that the myocardium of both the RV and LV exists as a continuous muscle band [334], the so-called *ventricular myocardial band* (VMB). This band, of course, is composed not only of cardiomyocytes, but also of connective tissue and other nonmuscular elements [171].

It was demonstrated that the ventricular myocardium can be relatively easily unwrapped in three steps, although with some resistance, along a natural *cleavage* plane. Uncoiling the myocardium reveals the existence of a single straight VMB, extending from the pulmonary artery to the aorta (figure 1-11). At the centre of the uncoiled band, a fold is observed that twists the band by 180° and delineates the basal and apical loops. The basal loop runs from the pulmonary artery root (a) to the central fold (b), and the apical loop runs from the central fold to the aortic root (c). The VMB band thus produces two helicoid spirals, which delimitate two cavities, being the RV and LV. A detailed description of the successive steps for unwrapping the myocardial band can be found in [334] or online at http://www.torrent-guasp.com.

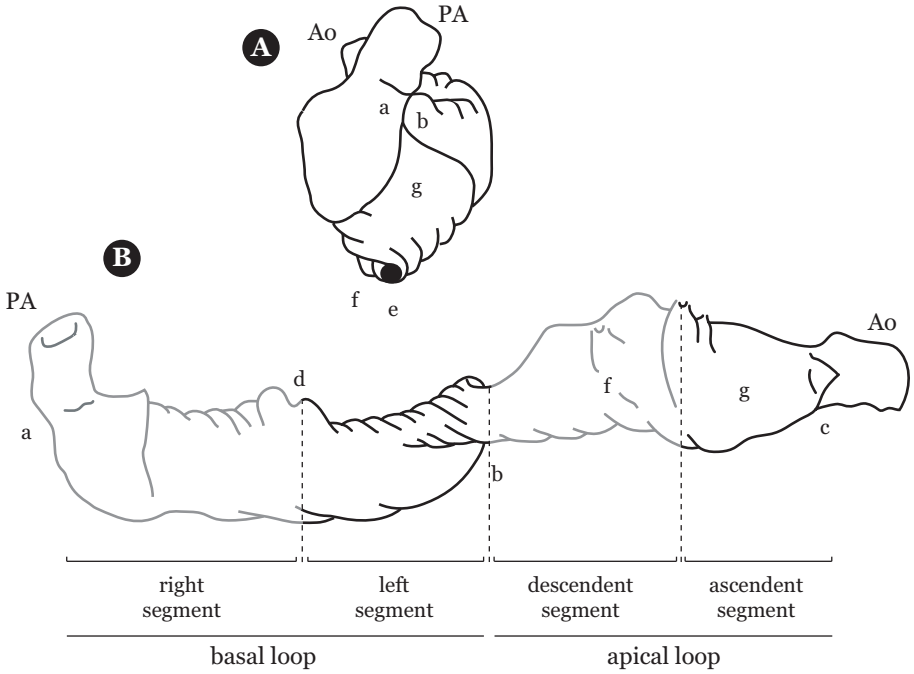

Figure 1-11: Torrent-Guasp's view of the ventricular myocardial band (VMB). A: Schematic representation of the ventricular mass; B: The myocardial band can be divided into two loops, the basal loop and the apical loop (PA: pulmonary artery, Ao: aorta) (adapted from [336]).

New ideas about the relationship between the sequential myocardial band contraction and the phases of the cardiac cycle have been outlined in detail in [334-336]. One of the most intriguing, but also most controversial aspects of Torrent-Guasp's unique "model", is the description of upward wall motion, which is supposed to cause suction of blood into the LV during early diastole [335]. He compared it to the way the contraction of the dorsal musculature of the snake is associated with lengthening and upward motion of the body structure. However, his theory is far from widely accepted. Well established knowledge about diastolic suction is summarized in chapter 5.

1.7 Cardiodynamics

1.7.1 Ventricular performance and function

Assessment of *ventricular performance,* i.e., the performance of the ventricle as a pump is of vital importance in clinical cardiology for diagnosis, monitoring, and treatment.

Stroke volume (SV) is the most important factor in an examination in a single cardiac cycle. It is the volume of blood that is ejected during one heartbeat, and is calculated as the difference between EDV and ESV (see paragraph 1.5.3). However, when

considering ventricular pump function over time, *cardiac output* (CO) is of interest. It is defined as

$$CO = SV \cdot HR \tag{1-1}$$

with HR the heart rate. CO is precisely adjusted so that all peripheral tissues receive an adequate blood supply under a variety of conditions. The usual resting values for adults are 5 to 6 l/min. Most healthy people showing a high *cardiac reserve* can raise their CO to 18 to 30 l/min during heavy exercise. CO and SV are controlled by various factors (figure 1-12), as outlined in paragraphs 1.7.2 and 1.7.3.

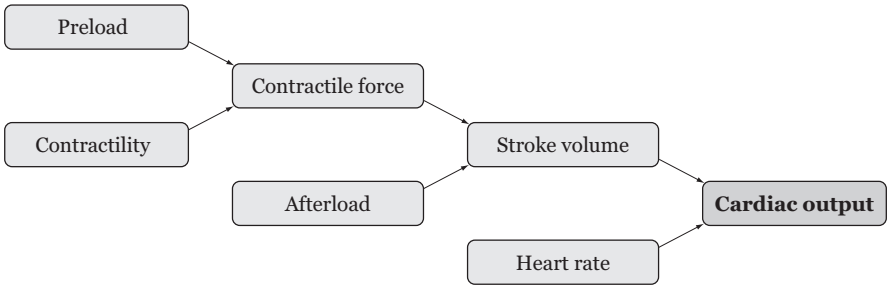

Figure 1-12: Determinants of cardiac output (CO), a measure of left ventricular pump performance.

Ejection fraction (EF), on the other hand, is a commonly used measure of *ventricular function*; it is defined as

$$EF = (SV/EDV) \cdot 100\% \tag{1-2}$$

Even though it is a non-specific index of ventricular contractility, it has proven to be valuable in predicting the severity of heart disease in individual patients.

1.7.2 Factors controlling stroke volume

Stroke volume, the major determinant of cardiac output, is influenced by the *contractile force* of ventricular muscle and the ventricular *afterload*.

1.7.2.1 Contractile force

Contractile force is mainly affected by (i) *ventricular preload* and (ii) *ventricular contractility* (or *inotropism*).

Preload can be defined as the *initial stretching* of the cardiomyocytes prior to contraction, and is thus related to the sarcomere length. In the intact heart, however, sarcomere length cannot be measured and alternative, clinically more useful indices such as EDP or EDV are used. Figure 1-13 summarizes the determinants of preload.

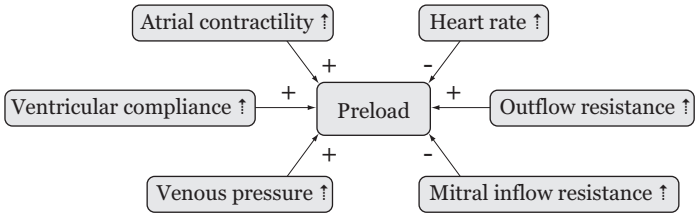

Figure 1-13: Primary determinants of left ventricular preload.

The relation between preload (either measured by EDV or EDP) and SV is known as the *Frank-Starling principle* (or *Starling's law of the heart*), and is considered one of the fundamental concepts in cardiovascular physiology (solid curve in figure 1-14A).

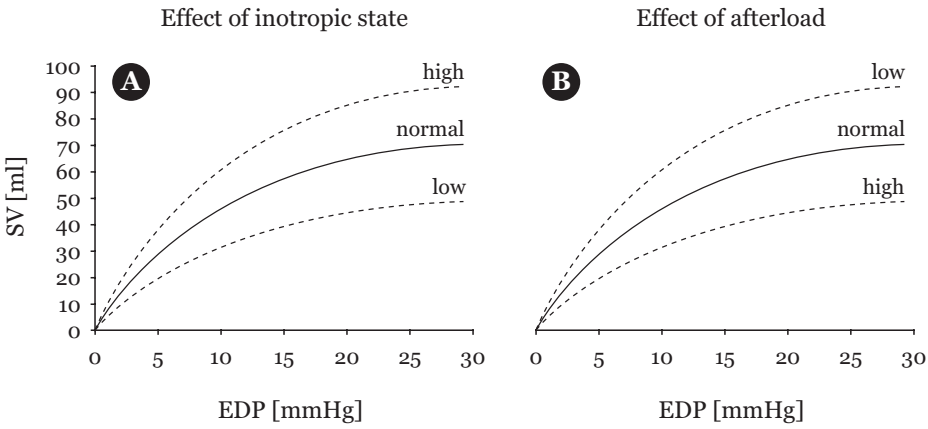

Figure 1-14: Starling's law of the heart: Ventricular performance, in terms of stroke volume (SV) or cardiac output (CO), increases as preload increases. A: Effect of inotropic stimulation on SV; B: Effect of afterload changes on SV.

Under a given contractile state, an increase in preload causes SV to increase, whereas a reduction in preload decreases SV by altering the force of contraction of the cardiac muscle. The underlying physiology can be found in the *length-tension relation* of the cardiomyocyte. This relation is generally agreed to be the result of changes in actin-myosin overlap with stretch [119] and, to a greater degree, to a length-dependent variation in Ca^{2+} release from the sarcoplasmic reticulum and to the cytosolic Ca^{2+} sensitivity of the contractile proteins (*length-dependent activation*). The latter phenomenon is illustrated in figure 1-15.

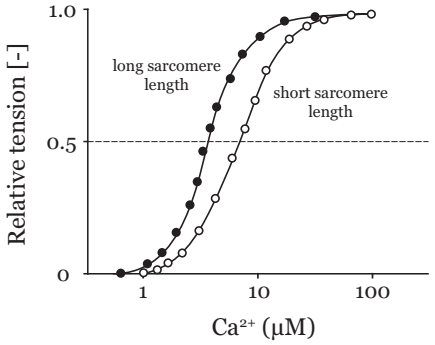

Figure 1-15: Sensitivity of the contractile machinery to Ca^{2+} concentration, illustrating the principle of length-dependent activation (adapted from [193] [159]).

Ventricular contractility is the second determinant of contractile force. It is an ill-defined concept referring to the *intrinsic strength* of the ventricle, independent of changes in preload. Valuable insights in the concept of ventricular contractility have been gained from studies on geometrically linear preparations such as trabeculae or isolated papillary muscle strips [37]. In those studies contractility is commonly defined as a certain level of *functional capacity* (as measured by a quantity such as isometric force development or initial shortening velocity) when measured at a *given sarcomere length* (preload).

To make adjustments to the varying demands of the circulatory system, contractility can be altered by *autonomic innervation* or *circulating hormones*. Contractility can be altered when one or both of the following events occur:

- The *amount* of Ca^{2+} is changed: in normal conditions, not enough Ca^{2+} is available to occupy all of the troponin molecules. Hence, an increase in the availability of Ca^{2+} would increase the number of cross-bridges activated.
- The *affinity* of the myofilaments for Ca^{2+} is changed.

Even though both regulatory mechanisms of contractile force (changes in preload and changes in contractility) were once believed to represent entirely different control mechanisms, it is now clear that they are actually *very similar*. As a result, it is cumbersome to distinguish length-dependent changes from changes in contractility in the intact heart, and to define a clinically useful index of ventricular contractility.

The effect of an *inotropic stimulation* on the Starling curves is shown in figure 1-14A. Factors that increase contractility are said to have a *positive* inotropic action, while those that decrease contractility have a *negative* inotropic action. Starling curves cannot be used to assess ventricular contractile state, though, because a change in the curves may indicate either a change in contractility or a change in afterload (see paragraph 1.7.2.2).

Contractility is also influenced by HR. An increase in HR, for instance, allows more separate influxes of Ca^{2+} per minute, yielding an increase in the amount of releasable Ca^{2+}. More cross-bridges are activated, and contractility increases. This phenomenon is generally known as the *force-frequency relationship*.

1.7.2.2 Afterload

Afterload refers to the *amount of active tension* that the cardiomyocyte must generate so that shortening (ejection) can occur. Its magnitude is increased by any factor that restricts blood flow through the arterial system, such as high blood pressure or aortic valve stenosis. Similar to preload and contractility, afterload cannot be measured directly in the intact heart.

In the clinical setting, *mean aortic pressure* (MAP) or *total peripheral resistance* (TPR) against which the LV has to pump are often used as a crude estimate of afterload. TPR is calculated from

$$TPR = (MAP - RAP)/CO \approx MAP/CO \tag{1-3}$$

with RAP right atrial pressure, which is usually small compared to MAP. However, a measure of *wall stress* (σ), instead of cavity pressure, would be a closer approximation of afterload. As myocardial wall stress is very difficult to measure (because the insertion of a transducer damages the tissue at the site of the measurement) various formulae, based on highly simplified models of the LV, have been presented to estimate wall stress. The earliest, simplest models assumed a thin-walled isotropic spherical LV obeying Laplace's law, which states that the stress within the wall is proportional to LVP and its internal diameter (LVID), and inversely proportional to the wall thickness (WT):

$$\sigma = \frac{LVP \cdot LVID}{4 \cdot WT} \text{ with } WT << LVID \tag{1-4}$$

A number of alternative formulae have later been proposed to quantify longitudinal and circumferential wall stresses within an ellipsoid of revolution, a geometry that better resembles the true geometry of the LV [103, 217]. However, because the myocardial wall is inhomogeneous, consisting of cardiomyocytes embedded in an extracellular matrix, the total mechanical wall stress is born from the combination of these structures. Fibre stress (σ_f), which is the stress born from the cardiomyocytes only, would therefore be a more appropriate measure of afterload. Arts et al. [8] introduced a formula to determine fibre stress from global haemodynamic parameters and the volume of the LV wall (V_{wall}):

$$\sigma_f = LVP \cdot (1 + 3 \cdot \frac{LVV}{V_{wall}}) \tag{1-5}$$

For present-day research purposes computationally intensive numerical models with realistic LV geometries and appropriate constitutive material laws are exploited to determine fibre stress and strain. In particular the cardiac mechanics research groups from Arts et al. [6, 7, 36, 340], Hunter et al. [137, 187, 300] and from McCullogh et al. [127, 342, 343] are widely known in the field.

Figure 1-14B illustrates the effect of changes in afterload on CO. When afterload is increased, an increase in ESV will be observed, resulting in a decrease in CO and SV. The basis for the afterload dependence of CO and SV is found in the *force-velocity relation* of cardiomyocytes, which describes how the initial shortening velocity of an afterloaded cardiomyocyte decreases with increasing afterload.

1.7.3 Factors affecting heart rate

Under normal circumstances, HR is influenced primarily by the *sympathetic* (which increase HR) and the *parasympathetic nerves* (which decrease HR) to the heart and, by a lesser extent, by *circulating hormones*, such that CO can meet the circulatory demands. At rest, a typical adult heart beats at 70 to 80 BPM (beats per minute), but HR can increase to more than 200 BPM during maximal exercise.

If SV is held constant, an increase in HR would be expected to cause a proportional increase in CO. However, there exists an interaction between HR and SV: when HR increases, the duration of diastole decreases, which results in a diminished time for the LV to fill. Less filling of the LV in turn leads to a reduced EDV and decreased SV, because of the Frank-Starling principle (see paragraph 1.7.2.1).

1.8 Conclusion

The left ventricle, the most *powerful pumping chamber* in the mammalian heart, can fulfil its function thanks to well-coordinated active contraction and relaxation of cardiomyocytes, embedded in a matrix of connective tissue. The energy to accomplish this is supplied by blood flow via the coronary arteries.

Chapters 2 to 5 deal with a number of concepts and indices for quantification of *global ventricular systolic and diastolic performance* that are used in clinical practice and/or in cardiovascular research. Many, if not all of them, are derived from or are related to *cardiomyocyte mechanics*. It should be remembered throughout this work, though, that they rely on highly simplified assumptions with respect to geometry, and temporal and spatial inhomogeneity of myocardial structure.

In chapter 6 the influence of systolic and diastolic wall mechanics upon *coronary blood flow* is discussed.

2

Chapter 2

Invasive Assessment of Global Left Ventricular Mechanics

The contents of this chapter were published in

American Journal of Physiology, Heart and Circulatory Physiology
2006 Apr; 290 (4): H1474-83
Nonlinear Isochrones in Murine Left Ventricular Pressure-Volume Loops: How Well Does the Time-Varying Elastance Concept Hold?
Claessens TE, Georgakopoulos D, Afanasyeva M, Vermeersch SJ, Millar HD, Stergiopulos N, Westerhof N, Verdonck PR and Segers P.

2.1 Introduction

In the past decades, continuous left ventricular (LV) *pressure* and *volume* measurements have been widely used both in the research laboratory and in the clinical setting to provide quantitative information about *global LV mechanics* and *LV function*. The simultaneous use of a *pressure catheter* and a *conductance catheter*, a device capable of providing a real-time continuous assessment of ventricular volume by measuring electrical conductivity of blood, is still considered the gold standard for invasive recording of real-time pressure-volume signals.

This chapter deals with the technical principles underlying left ventricular pressure (LVP) and volume (LVV) measurements and consequently explains how the acquired data can be used for quantification of the (time-varying) mechanical properties of the LV. The emphasis of this chapter is on the applicability of the *linear time-varying elastance concept* in the mouse LV.

2.2 Pressure measurements

In the catheterization laboratory, pressure is often measured with a *fluid-filled catheter–transducer system*, which transmits the pressure in the cardiac chamber to be examined to a hub transducer through a column of fluid in the catheter. Cardiac catheterization involves inserting a cardiac pressure catheter into a vein or artery and then carefully manipulating and advancing it under fluoroscopic control into the desired location, being the *LV* (or the *coronary arteries*). In cardiovascular research, however, the standard for high-fidelity pressure measurements is the more expensive *micromanometer catheter*, a flexible tube with a pressure sensor at the distal end [39]. When *simultaneous* pressure and volume measurements are required, such a micromanometer catheter can be equipped with a number of electrodes for measuring instantaneous volume.

2.3 Volume measurements

2.3.1 Conductance catheter

2.3.1.1 Technical aspects

Conductance catheterization is a technique that provides a *continuous volume signal* by measuring the *conductance* of the intraventricular blood pool. Basically, a catheter with a number of electrodes (depending on the size of the mammal's heart) is introduced along the *longitudinal axis* of the LV [222]. The electrodes are equally spaced near the far end of the catheter. The distal end of a conductance catheter is shown in figure 2-1.

The first and the last electrode generate an *electric field*, while the remaining electrodes are used pair wise to measure segmental *voltage gradients*. To generate the electric field and acquire the voltage signals, the device must be connected to dedicated equipment.

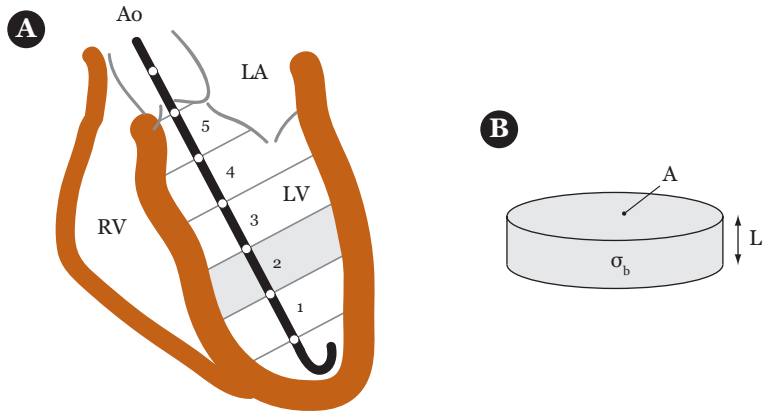

Figure 2-1: A: Conductance catheter, a device for measuring instantaneous left ventricular volume (LVV). The position of the catheter is shown for larger mammals, such as dogs and humans. In mice the catheter position is different; B: The blood pool is considered as a stack of cylindrical segments with ground surface A, height L and specific conductivity σ_b (LV: left ventricle, RV: right ventricle, Ao: aorta, LA: left atrium) (adapted from [299]).

To obtain the actual cavity volume from the measured voltage gradients, it is assumed that the blood pool consists of a stack of *cylindrical segments* (figure 2-1A), each with a uniform current density, so that the equipotential planes are assumed to be flat. Knowing that

$$R = 1/G = (1/\sigma_b)\cdot(L/A) \tag{2-1}$$

the *volume* of a single cylindrical segment V can be calculated from

$$V = L\cdot A = (L/\sigma_b)\cdot(L/R) = (L^2/\sigma_b)\cdot G \tag{2-2}$$

with R the electrical resistance, G the electrical conductance, σ_b the specific electrical conductivity of blood, L the height and A the ground surface of a single cylinder (figure 2-1B). However, in the real ventricle, the relation between $V_i(t)$, the true volume of the i^{th} segment, and $G_i(t)$, the measured conductance of the i^{th} segment, is given by

$$V_i(t) = (1/\alpha)\cdot(L_i^2/\sigma_b)\cdot(G_i(t) - G_{p,i}(t)) \tag{2-3}$$

where L_i is the interelectrode spacing of the i^{th} segment, $G_{p,i}(t)$ is the effective conductance of structures contributing to $G_i(t)$ but outside the blood pool of the i^{th} segment, and α is the *slope correction factor* (or *gain factor*). As L_i is fixed for catheters used in most studies, *total true cavity volume* V(t) can be written as

$$V(t) = (1/\alpha)\cdot(L^2/\sigma_b)\cdot G_{tot}(t) - V_c(t) \tag{2-4}$$

with V_c, a *correction term (volume offset)* caused by the conductance of structures surrounding the ventricular blood pool (myocardium, lungs, etc.), and given by

$$V_c(t) = (L^2/(\sigma_b \cdot \alpha)) \cdot \sum_{i=1}^{n} G_{p,i}(t) = (1/\alpha) \cdot V_p(t) \quad (2\text{-}5)$$

and

$$G_{tot}(t) = \sum_{i=1}^{n} G_i(t) \quad (2\text{-}6)$$

with V_p the non-calibrated volume offset and n the total number of volume segments. Blood conductivity σ_b is generally determined with a measuring cell [172]. Yet, in order to obtain a well calibrated volume signal, the volume offset V_c and the slope correction factor α remain to be determined.

2.3.1.2 Volume offset

Parallel conductance G_p is the consequence of electrical conductivity beyond the blood pool and results in a volume offset V_c [68]. Quantification of V_c, which may contribute for about 50 to 70% to the total volume signal [352], is required to measure *absolute* volumes [11]. Although many LV performance indices, such as stroke volume (SV) and cardiac output (CO), can be readily determined from *relative* volume changes, knowledge of absolute values is essential to calculate ejection fraction (EF) or to assess chamber remodelling, which often plays an important role in disease conditions. Difficulties in estimating V_c are considered the main reason that the conductance catheter has remained mainly a research tool [118], even after more than two decades following its introduction.

Two approaches for determining V_c have initially been described: *suction* and *dilution*. In the first method, introduced by Baan et al. [13], V_c is estimated from transiently reducing cavity volume to zero, so that all current flows through the tissues surrounding the cavity. The remaining conductance G_p was therefore entirely due to the parallel conductance, because cavity volume was zero. For obvious reasons, however, this method cannot be used in humans. White et al. [352] recently modified this approach so that it becomes applicable in mammals without reducing volume to zero.

Dilution is an alternative, more common method for estimating V_c. According to equation 2-4, the total conductance is given by

$$G_{tot}(t) = \frac{\alpha}{L^2} \cdot \sigma_b \cdot V(t) + G_p \text{ with } G_p = \frac{\sigma_b}{L^2} \cdot V_p \quad (2\text{-}7)$$

This equation allows to determine a single value for G_p by changing the value of σ_b (by injecting a hypertonic salt solution into the pulmonary artery) and assuming that V(t) as well as α and G_p remain unaffected by the intervention itself. During the intervention, *end-diastolic* and *end-systolic* $G_{tot}(t)$ are sampled and plotted one versus the other. Because actual SV is constant, changes in the measured conductance values are only due to altered blood conductivity. The following equation is then obtained:

$$G_{es}(\sigma_b) = G_{ed}(\sigma_b) + \frac{\alpha}{L^2} \cdot \sigma_b \cdot (ESV - EDV) \quad (2\text{-}8)$$

with EDV and ESV the end-diastolic and end-systolic volume. Assuming that the SV (i.e., the slope of this relationship) remains constant, parallel conductance G_p can be found as the intersection point between the *line of identity* ($G_{es} = G_{ed}$) and the line obtained by linear extrapolation of the experimental (G_{es}, G_{ed}) data points. This principle is illustrated in figure 2-2.

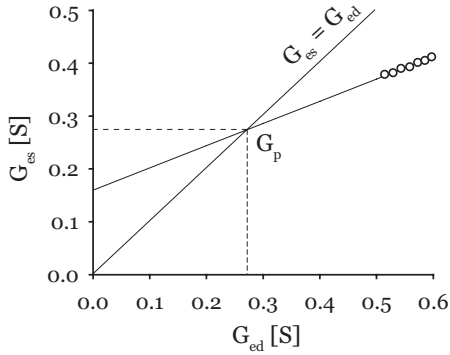

Figure 2-2: When σ_b goes to zero, $G_{es} = G_{ed} = G_p$. Thus G_p is the intersection point between the line of identity and the line obtained by linear regression of the experimental (G_{es}, G_{ed}) data points.

It should be acknowledged that this calibration technique only yields a *single value* for G_p (or V_p) that does not vary during the cardiac cycle. This assumption may appear questionable from a theoretical point of view, since atrial filling, myocardial shape changes and the simultaneous ejection of blood in the right ventricle (RV) could potentially influence G_p. Some studies where LVV was varied over a broad range have shown that G_p may be volume-dependent [3, 33], and employing a single value for G_p in such circumstances would result in significant inaccuracies. However, several other isolated and in situ heart studies revealed that $G_p(t)$ can be wel approximated by a single value for most purposes [48, 183, 322].

Another potential limitation of this extrapolation method is that a small variation in the values of G_{ed} and G_{es} will yield a large variation in the *extrapolated* value of G_p.

2.3.1.3 Gain factor

The *gain factor* α is introduced in the relation between actual LV cavity volume and measured conductance to account for the consequences of the *non-homogeneous dispersion* of the electrical field within the cavity, and for the fact that the cylindrical segments do *not fully cover* the LV long-axis. Most frequently, α is determined by means of an alternative, independent method for measuring SV (e.g., thermodilution or a flow probe):

$$\alpha = \frac{SV_{\text{conductance catheter}}}{SV_{\text{alternative technique}}} \quad (2\text{-}9)$$

Using this formula, a single value for α is obtained which is assumed invariant throughout the cardiac cycle [13]. This assumption may appear somewhat surprising given the number of theoretical studies that predict a volume-dependent α(V) [222, 276]. However, the extent to which it may affect conclusions drawn by any study employing the conductance catheter must therefore be assessed on an individual basis [321].

2.3.1.4 Conductance catheterization in small animals

The conductance catheter technique was initially applied and validated in large animals, where it showed highly reproducible serial volume measurements. Only recently, this technique has also become available for the in vivo mouse heart [112]. Apart from the obviously required *miniaturization* and *modification* of the devices (fewer electrodes are used), conductance catheterization in the mouse necessitates a great deal of experience from the researcher, in particular for the calibration procedure. Some potential practical limitations are mentioned further in paragraph 2.5.5. Nevertheless, the conductance catheter technique provides a very *powerful* technique to assess cardiovascular function in the mouse [58, 109, 112, 146, 282].

2.3.2 Sonomicrometry

Sonomicrometry is an alternative method to acquire continuous LVV signals. In this technique, LVV is estimated by continuously measuring the distance between a number of *microcrystals*, strategically placed on the endo- and/or epicardium. Microcrystals are small piezoelectric crystals that transmit and receive ultrasonic pulses; the measured time-of-flight of the ultrasonic pulses is related to the distance between the microcrystals. Skilful techniques for implanting the microcrystals are required, and important assumptions with respect to LV geometry need to be made.

2.4 Pressure-volume loops

2.4.1 Pressure-volume framework

For several decades, the pressure-volume (P-V) framework has provided physiologists with a single approach for studying the *active* and *passive* properties [128], the *energy consumption* [310], and the *pump performance* of the mammalian LV and its *interaction* with the arterial circulation [318]. Because of the general applicability of this framework to ventricles of all species, P-V analyses have become standard in studies of mice, humans, and animals of all sizes in between [46]. It has proven to be a fertile area of research, and has significantly broadened our understanding of LV mechanics and haemodynamics [156].

It is already more than one century ago, that Frank [98] represented the cycle of ventricular contraction as a loop in a P-V diagram. This method was well known to 19th century engineers who utilized pressure and volume to characterize the function of mechanical pumps [109]. A P-V loop is accomplished by plotting LVP and LVV on

appropriately scaled axes (LVV on the horizontal axis and LVP on the vertical axis). The P-V points loop in an *anticlockwise* direction (figure 2-3A).

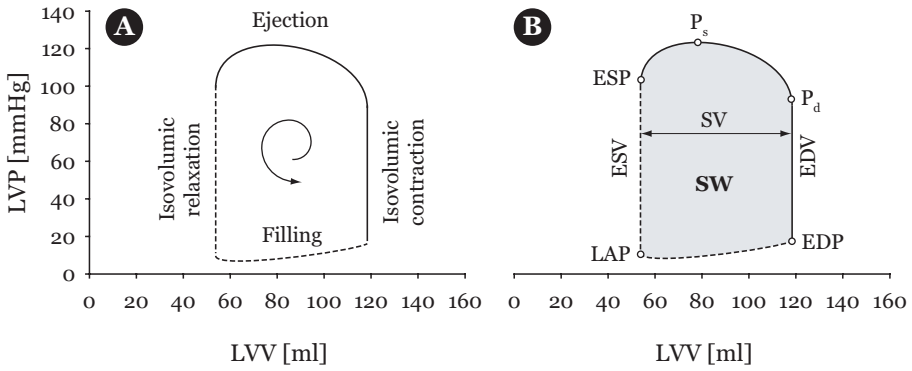

Figure 2-3: Schematic representation of a pressure-volume (P-V) loop with representative human left ventricular pressure (LVP) and volume (LVV). The systolic phase includes isovolumic contraction and ejection; the diastolic phase includes isovolumic relaxation and filling; B: Physiological measurements that can be retrieved from a P-V loop. Left atrial pressure (LAP) equals LVP at the beginning of early filling. The maximum aortic pressure (P_s) approximates maximum LVP. LVP at the onset of ejection approximates diastolic aortic pressure (P_d) (ESV: end-systolic volume, EDV: end-diastolic volume, ESP: end-systolic pressure, EDP: end-diastolic pressure).

Its major use in physiology textbooks is to illustrate the *external stroke work* (SW) that the LV does to the loading system represented by the area *circumscribed* by the loop [275]. Assuming that transvalvular pressure gradients are negligible, a P-V loop can also provide useful information about aortic pressure (P_{ao}) and left atrial pressure (LAP) at discrete time points in the cardiac cycle (figure 2-3B).

As will be outlined in the following paragraphs, there are many advantages to displaying LVP as a function of LVV on a P-V diagram under changing *preload* and *afterload* conditions. Altering loading conditions allows for the assessment of the end-systolic and end-diastolic pressure-volume relationship, and offers information about energy consumption. Acquisition of LVP and LVV also led to the concept of linear time-varying elastance, a semi-empirical concept that has been developed to describe the time-varying mechanical LV properties during the cardiac cycle.

2.4.2 End-diastolic and end-systolic pressure-volume relationships

2.4.2.1 Boundaries of P-V loops

If an intervention is performed that *acutely* alters *preload* or *afterload*, a family of P-V loops is obtained. Balloon occlusion of the inferior vena cava has shown to be an elegant way to achieve a change in preload. This procedure enables a rapid, purely mechanical reduction in preload, which prevents reflex mechanisms and is easily reversed by deflation of the balloon. Afterload can be changed for example by injection of phenylephrine, which increases blood pressure, or by mechanically

(partially) occluding the aorta. Note, however, that loading alterations ideally should be performed by interventions that minimally affect *intrinsic myocardial function*.

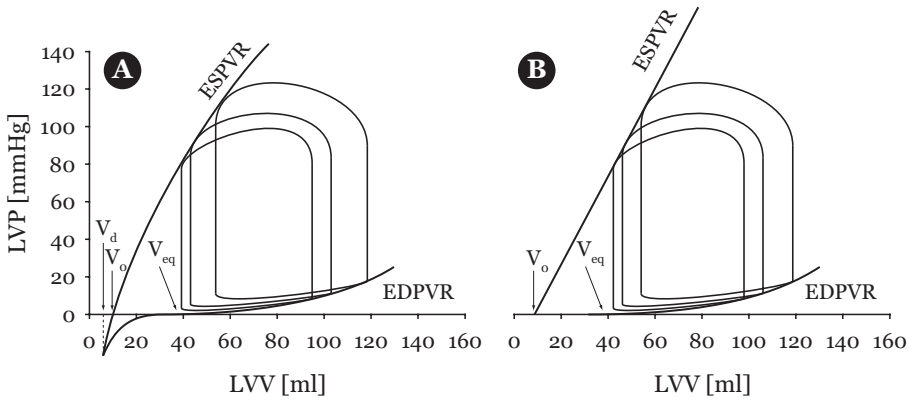

Figure 2-4: A: A family of P-V loops is obtained by gradually changing preload or afterload. The upper left and lower right P-V points delineate the end-systolic (ESVPR) and end-diastolic pressure-volume relationship (EDPVR), respectively; B: In practice, the shape of the ESPVR and EDPVR is often idealized (V_o: intercept of the ESPVR, V_d: functionally dead volume, V_{eq}: equilibrium volume).

The end-systolic and end-diastolic points of a family of P-V loops delineate *two distinct boundaries*, namely the *end-systolic* (ESPVR) and *end-diastolic pressure-volume relationship* (EDPVR). The ESPVR is commonly associated with the *active* mechanical properties of the LV, while the EDPVR provides information about the LV in its *passive* state. Both boundaries are shown in figure 2-4A. In practice, however, they are often idealized (figure 2-4B).

2.4.2.2 End-diastolic pressure-volume relationship

The shape of the EDPVR, the "*passive*" P-V relationship, is intrinsically *non-linear*, which can be attributed to the complex shape of the LV and to the different mechanical properties of myocardial constituents: in the lower pressure area, *compliant elastin* and *sarcomeric titin* account for the low stiffness [178], while at higher strains, stiffness is caused by titin and *collagen fibres* [46]. Several mathematical functions have been suggested to describe the EDPVR in the positive pressure range, such as *exponential*, *power* or *cubic* curves:

- Exponential: $P = \alpha + \beta \cdot e^{\gamma \cdot V}$
- Power: $P = \alpha + \beta \cdot V^{\gamma}$
- Cubic: $P = \alpha + \beta \cdot V + \gamma \cdot V^2 + \delta \cdot V^3$

with α, β, γ and δ constants. Nikolic et al. [233] proposed a *logarithmic* function to describe the P-V relation in the negative pressure range: $P = \alpha \cdot \ln((V - V_d)/(V_{eq} - V_d))$, with α a constant, V_d the dead volume, and V_{eq} the equilibrium volume (figure 2-4).

In the *isolated* LV, the *slope* of the EDPVR defines its compliance (dV/dP) and stiffness (dP/dV). Its non-linear character implies that these values change with LVV (and LVP). In *in situ* ventricles, however, it is important to realize that factors *extrinsic* to the myocardium, such as *pericardial restraint*, *interaction with the RV* and *intrathoracic pressure* modulate this relationship, so that the EDPVR does not only reflect the mechanical passive properties of the LV. Yet, the EDPVR does provide information about the extent to which LV filling is restricted during diastole. This discrepancy is particularly important in the clinical setting.

Estimation of $V_{eq,}$ i.e., the *intercept* of the EDPVR with the volume-axis, has shown to be very difficult, especially because of the existence of myocardial resting tone [190] and of the abovementioned extrinsic factors [116]. V_{eq} is an important mechanical property of the LV since *diastolic recoil* occurs when V_{eq} is above end-systolic volume (ESV).

Quantitative assessment of LV passive properties and the existence of diastolic recoil are major topics in diastology, and will be further discussed in chapter 5.

2.4.2.3 End-systolic pressure-volume relationship

Interest in the "*active"* P-V relationship, which is obtained by fitting a curve through the *upper left* P-V points of each loop, was revived when accurate canine P-V data became available [275]. Studies on the canine LV indicated that, as an approximation, the ESV to which an LV contracts is a linearly increasing function of end-systolic pressure (ESP), both during isovolumic and ejecting contractions [314]:

$$ESP = E_{es} \cdot (ESV - V_0) \tag{2-10}$$

This simple linear equation, known as the ESPVR, is used by many modellers of the cardiovascular system, and allows to evaluate LV performance (in terms of SV) when EDV and ESV are known:

$$SV = (EDV - V_0) - ESP/E_{es} \tag{2-11}$$

Although there was no a priori reason to expect that the ESPVR is linear – it was simply an *experimental observation* – it has been accepted for a long time, mainly because a straight line allows for uncomplicated definitions of its *slope*, $E_{es,}$ and its *intercept* with the volume-axis, V_0 (figure 2-4B).

In excised supported mammalian LV experiments, Suga et al. [316] found that with positive inotropic agents, E_{es} *increased* with relatively little change in V_0. Conversely, with negative inotropic agents (e.g., calcium channel blockers), E_{es} was shown to *decrease*, with relatively little change in V_0. A change in E_{es} was also observed when HR was altered (due to the *force-frequency relationship*). On the other hand, E_{es} was virtually *unaffected* by changes in preload and afterload, unless preload or afterload was excessively unphysiological [274]. For these reasons, E_{es} was considered a relatively *load-independent index* of *left ventricular contractility*. Since then, it has known a widespread use for research purposes to detect *changes* in LV inotropic state in cows [160], humans [125], pigs [133], dogs [140, 314] and rodents [109]. However, a crucial question that currently remains unanswered is how the measured values of E_{es} should

be interpreted for assessment of myocardial contractile state in *a given subject*. This intriguing topic is elaborated on in chapter 4.

The shape of the ESPVR has always been subject to great interest but is also subject to controversy [218]. Experiments in the dog [218, 308, 317, 338], mouse [109, 151] and rat [186] LV have shown a significantly curvilinear ESPVR when pressure and volume were analyzed under a *wider range* of loading conditions than did Suga et al. Additionally, it became evident that large alterations in *contractile state* could influence the non-linearity (curvilinearity) of the ESPVR [47, 154, 278]. Under such circumstances, the ESPVR obviously cannot be characterized by a single slope, and E_{es} should not be used as an index of ventricular contractility, because the slope intrinsically depends on the specific pressure range of the available data.

Therefore, some investigators proposed non-linear mathematical functions that better describe the ESPVR, such as *quadratic* (*parabolic*) [47, 154] or *exponential* [317] functions. Unfortunately, the suggested alternative fitting curves were merely phenomenological and did not allow for a physiological interpretation of the contractile process. The only model with a physiological basis was provided by Mirsky et al. [218], who introduced a *logarithmic* function incorporating stiffness, geometric variables and empiric constants. A considerable drawback of the different existing ESPVR functions, however, is the lack of a standardized definition of their (local) slope, which complicates *comparisons* between study groups or within individuals in experimental research or in clinical practice.

2.4.3 Performance and energetics

The utility of the P-V diagram has been extended beyond ventricular active and passive mechanical properties to include *ventricular energetics* and *mechano-energetics* [310, 311]. Suga et al. [310, 312] found that the LV *pressure-volume area* (PVA), bound by the ESPVR, the EDPVR and the systolic part of the P-V trajectory (figure 2-5A), is highly linearly correlated with LV *oxygen consumption* rate per beat (Vo_2), in ejecting as well as in isovolumic beats (figure 2-5B):

$$Vo_2 = \alpha + \beta \cdot PVA \qquad (2\text{-}12)$$

with α and β constants.

PVA represents the *total mechanical energy* needed for the contraction of the LV, and equals the sum of *mechanical external work* (EW) or *stroke work* (SW) and what can be considered the *end-systolic potential energy* (PE) in the wall of the ventricle [310]. The PE stored in the myocardial wall at the end of systole is assumed to be totally converted into heat during IVR, and cannot be used for the next contraction cycle. The EDPVR is neglected for the sake of simplicity. Knowledge of PVA thus allows for prediction of O_2 consumption. This method was validated by determining O_2 consumption as the product of coronary flow and arteriovenous O_2 content difference. A major advantage of the whole PVA-Vo_2 concept is that no assumptions are required on the shape of the LV, its structure and the mechanical model of muscle.

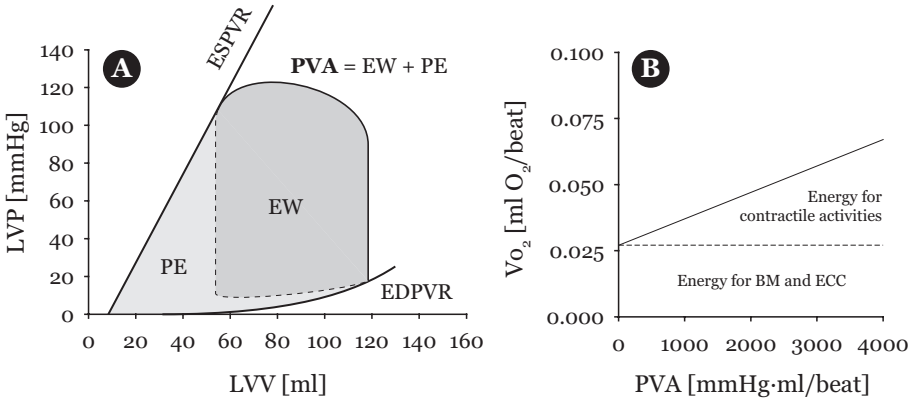

Figure 2-5: A: Illustration of the pressure-volume area (PVA). The total mechanical energy required for contraction is partially used for external work (EW). The rest is stored as potential energy (PE) in the LV wall; B: Representative example of the linear relation between oxygen consumption (Vo_2) and the PVA, obtained from pooled data in two canine ventricles [310] (BM: basal metabolism, ECC: excitation-contraction coupling).

Because both Vo_2 and PVA represent the energy input and output of the contracting LV, respectively, the Vo_2-PVA relation (equation 2-12) contains useful information on energy conversion and efficiency in a physically sound manner [311]. The *constant term* is required by the heart even when the LV is not developing any pressure nor performing any EW, and can be considered the energy needed mainly for the noncontractile activities (mainly *basal metabolism* and *excitation-contraction coupling* [313]). The *excess* Vo_2 is applied for PVA. When both PVA and Vo_2 are expressed in the same units, e.g., joule/beat, the reciprocal of the slope of the PVA-Vo_2 relationship ($1/\beta$) yields the *contractile efficiency* of energy conversion. The contractile efficiency is *load-* and *contractility-independent* and is generally about 40%, which means that 60% is dissipated as heat. Of this 40%, part is converted into EW and the remainder is stored as PE in the wall. The energy flow from O_2 consumption via ATP to mechanical EW (figure 2-6) is explained in detail in [311].

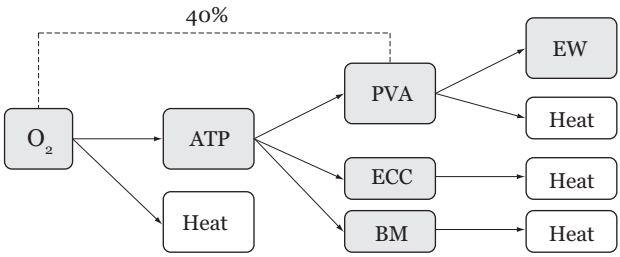

Figure 2-6: Energy flow from O_2 consumption to external work (EW) via ATP (ATP: adenosine triphosphate, ECC: excitation-contraction coupling, BM: basal metabolism, EW: external work) (adapted from [311]).

2.4.4 Linear time-varying elastance concept

2.4.4.1 Basic principles

By introducing the concept of *linear time-varying elastance*, Suga and Sagawa [314-316] contributed enormously to the understanding of ventricular mechanics. In the early 1970's, they reported very high correlation coefficients when fitting isochronal P-V data points (i.e., data points acquired at the same time instant after the onset of systole) with a *linear function* in canine hearts. They also showed that at the end of systole, all regressed isochrones seemed to converge closely to a *constant volume intercept* V_0 (figure 2-7A). Both observations led to the definition of the linear time-varying elastance function E(t) (figure 2-7B), which is given by

$$E(t) = P(t)/(V(t) - V_0) \tag{2-13}$$

This relationship implies that if one knows E(t), the time course of LVP can be predicted from the known LVV changes. As this function incorporates the time-varying proportionality between LVP and LVV, it was said to describe the time-varying stiffness throughout the cardiac cycle. As such, cardiovascular modellers started to conceive the LV as a chamber which periodically becomes stiff and soft independently of the loading condition [275].

Suga and Sugawa et al. [314] also showed that the shape of the E(t) curve was sensitively affected by inotropic interventions, so that an increase in inotropic state was reflected by an increase in the maximum value of E(t), and a reduction of the time instant of maximum elastance, t_{max}.

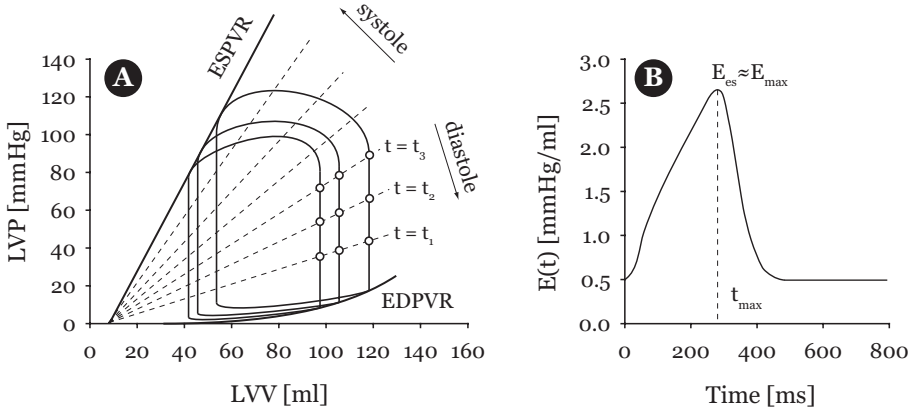

Figure 2-7: A: Principle of the linear time-varying elastance concept. Three sets of isochronal P-V data points (at $t = t_1$ to t_3) are shown. The P-V regression lines rotate anticlockwise during systole (increasing stiffness), and clockwise (decreasing stiffness) with progress of relaxation; B: The elastance function $E(t) = P(t)/(V(t)-V_0)$, representing the time-varying ventricular stiffness. The maximum value of E(t) and its timing relative to the onset of systole depend on the level of contractility.

Even though this concept has known a widespread use under cardiovascular modellers and physiologists, it should not be forgotten that the linear time-varying

elastance concept (further referred to as the E(t) concept) relies on the following *two assumptions*:

- a *linear shape of all isochrones* and *the ESPVR* in particular;
- a *common intercept of these isochrones* with the volume-axis.

In practice, these assumptions are seldom verified in P-V measurements. However, it may raise serious concerns when applied in the *mouse left ventricle*, which shows considerable non-linearities in the ESPVR. The ensuing potential non-linearities in the shape of the isochrones and its implications towards the applicability of the E(t) concept in mice are dealt with in paragraph 2.5.

2.4.4.2 Relation between E(t) and E_{es}

There is some controversy surrounding the relation between E(t) and E_{es} that may have resulted from confusion over their definitions [156].

The slope of the ESPVR, E_{es}, is found by linear regression of the upper left corners of a family of P-V loops, *regardless* of the actual timing. It may therefore not perfectly coincide with the maximum value of E(t), since the upper left corners need not to be isochronal data. However, negligible differences would be expected.

The confusion between the definitions has even increased when the index E_{max} was introduced. To determine E_{max}, one had to calculate $E(t) = P(t)/(V(t)-V_o(t))$ for a series of P-V loops – mind the time-varying volume intercept! – and determine its *maximum* value. It is possible that E_{max} is significantly higher than E_{es}, and in contrast to E_{es}, does not fall at the upper left corners of the P-V loops [156]. In literature, not much attention is paid to these discrepancies, and the indices are often used interchangeably. In most studies E_{es} is determined, although it is mistakenly referred to as E_{max}. E_{es} is, however, a more useful measure of ventricular contractility.

As outlined in paragraph 2.5, the difference between E_{es} and E_{max} can be substantial.

2.4.4.3 Normalization of linear time-varying elastance

It has been shown that the *normalized elastance curve* $E_N(t_N)$ (i.e., E(t) normalized both by its peak amplitude, E_{es}, and the time to peak elastance, t_{max}) in normal isolated canine hearts was fairly independent of loading conditions, contractile state, and heart rate (figure 2-8) [314, 316]. Senzaki, moreover, found a remarkable similarity in the shape of the $E_N(t_N)$ curves between subjects with various cardiac diseases [283].

The consistent shape of the $E_N(t_N)$ curves has led to the introduction of a number of methods to estimate the ESPVR and its slope E_{es} without loading interventions [283, 284]. These so-called *single-beat methods* are clearly advantageous over the conventional multiple-beat methods because changing loading conditions could lead to reflex-mediated changes in haemodynamics. An additional strength of these single-beat approaches is their potential to be applied *non-invasively*. The clinical applicability of such a non-invasive single-beat technique is demonstrated in chapter 4.

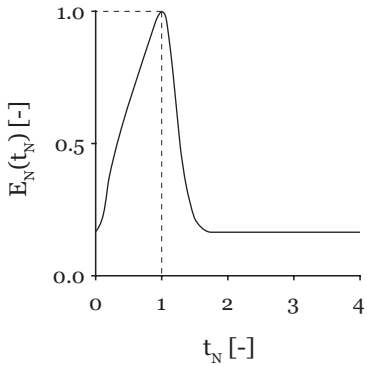

Figure 2-8: The normalized elastance curve $E_N(t_N)$ is obtained by normalizing E(t) by its peak amplitude, E_{es}, and the time to peak elastance, t_{max}.

2.5 Non-linear isochrones in mice

2.5.1 Study rationale

Manipulations of the mouse genome are increasingly being performed for the exploration and identification of the mechanisms underlying LV function in the healthy and diseased heart. However, the number of techniques for investigating the phenotypic expression of these alterations in vivo has been rather limited, due to the *small size* of the murine heart and its *rapid heart rate* (500 to 790 BPM) [146]. Thanks to recent advances in biomedical engineering technology, there is the opportunity to accurately acquire LVP and LVV with a *miniaturized* combined pressure and conductance catheter [109]. Imaging techniques that are used in larger mammals, such as echocardiography and magnetic resonance imaging (MRI), are also available for mice, but they require extensive offline analysis, have a limited temporal and spatial resolution, and are unable to visualize the P-V data during the study [109].

It was outlined in paragraph 2.4.4.1 how acquisition of LPV and LVV signals can provide information about the time-varying mechanical LV properties using the classic E(t) concept. In the present study, we critically analyzed the two assumptions underlying the E(t) concept (i.e., fixed volume intercept V_0 and linear isochrones) and discussed its applicability in the mouse LV. This study was undertaken because a pronounced curvilinear ESVPR has been observed in the mouse LV in baseline conditions, a finding that appears incompatible with the assumption of linear isochrones. More specifically, we have

- investigated the time-varying character of the volume intercept V_0;
- searched for the best regression algorithm for the ESPVR and the isochrones;
- analyzed the time-dependent changes in the shape of the isochrones throughout the cardiac cycle.

2.5.2 Methods

2.5.2.1 Experimental protocol

Thirteen anaesthetized, *open-chest mice* weighing 140±18 g (strains C57BL6 and C57BL6/129) were used in this study. The protocol was approved by the Animal Care and Use committee of the Johns Hopkins University and conformed to the institutional guidelines. Anaesthesia was initiated with methoxyflurane inhalation followed by intraperitoneal injection of urethane (750 mg/kg), etomidate (20-25 mg/kg) and morphine (1-2 mg/kg) dissolved in normal saline. Supplemental intraperitoneal anaesthesia (one-fifth dose) was provided if needed so that the animals remained unresponsive to tail pinch by forceps as assessed by changes in heart rate and blood pressure. A heating pad was placed underneath the animals, and the temperature was set to 37.5 °C. All animals were intubated with a blunt 19-gauge needle via a tracheotomy and were ventilated using a constant flow ventilator with 100% oxygen at 120 breaths/min and a tidal volume of 200 µl. The left external jugular vein was exposed by blunt dissection under topical lidocaine anaesthesia, and a 31-gauge needle was inserted directly into the lumen. Fluid supplementation was achieved using 12.5% human albumin infused at 20 µl/min for 5 min.

The chest was entered through an anterior thoracotomy by visualization under a dissecting microscope. An apical stab using a 26-gauge needle allowed for the placement of a *custom-made four-electrode conductance catheter* with a *dual pressure sensor* (Millar Instruments, Houston, TX). The catheter was advanced along the long-axis of the LV to place the distal tip (containing a pressure sensor) in the aortic root and the proximal electrode just inside the endocardium. With the catheter fixed in place, the animal was turned over on its side. A correct position of the catheter was verified by online visualization of the shape and position of the P-V loops (figure 2-9).

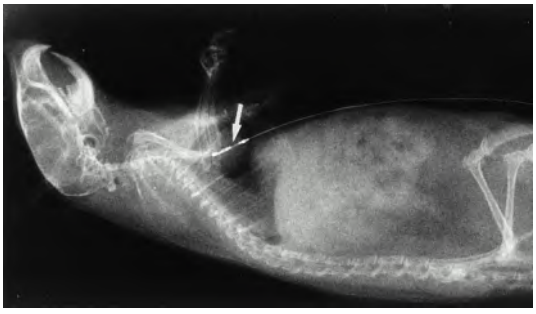

Figure 2-9: X-ray photograph of a mouse on its side with the catheter positioned in the LV and ascending aorta.

A limited lateral thoracotomy was performed, and the descending aorta was dissected free from the spinal column just above the level of the diaphragm. The time-varying LVV was determined using the formula of Baan et al. [13] (see paragraph 2.3.1.1). The *gain factor* α used for calibration of the conductance catheter was obtained by

matching the conductance-derived SV to the one measured with a flow probe (1 RB, Transonic, Ithaca, NY), positioned around the thoracic aorta and filled with conducting gel, on a beat-by-beat basis during transient vena cava occlusion (VCO). This provides an estimate of the gain over a large loading range instead of a single estimate at steady state [112]. In addition to the determination of the gain factor, the offset of the volume signal (V_c) due to parallel conductance G_p is required to obtain a fully calibrated signal. V_c was assessed by an infusion of hypertonic saline (bolus injection 5-10 µl 35% saline), as described by others [13, 48]. Pressure and volume signals were sampled at 2 kHz and transferred to an Intel Pentium IV PC for subsequent analysis.

2.5.2.2 Data acquisition and treatment

Data were obtained at baseline conditions (BL) and during gradual preload reduction, accomplished through manual VCO. The inotropic state was kept at basal level during the whole experiment. VCO generally yielded about 15-25 cycles, typically consisting of 180 samples each.

In order to obtain an objective, automated determination of the *onset of systole*, this moment was taken as the time instant in the P-V plane where LVP was 4 mmHg higher than the pressure corresponding to a volume of 98% of the maximum LVV (EDV). Visual control of the obtained time points proved this algorithm to be sufficiently robust (figure 2-11). These time points served as reference for the identification of the isochronal data points.

End-systolic data points were found using an iterative way described previously [154, 282]. Briefly, the P-V data points yielding the maximum P/V ratio were linearly regressed. The obtained volume intercept V_0 was subsequently used in the next iteration step to regress the data points corresponding to a maximum $P/(V-V_0)$ ratio. These steps were repeated until the slope of this regression line converged to a constant value E_{es} ($\varepsilon < 0.1\%$), which typically occurred after three to four iterations.

Both LVP and LVV data were filtered using a Savitsky-Golay filter of the 3rd order over a 15 sample points window sliding over the data [282]. For each cycle, standard haemodynamic parameters such as heart rate (HR), end-diastolic pressure (EDP), end-systolic pressure (ESP), stroke volume (SV) and end-diastolic volume (EDV) were derived. Further post-processing of the continuous P-V signals was performed using a custom-made application in Matlab Release 14 (The Mathworks, Natick, USA).

2.5.2.3 Fitting the ESPVR and the isochrones

The end-systolic P-V points were fitted to a

- linear: $ESP = \alpha_1 \cdot ESV + \alpha_0$,
- quadratic: $ESP = \alpha_2 \cdot ESV^2 + \alpha_1 \cdot ESV + \alpha_0$, and
- logarithmic: $ESP = (\alpha + \beta \cdot ESV)^{-1} \cdot \ln(ESV/V_0)$

function. The logarithmic model was chosen according to Mirsky's *elastance model* based on maximum systolic stiffness [218].

Isochronal data points were then fitted using six different regression algorithms (RA): two *linear* (Lin), two *quadratic* (Quad) and two *logarithmic* (Log), each with either a *fixed* (Fix) or a *variable* (Var) intercept with the volume-axis (all illustrated in figure 2-10).

- $RA_{Lin\text{-}Fix}$: $P = \alpha_1 \cdot V + \alpha_0$ and $P(V_{o,lin}) = 0$ (panel A)
- $RA_{Lin\text{-}Var}$: $P = \alpha_1 \cdot V + \alpha_0$ (panel B)
- $RA_{Quad\text{-}Fix}$: $P = \alpha_2 \cdot V^2 + \alpha_1 \cdot V + \alpha_0$ and $P(V_{o,quad}) = 0$ (panel C)
- $RA_{Quad\text{-}Var}$: $P = \alpha_2 \cdot V^2 + \alpha_1 \cdot V + \alpha_0$ (panel D)
- $RA_{Log\text{-}Fix}$: $P = (\alpha + \beta \cdot V)^{-1} \cdot \ln(V/V_0)$ and $P(V_{o,log}) = 0$ (panel E)
- $RA_{Log\text{-}Var}$: $P = (\alpha + \beta \cdot V)^{-1} \cdot \ln(V/V_0)$ (panel F)

For the RA with the fixed volume intercept (figure 2-10A, C and E), we extrapolated the linear, quadratic and logarithmic ESPVR to the volume-axis, yielding the constant volumes $V_{o,lin}$, $V_{o,quad}$ and $V_{o,log}$, respectively. These values were subsequently used to fit all other isochrones, such that they were mathematically restricted to include $V_{o,lin}$, $V_{o,quad}$ or $V_{o,log}$.

For the remaining $RA_{Lin\text{-}Var}$, $RA_{Quad\text{-}Var}$ and $RA_{Log\text{-}Var}$ (figure 2-10B, D and F) on the other hand, all isochronal P-V data were fitted using linear, quadratic and logarithmic functions, respectively. Next, every single isochrone was extrapolated to the volume-axis to obtain the time-varying volumes $V_{o,lin}(t)$, $V_{o,quad}(t)$ and $V_{o,log}(t)$.

In $RA_{Lin\text{-}Fix}$ and $RA_{Lin\text{-}Var}$, coefficient α_1 represents the slope of the linear isochrones. In algorithms $RA_{Quad\text{-}Fix}$ and $RA_{Quad\text{-}Var}$, α_2 represents the coefficient of curvilinearity. The coefficients α and β used in the logarithmic description combine myocardial stiffness, chamber geometry and other empiric constants [154].

2.5.2.4 Statistical analysis

The appropriateness of applying a non-linear model function (quadratic or logarithmic) to describe the ESPVR has been evaluated using *Akaike's Information criterion* (AIC), based on the principle of parsimony [177]. AIC values are calculated as

$$AIC = n \cdot \ln\left(\sum_{i=1}^{n}(P_{meas,i} - P_{est,i})^2\right) - n \cdot \ln(n) + 2 \cdot k \qquad (2\text{-}14)$$

with n the number of data couples (i.e., the number of loops), and $P_{meas,i}$ and $P_{est,i}$ the measured and estimated pressures, respectively. The number of model parameters is represented by k (linear: k = 2; quadratic and logarithmic: k = 3). The k-value that minimizes AIC corresponds to the best model. For each isochronal regression algorithm, the difference between the estimated (fitted) and the measured pressures was assessed by RMSe (*Root Mean Square error*) values, defined as

$$RMSe = \sqrt{\frac{\sum_{i=1}^{n}(P_{meas,i} - P_{est,i})^2}{n}} \qquad (2\text{-}15)$$

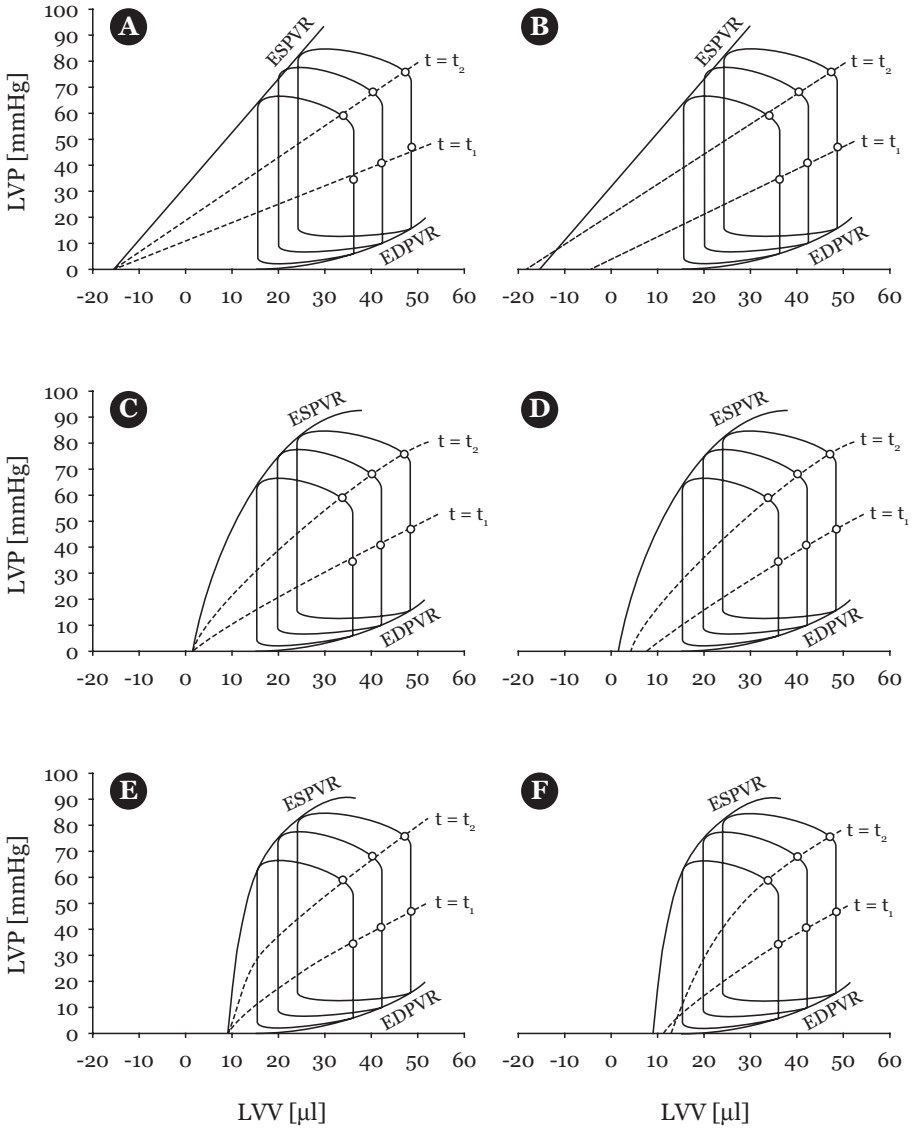

Figure 2-10: Overview of six regression algorithms (RA) for fitting isochronal pressure-volume (P-V) data. A: $RA_{Lin-Fix}$; conventional algorithm: linear isochrones converging to a fixed volume intercept $V_{o,Lin}$; B: $RA_{Lin-Var}$; linear isochrones resulting in a time-varying $V_{o,Lin}(t)$; C: $RA_{Quad-Fix}$; quadratic isochrones converging to a fixed $V_{o,Quad}$; D: $RA_{Quad-Var}$; quadratic isochrones resulting in a time-varying $V_{o,Quad}(t)$; E: $RA_{Log-Fix}$; logarithmic isochrones converging to a fixed $V_{o,Log}$; F: $RA_{Log-Var}$; logarithmic isochrones resulting in a time-varying $V_{o,Log}(t)$ (Lin: linear, Fix: fixed, Var: variable, Quad: quadratic, Log: logarithmic, ESPVR: end-systolic P-V relation, EDPVR: end-diastolic P-V relation, t_1 and t_2: two arbitrary time points during systole).

The goodness of fit was additionally assessed by the commonly used *coefficient of determination* R^2.

All time-dependent data were normalized for HR and subsequently averaged for all 13 animals. The results are expressed as mean ± SD. Statistics were performed using SPSS 12 (SPSS Inc., Chicago, IL, USA). Differences between groups were analyzed using paired t-tests. Statistical significance was assumed when $p < 0.05$.

2.5.3 Results

Table 2-1 summarizes the mouse haemodynamic data acquired at baseline (BL) and after preload reduction, accomplished by vena cava occlusion (VCO). End-diastolic pressure (EDP) and volume (EDV), stroke volume (SV) and end-systolic pressure (ESP) were significantly different between BL and VCO. A statistically significant difference was also seen for the heart rate (HR, 620 ± 36 BPM vs. 624 ± 35 BPM), because the majority of mice experienced a minute increase in HR. HR and systolic pressure were nearly identical to values reported in conscious mice [26]. Thus, despite the open-chest preparation, the cardiovascular data were very physiological.

Table 2-1: Summary of haemodynamic data during baseline (BL) and vena cava occlusion (VCO).

No.	Baseline (BL)					Vena cava occlusion (VCO)				
	HR	EDP	ESP	SV	EDV	HR	EDP	ESP	SV	EDV
	BPM	mmHg	mmHg	µl	µl	BPM	mmHg	mmHg	µl	µl
1	638	8	102	31	53	648	4	58	25	32
2	600	8	123	22	40	600	4	74	16	20
3	553	12	84	29	46	558	6	53	26	31
4	619	11	121	24	48	625	5	72	19	24
5	663	22	121	26	42	666	5	78	21	22
6	588	13	105	37	54	600	7	59	31	31
7	641	12	147	25	47	645	5	80	19	21
8	612	10	115	25	50	612	4	79	18	23
9	558	9	101	19	50	566	4	73	10	26
10	645	10	114	20	37	645	4	82	13	19
11	638	14	126	12	33	641	4	84	9	22
12	666	14	114	20	39	670	6	81	10	13
13	638	10	113	23	41	641	5	81	12	16
Mean	620	12	114	24	45	624*	5*	73*	18*	23*
SD	36	4	15	6	6	35	1	10	7	6

HR: heart rate, EDP: end-diastolic pressure, ESP: end-systolic pressure, SV: stroke volume, EDV: end-diastolic volume; * indicates $p < 0.05$ vs. baseline using a paired t-test.

The estimated parameters derived from the linear, quadratic and logarithmic ESPVR and the extrapolated volume intercepts are shown in table 2-2. The AIC values for the

quadratic and logarithmic model are consistently smaller than those for the linear ESPVR, indicating that the ESPVR is indeed better modelled with a non-linear function.

Figure 2-11 shows a representative example of a series of 24 P-V loops obtained under gradual preload decline, demonstrating curvilinear isochrones (with an interval of 5 samples, i.e., every 2.5 ms), and a linear, quadratic and logarithmic extrapolation of the ESPVR, yielding $V_{o,lin}$, $V_{o,quad}$ and $V_{o,log}$, respectively. The onset and the iteratively determined end of systole are also shown.

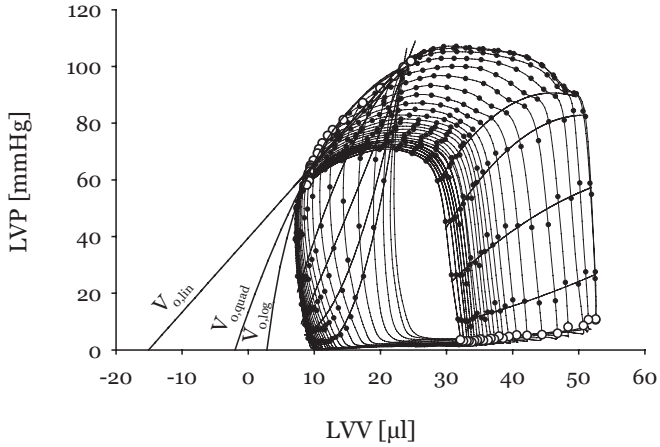

Figure 2-11: Representative example of a series of 24 P-V loops under transient preload reduction. Extrapolation of a linear, quadratic, and logarithmic ESPVR yields $V_{o,Lin}$, $V_{o,Quad}$, and $V_{o,Log}$, respectively. Isochronal P-V couples are shown as black dots with an interval of 2.5 ms. Four isochrones fitted with $RA_{Quad\text{-}Var}$ (compare with figure 2-10D) during isovolumic relaxation (IVR) and isovolumic contraction (IVC) are shown. Open circles: onset and end of systole.

The time courses of curvilinearity (α_2 = coefficient of V_2) of the quadratic isochrones obtained with $RA_{Quad\text{-}Fix}$ and $RA_{Quad\text{-}Var}$ are given in figure 2-12. In $RA_{Quad\text{-}Var}$, coefficient α_2 decreases from virtually 0 (linear isochrones) at the onset of systole to about -0.1 mmHg/µl² (concave to the volume-axis) during ejection. The curvilinearity remains constant until end ejection, after which its coefficient α_2 decreases rapidly to a minimum of 0.43 ± 0.40 mmHg/µl² in the first half of isovolumic relaxation (IVR). During IVR, the shape of the isochrones quickly shifts from concavity to the volume-axis towards convexity (α_2 = 0.86 ± 0.67 mmHg/µl²) and back to linearity during the filling phase. During isovolumic contraction (IVC) and ejection, the results for $RA_{Quad\text{-}Fix}$ are comparable with those for $RA_{Quad\text{-}Var}$. The pronounced shift in curvilinearity observed during IVR, however, is not seen during IVC. In both algorithms, the isochrones simultaneously return to linearity (t_N = 0.62).

Table 2-2: Summary of regression data.

	Linear regression				Quadratic regression					Logarithmic regression			
No.	AIC	α_1 mmHg/µl	α_0 mmHg	$V_{0,lin}$ µl	AIC	α_2 mmHg/µl²	α_1 mmHg/µl	α_0 mmHg	$V_{0,quad}$ µl	AIC	α	β	$V_{0,log}$ µl
1	53.47	2.6	39.2	-15.1	31.7	-0.1	6.4	13.2	-2.0	20.73	0.017	1.659	2.8
2	54.83	3.8	65.1	-17.1	37.5	-0.4	11.4	38.0	-3.0	30.45	0.016	3.754	1.1
3	53.92	2.3	40.9	-17.8	34.7	-0.1	5.8	22.8	-4.0	27.82	0.025	2.928	1.5
4	39.71	2.6	61.1	-23.5	27.6	-0.1	5.9	42.3	-6.4	19.59	0.023	1.054	1.1
5	69.49	4.6	69.2	-15.0	53.7	-0.5	11.9	51.6	-3.7	42.46	0.021	5.235	0.5
6	9.80	2.2	59.1	-26.9	-24.9	0.0	2.8	58.0	-17.8	23.97	0.229	-0.003	0
7	55.55	3.8	74.8	-19.7	38.2	-0.1	6.8	64.5	-8.2	18.02	0.037	-2.176	0.2
8	32.84	2.1	69.2	-32.9	7.6	-0.1	5.4	48.8	-7.8	-9.49	0.024	1.800	0.9
9	47.72	2.7	31.8	-11.8	30.3	-0.3	18.5	-143.0	9.4	25.13	-0.003	3.496	13.9
10	38.87	2.8	64.4	-23.0	20.3	-0.3	11.5	16.4	-1.4	18.19	0.008	4.202	3
11	51.71	5.4	16.7	-3.1	31.3	-1.0	41.5	-296.8	9.2	22.71	-0.003	3.548	11.8
12	32.78	3.7	66.9	-18.1	-22.1	-0.3	8.6	50.3	-5.0	-8.14	0.030	1.351	0.4
13	17.21	2.9	64.1	-22.1	6.7	-0.1	5.2	54.5	-8.9	6.85	0.041	-1.760	0.2
Mean	-	3.2	55.6	-18.9	-	-0.28	10.9	1.6	-3.8*	-	0.036	1.930	2.9*
SD	-	1.0	17.6	7.3	-	0.26	10.1	104.4	7.2	-	0.060	2.252	4.6

AIC: Akaike's Information Criterion value; α_2, α_1 and α_0: parameters in the linear and quadratic regression function, modelled as $ESP = \alpha_1 \cdot ESV + \alpha_0$ and $ESP = \alpha_2 \cdot ESV^2 + \alpha_1 \cdot ESV + \alpha_0$, respectively. α and β are parameters in the logarithmic regression function, modelled as $ESP = (\alpha + \beta \cdot ESV)^{-1} \cdot \ln(ESV/V_0)$. $V_{0,lin}$, $V_{0,quad}$ and $V_{0,log}$ are intercepts of the ESPVR with $V_{0,lin} < V_{0,quad} < V_{0,log}$ (* $p < 0.05$ vs. baseline using a paired t-test).

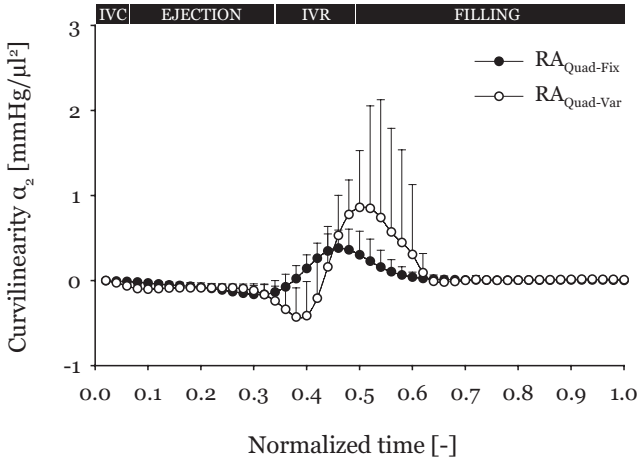

Figure 2-12: Normalized time course of the degree of curvilinearity α_2 (coefficient of V^2) for quadratic regression algorithms $RA_{Quad\text{-}Fix}$ and $RA_{Quad\text{-}Var}$. Data are averaged for all animals. Data are shown as means ± SD.

The quality of the fit, quantified by RMSe values (A and B) and the coefficient of determination R^2 (C and D), are shown in figure 2-13 as a function of normalized time in the cardiac cycle. As anticipated, non-linear regression yields better results (i.e., lower RMSe values) than the commonly used linear regression. Moreover, when comparing the left (fixed V_o) with the right (variable V_o) panels, regression with a fixed V_o yields higher values of RMSe, due to fewer degrees of freedom. The worst fit is obtained with the conventionally used $RA_{Lin\text{-}Fix}$, particularly during IVR. Quadratic and logarithmic regression algorithms perform similarly and thus can be used interchangeably for describing the shape of the isochrones. All algorithms perform comparably during filling, when the EDPVR is virtually linear. Similar conclusions can be drawn from the analysis of the time course of R^2 during IVC and ejection, except that now $RA_{Lin\text{-}Var}$, instead of $RA_{Lin\text{-}Fix}$, yields the lowest R^2 (poorest goodness of fit). During IVR and filling, $RA_{Lin\text{-}Fix}$ performs unacceptably ($R^2 < 0.75$).

The time-varying character of $V_{o,lin}(t)$, $V_{o,quad}(t)$ and $V_{o,log}(t)$, as well as the constant volume intercepts $V_{o,lin}$, $V_{o,quad}$ and $V_{o,log}$ are presented in figure 2-14. From the onset of systole until mid IVR, $V_{o,log}(t) > V_{o,quad}(t) > V_{o,lin}(t)$. As can be predicted from the theoretical concept, the time-varying intercepts intersect their respective constant intercepts at the end of ejection ($t_N = 0.33$). $V_{o,lin}(t)$ ranges between -39.1 and 15.5 µl, while $V_{o,quad}(t)$ acts in a smaller interval between -8.3 and 14.2 µl. $V_{o,log}(t)$ changes considerably less during the cardiac cycle, and ranges between 0.69 and 12.77 µl. The SD and the slope of $V_{o,log}(t)$ at end-ejection are considerably smaller than those for $V_{o,quad}(t)$ and $V_{o,lin}(t)$, suggesting that logarithmic regression is the most reliable fitting technique to estimate V_o. During the second half of IVR and the filling phase, all algorithms result in comparable volume intercepts.

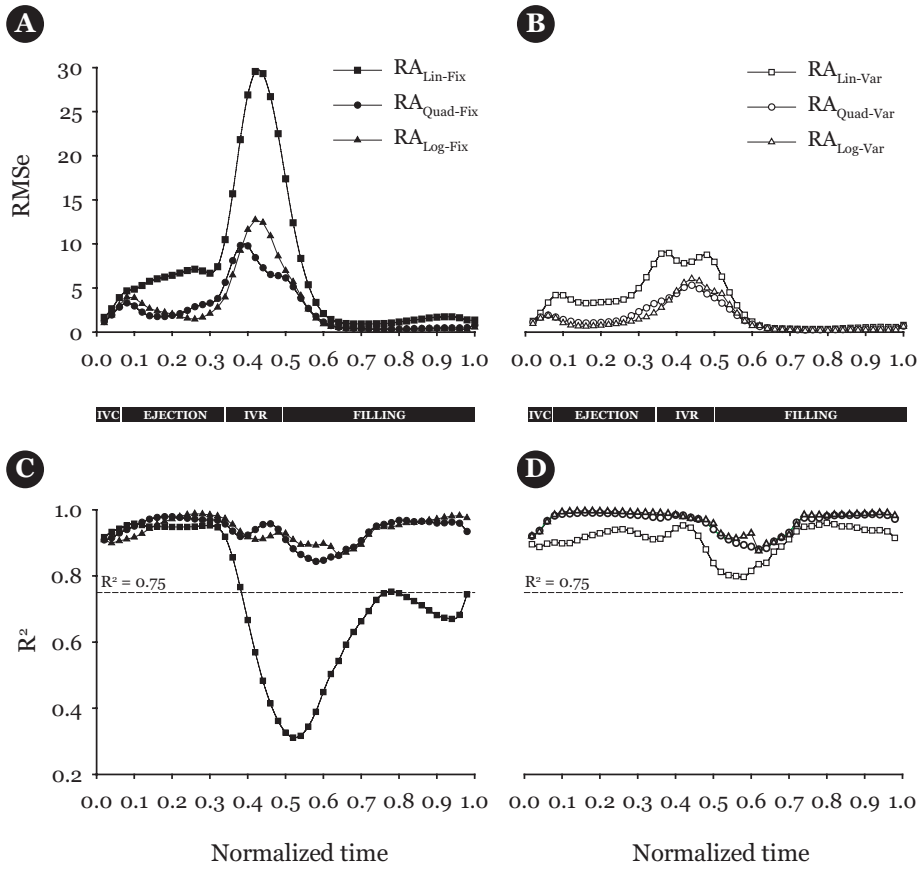

Figure 2-13: Normalized time course of the agreement between measured and fitted pressures, quantified by the root mean square error (RMSe; A and B) and the coefficient of determination (R^2; C and D). A and C: Regression algorithms with a fixed V_0. B and D: Regression algorithms with a time-varying V_0. Data are averaged for all animals.

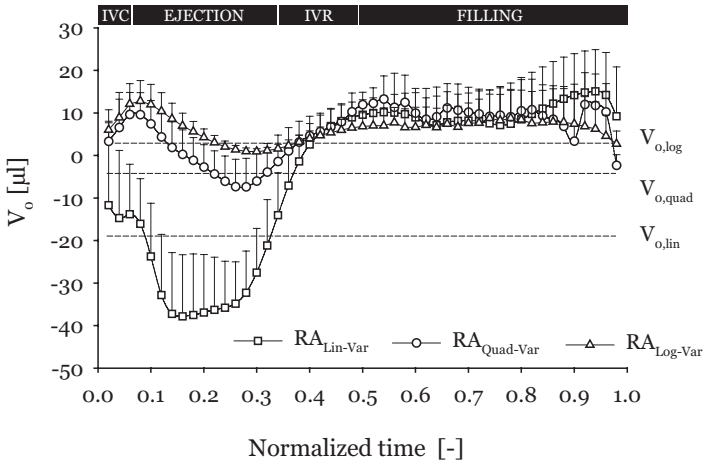

Figure 2-14: Normalized time course of $V_{o,Lin}(t)$, $V_{o,Quad}(t)$, and $V_{o,Log}(t)$ obtained with regression algorithms $RA_{Lin\text{-}Var}$, $RA_{Quad\text{-}Var}$, and $RA_{Log\text{-}Var}$, respectively. Dashed lines represent constant values $V_{o,Lin}$ (obtained with $RA_{Lin\text{-}Fix}$), $V_{o,Quad}$ (obtained with $RA_{Quad\text{-}Fix}$), and $V_{o,Log}$ (obtained with $RA_{Log\text{-}Fix}$). Data are shown as means ± SD.

2.5.4 Discussion

Our analyses have revealed that

(i) the isochrones measured in a mouse LV show a *time-varying curvilinearity* during IVC, ejection and IVR;

(ii) the shape of the isochrones is best described using a *non-linear function* (quadratic or logarithmic) with a *time-varying volume intercept*, while the *linear approximation* with *fixed volume intercept* offers the poorest results, particularly during IVR and early filling;

(iii) the *logarithmic fitting* appears superior in estimating the fixed volume intercept of the ESPVR and, moreover, yields a physiological (i.e., positive) value;

(iv) the intercepts $V_{o,lin}(t)$, $V_{o,quad}(t)$ and $V_{o,log}(t)$ *vary with time* and *differ from each other* during IVC and ejection.

In the early 1970's, using a canine isolated heart preparation, Suga and Sagawa [314] and Suga et al. [316] reported very high coefficients of determination R^2 when fitting isochronal P-V data points with a linear function. Additionally, the extrapolated volume intercepts of the isochrones were found to converge closely to a constant value V_o (i.e., the minimal volume required for the LV to generate supra-atmospheric pressure) [314, 316]. V_o also represents the intercept of the isochrone with the highest slope, the ESPVR. Based on their experimental observations, they introduced the *concept of a linear time-varying elastance* $E(t) = P(t)/(V(t)-V_o)$.

While the E(t) concept allows to demonstrate many of the *mechanical characteristics* of the LV, the physiological interpretation behind it has remained unclear, as it is essentially that of a *spring* that alters its stiffness with time (maximum stiffness at end-systole and minimum stiffness during diastole). However, attempts have been

made to relate the P-V relationship and the mechanical properties of the cardiomyocyte. Beneken and DeWit [24] synthesized the P-V loops from physiological data on the force-velocity relation. The synthesized P-V relationships compared favourably with physiological data, but it was not clearly described how the instantaneous elastance changes with alterations in preload, afterload and contractile state. Later, Suga and Sagawa [315] applied an inverse method and attempted to link ventricular performance to mechanical cardiomyocyte properties by mathematically deriving the time course of the P/V ratio from the known myocardial force-velocity relation using a two-element model of the myocardial fibre (contractile element in series with an elastic element). Their results indicated that that the P-V ratio and the force-velocity relations are mutually transformable by employing the geometry of the LV.

In the late 1980's, Drzewiecki et al. [81] presented a direct relationship between the basic mechanisms of cardiomyocyte contraction and the shape of the isochrones. They developed a thin-walled cylindrical model of the LV to deduce the P-V relation and corresponding isochrones in a rabbit LV from the stress-strain relation in a contractile myofibril. In contrast to the serial model of Suga et al., Drzewiecki et al. used a structural model consisting of a contractile unit in *parallel* with a passive unit.

Various researchers [12, 208, 338] have reported some limitations of the conventional E(t) concept, particularly its sensitivity to afterload. However, the most marked deviations from the simple linear model were manifest when extremes of LV loading were contrasted, such as between isovolumic and ejecting beats. A possible *refinement* of the E(t) model to make it more realistic has been suggested by Little et al. [199]. He investigated the adequacy of E(t) to describe the difference between an ejecting and isovolumic beat and concluded that a flow-dependent term should be added to the E(t) model, accounting for an *internal* or *source resistance* R. The modified E(t) model was then defined as

$$P(t) = E(t) \cdot \left[V(t) - V_0\right] + R \cdot dV/dt \qquad (2\text{-}16)$$

The source resistance reduces the pressure generated at any LVV in proportion to the rate of volume ejection or aortic flow.

Although these drawbacks are well recognized by most researchers, the simplified concept is still quite generally accepted for practical research purposes. It is mainly applied to derive the maximum value, which is used as a relatively load-independent index of ventricular contractility in isolated canine hearts [274, 275], conscious dogs [289] and humans [125].

While during systole the E(t) concept has proven relatively accurate for predicting pressures from volumes in different loading conditions, the diastolic phase of the E(t) curve showed a *much greater variation* [314]. In literature, very little attention has been paid to this discrepancy and virtually no description of the shape change of isochrones during relaxation has been provided.

In this study, the P-V data acquired with a miniaturized combined pressure-conductance catheter demonstrated a markedly curvilinear ESPVR, according to Akaike's Information Criterion. Because the assumption of linear isochrones does not

seem to be compatible with the presence of a non-linear ESPVR, we systematically analyzed the isochrones in P-V diagrams.

The description of the shape change of the isochrones was based on the quadratic regression algorithms, since parameter α_2 provides a direct quantification of their curvilinearity. Although the curvilinearity of both $RA_{Quad\text{-}Fix}$ and $RA_{Quad\text{-}Var}$ appears relatively small during IVC and ejection, it should not be underestimated as it is masked by the high level of curvilinearity during IVR (figure 2-12). Drzewiecki et al. [81] attributed the curvilinear shape to the combination of a non-linear active muscle function, the passive exponential stress-length relationship of myocardial tissue and the geometry of the LV.

In our results, the time-varying $V_{o,lin}(t)$, $V_{o,quad}(t)$ and $V_{o,log}(t)$ differed considerably from the constant intercepts, indicating that the assumption of a constant volume intercept is *violated* in a murine LV, regardless of the regression algorithm used (figure 2-14). The most accurate, and more importantly, the only physiological volume intercept was obtained using the logarithmic regression function, established by Mirsky et al. [218] The relatively large SD observed during filling for all regression algorithms was due to the shallow slope of the EDPVR. The time-varying character of V_o was previously explained by Drzewiecki et al. [81] as "*apparently*" time-varying. In their theoretical study, the isochrones are obtained by *summation* of a passive and an active component (figure 2-15). The passive component represents the passive P-V relation of the elastic structure, which has an equilibrium volume V_{eq}. The active component refers to the set of active function isochrones with a common intercept V_d (i.e., the functionally dead volume, occurring at negative pressures). Because the active zero-pressure volume V_d is assumed smaller than V_{eq}, all isochrones (consisting of an active and a passive component) are concurrent at a negative pressure, which results in an "apparently" time-varying $V_o(t)$. Whether the time-variation of this quantity has physiological meaning, is not clear.

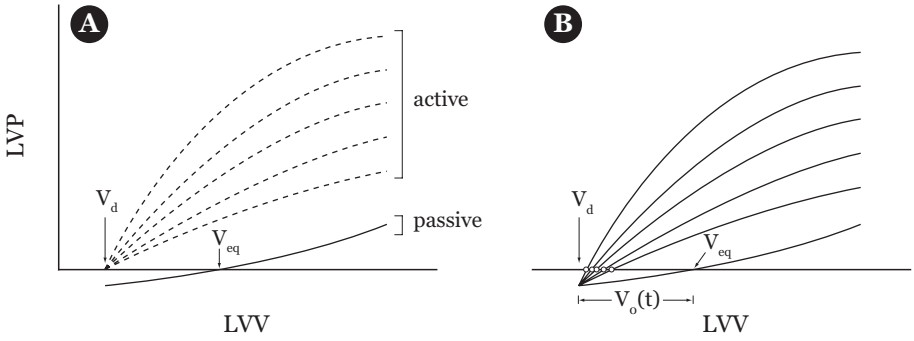

Figure 2-15: Results of Drzewiecki's numerical simulations [81], explaining the time-varying character of the isochrones. All ischrones are the result of a time-varying active isochrone (with a fixed intercept V_d) superposed on one and the same passive isochrone (with an intercept V_{eq}).

The subsequently applied curve fitting using fixed intercepts as boundary conditions showed to what extent such a mathematical restriction *reduces* the quality of the fit

(figure 2-13). The agreement of the measured and fitted data was assessed by RMSe values and R^2. Although both frequently used agreement measures may yield slightly different results in some cases (due to R^2 being also dependent on the range in predictor values, i.e., the volumes [177]), they pointed out that during IVR and early filling, the conventional linear E(t) concept with fixed $V_{o,lin}$ showed a poor agreement with the data, with R^2-values far below 0.75.

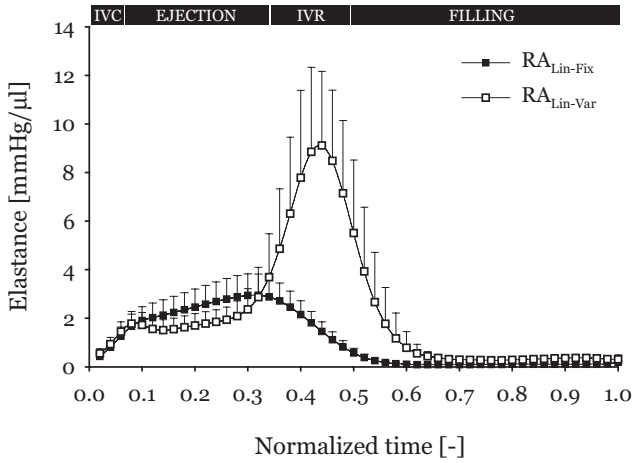

Figure 2-16: Normalized time course of the slope of the isochrones fitted with $RA_{Lin-Fix}$ and $RA_{Lin-Var}$. Data are averaged for all animals. Data are shown as means ± SD.

Figure 2-16 illustrates the deleterious effects of using the boundary condition $P(V_{o,lin}) = 0$ on the definition of elastance (instantaneous slope of the isochrones). During ejection, the conventional elastance ($RA_{Lin-Fix}$) overestimates the slope by 26.41% on average. Surprisingly, during IVR the time course of $RA_{Lin-Var}$ shows a striking dissimilarity to the time course of $RA_{Lin-Fix}$, resulting in a significantly higher E_{es} = 8.41 ± 2.77 mmHg/µl, before reaching its minimum value. On the other hand, a gradual decrease towards the end-diastolic elastance is observed in $RA_{Lin-Fix}$. The latter time course is similar to what is seen in literature, and the E_{es} (2.8 ± 0.7 mmHg/µl) is in agreement with data from Reyes et al. (3.3 ± 1.9 mmHg/µl) [262]. The large discrepancy between these two elastance values was already explained by Kass et al. [156], who pointed out the important difference between E_{max} and E_{es}. E_{max} corresponds to the maximum value of E(t) defined with a time-varying $V_o(t)$, while E_{es} corresponds to the maximum of the generally used definition of E(t), i.e., with a constant V_o (see 2.4.4.2). The unexpected difference between $RA_{Lin-Fix}$ and $RA_{Lin-Var}$ also demonstrates that the linear E(t) concept is meaningless during IVR and early filling, although in literature the E(t) curve is frequently shown for the whole cardiac cycle. As volume remains constant during IVR, a simple *exponential* decay of the pressure waveform [350] or Matsubara's logistic model [205] would be sufficient to describe the pressure changes during IVR (see chapter 5).

In this study, we provided ample evidence that the E(t) concept is not the ideal method to describe LV performance in mice during both systole and diastole. While it

is always feasible to construct an elastance curve once V_0 is determined, it is not clear whether E(t) represents the instantaneous stiffness of the LV. Consequently, various questions remain to be answered about the relation between *ventricular elastance* and *isochronal* P-V data in mice.

This debate can be summarized visually in figure 2-17, where the averaged parameters obtained from $RA_{Lin\text{-}Fix}$ (panel A) and $RA_{Quad\text{-}Var}$ (panel B) are used to reconstruct isochrones during IVR and IVC. In panel A, the lines simultaneously represent isochronal and "iso-stiffness" P-V data in the LV. The LV functionally operates at the same stiffness level during two moments in the cardiac cycle, once at a large volume during IVC, and later at a smaller volume during IVR. In panel B on the other hand, only isochronal P-V data can be seen and no information about stiffness can be obtained. Interestingly though, when considering the isochrones during both IVC and IVR, at least the visual suggestion appears that the isochrones during IVC and IVR could/should be interconnected by means of a sigmoidal curve. It remains to be assessed whether this behaviour is strictly a phenomenological observation (which we aimed to quantify in this study), or whether an alternative "*non-linear*" *time-varying elastance* theory can be deployed, where ventricular behaviour (stiffness) is described by a sigmoidal curve varying in time, and changing its shape throughout the cardiac cycle.

The *sigmoidal shape* (and the changes throughout the cardiac cycle) certainly resembles force-length relationships in isolated muscle experiments, where the shape of the sigmoid curve is modulated by calcium concentration (figure 1-15). On the other hand, one can also follow a more pragmatic approach, and describe diastole with a different time-varying quantity than systole. If so, a new reference time-point for the onset of diastole should be looked for, instead of the end of ejection which is used in our and other studies. A reasonable, but impractical reference point could be the time instant of transition from systole to diastole on myocardial level (i.e., when load ceases to sustain the cross-bridges), determined by Solomon et al. [292].

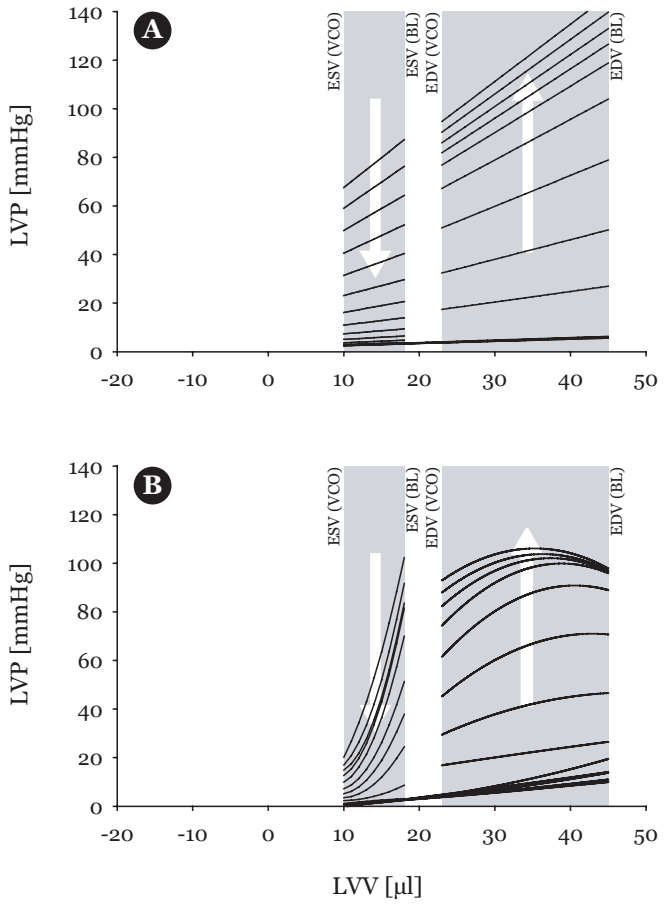

Figure 2-17: Reconstruction of isochrones during IVC and IVR by using average values of the parameters. A: Regression and reconstruction according to $RA_{Lin\text{-}Fix}$; B: regression and reconstruction according to $RA_{Quad\text{-}Var}$ (ESV: end-systolic volume, EDV: end-diastolic volume, BL: baseline, VCO: vena cava occlusion).

2.5.5 Methodological considerations

It is to be acknowledged that our study has the following potential limitations, related to the use of the conductance catheter in mice:

(i) A fundamental assumption of the hypertonic saline injection method (for varying the conductivity of the intraventricular blood pool) is that the underlying *haemodynamics* remain *unchanged* by the hypertonic saline bolus. Whereas this method has been validated by previous investigators in larger animals [33, 183, 321], it poses potential risks to mice because of volume loading and/or contractility changes [93]. The bolus can present a salt load and induce a negative inotropic response [111]. These limitations may become problematic in mice, particularly those with genetically engineered models of cardiac dysfunction, given the small circulating blood volume [17]. This

potential limitation was addressed by Feldman et al. [94] who developed a *dual-frequency catheter system* to eliminate the need for bolus hypertonic saline for calibration for parallel conductance. Note, however, that the injected volume of saline in the mouse is only 5-10 µL, which is about 31% of its average SV from table 2-1 (24 µL) and approximately 0.05% of its CO (HR of 620 BPM). On the other hand, Kass et al. reported injecting 2-3 mL of saline in dogs, which is about 22% of the SV of 11 mL and 0.27% of the CO (HR of 85 BPM).

(ii) The data were obtained using a single-frequency conductance system with the assumption of a *constant volume signal offset* (V_c) during the whole experiment. However, this should not be a major concern. Firstly, the study of Lankford et al. [183], performed in isolated and in situ hearts, revealed no significant time-variation of V_c. On the basis of their results, it appears that V_c can be reasonably approximated by a single value for most data analyses. Secondly, using a dual-frequency conductance catheter, Georgakopoulos et al. [111] showed that V_c determined with the dual field method varied only very slightly with time, and that it correlated very well with V_c found from saline dilution ($R^2 = 0.97$). Their results revealed that nearly all of the V_c can be attributed to near-field effects, i.e., the LV wall. This is probably due to the fact that the murine heart is relatively thick, with thickness to cavity radius of 1.0 in normal hearts [356] thus lowering far-field effects. The variation of V_c during the cardiac cycle is therefore very limited. In addition, if V_c were changing during the IVC occlusion, it would cause the P-V loops to shift *leftwards*, because overall there would be a decrease in parallel conductance resulting from an decrease in total cardiac volume, including RV volume. If the P-V loops actually shifted to the left, the end-systolic point would also shift leftwards resulting in what would "appear" as a more linear or flatter ESPVR, which was clearly not observed in our experiments.

Even though our conductance catheter technique may still benefit from technical improvements, we believe that our observations about the non-linearity of the ESPVR and the isochrones are not due to measurement errors, as non-linear ESPVR's have also been reported using other technology than the conductance catheter. Using sonomicrometry measurements, Takaoka et al. [323] and Esposito et al. [87] also showed non-linear ESPVR's. However, we agree that the use of a dual-frequency catheter system as described in [93] would have resulted in more accurate volume measurements.

We also need to mention some other potential shortcomings of this study:

(iii) Although our automated detection of the onset of systole seems artificial, it was extremely *robust* in our measurements. However, false identifications may occur when the measured maximum volume is about 2% higher than the EDV. Manual definition of the onset of systole is then required. An alternative technique for detecting the onset of systole has been proposed by Kass et al. [154]. They defined it as the time point where $dE/dt \approx d(P/V)/dt$ exceeds 10% of $(dE/dt)_{max}$. Even though both algorithms lack a physiological meaning, it is anticipated that they yield comparable results. We preferred our technique

over others because of the difficulties in *defining* end-systolic elastance in case of a curvilinear ESPVR.

(iv) The experiments were not repeated under *different inotropic conditions*, so we were not able to assess the influence of contractility on the time course of all of the calculated parameters. Nevertheless, we believe that this does not affect the general idea presented in this study.

(v) Significant decreases in the *systemic pressure* during the VCO could potentially result in myocardial ischaemia and changes in contractility (and HR). Yet, Burkhoff et al. [46] stated that as long as the systemic pressure stays above 60 mmHg, myocardial contractility is virtually unaffected. Since in our experiments ESP (during the last loop of VCO) was on average 71 mmHg, we can reasonably expect that the effect of the lowered coronary artery pressure is negligible.

(vi) A statistically significant increase in HR between baseline and VCO was observed (620 vs. 624 BPM). We believe, however, that these small changes in HR should not affect the contractility because the *force-frequency response* of the mouse has been shown to be *flat* at HR above 600 BPM [110].

(vii) The data shown in figure 2-12 to figure 2-16 were averaged for all animals included in the study. Even though all data have been represented on a normalized time scale, the peaks of the curves could be *slightly blunted* if they do not occur at the same normalized time for each subject.

(viii) Finally, our experiments were done in *open-chest mice*. Even though it is the most frequently reported approach to date, it has some theoretical disadvantages compared to a closed-chest approach. In the closed chest, the lungs remain untouched and the cardiac position remains intact. Lips et al. [197] published significant differences in SV, ESV and EDV and ESP between the two approaches. Since our method produced physiologic pressures and SV, we assume that our findings can be extrapolated to the closed-chest approach.

2.5.6 Inferences towards larger mammals

A critical question that one may ask is to what extent the results in our investigation, performed in murine LV's, can be inferred to larger mammals, such as humans. Basic differences in cardiovascular physiology between mice and humans are summarized in table 2-3 [109].

Despite the demonstrated questionable applicability of the E(t) concept in murine LV's for describing time-varying stiffness, remarkable similarities in the shape of the E(t) curve between *humans* and *mice* have been reported. This finding was considered very interesting and may perhaps allow for direct comparisons to be made between mice and humans in relation to the mechanisms behind ventricular contraction and relaxation and to the pathophysiology of disease processes [112].

However, caution is warranted on blind extrapolation of our results to hearts of larger mammals, because the determinants of ventricular contractility are different in mice and men. One of the most frequently reported differences is related to the eight-fold increase in HR in mice compared to humans. The human heart is able to markedly

increase force in response to increase frequency, with a 2-3 fold increase in force when the HR is doubled. In the mouse, on the other hand, the reduced quantitative response to an increase in frequency is flat at physiological HR [110], suggesting that the HR of the unstressed mouse is near the upper rate limits of actin-myosin cross-bridge kinetics and/or the maximal speed of calcium handling [307]. It has therefore been hypothesized that the intact murine heart functions *at* or *near maximal contractility* in the *basal state*, such that there is an inherently *limited cardiac reserve* [155]. Note that this unique feature of the mouse LV may partially explain why curvilinear isochrones are observed in the mouse during baseline, whereas an increased contractile state is required to obtain curvilinearity in larger mammals.

Table 2-3: Haemodynamic parameters in the mouse derived from P-V relationships [109].

Parameter	Mouse	Human	Mouse/human
HR (BPM)	597 ± 58	71	8.4
Systole (% of cardiac cycle)	36.4 ± 3.5	35	1
Diastole (% of cardiac cycle)	63.6 ± 3.5	65	1
EDP (mmHg)	5.7 ± 2.1	12.5	½
ESP (mmHg)	117.5 ± 10.1	121	1
EDV (µl)	29.3 ± 3.1	$108.1 \cdot 10^3$	1/3700
ESV (µl)	6.1 ± 4.1	$43.9 \cdot 10^3$	1/7200
SV (µl)	23.2 ± 2.6	$64.9 \cdot 10^3$	1/2800
CO (ml/min)	13.8 ± 2.5	$4.6 \cdot 10^3$	1/333
Body mass (g)	25.3 ± 4.6	$70 \cdot 10^3$	1/2800
Heart mass (g)	118.4 ± 18.3	$325 \cdot 10^3$	1/2800
LVM (g)	95.4 ± 9.6	$130 \cdot 10^3$	1/1400
Heart mass / body mass (mg/g)	4.3 ± 0.42	4.6	1
EDV / V_{wall} (-)	0.31 ± 0.04	0.8-1	0.31
CO / body mass (ml/min·kg)	533.6 ± 23.4	65.7	8.1

HR: heart rate, EDP: end-diastolic pressure, ESP: end-systolic pressure, SV: stroke volume, CO: cardiac output, LVM: left ventricular mass, V_{wall}: left ventricular wall volume.

2.5.7 Conclusions

In conclusion, we have demonstrated that the conventional linear time-varying elastance concept does not fully describe LV performance during the whole cardiac cycle in the mouse. In a recent review, Burkhoff et al. [46] emphasized that accurate P-V analyses continue to be very important, because (i) P-V data often constitute the critical information in *proving* the consequences and the relevance of primary biochemical, molecular or cellular discoveries, and (ii) these P-V data may, in the end, be the basis for acceptance of *new concepts*. Our detailed description of the curvilinearity of the murine P-V isochrones provides important insights for the

development of new standardized methods of P-V data analysis and also provides the basis for a coherent framework that needs to be developed to account for cardiac physiology and the variation in time of non-linear isochrones throughout the complete cardiac cycle.

3

Chapter 3

Echocardiography as a Non-invasive Tool for Assessing Left Ventricular Function

The contents of this chapter were published in

IEEE Transactions on Ultrasonics, Ferroelectrics, and Frequency Control
2004 Nov; 51 (11): 1537-1545
RF-based Two-Dimensional Cardiac Strain Estimation: A Validation Study in a Tissue-Mimicking Phantom
Langeland S, D'hooge J, Claessens TE, Claus P, Verdonck PR, Suetens P, Sutherland GR and Bijnens B.

3.1 Introduction

In the previous chapter we proved invasive pressure and volume measurements to be powerful means for characterizing the global "active" and "passive" mechanical properties of the left ventricle (LV) in a research environment. Nonetheless, few would debate that these invasive measurements, which require highly specialized devices, are not suitable for everyday clinical practice. Alternative, *non-invasive* techniques are therefore desired.

Echocardiography is such a non-invasive ultrasound-based application for imaging cardiac structures and evaluating global and regional cardiac function. It is a critically important diagnostic tool in any modern medical facility, and probably the most frequently used cardiac imaging technique, because it is fast, painless, safe, relatively cheap, and because it can be applied on the bedside. As such, it is still preferred over other imaging techniques like computed tomography (CT), magnetic resonance imaging (MRI) or nuclear imaging.

This chapter starts with an overview of the most commonly used echocardiographic (Doppler) imaging modalities in clinical cardiology, and explains how *blood flow* and *myocardial tissue velocities* can be visualized using ultrasound. It furthermore highlights the current state of the art in *myocardial deformation imaging,* and describes a newly developed *two-dimensional* approach which solves the angle dependence inherent to all ultrasound Doppler applications, and which will likely accelerate the clinical acceptance of deformation imaging in clinical practice.

3.2 Echocardiography: technical aspects

3.2.1 Physical background

Medical ultrasound imaging is based on the transmission and reception of *acoustic ultrasound waves* travelling through a medium. Ultrasound waves are *longitudinal* (i.e., the displacement of the particles in the medium is perpendicular to the direction of the propagation) compression waves with a frequency above 20 kHz, above the audible range of the human ear. The propagation velocity of the ultrasound energy is defined as the *sound propagation velocity*, and is virtually constant in human tissue (c = 1540 m/s) [286, 320].

To transmit and receive ultrasound waves, an ultrasound imaging system requires an ultrasound *transducer* (or *probe*) containing a series of piezo-electric crystals (figure 3-1). These crystals change their physical dimensions upon the application of an electric field and, vice versa, they generate an electrical potential when they are deformed. This *piezo-electric effect* was discovered in 1880 by the French physicists Pierre and Jacques Curie [286].

When such a piezoelectric crystal is brought in contact with human tissue, an acoustic wave will propagate through the medium. The wave amplitude gradually *declines* as it propagates through the medium because of *attenuation* (absorption of energy) and because the acoustic energy is *spread in three dimensions*. The degree of attenuation depends both on the properties of the medium (mass density and compressibility)

and the signal frequency. The acoustic waves that are received by the transducer and finally used to reconstruct the ultrasound image, originate either from *reflected echoes* due to planar interfaces between two media of different acoustic impedance, or from *diffusely scattered echoes* due to small inhomogeneities in the medium. These local inhomogeneities (or "scatterers") re-emit acoustic energy as if they were sources of ultrasonic waves. The amplitude of the scattered signals is far less than that of the reflected signals [286, 320].

Depending on the way that the crystals are electronically excited and the received radio-frequency (RF) signals are processed, many different types of echocardiographic images can be achieved. The most common imaging modalities are briefly outlined in paragraphs 3.2.2 to 3.2.4.1. *Deformation imaging*, a relatively new echocardiographic imaging modality, is dealt with in paragraphs 3.2.4.2 and 3.3.

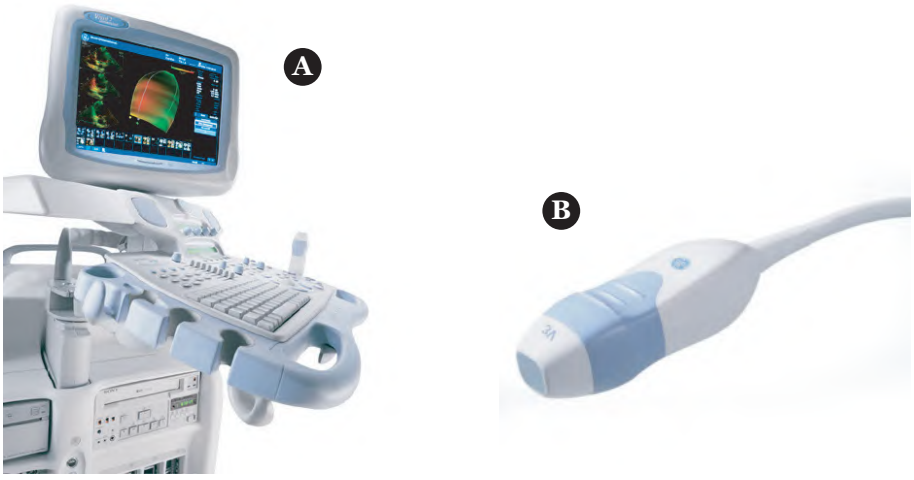

Figure 3-1: A: Commercially available high-end ultrasound system (Vivid 7 Dimension, GE Vingmed Ultrasound, Horten, Norway); B: Ultrasound transducer (probe) with a matrix of electronically steerable piezo-electric crystals.

3.2.2 Greyscale imaging

Two-dimensional greyscale imaging provides *anatomical* images of cardiac *structure* as well as semi-quantitative information about global and regional *cardiac function* (figure 3-2A). They are created by firing a pulse and processing the received RF echo *repeatedly* in several neighbouring beam positions in order to cover a sector. Rotation of the ultrasound beam is nowadays accomplished electronically by exciting the array of crystals in a specific order.

Because the sound propagation velocity is known, the location of a reflector can be readily determined from the RF echo. The amplitude of the RF echo is a measure of the reflectivity of the reflectors and ultimately determines the brightness of the corresponding pixel on the greyscale image. However, before turning the received RF signals into a two-dimensional greyscale image, they have to undergo a few post-

processing steps. They include (i) *envelope detection* to remove the high-frequency components that are not required for the image, (ii) *time-gain-compensation* to compensate for attenuation of ultrasound energy as the beam penetrates deeper into the tissue, (iii) *logarithmic compressio*n of the amplitude to account for the large dynamic range of the echo, and (iv) *scan conversion* to convert the data from the ultrasound beams back into a sector image [320].

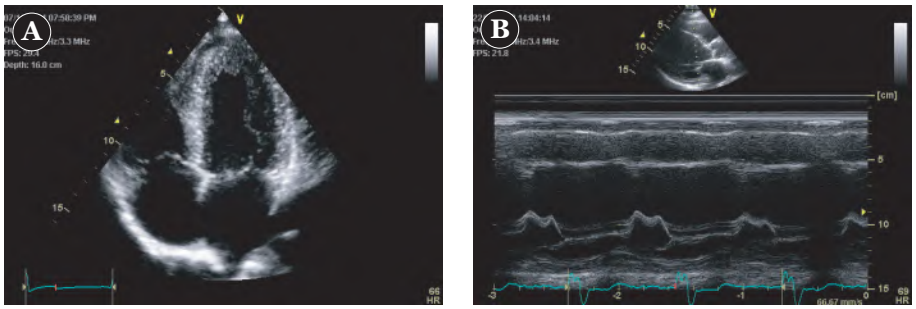

Figure 3-2: Example of a two-dimensional image (A) and an M-mode image (B).

The *temporal resolution* (ms) or *frame rate* (Hz) of the images is limited by the sweep speed of the beam. The sweep speed, in its turn, is limited by the sound propagation velocity, because the echo of the farthest point must be able to return before the next pulse is fired in the neighbouring beam. The frame rate can thus be increased by decreasing the sector angle (i.e., "width" of the image) or by reducing the number of beams in the sector, and thus the lateral resolution.

In greyscale *M-mode imaging*, the amplitudes of the echoes are displayed as a function of *depth* and *time* along a single scanline (figure 3-2B). Accordingly, M-mode images provide the maximum achievable temporal resolution.

3.2.3 Doppler imaging

3.2.3.1 Doppler principle

The *Doppler principle* was first described in 1842 by the Austrian physicist Christian Johann Doppler. It refers to a phenomenon in which an observer perceives a change in the frequency of sound emitted from a source when the source or the observer, or both, are moving (figure 3-3A) [286]. The difference in frequency between the transmitted (f_t) and the received (f_r) signal is referred to as the *Doppler frequency* or *Doppler shift* (f_d). Assuming that the velocity of the reflector (v = maximum 5 m/s) is much smaller the sound propagation velocity (c = 1540 m/s), which is common in medical applications, the Doppler frequency and the velocity of the reflector relate to one another as

$$f_d = f_r - f_t = \frac{2 \cdot v \cdot \cos(\theta)}{c} \cdot f_t \qquad (3\text{-}1)$$

This equation can be exploited to determine the *velocity of a moving reflector* (e.g., a red blood cell or tissue segment) when f_d is known. The term $\cos(\theta)$ is used as a scaling factor in equation 3-1 since only the component of the velocity vector parallel to the transmitted wave direction can be perceived. This makes all conventional Doppler applications inherently *angle-dependent*.

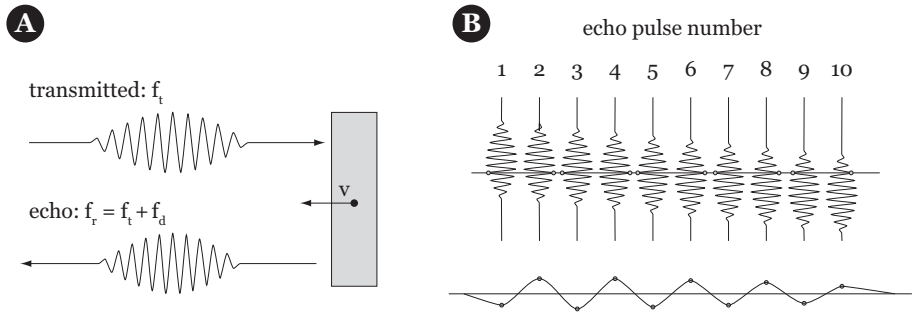

Figure 3-3: A: Illustration of the Doppler principle. The frequency of the echo (f_r) is higher than the transmitted signal frequency (f_t) when the reflector moves towards the observer. The difference between both frequencies is the Doppler frequency (f_d); B: Principle of pulsed wave (PW) Doppler: The echo signal is always sampled at the same time instant after emission of the ultrasound pulse (range gate) (adapted from [320]).

In 1955, two Japanese investigators, Shigeo Satomura and Yasuhara Nimura, were among the first to develop an ultrasonic Doppler device for monitoring blood flow and tissue motion [286]. Nowadays, a modern ultrasound device can display the measured velocities under various modalities: continuous and pulsed wave Doppler, colour flow mapping and colour M-mode Doppler. They are briefly explained below. More detailed information can be found in specialized literature [286, 319].

3.2.3.2 Continuous wave Doppler

A *continuous wave* (CW) Doppler image displays the distribution of the detected Doppler frequencies (and thus velocities) along a scanline as a function of time (figure 3-4A). The transmitted signal is a continuous sinusoidal signal (i.e., a theoretically infinite pulse). By calculating spectral information for sequential time intervals from the received signal, a whole *spectrum* of Doppler shifts is obtained as a function of time. CW systems have the ability to measure high velocities and to acquire the peak velocity along the ultrasound beam. A major limitation of the simplest CW Doppler systems is that they do not contain *spatial* nor *directional* information. However, most modern ultrasound devices are equipped with additional circuitry to extract the flow direction from the Doppler signal. As such, they are able to distinguish between motion towards and away from the transducer. The most widespread technique to achieve this is *quadrature phase demodulation*.

3.2.3.3 Pulsed wave Doppler

In contrast to CW Doppler, *pulsed wave* (PW) Doppler has the ability to determine the velocity at a small region (*sample volume*). Transmission of a *series* of ultrasonic

(broadband) pulses, as opposed to a continuous wave, permits the user to define a range or *depth* of interrogation. The range specification allows the system to calculate the time required for each pulse to reach the desired depth and allows the reflected signal to return to the receiver.

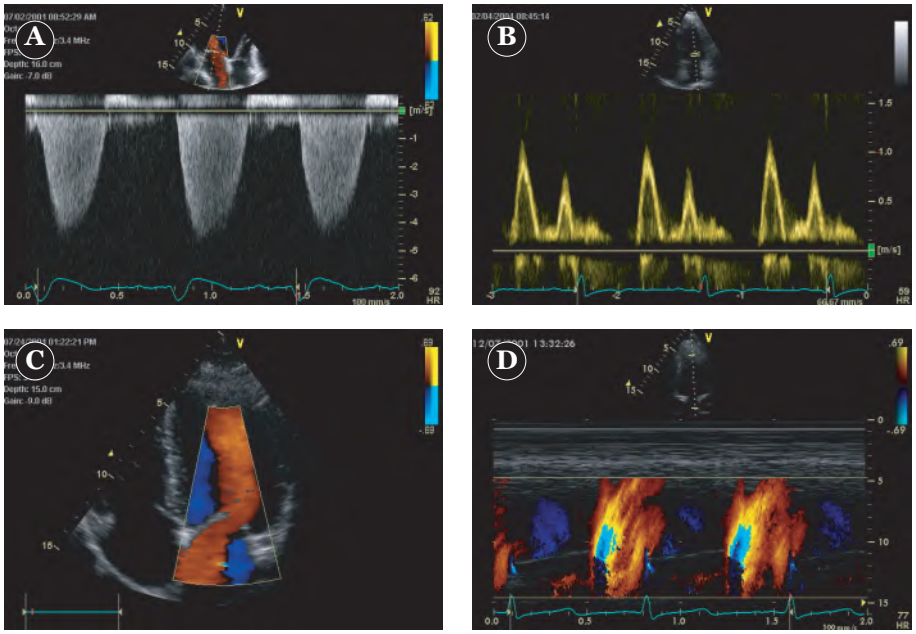

Figure 3-4: Various Doppler imaging modalities: Continuous wave (A), pulsed wave (B), colour flow mapping (C) and colour M-mode imaging (D).

It needs to be emphasized, though, that PW Doppler systems do not measure the Doppler shift in order to determine velocities, due to the relatively small Doppler shift (≈ 2 kHz) compared to the attenuation-dependent shift in centre frequency (≈ 16 kHz). In fact, the Doppler shift (f_d) even causes a small artefact in the acquisition. Instead, ultrasonic pulses are transmitted with a given *pulse repetition frequency* (PRF), which is limited by the distance of the sample volume (d_s) in the tissue:

$$PRF_{max} = \frac{c}{2 \cdot d_s} \tag{3-2}$$

The returning RF signals are all sampled at the same time instant relative to the *pulse emission time* after transmission (range gate). If the sampling is done t_s seconds after the pulse emission, the *sampled depth* is

$$d_s = \frac{t_s \cdot c}{2} \tag{3-3}$$

A subsequent spectral analysis of the sampled signal, as shown in figure 3-3B, results in a typical PW Doppler image (figure 3-4B).

Even though a PW Doppler system does not directly measure Doppler shifts, the displayed velocities do correspond with the Doppler shift from a theoretical point of view. This can be shown as follows: the time of flight (t_x) for a pulse to travel towards a sample volume at distance x and back to the transducer is given by:

$$t_x = \frac{2 \cdot x}{c} \tag{3-4}$$

The *phase shift* between the transmitted and the received signal is determined as

$$\varphi = 2\pi \cdot f_t \cdot t_x = 2\pi \cdot f_t \cdot \frac{2 \cdot x}{c} \tag{3-5}$$

The *frequency* of this signal is, by definition, calculated as

$$\frac{1}{2\pi} \cdot \frac{d\varphi}{dt} = 2 \cdot \frac{f_t}{c} \cdot \frac{dx}{dt} = 2 \cdot \frac{f_t}{c} \cdot v \tag{3-6}$$

which clearly corresponds to the Doppler frequency (equation 3-1).

A drawback of a PW Doppler system is that the highest Doppler frequency or maximal velocity that can be measured is limited because of *frequency aliasing*. According to Shannon's theorem [148], frequency shifts will be appropriately displayed only if PRF is at least twice the maximum Doppler shift to be detected in the sample. The maximum velocity that can be detected is called the Nyquist velocity:

$$v_{max} = v_{Nyq} = \frac{c}{2 \cdot f_t \cdot \cos(\theta)} \cdot \frac{PRF}{2} \tag{3-7}$$

3.2.3.4 Colour flow mapping

Instead of showing the blood velocity distribution as a function of time (as in a PW and CW Doppler system), *colour flow mapping* provides a colour-coded map that represents the *velocities* and *direction* of blood. Red colours are conventionally used to indicate motion towards the transducer, while blue velocities indicate the opposite direction (figure 3-4C).

To obtain velocities in the whole image sector with an acceptable frame rate, a certain number of pulses (i.e., a "*packet size*" of usually 3 to 7 pulses) are fired in one direction. This sequence is repeated in every beam direction until the whole sector is covered. In between the Doppler pulses, regular pulses are also fired to construct the background greyscale image simultaneously with the colour-coded velocity map. From the captured RF signals, the local phase shift ($\Delta\varphi$) between the subsequent acquisitions is estimated [320]. The velocity can be subsequently estimated from this phase shift using the following formula:

$$v = \frac{c \cdot \Delta\varphi \cdot PRF}{2 \cdot f_t} \tag{3-8}$$

However, in practice the computationally more efficient *autocorrelation* estimator [153] is often employed to estimate the phase shift and blood velocity. Autocorrelation is a common method in which each echo is correlated with the corresponding one from a previous pulse.

3.2.3.5 Colour M-mode Doppler

Colour M-mode Doppler imaging can be considered as a special application of colour flow mapping. It is used to obtain velocity data along a *single image line* as a function of time. A very high temporal and/or velocity resolution can be obtained because the ultrasound beam doesn't need to sweep across the image (figure 3-4D).

3.2.4 Doppler myocardial imaging

3.2.4.1 Tissue Doppler imaging

Tissue Doppler imaging (TDI), also referred to as *Doppler myocardial imaging* (DMI), is a relatively new echocardiographic technique used for measuring *tissue* velocities. The basic principles underlying TDI are identical to classic blood pool Doppler imaging (see paragraph 3.2.3). The only difference lies in the way the received signals are processed. In classic Doppler imaging wall filters are used to eliminate the high-amplitude and low-frequency signals reflected by slowly moving tissue in favour of the low-amplitude and high-frequency signals reflected from high-velocity red blood cells. In TDI, on the other hand, the high-pass filter is bypassed and a lower gain amplification is used to eliminate the weaker intensity blood flow signals (figure 3-5).

Tissue velocities can also be displayed in various ways: pulsed wave, colour mapping and M-mode [107, 320].

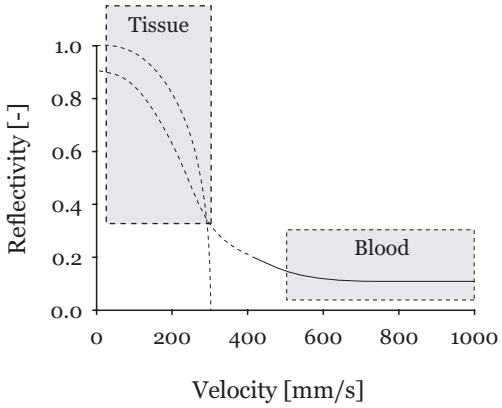

Figure 3-5: Differences in reflectivity and velocities between tissue and blood require the filter settings of the ultrasound system to be altered in order to measure tissue velocities (adapted from [320]).

3.2.4.2 Strain (rate) imaging

Echocardiography-based *strain* and *strain rate imaging* (SRI) are complementary imaging modalities for quantification of regional deformation and deformation rate of myocardial tissue [66, 131, 348]. This task cannot be fulfilled using TDI, as velocity measurements do not allow for differentiating between wall translations and tethering on one hand (due to rotation and contraction of adjacent myocardial

segments), and actual *deformation of tissue* (due to myocardial contraction and relaxation) on the other hand [337].

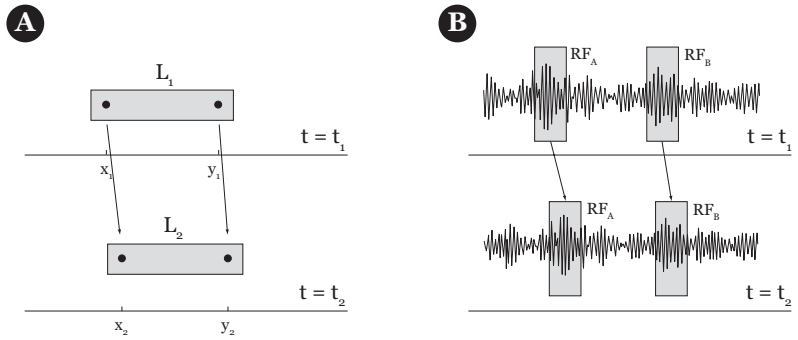

Figure 3-6: Principles underlying the determination of strain and strain rate on the basis of auto-correlation (A) and cross-correlation (B) techniques. Coordinates x_1, y_1 and x_2, y_2 are the positions of a specific material point of a deforming object at time instants t_1 and t_2. L_1 and L_2 denote the length of the object (adapted from [66]).

Two techniques for estimating strain and strain rate currently exist: the *velocity gradient method* and the *cross-correlation* method [65, 66].

The first approach relies on the fact that *strain rate* can be theoretically expressed as the difference in velocities at both ends of a deforming object with initial length L_1 (figure 3-6A). Indeed, strain ε is defined as

$$\varepsilon = \frac{L_2 - L_1}{L_1} = \frac{(y_2 - x_2) - (y_1 - x_1)}{y_1 - x_1} \tag{3-9}$$

where x_1, y_1 and x_2, y_2 are the positions of a specific material point of a deforming object at time instants t_1 and t_2, respectively. Strain rate can than be found as

$$\frac{d\varepsilon}{dt} \approx \frac{\varepsilon}{\Delta t} = \frac{(y_2 - y_1)/\Delta t - (x_2 - x_1)/\Delta t}{y_1 - x_1} \approx \frac{v_2 - v_1}{L_1} \tag{3-10}$$

Because the velocities are measured with TDI (which utilizes *auto-correlation* techniques), this approach is also referred to as the auto-correlation technique. It also inherits the limitations common to Doppler applications: the received signals are dependent on the insonation angle, and aliasing can induce artefacts in the strain rate data. Information about *myocardial strain* can be obtained from *temporal integration* of the strain rate data.

In the *cross-correlation* method two RF signals are acquired at two different time instants ($t = t_1$ and $t = t_2$) during deformation of myocardial tissue (figure 3-6B). The point of this method is to track a specific part of the received RF signal, say RF_A (resulting from a specific distribution of scatterers) from one time interval to another. A similarity function (cross-correlation function) is then applied to quantify the degree of similarity between both patterns as a function of the *relative time shift* between both. This function reaches its maximum whenever the similarity is optimal. Because the time shift is a measure for the motion of the local RF pattern, the change

in distance between *two* specific RF patterns, e.g., RF_A and RF_B, can be used to determine the *strain* in the tissue. The *strain rate* is then obtained from *temporal derivation* of the strain signal. In contrast to the auto-correlation technique, cross-correlation does not suffer from aliasing problems, as the RF patterns can be found in a region with a considerable size. Strain estimation using cross-correlation has shown to be computationally more intensive and has not been made available in clinical systems [65].

The required operations for obtaining strain and strain rate information in both techniques are summarized in figure 3-7. As the calculation of gradients is very noise sensitive, smoothing of the data is required to yield acceptable noise levels in strain and strain rate.

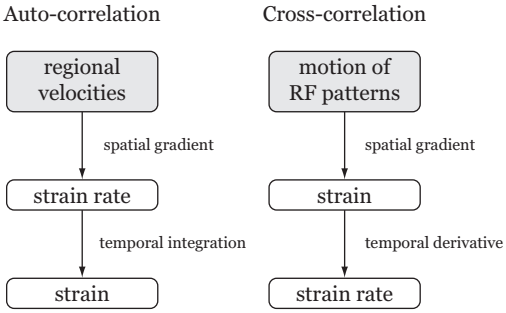

Figure 3-7: Schematic overview of the operations required for strain and strain rate estimation based on auto-correlation and cross-correlation (adapted from [66]).

An important potential advantage of the cross-correlation approach is that the RF patterns cannot only be compared to RF patterns in the same scanline, but also to RF patterns in *neighbouring* lines, in such a way that *two-dimensional strains* can be obtained. This relatively unexplored, but very intriguing topic is further elaborated on in the next paragraph.

3.3 Two-dimensional deformation imaging

3.3.1 Need for multi-dimensional strain and strain rate imaging

One of the major drawbacks of the existing approaches for measuring strain and strain rate is that the techniques are limited to measurements only in the direction of the ultrasound beam. This limitation causes the technique to be angle-dependent [53]. Angle dependence renders the clinical applicability more difficult because an appropriate alignment of the ultrasound beam with the direction of deformation is often hard to obtain, due to the limited number of acoustic windows through the human thorax. Moreover, this approach implies that only one component can be assessed of the three-dimensional myocardial deformation tensor.

In order to overcome this limitation, a method for estimating *two-dimensional strain rate* using tracking of RF data has been presented by D'hooge et al. [67]. Recently,

Langeland et al. [180] improved this methodology in order to assess *two-dimensional strain* and validated it in a tissue-mimicking phantom setup.

3.3.2 Two-dimensional strain estimation

Ultrasound-based two-dimensional strain was estimated as follows: the algorithm first finds the angle-independent *two-dimensional velocity field* of the deforming object. This is accomplished by choosing a one-dimensional kernel along an RF line within a region of interest. This kernel is subsequently shifted along the corresponding RF line and its *neighbouring* lines in the next RF frame. A similarity measure, described by the two-dimensional displacement estimator function, decides where the best match is found by looking for the absolute optimum of this function. The shift of the best match along a line defines the *axial velocity* (v_{ax}) while the shift among lines defines the *azimuthal velocity* (v_{az}) (figure 3-8). As such, the principle can be considered as a two-dimensional extension of the one-dimensional cross-correlation method described in paragraph 3.2.4.2. Once both velocity components (axial and azimuthal) are found as a function of time, the motion pattern of the underlying tissue can be reconstructed. From this motion pattern, the Lagrangian strain can be determined in two directions. A major advantage of this technique is that the anatomic tracking procedure, which is time-consuming and had to be performed manually in previous methods, is embedded in this method.

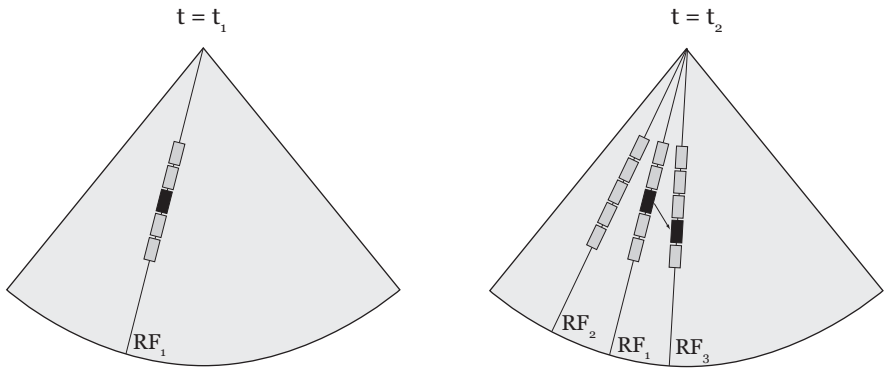

Figure 3-8: Both axial (v_{ax}) and azimuthal (v_{az}) velocity components can be estimated by tracking the motion of a particular RF pattern within two consecutive (at $t = t_1$ and $t = t_2$) two-dimensional RF images.

3.3.3 Validation of the algorithm

To validate the proposed two-dimensional strain imaging technique, ultrasound-based axial and azimuthal strains were compared to reference strains obtained with sonomicrometry in a *cyclically deforming cylindrical phantom* (figure 3-9). This phantom geometry was chosen because, for symmetry reasons, a true two-dimensional deformation could be expected. The phantom had an outer radius of 15 mm, a lumen radius of 5 mm, and a length of 200 mm. It was made of 15% (mass%) polyvinylalcohol (PVA, Sigma Chemicals, St. Louis, MO, USA, Av. Mol. Wt. 70000-

100000) dissolved in hot water. In order to ensure backscattering of the ultrasonic waves, 0.5% graphite powder was added to the solution. This PVA solution is a viscous liquid, and as a cryogel it gets its elastic properties from a freeze-thaw process. Three freeze-thaw cycles were found to give the desired stiffness and robustness. The PVA phantom was subsequently fixed in a water tank and attached to pipes that were connected to an external pump. With this pump, the pressure in the lumen of the phantom could be changed cyclically, resulting in a cyclic radial deformation of the phantom wall. RF data were acquired with a frame rate of 167 Hz using a Toshiba PowerVision 6000 equipped with an RF interface for research purposes. The circumferential and radial strains in the top and side walls were then measured with the method outlined in paragraph 3.3.2.

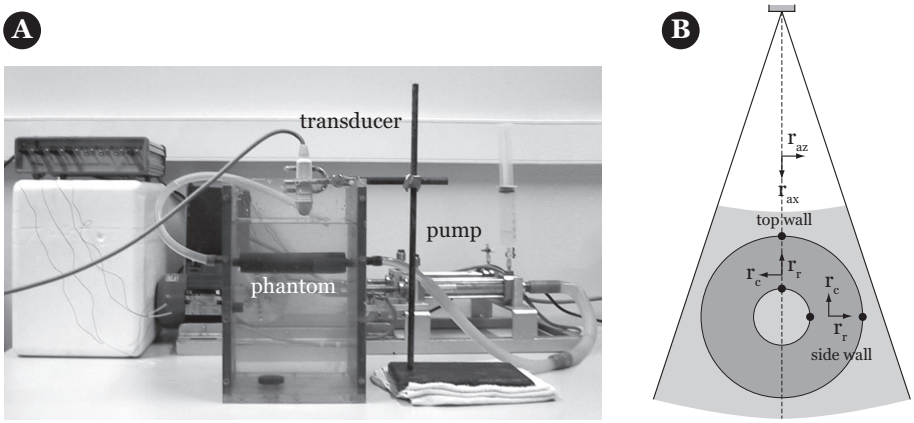

Figure 3-9: A: Experimental setup, showing the PVA phantom, the ultrasound probe and the pump; B: The reference strains in the top and side walls are obtained by continuously measuring wall thickness using two pairs of microcrystals. Both the ultrasound coordinate system with axial (r_{ax}) and azimuthal (r_{az}) directions and the phantom coordinate system with radial (r_r) and circumferential (r_c) directions are indicated.

The *reference* measurement for the two-dimensional strains was obtained with two pairs of *ultrasonic microcrystals* (Sonometrics Corporation, London, Ontario, Canada) (figure 3-9B). These crystals were attached to the inner and outer layers of the top and side walls of the phantom to provide an instantaneous measure of wall thickness throughout the deformation cycle. Assuming incompressibility of the phantom material (conservation of area) and a purely two-dimensional deformation, radial strains can be easily calculated from the change in wall-thickness. Circumferential strains were determined indirectly using continuum mechanics.

Ultrasound (US) and sonomicrometry (SM) strains were finally compared to each other in terms of:

- The time course of radial and circumferential strain during the deformation cycle;
- The absolute peak radial ($\varepsilon_{r,max}$) and circumferential ($\varepsilon_{c,max}$) strain;
- The time to peak strain values, $t_{max,r}$ and $t_{max,c}$ (as a measure of the time interval to maximum deformation).

3.3.4 Results and discussion

A representative example of strain curves measured with ultrasound and with sonomicrometry is shown in figure 3-10. Very high mean correlations between both measurement techniques were obtained (table 3-1). This finding was considered important as several studies have shown the clinical importance of the shape of the deformation curves [145, 347]. The time to peak strain estimates were found to be very accurate in both the radial and circumferential directions. Again, this was considered important because the timing of the deformation characteristics has been shown to contain clinically important information [144].

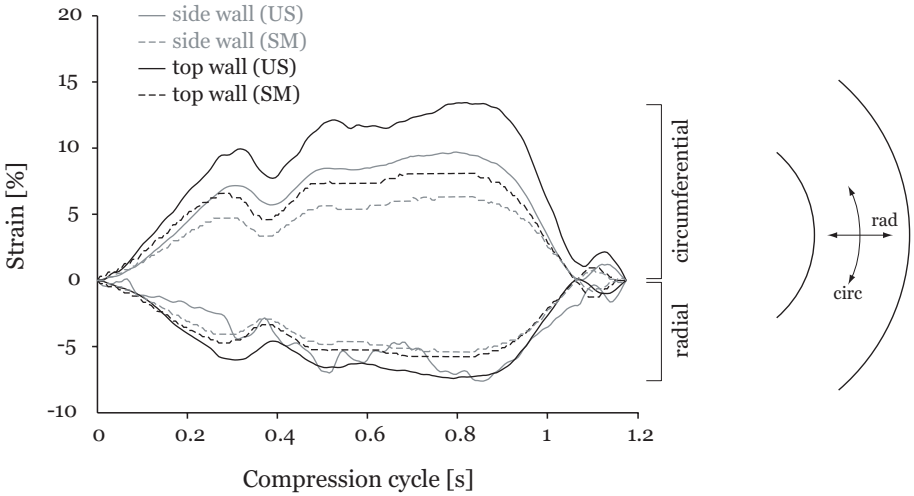

Figure 3-10: Example of strain curves extracted in the two walls, measured with ultrasound (solid) and sonomicrometry (dashed). The grey curves are measured in the side wall and the black curves are measured in the top wall. Positive curves show the circumferential strain and the negative curves show the radial strain.

Table 3-1: Correlation between sonomicrometry (SM) and ultrasound (US) strain curves and the difference between their time to peak values.

	Top wall	Side wall
	Correlation (R)	
ε_r	0.97	0.71
ε_c	0.95	0.97
	Absolute difference in time to peak	
$t_{max,r}$	0.02 ± 0.09 s	0.04 ± 0.20 s
$t_{max,c}$	0.05 ± 0.09 s	0.05 ± 0.07 s

$\varepsilon_{r,max}$ and $\varepsilon_{c,max}$: maximum strains in the radial and circumferential direction; $t_{max,r}$ and $t_{max,c}$: time to peak strain in the radial and circumferential direction.

The strain measurements dominated by the axial and azimuthal displacement estimates were analyzed separately in the regression and Bland-Altman analyses (figure 3-11). The radial strain in the top wall and the circumferential strain in the side wall were merged and analyzed in combination as *axial strain* (ε_{ax}). Similarly, the circumferential strain in the top wall and the radial strain in the side wall were analyzed in combination as *azimuthal strain* (ε_{az}). This was done because earlier simulation work [181] had already shown that the accuracy of the axial and azimuthal strain estimate is different.

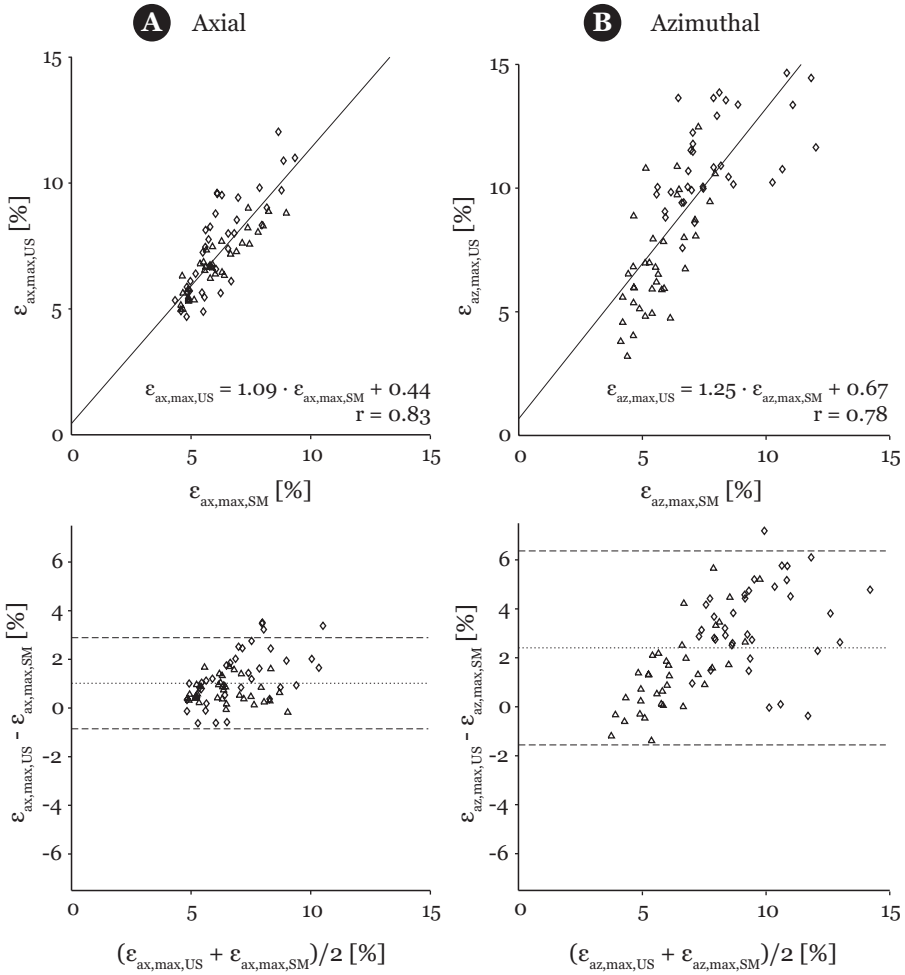

Figure 3-11: A: Correlation between ultrasound (US) and sonomicrometry (SM) axial strain. The Bland-Altman plot shows the mean difference with dotted lines and the limits of agreement (mean ± 2 · SD) with dashed lines. The radial strain in the top wall is indicated with △ and the circumferential strain in the side wall is indicated with ◇; B: The correlation and Bland-Altman plot for the azimuthal strains.

As could be expected, figure 3-11 showed that ε_{ax} is estimated with a higher accuracy than ε_{az}. Most likely, this is due to the intrinsic higher axial resolution of ultrasonic imaging. Indeed, for RF tracking, the accuracy of the velocity estimates is dependent on the resolution of the RF image [147]. In the case of ultrasonic imaging, the axial resolution is determined by the length of the ultrasonic pulse, while the azimuthal resolution is determined by the beam width (≈ 1.5 mm), which is typically much wider than the length of the pulse (≈ 0.25 mm). Nevertheless, the Bland-Altman analysis for the azimuthal strains showed the 95% limits of agreement to be ±3.9% (figure 3-11), which is still smaller than the changes that have to be measured for clinical decision making. The expected strain range in normal subjects is 10 - 60% and clinically important changes are typically larger than 10 - 15% [108, 145].

The linear regression of the azimuthal strains (figure 3-11) showed that the new methodology has a tendency to overestimate the actual value (slope = 1.25). This can also be recognized in the Bland-Altman analysis (figure 3-11) as an increasing error with an increasing strain magnitude. It should be noted, however, that the regression might be influenced by the limited strain range obtained in this setup (ranging from 4 to 14%). Increasing the strain range further in the tubular phantoms proved to be very difficult since a significant expansion is required to induce only a relatively small radial strain. Nevertheless, additional validation studies with larger strains (>15%) are required to validate the algorithm.

3.3.5 Validation in vivo

The proposed technique for assessing two-dimensional deformation has recently been further validated in five open-chest sheep [182]. In that experimental study, the radial (ε_{rad}) and longitudinal (ε_{long}) strain components were compared to reference strains obtained from microcrystals placed directly on a beating heart. Experiments were performed during baseline, after changing contractility (esmolol and dobutamine infusion), and after induction of ischaemia.

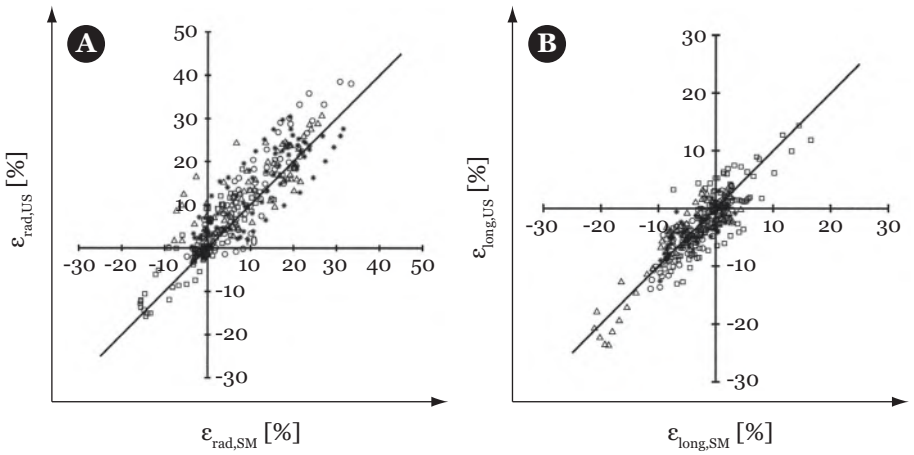

Figure 3-12: Correlation between ultrasound (US) and sonomicrometry (SM) strains measured in the radial (A) and longitudinal (B) direction. ✳ Indicates baseline, ○ esmolol infusion, △ dobutamine infusion, and □ induction of ischaemia.

Both methods agreed very well: the bias and the 95% limits of agreement for ε_{rad} and ε_{long} estimates equalled 2.0 ± 9.3% and 0.4 ± 5.5%, respectively. The intraclass correlation coefficients were found to be 0.72 and 0.80 for the ε_{rad} and ε_{long}, respectively. The relation between both measurement techniques is shown graphically in a scatterplot (figure 3-12).

3.3.6 Conclusion

The proposed two-dimensional strain method solved the problem of *angle dependence* by showing that only one transducer position is required to simultaneously obtain two deformation components of myocardial tissue. Excellent agreements were found between *sonomicrometry* and *ultrasound-based strains*. The technique is less time-consuming because anatomic tracking is performed automatically. This approach could potentially accelerate the clinical acceptance of deformation imaging in cardiology.

4

Chapter 4

Non-invasive Assessment of Ventricular and Myocardial Contractility

The contents of this chapter have been accepted for publication in

American Journal of Physiology, Heart and Circulatory Physiology
Non-invasive Assessment of Left Ventricular and Myocardial Contractility in Middle-aged Men and Women: Disparate Evolution above the Age of 50?
Claessens TE, Rietzschel ER, De Buyzere ML, de Bacquer D, De Backer G, Gillebert TC, Verdonck PR and Segers P.

4.1 Introduction

In present-day clinical cardiology, a plethora of indices exist for quantifying several aspects of left ventricular (LV) systolic contractile behaviour. With the risk of oversimplification, systolic contractile behaviour can be evaluated on different levels. It can be assessed by (i) its mechanical *pump performance* and *function* under a given preload and afterload, and (ii) by its *contractile state* [38].

Ventricular performance refers to the pumping properties of the LV. It is described by the amount of blood it can pump into the circulation under a given pressure head, i.e., the pressure difference between left atrial pressure (LAP) and aortic pressure (P_{ao}). In a clinical setting, LV performance is usually assessed by measuring the generated stroke work (SW), which combines both pressure generation and shortening in an integrated index. *Ventricular function,* on the other hand, expresses the relation between ventricular performance and a measure a preload, as shown in Frank-Starling curves. Yet, frequently used ultrasound-derived indices, such as ejection fraction (EF), strain and strain rate and systolic mitral annular velocity, are also considered as indices of ventricular function. Ventricular function indices are, just like ventricular performance indices, influenced by *loading conditions*.

Contractility refers to a *basic property* of cardiomyocytes and reflects the intensity of cross-bridge activity. It encompasses the performance of all cellular mechanisms that result in an increase in the velocity of tension development and/or shortening, under a given sarcomere length (i.e., preload). Contractility is said to be increased when fibre shortening velocity is increased, and a higher peak tension and steeper tension rise are observed, when preload and/or afterload, and stimulation frequency are kept constant [34]. Many insights about contractility have been gained from investigations concerning the relation between length, tension and velocity in isometrically and isotonically contracting papillary muscles. Brutsaert et al. [44] showed that the contractile state of the contractile units in an isolated muscle can be characterized by a *three-dimensional surface* describing the instantaneous relation between *force*, *length* and *velocity* (or *time*). However, ever since the earliest experiments on isolated muscles, controversy exists about the various concepts that aim to *quantify* contractility of the isolated cardiac muscle *and* the intact heart by a *single number*. Consequentially, a universally accepted quantitative description of contractility is still lacking. To the clinician, a reliable measure of contractility or contractile state would be very helpful though for early detection of myocardial disease.

End-systolic elastance (E_{es}), calculated as the slope of the end-systolic pressure-volume relationship (ESPVR), is a widely accepted index for detecting changes in *global left ventricular contractility* in the research setting, because it is *relatively insensitive* to changes in preload and afterload, but *sensitive* to alterations in contractility (see paragraph 2.4.2.3). Even though some criticisms and potential shortcomings of this index have been previously reported in literature [45, 156, 275], assessment of E_{es} has undoubtedly shown to be useful in some sophisticated clinical studies including left heart catheterization. Unfortunately, the relation between E_{es} and the *intrinsic contractile state* of the myocardium (i.e., *myocardial contractility*) is currently not yet elucidated.

In this chapter, an attempt was made to set up a relationship between E_{es} and myocardial contractility, based on the geometric characteristics of the LV. We therefore relied on the Asklepios data set. The obtained relationship was then used to investigate the influence of *age* and *gender* on *ventricular* and *myocardial* contractility (paragraph 4.2).

4.2 Ventricular and myocardial contractility: effects of age and gender

4.2.1 Introduction

The ESPVR uniquely represents the end-systolic state of the ventricle irrespective of the mode of contraction. E_{es}, calculated from the slope of the ESPVR, is considered a relatively preload- and afterload-independent index of *left ventricular contractility*, which is often used in basic research, where it is considered a "gold standard" [274, 309]. Its clinical application, however, is somewhat limited due to its invasive nature and the need for considerable changes in loading conditions upon assessment of E_{es}.

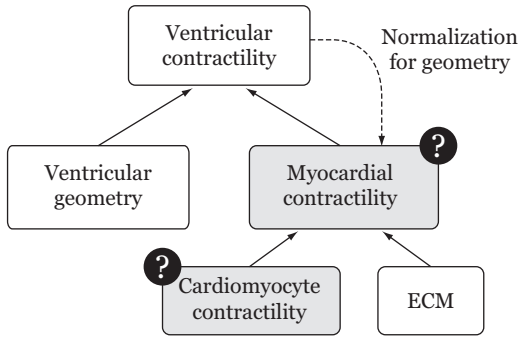

Figure 4-1: Left ventricular (LV) contractility, commonly assessed with E_{es}, is determined by myocardial contractility and LV geometry. E_{es} needs to be normalized for LV geometry in order to estimate myocardial (intrinsic) contractile properties. In the ideal case, this procedure would also allow for estimating contractility of cardiomyocytes embedded in an extracellular matrix (ECM).

Whereas the concept of E_{es} is generally applied to assess *changes* in ventricular contractile state (e.g., due to inotropic stimulation) within a *single individual*, interpretation of differences in E_{es} in ventricles with different geometries appears cumbersome [46, 51, 52], since E_{es} is intrinsically influenced by LV *dimensions* [16, 51]. Indeed, because LV volume can differ widely for various subjects while LVP remains constant, it is expected that the pressure-volume ratio E_{es} is a function of LV volume. *Normalizing* or *scaling* ventricular contractility E_{es} is thus required to cancel out the effect of geometry and to obtain a useful index of *myocardial contractile state*, which ideally should reflect the mechanical characteristics of the cardiomyocytes (figure 4-1). The use of such a scaled index would, moreover, allow to investigate age- and gender-related differences in myocardial contractility. A number of normalization methods have already been proposed in literature [30, 275], but a generally accepted

standard has not yet been agreed upon, nor have the existing methods been compared to each other.

The primary aims of this study, conducted in a large population setting (the Asklepios Study), were

- to calculate ventricular contractility E_{es} in a non-invasive way,
- to propose a novel (population-specific) normalization method for E_{es}, and
- to assess the effects of age and gender on myocardial contractility as determined with the new and existing normalization methods.

4.2.2 Methods

4.2.2.1 The Asklepios Study

The Asklepios Study is a longitudinal population study focusing on the interplay between *ageing*, *cardiovascular haemodynamics* and *inflammation* in (preclinical) cardiovascular disease. The 2524 participants (1301 F and 1223 M) are a representative cohort of 35-55 year-old subjects, free from overt cardiovascular disease at study initiation, randomly sampled from the twinned Belgian communities of Erpe-Mere and Nieuwerkerken (Belgium). Baseline examinations (questionnaires, conventional risk factors and biochemistry) are performed by a single observer, with a single device, at a single site, and in a single two-year consecutive timeframe (between October 2002 and September 2004). The ethical committee of the Ghent University Hospital approved the study protocol. Written informed consent was given by all subjects.

Additional phenotypes under study include:

- *vascular structure and function*: carotid and femoral atherosclerosis, arterial distension and pressure curves;
- *cardiac structure, diastolic and systolic function* (ultrasound scanning);
- integrated non-invasive biomechanical assessment of *cardiac, arterial and ventriculo-vascular function* through combination of modelling, fundamental haemodynamic measurements and system identification techniques;
- systematic determination of *peripheral blood leukocyte telomere length* as a marker for biological ageing.

The *primary aim* of the Asklepios Study is to build a combined dataset that will act as a tool to answer a cluster of questions about *ageing*, *haemodynamics* and emergence of *cardiovascular disease*, in particular incidence of atherothrombotic events and development of adverse haemodynamic profiles (arterial stiffening, heart failure). The study will reassess current risk factors and provide a long-term base for detection of novel risk factors and for better performing risk stratification modalities [264].

4.2.2.2 Subject population

For the present investigation we selected 2184 (1115 F and 1069 M) subjects from the original Asklepios data set of 2524 subjects. We excluded 340 subjects, because (i)

264 subjects were drug treated for hypertension and, hence, excluded from the study, and because (ii) data about SV, timings of onset and cessation of aortic flow, and/or EF data could not be obtained in 76 additional subjects due to various technical reasons.

4.2.2.3 Blood pressure measurement

Brachial systolic (P_s) and *diastolic blood* (P_d) pressures were recorded using bilateral triplicate measurements on a rested subject using a validated oscillometric Omron HEM-907 device (Omron Matsuka Co. Ltd., Japan). Subjects were blinded to the blood pressure results during measurements. Cuff size was individually chosen based on arm circumference. Blood pressure values of these six readings were averaged and the mean value is used throughout the whole study, except when there was a persistent discrepancy of more than 20 mmHg between left and right sided blood pressures after a second bilateral triplicate measurement. In that case, the mean value from the limb with the highest pressure was taken to represent blood pressure.

4.2.2.4 Echocardiography

Echocardiographic measurements were performed using a commercially available ultrasound system (Vivid 7, GE Vingmed Ultrasound, Horten, Norway) equipped with a cardiac transducer (M3S 1.7/3.4 MHz matrix transducer). Subjects were examined in the left lateral recumbent position using standard parasternal short- and long-axis and apical views. All measurements were ECG-gated and consisted of cineloops of recordings of at least 5 (up to 30) cardiac cycles during normal breathing. Images and loops were exported in RAW Dicom format to magneto-optical discs and an image server. Measurements were performed offline in a blinded fashion on a dedicated Compaq Evo W4000 workstation running GE Vingmed EchoPAC Version 2.0.1 software (GE Vingmed Ultrasound, Horten, Norway).

4.2.2.5 Data analysis

LV geometry-related parameters. Left ventricular geometry is commonly characterized by its resting *end-diastolic volume* (EDV), *wall mass* (LVM), and *relative wall thickness* (RWT) (figure 4-2).

LV volumes at end-diastole were calculated from the two-dimensional parasternal long-axis images using the standard volumetric methods (Teichholz' formula) [325]:

$$EDV = (7 \cdot LVID^3)/(2.4 + LVID) \quad (4\text{-}1)$$

where LVID represents the LV internal diameter. End-diastolic LV dimensions were also used to calculate LVM with a validated formula, shown to yield LVM values closely related to necropsy measurements [77]:

$$LVM = 0.8 \cdot (1.04 \cdot ((SWT + LVID + PWT)^3 - LVID^3)) + 0.6 \quad (4\text{-}2)$$

where SWT and PWT are the septal and posterior wall thickness at end-diastole, respectively. RWT was calculated as 2 · PWT / LVID.

$$RWT = \frac{2 \cdot PWT}{LVID}$$

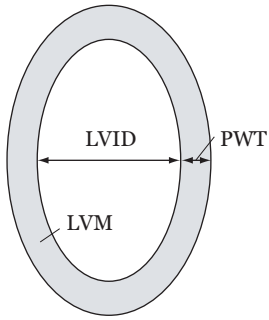

Figure 4-2: The ellipsoid model of the LV is characterized by its end-diastolic dimensions: internal diameter (LVID) and posterior wall thickness (PWT). LVM denotes left ventricular mass. The relative wall thickness (RWT) is calculated is 2·PWT / LVID.

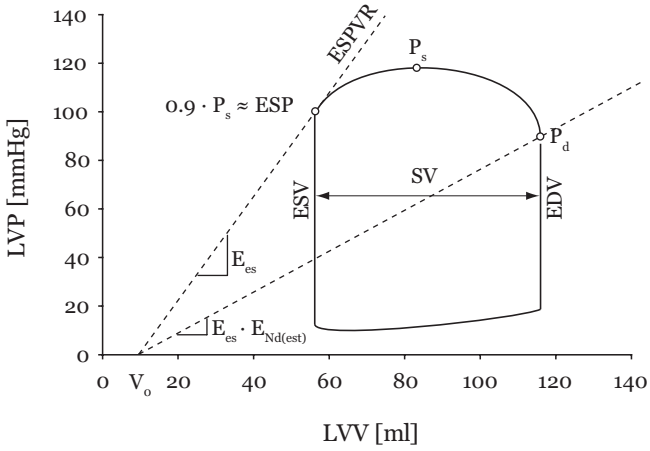

Figure 4-3: Illustration of the method for non-invasive assessment of the single-beat left ventricular end-systolic elastance (E_{es}). $E_{Nd(est)}$ represents the ratio of the elastance at the onset of ejection to the maximum elastance at end-ejection. Detailed information is provided in [57] (P_s: brachial systolic pressure, P_d: brachial diastolic pressure, ESP: left ventricular end-systolic pressure, ESV: end-systolic volume, EDV: end-diastolic volume, SV: stroke volume, ESPVR: end-systolic pressure-volume relationship, V_o: volume intercept of the ESPVR).

End-systolic elastance. In each subject, ventricular contractility was estimated as the slope of the ESPVR using the *non-invasive single-beat* technique (appendix 4.3.1), described by Chen et al. [57] and also applied in a recent population-based study by Redfield et al. [260]. This algorithm assumes a linear ESPVR and a constant volume intercept (V_o, not varying in time) of the ESPVR, and was validated against invasive measurements of E_{es} (figure 4-3). Briefly, the single-beat elastance is calculated as

$$E_{es} = (P_d - 0.9 \cdot E_{Nd(est)} \cdot P_s) / (SV \cdot E_{Nd(est)}) \qquad (4\text{-}3)$$

The stroke volume (SV) is obtained from the LV outflow tract diameter and the pulsed wave Doppler signal as previously described [240]. $E_{Nd(est)}$ represents the individual non-invasively estimated LV elastance at the onset of ejection:

$$E_{Nd(est)} = 0.0275 - 0.165 \cdot EF + 0.3656 \cdot (P_d / ESP) + 0.515 \cdot E_{Nd(avg)} \quad (4\text{-}4)$$

EF was acquired with Teicholz' method [325]. ESP was estimated as $0.9 \cdot P_s$. Previous studies have reported high correlations between this estimation and invasively measured ESP in patients of widely varied ages and vascular properties [161]. $E_{Nd(avg)}$ is approximated by a seven-term polynomial function:

$$E_{Nd(avg)} = \sum_{i=0} a_i \cdot t_{Nd}{}^i \quad (4\text{-}5)$$

with the normalized time t_{Nd} obtained as t_d/t_{es}. Both t_d and t_{es} were assessed from the continuous wave Doppler flow measurements as the time delay between the QRS-peak and the onset and cessation of aortic flow, respectively (figure 4-4). The values of the regression coefficients a_i are 0.35695, -7.2266, 74.249, -307.39, 684.54, -856.92, 571.95, -159.1 for i = 0 to 7, respectively [57].

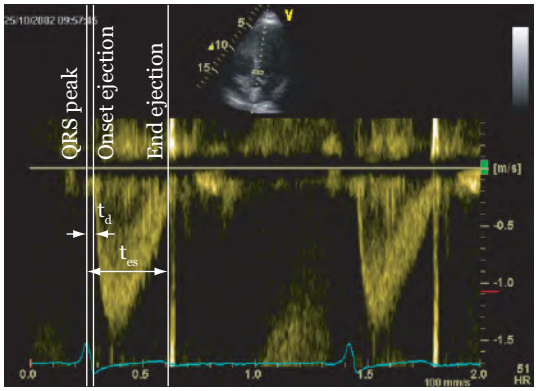

Figure 4-4: Determination of the time delays between the QRS-peak and the onset of ejection (t_d), and between the QRS-peak and the end of ejection (t_{es}) on the Doppler aortic flow measurements.

Normalization of E_{es} for LV geometry: existing methods. Linear regression was used to estimate the sensitivity of end-systolic elastance (E_{es}) for geometry-related parameters EDV and LVM. Since E_{es} is intrinsically dependent on LV geometry [46, 51, 52, 274, 275], it cannot be applied to estimate and compare myocardial contractility between subjects with different LV geometries (table 4-1). Hence, an appropriate *normalization method* that converts E_{es} into a measure of myocardial contractility is highly desired to estimate gender- and age-related differences in myocardial contractile state. A number of normalization methods can be found in literature [30, 275], but a single accepted standard has not been agreed upon [46].

Existing methods to normalize E_{es}, and applied in this work, include:

- Normalizing for EDV: $E_{es} \cdot EDV$

- Normalizing for LVM: $E_{es} \cdot LVM$
- Elastance index EI: $0.433 \cdot E_{es} \cdot LVM / RWT$

EI is an index of myocardial contractility, introduced by Beyar and Sideman, based on a mathematical but *physiologically realistic ellipsoid model* of the LV [27]. The rationale behind this index is outlined briefly in appendix 4.3.2.

Table 4-1: Requirements for ideal indices of ventricular and myocardial contractility.

Ventricular contractility
(1) insensitive to changes in loading conditions
(2) sensitive to changes in inotropic state
Myocardial contractility
(1) + (2) + independent of LV geometry

Novel normalization method. In addition to these methods, we developed an alternative, semi-empirical approach to normalize E_{es}. From our population of healthy middle-aged subjects, we have first selected a subpopulation of "*physiologic reference*" subjects, based on a list of 12 criteria (table 4-2).

We subsequently assumed that in this subpopulation the spectrum of E_{es}-values is largely explained by the differences in LV geometries, rather than by the differences in myocardial contractility. Minimization of variance in E_{es} using a linear regression model would allow us to propose a formula to determine a geometry-normalized measure of contractility. We specifically opted for obtaining a formula of a general form that is similar to Beyar and Sideman's elastance index. Appendix 4.3.3 describes how we derived our geometry-adjusted $E_{es,adj}$, which is of the general form:

$$E_{es,adj} = a \cdot E_{es} \cdot LVM^{b} \cdot RWT^{c} \qquad (4\text{-}6)$$

where a, b and c represent the coefficients of a log-converted linear regression model.

4.2.2.6 Statistics

Statistics have been performed in commercially available software (SPSS 12.0, SPSS Inc., Chicago, IL, USA). All parameters were screened for deviation from normality. Measures of central tendency are mean ± SD (normal distribution) or median and interquartile range. Pearson's correlation coefficients were used to quantify the agreement between two variables. The geometry dependence (in terms LVM and EDV) of the various contractility indices was analyzed using simple and multiple linear regression models. Two-way analysis of variance (ANOVA) was used to detect differences in contractility due to gender and age. When using analysis of covariance (ANCOVA), homogeneity of the regression slopes (response variable versus the potential covariates) was verified by testing for significance of the interaction term between the covariate and the grouping variable. All p-values are specified in the results section, unless $p < 0.001$.

Table 4-2: Criteria for determining the "physiologic reference" subpopulation.

Parameter	Criterion
P_s (mmHg)	$100 < P_s \leq 140$
P_d (mmHg)	$60 < P_d \leq 90$
HR (BPM)	$50 \leq HR < 90$
EF (%)	$EF \geq 60$
Systolic Tissue Doppler (mm/s)	$TDI \geq 70$
Filling pressure index (-)	$E/E' \leq 8$
BMI (kg/m²)	$BMI < 30$
Waist circumference (cm)	Waist < 88 (f) and Waist < 102 (m)
Diabetes type 2	No diabetes
Atherosclerosis (carotid and/or femoral)	No echographically detectable atherosclerosis
Hematocrit	Hematocrit ≥ 30
High sensitive CRP (mg/l)	CRP < 3

Carotid and femoral arteries were carefully scanned bilaterally for the presence of plaque (focal protrusion > 50% compared to adjacent sites, absolute thickness > 1.5 mm). IMT was defined as the distance from the leading edge of the lumen-intima interface to the leading edge of the media-adventitia interface, measured in lateral plane B-mode projection, in end-diastole, at the far wall, 1-2 cm before the bifurcations. Atherosclerosis was defined as a carotid or femoral IMT ≥ 0.9 mm and/or the presence of carotid or femoral plaque (IMT: Intima-media thickness, P_s: brachial systolic blood pressure, P_d: brachial diastolic blood pressure, HR: heart rate, EF: ejection fraction, BMI: body mass index).

4.2.3 Results

4.2.3.1 Baseline demographics and haemodynamics

Table 4-3 displays baseline demographic and haemodynamic data and geometry-related parameters for the study population and the selected "reference" subpopulation. In the study population, women had higher resting heart rates and lower brachial blood pressure values. As expected, women had smaller hearts with significantly smaller EDV and lower LVM. No age difference was observed between men and women. EF, a commonly used index of systolic function, was significantly higher in women (figure 4-5A).

4.2.3.2 End-systolic elastance

E_{es} was significantly higher in women than in men at all ages (two-way ANOVA, $p < 0.001$, post hoc t-test, $p < 0.001$). On average, E_{es} in men is 2.40 ± 0.64 mmHg/ml, versus 2.89 ± 0.80 mmHg/ml in women ($p < 0.001$, table 4-3). When analyzing the evolution of E_{es} with age, the curves in figure 4-5B suggest a more or less parallel time course of E_{es} in men and women until the age of 50. After age 50, however, E_{es} in women tends to increase ($p = 0.058$ vs. age 46-50), whereas E_{es} remains constant in men ($p = 0.82$).

Table 4-3: Characteristics of the study population and "physiologic reference" subpopulation.

	Study population		"Physiologic reference" subpopulation	
	F (n = 1115)	M (n = 1069)	F (n = 175)	M (n = 119)
Baseline demographics				
Age (y)	45.2 [40.6 - 50.3]	45.7 [40.9 - 50.4]	42.8 [39.0 - 47.8]	40.9 [38.2 - 44.8] †
Height (cm)	163.3 ± 6.0	175.8 ± 6.5 *	164.5 ± 5.7	177.5 ± 6.4 *
Weight (kg)	65.7 ± 11.9	81.2 ± 12.2 *	60.7 ± 7.0	76.7 ± 8.2 *
BSA (m^2)	1.71 ± 0.15	1.97 ± 0.15 *	1.66 ± 0.11	1.94 ± 0.12 *
BMI (kg/m^2)	24.61 ± 4.29	26.21 ± 3.59 *	22.39 ± 2.28	24.31 ± 2.32 *
Left ventricular geometry				
LVM (g)	121.40 ± 29.07	177.22 ± 39.53 *	108.88 ± 21.45	159.24 ± 33.10 *
LVMI (g/m^2)	70.91 ± 14.35	89.73 ± 17.75 *	65.40 ± 11.58	82.13 ± 16.45 *
RWT (-)	0.36 ± 0.06	0.39 ± 0.07 *	0.35 ± 0.05	0.37 ± 0.05 §
PWT (mm)	8.12 ± 1.17	9.55 ± 1.30 *	7.70 ± 0.99	8.97 ± 1.10 *
EDV (ml)	92.60 ± 18.26	115.79 ± 23.71 *	88.28 ± 16.03	111.43 ± 20.26 *
EDVI (ml/m^2)	54.33 ± 9.81	58.78 ± 11.31 *	53.16 ± 9.16	57.50 ± 10.11 *
Haemodynamics				
HR (BPM)	72.12 ± 9.82	68.39 ± 11.11 *	71.10 ± 7.65	65.55 ± 8.21 *
P_s (mmHg)	121.87 ± 13.72	129.76 ± 12.18 *	115.46 ± 8.39	125.29 ± 7.36 *
P_d (mmHg)	77.12 ± 9.47	81.74 ± 9.42 *	72.91 ± 6.39	77.07 ± 7.04 *
PP (mmHg)	44.76 ± 8.47	48.02 ± 7.21 *	42.55 ± 5.47	48.22 ± 5.56 *
SV (ml)	64.15 ± 12.56	78.92 ± 16.34 *	63.63 ± 11.80	78.37 ± 14.28 *
CO (l/min)	4.59 ± 0.96	5.34 ± 1.16 *	4.51 ± 0.87	5.10 ± 0.99 *
EF (%)	66.88 ± 7.66	64.50 ± 8.26 *	68.98 ± 5.08	66.76 ± 4.90 *
E_{es} (mmHg/ml)	2.89 ± 0.80	2.40 ± 0.64 *	2.82 ± 0.73	2.42 ± 0.54 *

HR: heart rate, P_s: brachial systolic blood pressure, P_d: brachial diastolic blood pressure, PP: pulse pressure, BSA: body surface area, BMI: body mass index, LV: left ventricle, LVM: LV mass, LVMI: LV mass index (= LVM / BSA), RWT: relative wall thickness, PWT: posterior wall thickness, EDV: end-diastolic volume, EDVI: end-diastolic volume index, SV: stroke volume, CO: cardiac output, EF: ejection fraction, E_{es}: end-systolic elastance. Data are expressed as mean ± SD or median [interquartile range] where appropriate. § and * indicate $p < 0.05$ and $p < 0.001$ male vs. female using a t-test, respectively. † indicates $p < 0.05$ male vs. female using a non-parametric Mann-Whitney test.

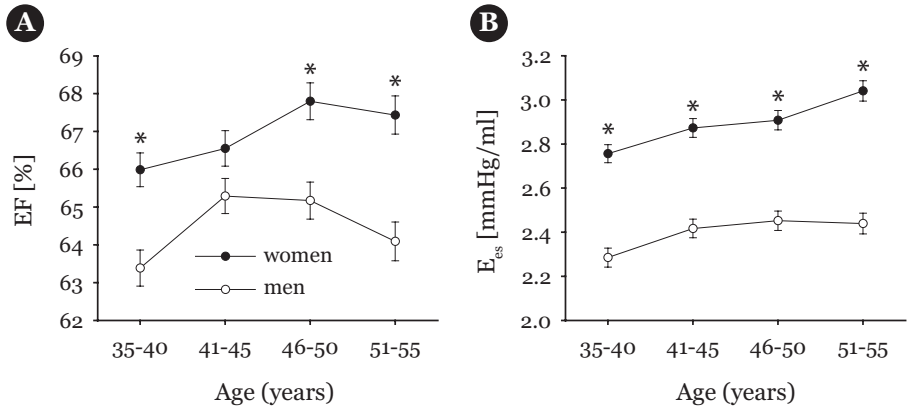

*Figure 4-5: Ejection fraction (EF), a measure of systolic function, is higher in women than in men (ANOVA, p < 0.001); B: E_{es} is higher in women than in men (ANOVA, p < 0.001). The curves suggest a more or less parallel time course of E_{es} until the age of 50. After age 50, E_{es} in women tends to increase, whereas E_{es} remains constant in men. Data are shown as mean ± SEM. * indicates p < 0.05 male vs. female using a t-test.*

Differences in LV geometry are likely to be one of the major contributors to the gender-related differences in E_{es}, with EDV (115.79 ± 23.71 ml vs. 92.60 ± 18.26 ml, $p < 0.001$) and LVM (177.22 ± 39.53 g vs. 121.40 ± 29.07 g, $p < 0.001$) being higher in men. In men, E_{es} is significantly influenced by the geometry-related parameters LVM and EDV ($E_{es} = 3.616 - 0.002 \cdot LVM - 0.008 \cdot EDV$; $p < 0.001$; $R^2 = 0.134$) with EDV about 2.5 times as important as LVM. In women, on the other hand, E_{es} was only determined by the geometry-related parameter EDV ($E_{es} = 4.238 - 0.015 \cdot EDV$; $p < 0.001$; $R^2 = 0.111$); LVM did not enter the model. Figure 4-6A and B show the relation between E_{es} and both predictor variables separately. It can be seen that women are positioned in the upper left region of the graphs, tending to have smaller EDV and LVM as well as higher E_{es}.

Due to its geometry dependence, E_{es} thus requires normalization to study differences across subgroups (such as men and women) with varying geometry.

4.2.3.3 Normalization based on the "physiologic reference" subpopulation

294 subjects (175 F, 119 M) from the study population (13.5%) fulfilled the criteria to be designated as "physiologic reference" subjects. Their baseline characteristics are presented in table 4-3. The prevalence of women is somewhat higher in the subpopulation than in the complete population. Based on the principles that are outlined in appendix 4.3.3, the following formula was obtained which converts E_{es} into a geometry-adjusted index of myocardial contractility ($E_{es,adj}$):

$$E_{es,adj} = 0.0941 \cdot E_{es} \cdot LVM^{0.455} \cdot RWT^{-0.159} \qquad (4\text{-}7)$$

As anticipated, this expression is similar to the elastance index ($EI = 0.433 \cdot E_{es} \cdot LVM \cdot RWT^{-1}$) in terms of its functional form.

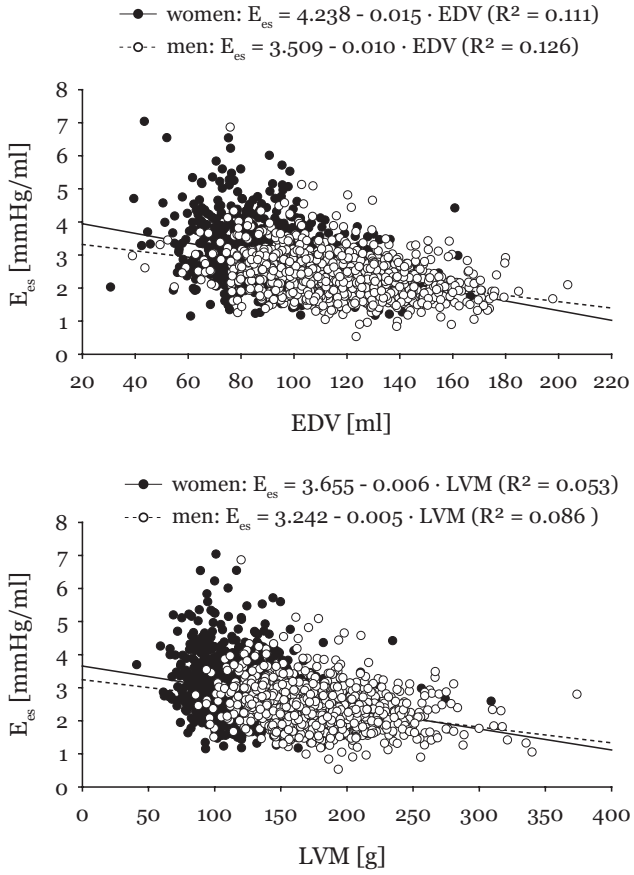

Figure 4-6: In men as well as in women, E_{es} is largely affected by end-diastolic volume (EDV) and left ventricular mass (LVM).

4.2.3.4 Comparison of normalization techniques

To verify whether our normalization method worked well, linear regression was performed between $E_{es,adj}$ and the geometry-related predictor variables EDV and LVM in the subpopulation. As anticipated, no statistically significant regression model could be found (table 4-4). Note, however, that this was not the case for the three other normalization methods, where significant regression functions were found in the subpopulation. Whether this implies that we "overcompensate" the effect of geometry using our normalization approach, or that it is a manifestation of the inability of the existing methods to compensate for geometry, is an open question, as none of the indices has been validated against gold standard indices of myocardial contractility insofar this would be possible. Note also that E_{es} · EDV was even dependent on both EDV and LVM. Nevertheless, the coefficient of variation (CV), an indication of the relative amount of scatter in the data, is minimal in case of $E_{es,adj}$, showing that $E_{es,adj}$ performed best in reducing the amount of variance in the subpopulation.

Table 4-4: Linear regression of myocardial contractility indices versus geometry-related parameters in the subpopulation.

	a_1	a_2	a_3	R^2	p	CV
E_{es}	3.985	-0.006	-0.006	0.210	<0.001	25.9
	[3.650;4.320]	[-0.011;-0.001]	[-0.009;-0.003]			
$E_{es,adj}$	-	-	-	-	-	22.3
$E_{es} \cdot EDV$	124.4	2.090	-0.578	0.234	<0.001	25.1
	[94.0;154.8]	[1.605;2.575]	[-0.859;-0.296]			
$E_{es} \cdot LVM$	142.7	-	1.471	0.342	<0.001	27.5
	[111.1;174.3]		[1.236;1.706]			
EI	127.2	2.839	-	0.296	<0.001	27.3
	[76.9;177.6]	[2.335;3.344]				

Regression coefficients of the regression function: myocardial contractility index = $a_1 + a_2 \cdot EDV + a_3 \cdot LVM$. The 95% confidence intervals of the coefficients are shown between brackets. As expected, $E_{es,adj}$ is a myocardial contractility index which is totally independent of geometry in the subpopulation of "physiologic reference" subjects. CV is minimal for $E_{es,adj}$ (E_{es}: end-systolic elastance, $E_{es,adj}$: geometry-adjusted contractility, EI: elastance index, LVM: left ventricular mass, RWT: relative wall thickness, EDV: end-diastolic volume, CV: coefficient of variation).

Table 4-5 provides Pearson's correlation coefficients (R) between myocardial contractility according to the various normalization methods in the whole study population. Correlation coefficients vary between 0.782 ($E_{es} \cdot EDV$ vs. $E_{es} \cdot LVM$) and 0.943 (EI vs. $E_{es} \cdot EDV$). Despite the rather complex mathematical description of our approach, our novel $E_{es,adj}$ appears to correlate well with the previously reported normalization methods.

Table 4-5: Pearson's correlation coefficients (R) between the various geometry-adjusted contractility indices in the whole study population.

	$E_{es,adj}$	$E_{es} \cdot EDV$	$E_{es} \cdot LVM$
$E_{es} \cdot EDV$	0.858	-	-
$E_{es} \cdot LVM$	0.834	0.782	-
EI	0.802	0.943	0.854

E_{es}: end-systolic elastance, $E_{es,adj}$: geometry-adjusted contractility, EI: elastance index, LVM: left ventricular mass, RWT: relative wall thickness, EDV: end-diastolic volume.

4.2.3.5 Age- and gender-related differences in myocardial contractility

Figure 4-7 depicts the age- and gender-related differences in myocardial contractility, obtained from the various normalization methods. A common finding is that, similar to E_{es}, myocardial contractility continues to rise after the age of 50 in women, whereas myocardial contractility in men seems to top off at that age. However, there

are serious inconsistencies with regard to the absolute values of the calculated indices and, hence, the relative position of the female and male curves.

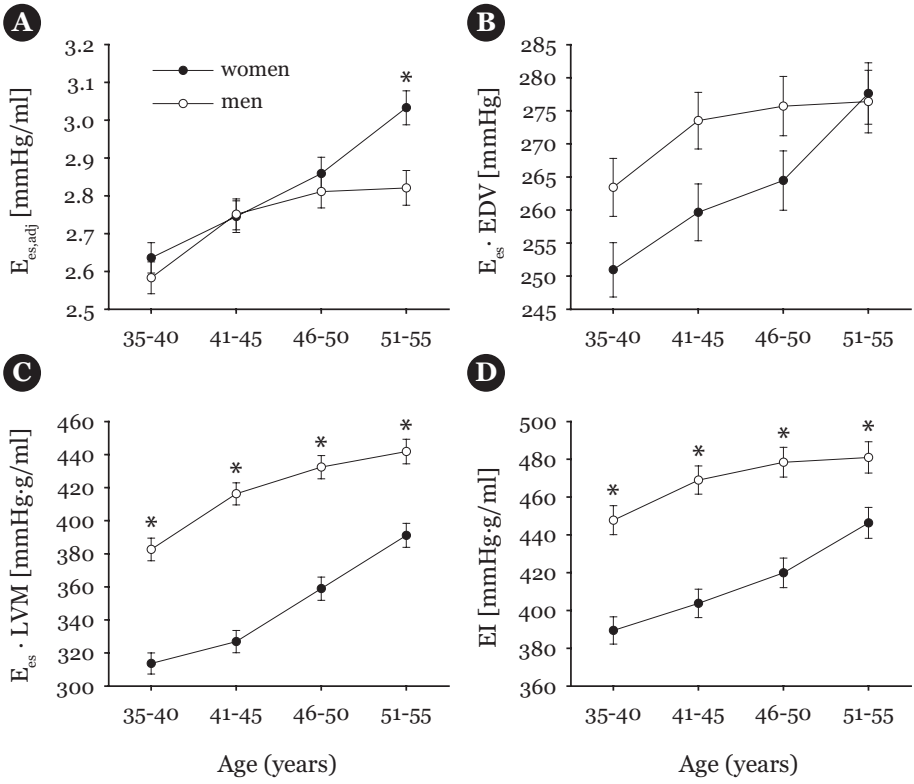

*Figure 4-7: Myocardial contractility indices $E_{es,adj}$ (A), E_{es} · EDV (B), E_{es} · LVM (C), and EI (D) as a function of age (in half decades). There is a noticeable vertical shift in the curves of men and women between the different contractility indices. $E_{es,adj}$ reveals the apparently different time course of myocardial contractility in men and women, being similar up to the age of 50, where after it becomes significantly higher in women. Data are shown as mean ± SEM. * indicates $p < 0.05$ male vs. female using a t-test (E_{es}: end-systolic elastance, $E_{es,adj}$: geometry-adjusted contractility, EI: elastance index, LVM: left ventricular mass, RWT: relative wall thickness, EDV: end-diastolic volume).*

All indices, except $E_{es,adj}$, yield higher values in men than in women, thus reversing the higher values of ventricular contractility (E_{es}) in women. Nevertheless, for E_{es} · EDV, the differences were not significant. Both E_{es} · LVM and EI are higher in men than in women by 13.0% and 7.6%, respectively (two-way ANOVA, $p < 0.001$). In contrast to the other myocardial contractility indices, $E_{es,adj}$ eliminates the systematic gender difference, and reveals the apparently different time course of myocardial contractility in men and women, being similar up to the age of 50, where after it becomes significantly higher in women: 3.03 ± 0.85 vs. 2.82 ± 0.72 mmHg/ml ($p < 0.005$).

4.2.4 Discussion

Studies in isolated dog ventricles, performed by Suga and Sugawa et al. [309, 314, 316] in the 1970's, have shown that the slope of the end-systolic pressure-volume relationship (ESPVR), E_{es}, is a relatively load-independent index of ventricular contractility. E_{es} has since then known a widespread use for research purposes to detect changes in LV inotropic state in humans [125], dogs [140, 314], and rodents [109].

One has to realize that the concept of E_{es} was originally applied in acute experiments within a *single* individual, where it will show an increase as a result of a positive inotropic stimulation. In these circumstances, the increase in the slope of the ESPVR is easily interpreted as a change in ventricular contractility, since only the inotropic state has altered and LV geometry stays unaffected. However, appreciation of differences in E_{es} becomes much more complicated when evaluating and comparing contractility in *cross-sectional studies*, in which the ventricles have a spectrum of different geometries. Since E_{es} is highly affected by LV geometry [16, 51], a difference in E_{es} between two given ventricles does not necessarily indicate a different myocardial contractile state. *Scaling* or *normalization* for geometry is thus required to provide information about myocardial contractile state.

Stress-strain relationships, derived from invasively acquired pressure-volume signals, have been used successfully in the past as a virtually load- and geometry-independent measure of contractility [218, 332]. In our large population, invasive techniques are obviously not feasible. To the best of our knowledge, normalization of E_{es} for LV geometry is the only approach that permits to estimate myocardial contractility non-invasively. Even though the geometry dependence of E_{es} was already acknowledged in the 1970's, a single accepted standard to convert E_{es} into a measure of myocardial contractility (i.e., an intrinsic muscle property) has not yet been defined [46], nor have the existing normalization methods been *evaluated* and *compared* in a large population sample of apparently healthy middle-aged subjects. Sagawa et al. [275] mentioned that normalization with respect to LVM or EDV measured under a standardized resting condition, may provide information regarding myocardial contractility. Normalizing by the *volume intercept* of the ESVPR (V_0) has also been suggested [232]. However, the fact that V_0 may take on negative values, renders it practically useless as a scaling factor. From a conceptual point of view, multiplication with EDV could indeed provide an acceptable index of myocardial contractility as $E_{es} \cdot EDV$ would remain virtually constant. This method, however, can in theory only be applied accurately when E_{es} is inversely proportional with EDV. Under the assumptions that (i) EF is virtually constant in normal ventricles, (ii) the volume intercept of the ESPVR equals zero, and (iii) ESP remains constant, E_{es} can be expressed as $ESP / ESV = ESP / (EDV \cdot (1 - EF)) = k \cdot EDV^{-1}$, which indeed fulfills the criterion. Unfortunately, these assumptions are not entirely fulfilled, introducing scatter and uncertainty in this method of normalization. Other potential limitations of this normalization method include its undesired *preload dependence* (as it incorporates EDV) [30], and the fact that wall thickness is not directly accounted for.

Normalization by LVM can arguably be considered a superior method, because LVM is an invariant property of ventricular muscle and is thus not subject to changes in loading conditions. Beyar and Sideman [30] stated that this approach works well in

ventricles with a normal RWT. However, in particular when RWT deviates from normal (as in concentric hypertrophy or concentric remodelling), the reliability of this method becomes questionable.

Based on a *mathematical model* of LV mechanics, Beyar and Sideman [30] introduced the elastance index (EI = 0.433 · E_{es} · LVM / RWT), a measure of myocardial contractility that was shown to be superior to E_{es} · EDV and E_{es} · LVM in their numerical experiments, because it accounts for changes in both LVM and RWT. Within a wide range of different values of RWT and LVM, their EI showed a coefficient of variation (SD / mean) of no more than 3.5%, in contrast to 25% and 17% in case of E_{es} · EDV and E_{es} · LVM, respectively. We believe that by raising the main factors (LVM and RWT) in their index to a certain power, their elastance index could even be optimized. However, no such attempts were made in their study.

Our normalization method relies on a principle that is somewhat comparable to EI. In a subpopulation of 294 "*physiologic reference*" subjects, selected on the basis of very strict criteria, we have made a critical, but reasonable assumption, namely that myocardial contractility is similar (apart from some natural dispersion) in this population sample. In other words, we assumed that there is *no relationship* between myocardial contractility and a geometry-related parameter. In this sense, we wish to draw the parallel with experimental work, where control animals would also be sampled from a normal population that would also exhibit a range of myocardial contractility values. Using linear regression on log-converted variables, we were able to define a geometry-adjusted $E_{es,adj}$ to quantify myocardial contractility. An important benefit of this method is that it does not require any modelling assumptions regarding passive and active stress-strain relations, activation function, depolarization sequence or fibre orientation, in contrast to the elastance index. A practical limitation of our method, however, lies in its population-specific character, which may render $E_{es,adj}$ *less suitable* to make comparisons with *other populations* and/or *species*. One must realize that normalization methods based on a regression function can only guarantee reliable values for myocardial contractility when they are used *within* the range of the studied variables (RWT and LVM). As such, application of our method in species with much larger or smaller ventricular dimensions (such as mice or rats) should be clearly *discouraged* at the moment, in order not to arrive at incorrect conclusions regarding myocardial contractility.

The difference between the multipliers (0.0941 vs. 0.45) of our and Beyar and Sideman's contractility index, although dramatic, is irrelevant, as both $E_{es,adj}$ en EI represent (differently) scaled indices. The exponents of RWT (-0.159 ± 0.098, $p = 0.1$) and LVM (0.455 ± 0.052, $p < 0.001$) are much lower than in EI, suggesting that $E_{es,adj}$ is far less affected by LV geometry than is EI. This was confirmed by comparing the R^2 values obtained from linear regression between contractility indices and geometry (EDV and LVM): $E_{es,adj}$ = 2.964 - 0.006 · EDV + 0.003 · LVM, $R^2 = 0.022$, $p < 0.001$, while EI = 160.243 + 2.162 · EDV + 0.371 · LVM, $R^2 = 0.245$, $p < 0.001$. The exact reason for this discrepancy between the exponents could not be determined. However, it might be related to the fact that we assumed a constant myocardial contractility, while in reality even in the subpopulation a statistically significant relationship between myocardial contractility and geometry can probably not be excluded.

From the discussion above, it should be clear that all normalization methods have their strengths and limitations. Moreover, because these methods all rely on different assumptions, the gender discrepancies are not really surprising. Ultimately, *validation* of the approaches is mandatory to know which one is the most reliable.

One of the major questions that have been the issue of many investigations is whether basal myocardial contractile state is different for men and women. Do men simply happen to be larger mammals than women, with a bigger ventricle, but with an identical myocardial contractile state?

Ejection fraction, a geometry-independent but load-dependent index of systolic function, was higher in women than in men in our population (66.88 ± 7.66 % vs. 64.50 ± 8.26 %, $p < 0.001$), confirming the findings in other studies [55, 130, 260]. Even though EF is load-dependent and therefore not a proper index of contractility, the reported differences in EF between men and women may actually suggest a *true* gender-specific difference [130].

The higher E_{es} in women compared to men, as was shown in our study, was already observed in an invasive study performed in patients (age 48-75 years) undergoing routine cardiac catheterization [130], and in a cross-sectional population study (age > 45 years) on ventriculo-vascular interaction [260]. However, this difference in E_{es} only offers a limited amount of information from a physiological point of view, and does not provide specific mechanical information about the myocardium. Here, a higher E_{es} in women simply signifies an *increased sensitivity* of systolic pressure to changes in volume. Using linear regression analysis, Redfield et al. [260] showed that the relation between E_{es} and age is steeper in women than in men. Although linear regression analysis of our data (women: $E_{es} = 2.075 + 0.018 \cdot age$, $p < 0.001$; men: $E_{es} = 2.008 + 0.008 \cdot age$, $p < 0.012$) confirms their findings, only after grouping the continuous variable age into half decades, an apparently different time course between men and women (which is also reflected in the analysis of myocardial contractility) from the age of 50 could be revealed. Note, however, that age in the study of Redfield et al. [260] ranged from 45 to about 95, while the studied range in our study is much narrower and limited to the age of 55.

We are convinced that differences between men and women could more objectively be assessed on the basis of *direct* measurement of myocardial contractility instead of indirect estimation. This is, however, a difficult (and probably virtually impossible) task. As such, literature about quantification of myocardial contractility is limited and mostly restricted to papillary muscle studies in rodents. Even then, there are a number of inconsistencies between these studies, partially due to differences in age, animal strains and measurement methods [189]. Over a wide range of muscle lengths and bath concentrations of calcium, Capasso et al. [50] did not detect a significant difference in peak tension between male and female rats. In isotonic measurements peak shortening was higher in female rats, but maximum velocity of shortening was similar in male and female animals. In another study by Leblanc et al. [185], it was found that papillary muscles of female rats aged 6 months and older exhibited smaller isometric and isotonic contractions, smaller maximal rates of tension and shortening development and declined velocities during both the contraction and relaxation phases, and shorter contractions than age-matched males.

In our study, analysis of EI and $E_{es} \cdot LVM$ suggested that basal myocardial state is mildly higher in men than in women, while no statistical difference was seen in terms of $E_{es} \cdot EDV$. The latter observation was confirmed in the study of Redfield et al. [260]. Hayward et al. [130], on the other hand, found that $E_{es} \cdot EDV$ was higher in men (265.8 ± 12.5 (SEM) mmHg) than in women (221.5 ± 9.3 (SEM) mmHg). Our novel index, $E_{es,adj}$, suggests that myocardial contractility remains nearly identical in men and women until the age of 50. After the age of 50, a *relative decline* in myocardial contractility is observed in men. In order to approach the problem in a slightly different way, we also calculated E_{es} values that were statistically *adjusted* for the subject's length and weight using covariance analysis (ANCOVA). These data are shown in figure 4-8. Note the remarkable resemblance with $E_{es,adj}$. This approach thus appears to confirm that there are no differences between men and women in contractility, when adjusting the measurements for geometric and/or morphological differences between both sexes. It is to be mentioned that, in contrast to $E_{es,adj}$, there was no significant difference between the curves in figure 4-8 at the age of 51-55 ($p = 0.264$). Nevertheless, all normalized contractility indices show a time course that is *very similar* to the one of the non-normalized index, but shifted vertically. This is explained by the fact that the geometry-related parameters EDV, LVM and RWT (i.e., the variables that are used to convert E_{es} into a measure of myocardial contractility) are *not* or *very poorly* related with age (R^2-values ranging between 0.021 and 0.045).

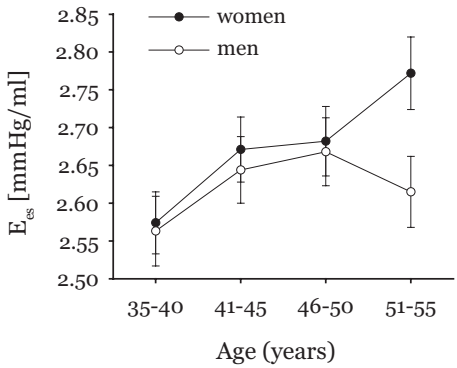

*Figure 4-8: After adjusting E_{es} for length and weight, E_{es} shows a phenomenon that is comparable to $E_{es,adj}$, i.e., contractility in women and men behaves differently after the age of 50. The difference however, is not significant. Data are shown as mean ± SEM of the adjusted values. * indicates $p < 0.05$ male vs. female using a t-test.*

A remarkable phenomenon that definitely deserves further investigation is that, regardless of the index that was used, contractility *increases consistently* in women with age, while in men, it seems to reach a *plateau value* at the age of 51-55. The gender-specific time course after the age of 50 has not been described before and was not related to a possible selection bias due to age differences between men and women (age 51-55: $p = 0.672$). Therefore, other factors must have come into play. In recent publications, attention was focused on the protective effect of *sex hormones* (mainly oestrogen) on the heart and vascular system in premenopausal women. However, the impact of menopause and loss of oestrogen remains controversial, and

the higher prevalence of cardiovascular risk in postmenopausal women compared to premenopausal women has not been fully elucidated [31].

However, women do have a specific preponderance for diastolic heart failure, characterized by heart failure symptoms in the presence of a preserved EF, whilst men more often present with systolic heart failure (decreased EF) [245, 261]. In this regard, the relative decrease in E_{es} in men from age 50 onwards, and the better preservation in women do have a clinical mirror-image, although the underlying mechanics are probably more complex and need to be investigated.

4.2.5 Methodological considerations

We also acknowledge that our methology has a number of potential limitations:

(i) A considerable number of geometric *assumptions and simplifications* was required to calculate LV mass and volumes, pressures, and to estimate end-systolic elastance, because of the non-invasive nature of our measurement methods. These assumptions are expected to reduce the accuracy of our calculations. However, each of the assumptions was based on correlations that were previously published in *validation studies*, and it is therefore unlikely that a bias in our results would alter our conclusions. It should, moreover, be realized that the large sample size in this study significantly strengthens our conclusions, and that this study simply could not have been completed by using invasive methods.

(ii) All of the suggested normalization procedures intrinsically assume that a difference in geometry between two ventricles is accompanied by a *proportional difference* in volume of contractile units. As a result, potential changes in the volume or mechanical properties of the extracellular matrix, which may vary with age and between genders, were not accounted for. In this sense, one might wonder whether geometry normalized indices of contractility could ever assess fibre contractility as such (figure 4-1).

(iii) We also wish to point out that the E_{es}-values were obtained using a so-called *single-beat method*. This technique, while not really based on one single beat, is non-invasively applicable and does not require changing loading conditions. Although the method has been validated [57] and has recently been applied in a population study on ventriculo-vascular interaction [260], it remains an estimate of E_{es} with potential limitations, as pointed out by Kjørstad et al. [168] in a validation study.

(iv) In our novel normalization method, we assumed that the formula for $E_{es,adj}$, which is derived from the data in the *subpopulation*, is also applicable in the whole population. Care should be taken as the range of geometric and demographic characteristics in the study population is broader than the subpopulation range. On the other hand, there is no proof that this formula would not be valid for the whole group either.

(v) A last potential limitation is that the end-systolic elastance ultimately should be calculated with different *heart stimulation frequencies* (due to the force-frequency effect). However, to the best of our knowledge, no methods for accounting for heart rate have been suggested. We, moreover, speculate that

the influence of the minor difference in heart rate between men and women is negligible.

4.2.6 Conclusion

The present study showed that E_{es} as such *cannot* be used to compare myocardial contractile state between men and women of various ages in a cross-sectional study. *Normalization* is required to cancel out the effect of geometry. Due to the difference in their underlying assumptions, the various myocardial contractility indices do *not* provide *consistent* information with respect to gender differences. Despite these discrepancies, it was found that myocardial contractility appears to be *better* preserved in women than in men after the age of 50. This finding at the population level could have potentially important clinical implications that require further investigation.

4.3 Appendix

4.3.1 Single-beat elastance

Chen et al. [57] developed a method to determine E_{es} in a non-invasive way, without the need to change loading conditions. The algorithm is slightly superior to the previously reported single-beat method of Senzaki et al. [283] because it accounts for possible influences of load and systolic function on the shape of the elastance curve. However, the method still assumes a linear ESPVR and a constant volume-axis intercept V_o.

The relation between LVP and LVV at end-systole is given by

$$E_{es} = ESP/(ESV - V_o) \tag{4-8}$$

Assuming that LVP at the onset of ejection is equal to arterial diastolic pressure (P_d), elastance equals

$$E_d = P_d/(EDV - V_o) \tag{4-9}$$

Since by definition, $E_{Nd} \cdot E_{es} = E_d$, equation 4-9 can be rewritten as

$$EDV - V_o = (P_d/E_{Nd})/E_{es} \tag{4-10}$$

Rearranging equation 4-8 and combining it with equation 4-10 yields

$$EDV - ESV = (P_d/E_{Nd} - ESP)/E_{es} = (P_d - (E_{Nd} \cdot ESP))/(E_{Nd} \cdot E_{es}) \tag{4-11}$$

Solving for E_{es} yields

$$E_{es} = (P_d - (E_{Nd} \cdot ESP))/((EDV - ESV) \cdot E_{Nd}) \tag{4-12}$$

When approximating ESP by $0.9 \cdot P_s$, with P_s the systolic brachial pressure, and substituting (EDV - ESV) by the stroke volume SV, the single-beat end-systolic elastance can be obtained as

$$E_{es} = (P_d - (E_{Nd} \cdot 0.9 \cdot P_s))/(SV \cdot E_{Nd}) \tag{4-13}$$

Because the normalized elastance value E_{Nd} occurs at the onset of ejection, there is a possible load- and systolic function-dependent deviation from the population average [284]. The estimated $E_{Nd(est)}$ of each individual was therefore estimated as a function of the group averaged $E_{Nd(avg)}$ using regression analysis with EF (as a measure of systolic function) and P_d/ESP (as a measure of arterial load) as additional predictor variables:

$$E_{Nd(est)} = 0.0275 - 0.165 \cdot EF + 0.366 \cdot (P_d/ESP) + 0.515 \cdot E_{Nd(avg)} \quad (4\text{-}14)$$

Using this method, Chen et al. [57] reported a very low bias of -0.1 mmHg/ml and an good agreement between non-invasive single-beat and invasive multiple-beat measurements during baseline in 43 pig ventricles. We therefore considered Chen's technique acceptable for evaluating E_{es} as a measure of baseline ventricular contractility in our large population sample.

4.3.2 Normalization based on the elastance index

The thick-walled ellipsoid LV model (figure 4-2), developed by Beyar and Sideman in 1984, describes the mathematical relation between fibre mechanics and ventricular mechanics [27]. It incorporates both the passive and active properties of the myocardial fibres, accounts for the anatomical fibre angle distribution throughout the wall, and assumes a radial propagation of the electrical activation front from the endocardium towards the epicardium. The maximum stress (σ_o) developed by the sarcomere at its optimal length characterizes myocardial contractility [30]. In 1986, they used this model to propose a new normalized contractility index, the elastance index EI, calculated as

$$EI = 0.433 \cdot E_{es} \cdot LVM/RWT \quad (4\text{-}15)$$

A coefficient of variation (SD / mean) of only 3.5% (in contrast to 44% in case of Ees!) was obtained when analyzing EI under a constant fibre contractility σ_o and different combinations of ventricular mass (LVM) and relative wall thickness (RWT). They furthermore discovered a linear relation between EI and σ_o when geometric properties were kept constant. From a theoretical point of view, this index could therefore be considered as a reliable index of myocardial contractility, because it is independent of ventricular size, and only reflects the fibre's contractility parameter σ_o.

4.3.3 Normalization based on reference population

Based on the linear relationship between the dependent variable E_{es} and the independent variables LVM and RWT, a geometry-adjusted E_{es} can be determined as $E_{es,adj}$ = mean (E_{es}) + $d_{y \cdot x}$, with $d_{y \cdot x}$ the deviation from regression, i.e., E_{es} - $\hat{E}_{es}$ where $\hat{E}_{es}$ is the predicted value. This adjustment removes the variation in E_{es} that is accounted for by the variation in geometry, so that the adjusted values are those to be expected if all E_{es} values were taken at the mean geometry [21]. The adjusted $E_{es,adj}$ can then be determined as $E_{es,adj}$ = mean (E_{es}) + E_{es} – (a + b · LVM + c · RWT), where a, b and c are determined from linear regression.

To obtain a formula that has the same functional form as Beyar and Sideman's elastance index, the very same principle is applied to the logarithms of variables E_{es}, LVM and RWT. Log-converted variables are defined as

- $E'_{es} = \log (E_{es})$
- $RWT' = \log (RWT)$
- $LVM' = \log (LVM)$
- $E'_{es,adj} = \log (E_{es,adj})$

Linear regression yields coefficients a, b and c: $E'_{es} = a + b \cdot LVM' + c \cdot RWT'$

The adjusted $E'_{es,adj}$ is then found as:

$$\begin{aligned} E'_{es,adj} &= \text{mean}(E'_{es}) + E'_{es} - a - b \cdot LVM' - c \cdot RWT' \\ &= \text{mean}(E'_{es}) - a + \log(E_{es}) - b \cdot \log(LVM) - c \cdot \log(RWT) \\ &= \log [10^{(\text{mean}(E'es) - a)} \cdot E_{es} \cdot LVM^{-b} \cdot RWT^{-c}] \end{aligned}$$

$E_{es,adj}$ is thus defined as: $E_{es,adj} = 10^{(\text{mean}(E'es) - a)} \cdot E_{es} \cdot LVM^{-b} \cdot RWT^{-c}$

5

Chapter 5

Non-invasive Assessment of Left Ventricular Diastolic Funtion

Parts of this chapter were published in

Computers in Cardiology (2004)
A New Thick-Walled Hydraulic Model of the Left Heart for the Assessment of Blood-Wall Interaction Using Ultrasound
Claessens TE, Segers P and Verdonck PR.

Parts of this chapter have been submitted for review in

Ultrasound in Medicine and Biology
New Echocardiographic Applications for Assessing Global Left Ventricular Diastolic function
Claessens TE, De Sutter J, Vanhercke D, Segers P and Verdonck PR.

5.1 Introduction

This chapter begins with a brief description of the physiological aspects of left ventricular (LV) *relaxation* and *diastole* in the healthy and the diseased heart. The contribution of the *active* and *passive* components in the myocardial relaxation process is discussed from a mechanical point of view with the help of a newly developed hydraulic thick-walled model of the LV.

LV diastolic function is considered normal when the LV is able to relax fast and to fill with a blood volume that is sufficient to maintain a normal stroke volume (SV) while maintaining normal diastolic pressures at rest and during exercise. Non-invasive assessment of diastolic function has become an important challenge in clinical practice because many patients presenting with symptoms of heart failure have *preserved systolic function* but *impaired diastolic function*. In a clinical setting, LV diastolic function is conceptually characterized in terms of *relaxation* and *compliance*. LV compliance (LVC) is a *passive property* of myocardial tissue related to the distensibility of the LV in diastole, whereas relaxation is used to refer to an *active process* during which the LV shifts from its systolic to its diastolic pressure-volume (P-V) relationship.

Doppler echocardiography is the most commonly used non-invasive technique for the assessment of diastolic function because it is safe, fast, relatively cheap and painless. Analysis of the transmitral flow velocity profile using PW Doppler is still considered the *cornerstone* of diastolic function assessment. However, because the transmitral flow velocity profile is not only determined by relaxation and compliance, but also by the source pressure for LV filling (i.e., left atrial pressure, LAP), examination of transmitral flow is not an unequivocal method to determine *intrinsic LV diastolic function*.

A number of promising, highly technological echocardiographic imaging modalities have been introduced in recent years. They appear less influenced by LAP and may provide incremental value for intrinsic diastolic function assessment. These techniques permit quantification of distinct features of *intraventricular blood flow velocity* and *pressure fields*, and *longitudinal* and *rotational myocardial tissue velocities* in a non-invasive way. These new (parametric) images and corresponding clinical indices should be interpreted cautiously though, as basic knowledge about fluid dynamics and wall mechanics – and their interaction – may be inadequate.

A comprehensive and original overview of the *haemodynamic* and *mechanical* events occurring during diastole is provided in the second part of this chapter. That part also discusses how this new information can be used in the clinical and research setting for evaluating diastolic function in the healthy and the diseased heart, and summarizes the technical aspects concerning image acquisition of these novel echocardiographic imaging modalities.

5.2 Diastolic function

5.2.1 Definition of diastole

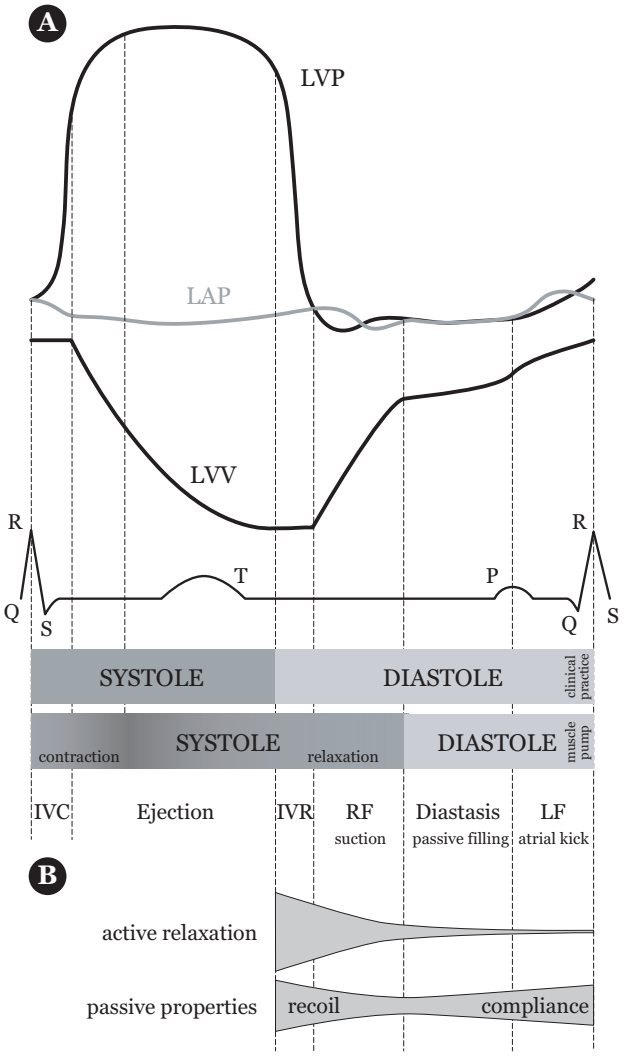

Figure 5-1: A: Time course of left ventricular pressure (LVP) and volume (LVV), and left atrial pressure (LAP) during the cardiac cycle. The cardiac cycle is divided into the systolic and diastolic phase (and their subdivisions) according to clinical definitions. From the point of view of muscle function, diastole only includes diastasis and late filling; B: Graphical representation of the determinants of intrinsic LV diastolic function as a function of time. Note that the passive properties contribute to recoil during early diastole and LV compliance (LVC) in late diastole.

Diastole, derived from the Greek word διαστολη ("expansion"), has received various definitions throughout history [45]. In clinical practice, diastole is viewed as the period

in the cardiac cycle from the *end of aortic ejection* (closure of the aortic valve) until the *onset of ventricular tension development in the succeeding beat* (closure of the mitral valve) [354]. It is subdivided into four phases: *isovolumic relaxation* (IVR), *early rapid filling* (RF), *diastasis* and *late filling* (LF) (figure 5-1A). From the point of view of muscle physiology, on the other hand, Brutsaert and Sys [45] defined diastole as the time period where the LV develops no active tension. According to the latter definition, diastole would only encompass diastasis and late filling.

5.2.2 Physiology of relaxation and diastole

Myocardial relaxation is an energy-consuming process during which the contractile elements are deactivated and the myofibrils return to their original length before contraction [164]. It takes place during the major part of ejection, IVR and early filling. The manifestation of this relaxation process is a decline of myofibre tension, which causes a rapid decrease in left ventricular pressure (LVP) during IVR.

The main factors that determine relaxation are the *prevailing loading conditions* and the *rate of inactivation (*i.e., the totality of processes leading to the disappearance of force-generating sites, presumably the detachment of cross-bridges) [42]. Relaxation is, moreover, affected by the degree of *mechanical non-uniformity* (incoordination) during systole, so that an imbalance in forces will decrease the rate of relaxation [43, 45]. Its onset depends on the (timing of the) loading conditions during the preceding systole. Gillebert et al. [117] showed that the transition from contraction to relaxation occurs when 81% to 84% of peak isovolumic LVP is reached, or the equivalent timing during early ejection. According to Solomon et al. [292], relaxation starts at about 16% of the ejection time (figure 5-1). The determination of the end point of active tension decay is still a matter of debate. It is usually assumed that active tension ends shortly after IVR. However, evidence suggests that cross-bridge interaction occurs even at low diastolic calcium, producing resting muscle tone [190].

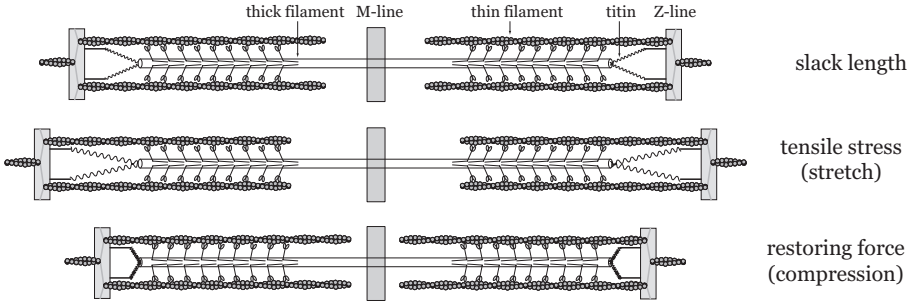

Figure 5-2: Principle of elastic recoil caused by restoring forces in the spring-like intracellular protein titin. Titin also contributes to the extensibility and passive force development in non-activated ventricular muscle. Recoil is also partially generated by extracellular collagen (not shown) (adapted from [157]).

Elastic recoil is considered as a kind of *intrinsic load* and is frequently invoked as a feature that *extends* and *accelerates* myocardial relaxation [56, 62, 97]. It originates from the *restoring forces* generated at end-ejection, i.e., when the LV has contracted below

its equilibrium volume V_{eq} (volume of the completely relaxed ventricle at zero transmural pressure). Therefore, the smaller the end-systolic volume (ESV), the greater the restoring forces. On the cardiomyocyte level, this means that muscle fibres have been shortened by active contraction to less than their equilibrium length (slack length). The energy released during decompression of elastic components, such as the intracellular protein *titin* (giant springlike molecule that resists both excessive shortening and elongation of the sarcomere) [54, 134] and *extracellular collagen* surrounding the cardiomyocyte [56, 220, 259], accelerates the relaxation process (figure 5-2). In this sense, the *end-systolic configuration* undoubtedly represents an important determinant of early diastolic performance.

When LVP decreases below LAP, the mitral valve opens and blood enters the LV, as a result of the transmitral pressure difference. The early transmitral flow wave is referred to as the *early filling wave* or *E-wave*, and contributes to about 70% of the SV [115]. As LV filling continues, the transmitral pressure difference decreases and subsequently reverses, causing the mitral inflow to decelerate (figure 5-3).

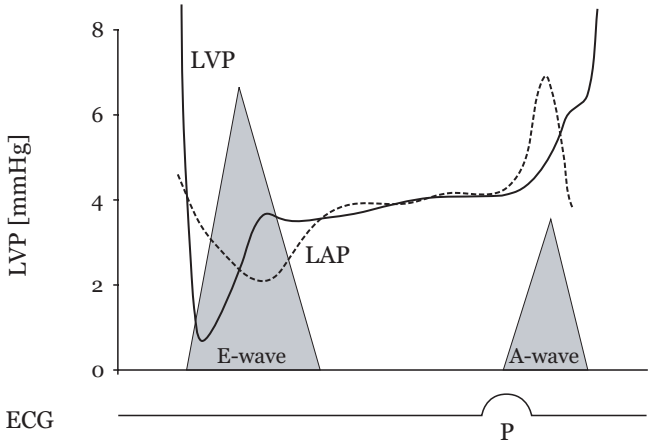

Figure 5-3: Representative example of the time course of LVP and LAP, and the ensuing transmitral flow velocities during early (E-wave) and late (A-wave) diastole. After the first pressure crossover (LAP > LVP), inflow velocity accelerates. When the transmitral pressure gradient is reversed (LAP < LVP), mitral inflow decelerates. A similar flow profile is noted during atrial contraction.

A rapid relaxation process, resulting in a rapid pressure decay and an early positive transmitral pressure gradient, is a critical aspect of normal diastolic function. Myocardial relaxation can be quantified by measuring the maximum rate of LVP decay, $(dP/dt)_{min}$, or the duration of isovolumic relaxation (IVRT). However, the *time-constant of isovolumic relaxation* (τ), either based on an empirical exponential model with a zero [350] or nonzero [233] asymptote (equations 5-1 and 5-2) or on a slightly superior logistic model [205] (equation 5-3), is commonly considered the "*gold standard*" method for quantifying relaxation [164]. The monoexponential two-parameter model was originally introduced by Weiss et al. [350]:

$$LVP(t) = LVP_0 \cdot e^{-t/\tau} \quad (5\text{-}1)$$

with LVP_0 representing the pressure at t = 0, i.e., at $(dP/dt)_{min}$. Subsequent investigators added a nonzero asymptote LVP_∞ to this model:

$$LVP(t) = (LVP_0 - LVP_\infty) \cdot e^{-t/\tau} + LVP_\infty \quad (5\text{-}2)$$

Matsubara et al. [205] defined the *logistic* model:

$$LVP(t) = LVP_A/(1 + e^{t/\tau}) + LVP_\infty \quad (5\text{-}3)$$

where LVP_A is an amplitude constant, and LVP_∞ is a nonzero asymptote. These measurements have been shown to be useful in the evaluation of relaxation disorders. All of these invasive measures are, however, difficult to obtain and not practical for daily clinical practice [258]. Moreover, they do not provide detailed insight into the fundamental process of relaxation in the intact LV as a muscle-pump system [42].

After early filling, there is a quiescent phase with no significant transmitral flow, called *diastasis*, during which the LA functions as a conduit vessel between the four pulmonary veins and the LV [198].

Diastasis is followed by LA systolic contraction, which induces a second pressure difference between the LA and LV. The ensuing transmitral flow wave is called the *late diastolic filling wave* or *A-wave*. The amount of blood flow during this atrial 'kick' is dependent on LA systolic function, LVC, and the electrical conduction system of the heart [164], and generally represents about 30% of the SV [115]. After LA systole, LAP decreases below LVP, causing the valve leaflets to start closing. The rapid increase in LVP at the initiation of LV contraction finally seals the mitral valve [198].

Rapid relaxation is not the only requirement for a good diastolic function. A healthy LV should also have a *normal compliance* which allows for unrestricted passive filling. LVC can be accurately obtained in an isolated ventricle as the inverse of the slope (dV/dP) of the passive P-V relationship. However, one must realize that LVC does not measure the intrinsic mechanical properties (i.e., passive stress-strain relation of myocardial tissue), as LVC is also determined by chamber geometry (cavity dimensions and wall thickness), pericardial constraint (influence of the sac that contains the heart) and ventricular interdependence (interaction with the RV). As a result, in a clinical setting, a stiff LV is often invoked to explain diastolic dysfunction, but it is seldom documented [115].

We close this paragraph with the notion that the primary physical determinants of intrinsic LV diastolic function include *myocardial relaxation* and *passive tissue properties*. Their time-dependent contributions are presented in figure 5-1B. It should be noticed that the passive properties determine both LVC during filling (stretching of tissue) and the intensity of elastic recoil during IVR and early diastole (decompression of tissue). As will be outlined in the following paragraphs, however, the LV haemodynamic and mechanical events are not only determined by the abovementioned intrinsic diastolic properties.

5.2.3 Heart failure and diastolic dysfunction

5.2.3.1 Heart failure

Congestive heart failure (CHF) is a common cause of death and an increasingly important health problem in most developed countries worldwide [149, 203]. It is a *clinical syndrome* in which an abnormality of cardiac function is responsible for failure of the heart to pump blood at a rate commensurate with metabolic requirements.

About 30 to 40% of all patients presenting with symptoms and signs of CHF (e.g., shortness of breath during exertion) have a *normal or slightly reduced systolic function* in terms of ejection fraction (EF greater than 40% - 50%). These patients are labelled as having *diastolic heart failure* (DHF) and are characterized predominantly by abnormalities in LV *diastolic function*, including slow and delayed active relaxation and increased passive stiffness [16, 35]. The majority of the CHF patients, on the other hand, have abnormalities in systolic performance, function and contractility, and are said to have *systolic heart failure* (SHF). Patients with SHF differ substantially from those with DHF in several ways: demographic characteristics, ventricular remodelling, ventricular function, mortality rate, underlying causal mechanisms, and pathophysiological mechanisms [102, 364].

The *diagnosis* of DHF requires reliable *evidence of heart failure*, a *normal EF*, and consideration of *LV volume, LV mass and diastolic function* [362]. According to the *criteria of Vasan and Levy* [339] and the *European criteria* [250], haemodynamic (echocardiography- and/or catheterization-based) evidence of abnormal LV diastolic function is required for making a diagnosis of definite DHF. Zile et al. [365], however, argued that *virtually all* patients with heart failure and a normal EF exhibit evidence of diastolic dysfunction and that echocardiographic or other documentation of diastolic dysfunction is *merely confirmatory*.

5.2.3.2 Diastolic dysfunction

The term *dysfunction* refers to an abnormal (systolic and/or diastolic) mechanical property of the myocardium, regardless of whether the patient is asymptomatic or symptomatic [363].

The term *diastolic dysfunction* is used when echocardiographic or other haemodynamic measurements indicate abnormalities in *relaxation* and/or *stiffness*, resulting in a disturbed pattern of LV filling. Abnormalities in diastolic properties can occur in the *presence* or *absence* of a clinical syndrome of heart failure and with *normal* or *abnormal* LV systolic properties. The effect of diastolic dysfunction on a P-V loop is shown in figure 5-4B.

Systolic dysfunction, on the other hand, describes a defect in the ability to eject blood in the high pressure aorta (examined by measuring systolic performance, function or contractility, as described in paragraph 4.1) (figure 5-4C). Similar to diastolic dysfunction, abnormalities in systolic properties can occur in the *presence* or *absence* of a clinical syndrome of heart failure and with *normal* or *abnormal* diastolic function [102].

The echocardiographic techniques outlined in paragraphs 5.4 to 5.7 aim to indirectly obtain quantitative information about the mechanical diastolic properties of the LV, primarily relaxation and compliance.

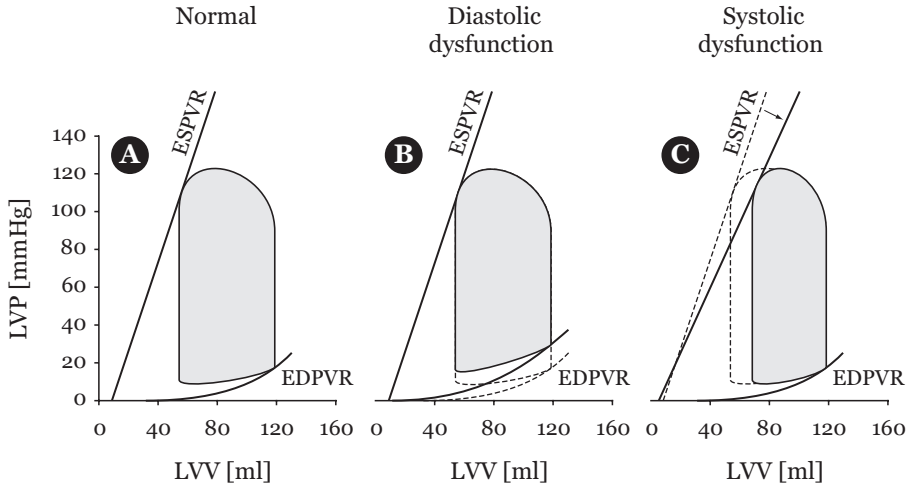

Figure 5-4: Pressure volume (P-V) loops in a normal LV (A) and in a LV with diastolic (B) and systolic (C) dysfunction. Diastolic dysfunction is characterized by an increase in chamber stiffness. Systolic dysfunction is characterized by a decrease in performance, function and contractility (ESPVR: end-systolic P-V relationship, EDPVR: end-diastolic P-V relationship) (adapted from [100]).

5.3 Hydraulic model of early diastole

5.3.1 Introduction

Because various interdependent physical factors influence *haemodynamics* and *wall deformation* during LV relaxation and filling, (Doppler) echocardiography-based diagnosis of DHF can be delicate and may yield conflicting results.

A first attempt was therefore made to construct a *computer-controlled hydraulic model* of the left heart (LV and LA). This model, based on a thick-walled phantom of the LV, aims to assess the effect magnitude of various physical factors upon diastolic function parameters. If this model resembles well the mechanics of a real LV during diastole, it can be applied for various echocardiographic imaging techniques (see paragraphs 5.6 and 5.7), and ultimately provide in-depth information about the interaction between fluid dynamics and wall motion during diastole.

The focus of this study was to analyze the (relative) impact of four important physical parameters that are commonly associated with early diastolic function upon the peak rate of pressure decay during IVR, $(dp/dt)_{min}$. They include the rate of inactivation (IR), end-systolic pressure (ESP), left ventricular compliance (LVC) and left atrial pressure (LAP). We furthermore examined whether the model sufficiently resembles

a real relaxation process from a physiological and mechanical point of view and evaluated the model's suitability for echocardiographic analyses.

5.3.2 Materials and methods

5.3.2.1 Left ventricular phantom

The LV was modelled as a *thick-walled truncated ellipsoid*. Its equilibrium volume (V_{eq}) is determined by the mould geometry, and amounts to 102 ml, which corresponds to a human LV. The base-apex length is 85 mm and the short-axis diameter is equal to 45 mm. The overall wall thickness is 10 mm, except at the apex, where wall thickness equals 5 mm [192].

Figure 5-5: Phantom of the left ventricle, made from a polyvinylalcohol (PVA) solution mixed with 1% graphite powder.

To mimic *mechanical* and *acoustic* myocardial tissue properties, the phantom is made from a polyvinylalcohol (PVA, Sigma Chemicals, St. Louis, MO, USA, Av. Mol. Wt. 70000-100000) solution mixed with 1% graphite powder to ensure sufficient backscatter of the ultrasonic waves. A unique property of this PVA solution is that its stiffness increases with the *number of freeze-thaw cycles* it undergoes during preparation [99]. Two phantoms with a different stiffness were made by using 11% and 13% (mass%) PVA, respectively. Both phantoms underwent three freeze-thaw cycles (12 hours at -19°C and 12 hours at 22°C). Their passive P-V relationships are shown in figure 5-6. Below V_{eq}, phantom 1 (low compliance) is about four times stiffer than phantom 2 (high compliance).

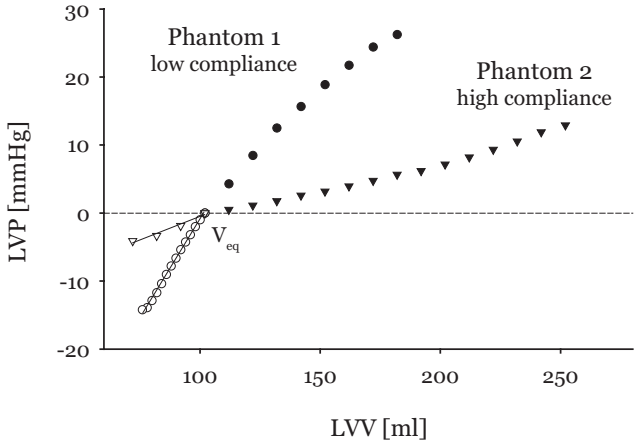

Figure 5-6: Passive P-V relationships of the LV phantoms. Below the equilibrium volume (V_{eq} = 102 ml), the compliance of phantom 1 (1.72 ml/mmHg) is about 4 times lower than in phantom 2 (7.27 ml/mmHg).

5.3.2.2 Experimental setup

The phantom is mounted in a *Plexiglas cylindrical chamber* containing water (figure 5-7B (7)). LV diastole was considered to start at the end of systolic ejection. This condition is characterized by a given ESP (e.g., 90 mmHg) and ESV (70 ml, fixed). The ESV was assumed smaller than V_{eq} to be able to simulate the effect of elastic recoil. To obtain these parameter values, we initially calculate the amount of fluid required in the LA (8) that corresponds to a certain LAP (e.g., 8 mmHg, corresponding to a volume of 705 ml). A volume of 705+70 ml is subsequently poured into the LV phantom and LA reservoir. LVP is then raised to ESP using pressurized air and kept constant by means of a PID (proportional-integral-derivative) control algorithm. Since LVP is significantly higher than LAP, fluid slowly leaks through the bioprosthetic mitral valve leaflets (3) until the predefined LAP of 8 mmHg is reached. At that moment, pressurization ceases and two mechanical valves (5 and 6) are switched open. The IVR phase starts now, followed by the early filling phase. All other parameters settings (LAP, ESP and IR) are obtained in an analogous way.

LVV is obtained indirectly by measuring the distance to the *fluid level* in an adjacent reservoir (9) using an ultrasonic sensor (Hydepark Superprox Ultrasonic, Daytona, OH, USA). LVP is measured using a Millar Mikro-Tip catheter transducer (Millar Instruments, Houston, TX, USA). Pressure and volume registration, as well as opening and closing of the mechanical valves is controlled by a virtual instrument panel created in LabView 7 (National Instruments, Austin, TX, USA) on a 2.4 GHz Intel Pentium IV personal computer.

A mixture of 60% water and 40% glycerine was used as a blood-mimicking test fluid.

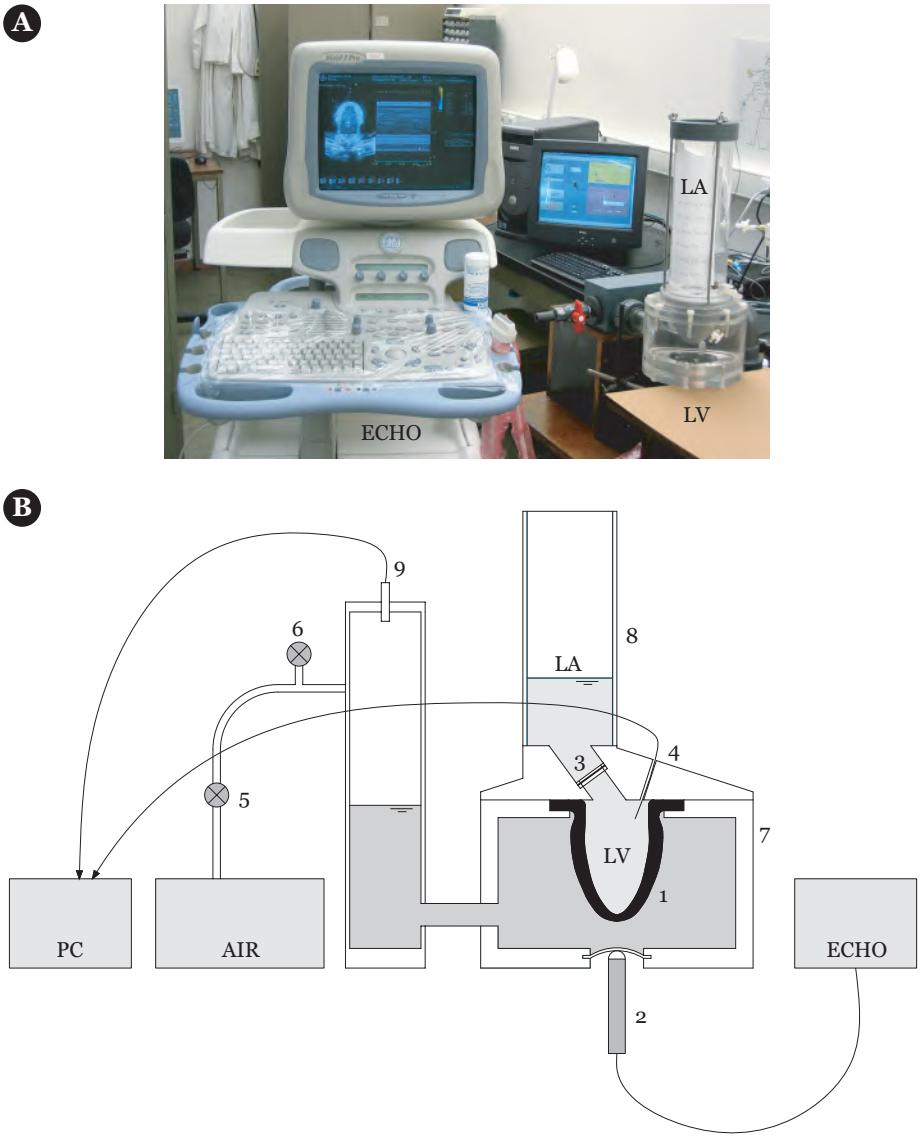

Figure 5-7: A: Photo of the experimental setup; B: Schematic representation of the experimental setup: (1) LV phantom, (2) ultrasound transducer, (3) bioprosthetic mitral valve, (4) pressure transducer, (5) proportional valve, (6) valve, (7) Plexiglas chamber, (8) LA and (9) device that measures the distance to the water level to obtain left ventricular volume.

5.3.2.3 Measurement protocol

Pressure measurements at the level of the LV base were performed with various combinations of ESP (70, 90, 110 and 130 mmHg) and LAP (6, 8, 10 and 12 mmHg), and by using two LV phantoms with a different compliance (1.72 ml/mmHg and 7.27 ml/mmHg). During relaxation, the area of the proportional valve 5 was adjusted to

100%, 75% and 50% of its maximum value, yielding three different rates of inactivation, referred to as “fast”, “average” and “slow”. Valve 6, however, was completely opened during relaxation. The peak rate of pressure decay, $(dP/dt)_{min}$, was derived from the pressure curve with a Matlab Release 13 SP1 code (The Mathworks, Natick, MA, USA).

5.3.2.4 Statistics

All measurements were repeated three times in the same setup. Single-factor analysis of variance (ANOVA) with a post-hoc LSD test was used to detect differences between groups. A general linear univariate model (GLM) was used to quantify the (relative) influence of the various physical factors on $(dP/dt)_{min}$. The actual linear model, yielding the best predictor variables was found by means of a forward stepwise and backward elimination method (starting from a full factorial model, which includes all interaction terms). All p-values of the test statistics are reported in the results section. Statistics were performed in commercially available software (SPSS 12.0, SPSS Inc., Chicago, IL, USA).

5.3.3 Results

An example of a measured LVP time course during relaxation is shown in figure 5-8. All values of $(dP/dt)_{min}$ ranged between -1.33 and -3.29 mmHg/ms. The coefficient of variation (SD/mean) averaged for every group amounted to 0.007.

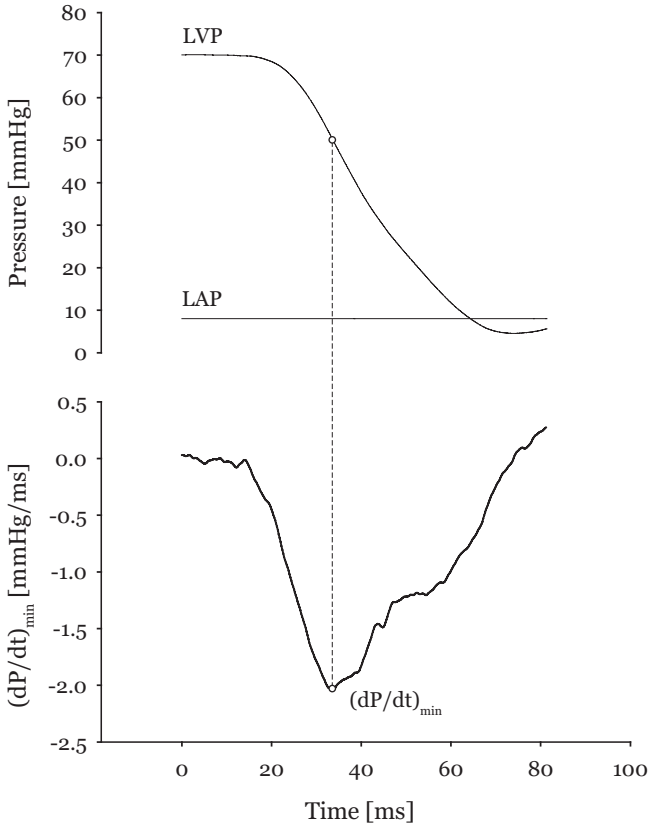

Figure 5-8: A: Example of a measured LVP time course. Left atrial pressure (LAP) and end-systolic pressure (ESP) equalled 8 mmHg and 70 mmHg, respectively. Inactivation rate (IR) was set at the average rate, i.e., valve 5 was opened for 75%; B: Corresponding time course of the rate of change of pressure (dP/dt). Its minimum value is a measure of LV relaxation rate.

Mean values of $(dP/dt)_{min}$ for the average IR are presented in figure 5-9A. The effect of various IR is shown in figure 5-9B. For both phantoms, there was a significant difference between the average and slow IR (t-test, $p < 0.01$). The difference between the fast and average IR, however, was not significant (t-test, $p = 0.56$), although a trend towards a lower $(dP/dt)_{min}$ in case of the fast IR was clearly observed. LAP did not influence $(dP/dt)_{min}$ (ANOVA, $p = 0.874$).

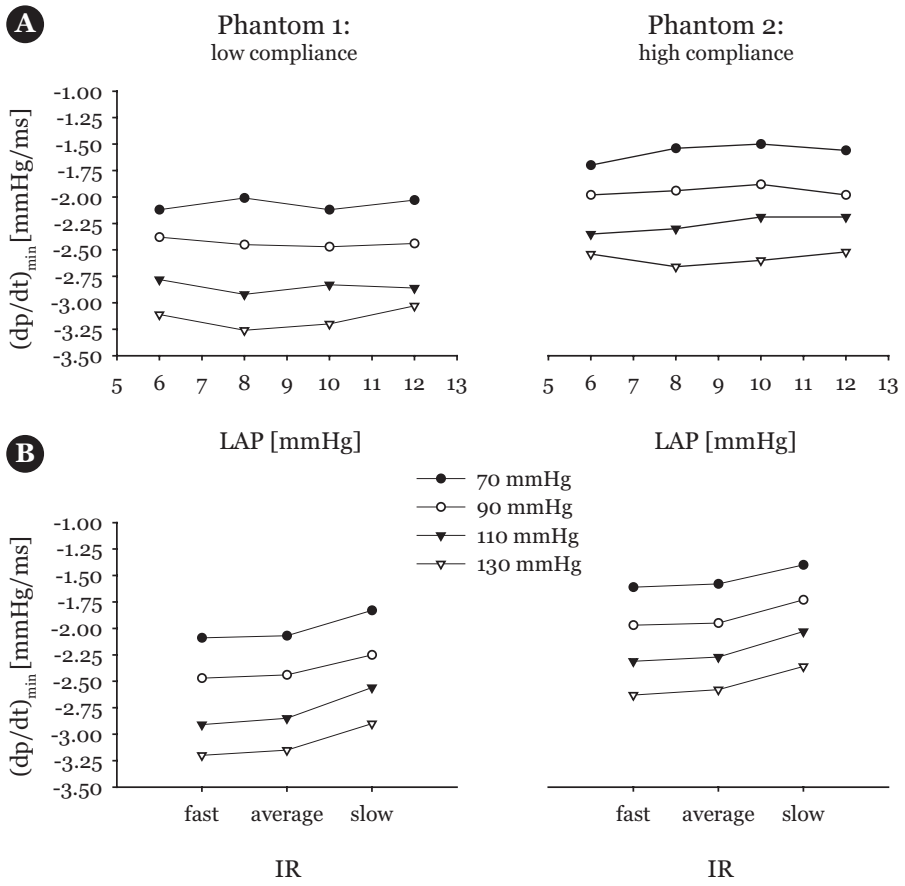

Figure 5-9: A: Peak rate of pressure decay, $(dP/dt)_{min}$, in a LV phantom with low (left) and high LVC (right). IR was set at the average rate. LVP decreases faster with decreasing LVC and with increasing ESP; B: $(dP/dt)_{min}$ for different IR, averaged for LAP. LVP decreases faster with increasing IR and increasing ESP (LAP: left atrial pressure, LVC: left ventricular compliance, IR: inactivation rate).

Using multiple linear regression, $(dP/dt)_{min}$ could be predicted from the analyzed variables. Both backward and forward methods yielded the same linear model, of which the coefficients are shown in table 5-1. The adjusted R^2-value corresponding with this model was 0.972. The existence of significant interaction terms (LVC · ESP and IR · ESP) did not allow us to analyze the isolated effect of one predictor variable at a time. A reduced linear model without interaction terms yielded virtually the same adjusted $R^2 = 0.971$, and only minimally increased the error on the estimated value of $(dp/dt)_{min}$ from 0.081 to 0.083 mmHg/ms. The reduced model dictates that during IVR pressure declines faster when ESP and IR increase and when LVC decreases. The relative importance of these predictor variables is represented by the absolute value of the standardized regression coefficients (β-coefficients). Within the range of studied variables, ESP had the highest impact on $(dP/dt)_{min}$, followed by LVC. IR affects $(dP/dt)_{min}$ only moderately.

Table 5-1: Original and reduced univariate general linear model

predictor	coefficient	stand. coef. (β)	p
		Original model	
constant	-0.775 ± 0.050	-	<0.001
ESP	-0.018 ± 0.000	-0.834	<0.001
LVC	0.064 ± 0.008	0.366	<0.001
IR	-0.081 ± 0.027	-0.135	<0.005
LVC · ESP	0.0003 ± 0.000	0.189	<0.001
IR · ESP	-0.001 ± 0.000	-0.092	<0.05
		Reduced model without interaction terms	
constant	-0.0173 ± 0.024	-	<0.001
ESP	-0.017 ± 0.000	-0.794	<0.001
LVC	0.095 ± 0.002	0.539	<0.001
IR	-0.132 ± 0.006	-0.222	<0.001

Standardized and unstandardized regressions coefficients of the linear regression model (LAP: left atrial pressure, ESP: end-systolic pressure, IR: inactivation rate: 2 = fast, 1 = average, 0 = slow, LVC: left ventricular compliance)

5.3.4 Discussion

5.3.4.1 Relevance of the hydraulic model

Even though knowledge about LV diastolic function is increasing vastly with the help of novel echocardiographic imaging techniques (see paragraphs 5.6 and 5.7), detailed information about the *effect* of isolated changes in one of the interacting physical determinants on *pressure* and *flow distribution* and *wall motion* and *deformation* is virtually impossible to obtain in vivo. We therefore aimed to construct a hydraulic model, in which all potentially important variables can be adjusted individually without initiating any compensating mechanisms, in contrast with in vivo situations.

This new hydraulic model, based on a *thick-walled LV phantom*, is an improvement over most of the existing *thin-walled* LV models. Thin-walled phantoms are not suitable for experimental model studies with the newer echocardiographic imaging modalities, such as tissue Doppler imaging and strain rate imaging. Moreover, the effect of elastic recoil, an important contributor to myocardial relaxation, cannot be simulated in a membrane LV phantom.

5.3.4.2 Phantom characteristics

The equilibrium volume (V_{eq}) of our LV phantom, measured after submerging the phantom in a bath, amounted to 102 ml. Estimation of V_{eq} in a real ventricle is a difficult task (see paragraph 2.4.2.2). It is sometimes considered to correspond to the LVV during diastasis, when LV wall stress should be minimal. Using a logarithmic

approach to characterize both the positive and negative range of the passive P-V relationship, Nikolic et al. [233] observed that the difference between V_{eq} and ESV was approximately 45% of SV. Accordingly, V_{eq} would approximate 82 ml in a normal human LV (assuming that ESV = 50 ml and EDV = 120 ml). Our phantom thus corresponds to a fairly large LV.

Quantitative data about passive P-V relationships below V_{eq} are very scarce to non-existant. A rough estimate of LVC based on the negative P-V relation in a dog [233] yielded a value of 1.6 ml/mmHg, which corresponds well to our phantom with the lowest LVC.

5.3.4.3 Describing relaxation rate

Peak rate of isovolumic pressure decline, $(dP/dt)_{min}$, and the time constant of isovolumic pressure decline, τ, have both been used as indices that reflect the activity of the LV relaxing system.

In the working heart it was found that the time instant of $(dP/dt)_{min}$ occurs very shortly after aortic valve closure [349]. It was therefore suggested by Weiss et al. [350] that the value of $(dP/dt)_{min}$ is not only influenced by the activity of the relaxing system, but also by changes in peripheral impedance to ejection, resulting in changes in peak P_{ao} and/or the timing of aortic valve closure and, hence, $(dP/dt)_{min}$. It was furthermore found that after $(dP/dt)_{min}$ the time course of LVP can be reasonably well described by an exponential curve. Because the corresponding time constant τ is independent of its initial pressure P_o (see equations 5-1 and 5-2) and thus also independent of aortic valve closure, τ can be assumed to more accurately reflect the relaxation process.

In our setup, we anticipated that $(dP/dt)_{min}$ and τ provide the same information in relation to the relaxation process, as we do not need to consider potential changes in the impedance because of altered peripheral properties. However, inconsistent fluctuations in the shape of the LVP curve near the end of the IVR phase (see paragraph 5.3.4.5) forced us to investigate $(dP/dt)_{min}$ instead of τ.

5.3.4.4 Physical determinants of pressure decay

Not surprisingly, analysis of variance and corresponding post-hoc LSD tests showed that there were no differences in $(dP/dt)_{min}$ under various LAP. Indeed, LAP will determine the onset and amplitude of the early filling wave, but there is no reason why LAP would affect the time course of LVP during IVR.

Multiple linear regression revealed how and to what extent the remaining predictor variables ESP, IR and LVC contributed to the variation in $(dP/dt)_{min}$. The existence of significant *interaction terms* in the original linear model may be explained as follows: pressurized air is required to increase the water pressure in the Plexiglas chamber and to bring the LV to its end-systolic conditions. It is evident that the air pressure will be function of LVC and ESP. However, it is by releasing this pressurized air that we modelled the process of inactivation. It is therefore likely that IR was not only determined by the area of the mechanical valves, but also to some extent by LVC and ESP. Because of these interaction terms, the effect of IR, ESP and LVC could not be analyzed separately.

Therefore, we opted to reduce the linear model by omitting all interaction terms. This reduced model explained equally well the amount of variance in the dependent variable (R^2 = 0.972 vs. 0.971), and only slightly augmented the error on the estimated mean value of $(dP/dt)_{min}$ (0.081 vs 0.083 mmHg/ms). More importantly, this method allowed us to investigate the effects of isolated changes in one of the predictor variables and revealed that *LVP declines faster* when *ESP* and *IR increase* and when *LVC decreases*. This approach furthermore demonstrated that changes in ESP (from 70 and 130 mmHg) had the largest impact on the $(dP/dt)_{min}$. Although there was a compliance ratio of more than 4, its effect magnitude (0.539) was smaller than that of ESP (0.794), but higher than that of IR (0.222).

The results of this study appear consistent with findings from previous experimental studies:

- *Effect of ESP*: Our findings that LVP declines faster at higher ESP, is in agreement with previous studies conducted in conscious [152] or anaesthetized [101, 349] mammals, in isolated papillary muscle [246] or in isolated LV preparations [350].
- *Effect of LVC*: To the best of our knowledge, the effect of isolated changes in LVC on $(dP/dt)_{min}$ has not been investigated before. However, continuum mechanics laws dictate that the potential energy stored in the LV wall at a given ESV is a function of tissue elasticity (or compliance). This elastic recoil energy augments the contribution of the "passive" part to the relaxation process and explains the increased relaxation rate in case of a stiffer LV.
- *Effect of IR*: From a mechanical point of view, it is obvious that an increase in IR causes a faster decrease in LVP.

5.3.4.5 Study limitations

It should be emphasized, though, that the goal of this study was not to make a model that can reflect all peculiarities of the biophysics of a real human LV and LA. However, some particular limitations of our computer-controlled experimental setup need to be addressed:

(i) Due to vibrations of the LV phantom at the end of the IVR phase and the initiation of early LV filling, the LVP signal was slightly distorted and did not consistently resemble an exponential curve. These vibrations might also be responsible for the random (insignificant) differences in $(dP/dt)_{min}$ between the various LAP. The "gold standard" of LV relaxation, the time constant of isovolumic relaxation, could therefore not be calculated. However, as explained earlier, in this setup $(dP/dt)_{min}$ is expected to be a good measure of relaxation rate.

(ii) Our model can only simulate IVR and early filling, starting from a predefined ESP and ESV. The amplitude and timing of loading (e.g., "contraction" vs. "relaxation" loading) during the contraction phase, which are known to influence the relaxation process, could therefore not be taken into account [45].

(iii) The effect of changes in ESV has not been studied. However, from a mechanical point of view, it is anticipated that its effect is comparable to that of a change in LVC, as both determine the potential energy within the wall and

the amplitude of the ensuing restoring forces in a similar way. The principle is similar to a squeezed tennis ball snapping back to its original size and shape. The greater the indentation, the greater will be the vigour with which the ball snaps back [101]. It should be noted, though, that our findings only apply when ESV < V_{eq}. In case ESV > $V_{eq,}$ a stiffer LV is expected to slow the rate of isovolumic relaxation.

Some additional practical limitations related to the model's applicability for echocardiographic measurements need to be explained.

(iv) For practical reasons, the LV phantom needed to be attached at its base, while in a real LV the atrioventricular plane moves up and down and the apex remains virtually fixed in space. Determination of basal longitudinal wall velocities using tissue Doppler imaging (see paragraph 5.7.2) is therefore not feasible.

(v) The use of PVA does not allow simulation of the complex helicoidal myocardial fibre structure (see paragraph 1.6.3). Neither early diastolic untwisting during IVR (see paragraph 5.7.3), nor its influence on $(dP/dt)_{min}$ can therefore be assessed.

(vi) Ultrasound images can only be acquired from the apical window. Acquisition of cross-sectional images is therefore not feasible.

5.3.5 Conclusion

In this study, a new hydraulic model was presented to determine the effect of left atrial pressure, end-systolic pressure, inactivation rate and left ventricular compliance on the peak rate of left ventricular pressure decay. Despite the relatively simple concept, this model mimics pretty well the process of LV isovolumic relaxation. However, a number of practical issues need to be resolved before the model can be used in echocardiographic studies.

5.4 Classic non-invasive technologies

5.4.1 Greyscale imaging

Greyscale imaging (two-dimensional and M-mode echocardiography) is the most widely applied tool in clinical practice. It is used to determine LV dimensions, volume, mass, wall thickness and ejection fraction, and it allows for assessing regional wall motion (excursion). Two-dimensional echo also permits to detect hypertrophy and remodelling phenomena, and left atrial enlargement, an extremely frequent finding in diastolic heart failure [179, 258].

5.4.2 Transmitral flow

5.4.2.1 The standard tool

Measurement of transmitral flow velocities using pulsed wave (PW) Doppler echocardiography is the principal tool to assess diastolic function. Transmitral flow is recorded from the *apical window* with the sample volume placed between the *mitral*

leaflet tips. Unfortunately, this technique does not provide a direct evaluation of *relaxation* or *compliance*, but instead measures the impact of both *intrinsic* LV diastolic properties and *external factors* on the transmitral filling pattern (figure 5-13A) [115, 164, 327]. Therefore, it offers no direct assessment of intrinsic myocardial diastolic abnormalities. Doppler measurements have become so widely used that this is often forgotten.

5.4.2.2 Normal filling pattern

A *normal transmitral flow profile* consists of an *early filling wave* (E-wave) and a *late filling wave* (A-wave). For clinical purposes, the Doppler velocity profile (figure 5-10) is quantitatively characterized by a number of parameters: *amplitude of the E-wave* (E), *amplitude of the A-wave* (A), their *ratio* (E/A), the *deceleration time of the E-wave* (DT, an index related to LVC in early diastole), and the *isovolumic relaxation time* (IVRT, the time interval between aortic valve closure and opening of the mitral valve).

A normal filling pattern, as seen in young healthy adults with a normal myocardial relaxation rate, is characterized by a *high E-velocity* relative to the *A-velocity* (E/A > 1.5) [258]. In healthy adults, the ratio is considered normal when E/A > 1.0 until age 60 years [107, 219]. DT is normally less than 220 ms.

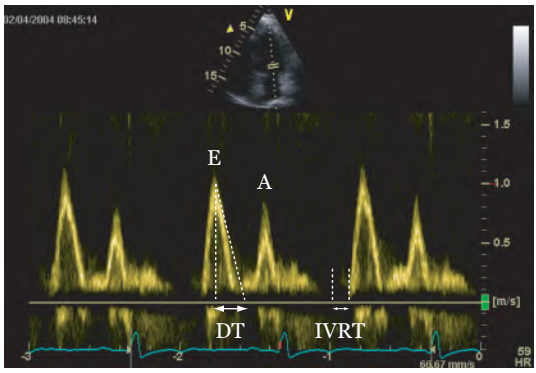

Figure 5-10: Typical example of a normal transmitral flow velocity profile, measured with a conventional pulsed wave (PW) Doppler system. The clinically useful indices (peak amplitudes E and A, the ratio E/A, DT and IVRT) are briefly explained in the text.

5.4.2.3 Abnormal filling patterns

The abovementioned flow-derived parameters are commonly used to *stratify* the *degree* of diastolic function abnormality. Three *abnormal* filling patterns are recognized (figure 5-11B) [235]:

- *Impaired relaxation* ("type I diastolic dysfunction" [236]): Relaxation rate will gradually decrease in response to ageing, increased afterload, ischaemia and myocardial disease, resulting in increases in IVRT and DT, a reduction in E and a *compensatory* increase in A [258]. The compensatory increase in A is the result of a relatively high residual LA preload with preserved LA contractility

[206]. As a result, a reversal of the E/A ratio is present with E/A < 1.0. LAP and LVP, however, are still in the normal range, as LA and LV compliance is normal.

- *Pseudo-normalization* ("type II diastolic dysfunction" [236]): In more advanced diastolic disease, an increase in mean LAP will occur due to a decrease in LVC. The elevated mean LAP, however, tends to *override* the effect of delayed LV relaxation on transmitral flow and a *pseudo-normal filling pattern* is observed (figure 5-10A), which closely resembles the normal pattern in terms of the E/A ratio (E/A = 1-1.5). DT is slightly reduced due to the decreased LVC [164].
- *Restricted filling* ("type III diastolic dysfunction" [236]): When LVC continues to decrease and LAP further increases, E appears more than normal, resulting in a "*super normal*" E/A > 2.0. The contribution of the A-wave is very limited, because of the small pressure difference between the LA and the stiff LV. Restrictive filling is a good evidence of a raised LAP, as it over-compensates all relaxation abnormalities. DT is usually less than 150 ms [258]. Depending on the result of the application of the *Valsalva manoeuvre*, an *irreversible restrictive pattern* ("type IV diastolic dysfunction") can be observed; this is the worst stage of diastolic dysfunction that can develop and is associated with a *poor prognosis* [164]. A Valsalva manoeuvre (i.e., an attempted exhalation against a closed mouth and nose) causes a drastic increase in pressure in the thoracic cavity and a reduction in preload, and is used to assess possible *reversibility* from one stage to another (from type III to II or from type II to I) [139].

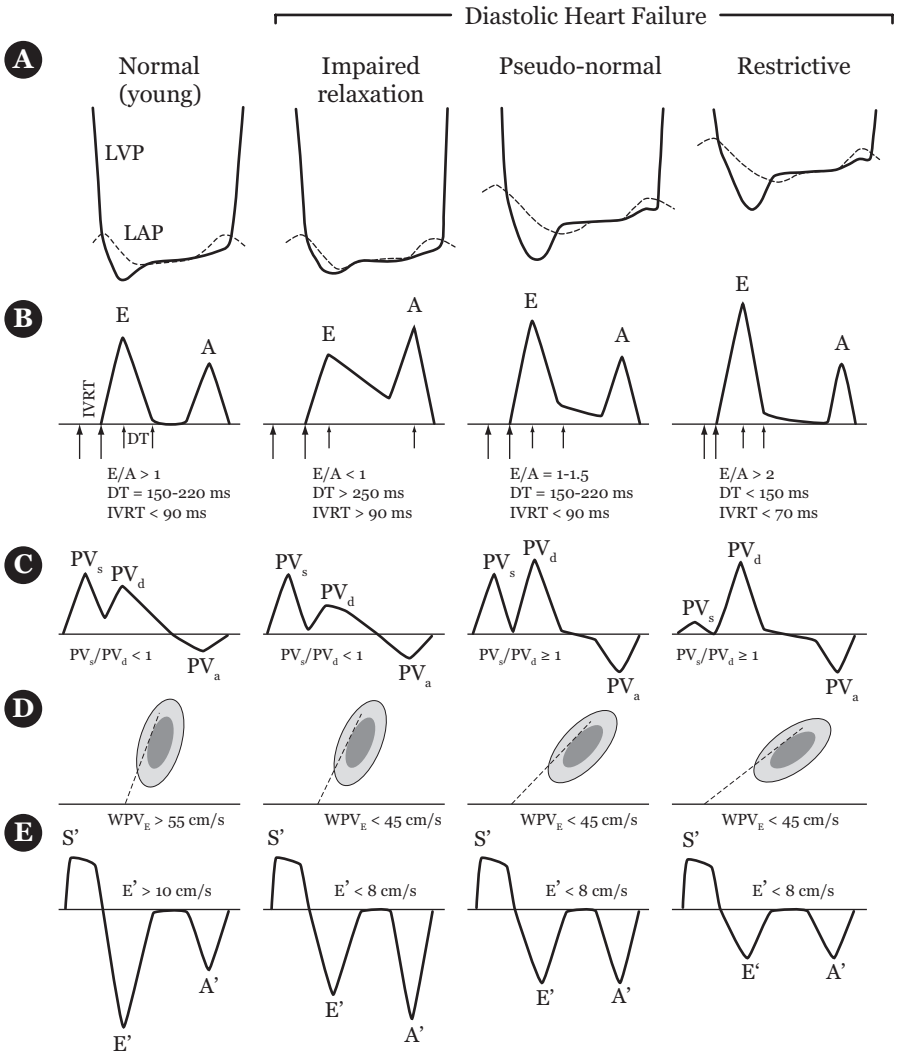

Figure 5-11: A: LVP and LAP during diastole; B: Transmitral flow velocity; C: Pulmonary vein velocity, D: Wave propagation velocity (WPV_E) during during early filling; E: Tissue Doppler velocity (IVRT: isovolumic relaxation time, E: early LV filling velocity, A: late LV filling velocity, PV_s: systolic pulmonary vein velocity, PV_d: diastolic pulmonary vein velocity, PV_a: pulmonary vein velocity resulting from atrial contraction, S': myocardial velocity during systole, E': myocardial velocity during early filling, A': myocardial velocity during late filling) (adapted from [364]).

Investigation of the transmitral velocity profile suffers from two limitations:

- Because the pseudo-normal filling pattern (caused by the counterbalancing effects of myocardial relaxation and LAP) is practically indiscernible from a normal filling pattern, the *underlying diastolic abnormalities* can be *overlooked* (figure 5-11B and figure 5-12). As a result, invasive measures of

early and late diastolic function will poorly correlate with non-invasive measures derived from the filling pattern.

- As early transmitral flow is inherently dependent on the interplay between myocardial relaxation and LAP, it is not feasible to non-invasively estimate one of these variables *separately*.

Distinguishing the normal from the pseudo-normal pattern is one of the major challenges in the interpretation of transmitral filling patterns. Other (newer) echocardiographic techniques that are discussed later in this chapter appear less affected by LAP and are thus likely able to distinguish between a normal and a pseudo-normal flow profile, such that the issue of pseudo-normality is currently less of a problem than literature might suggest.

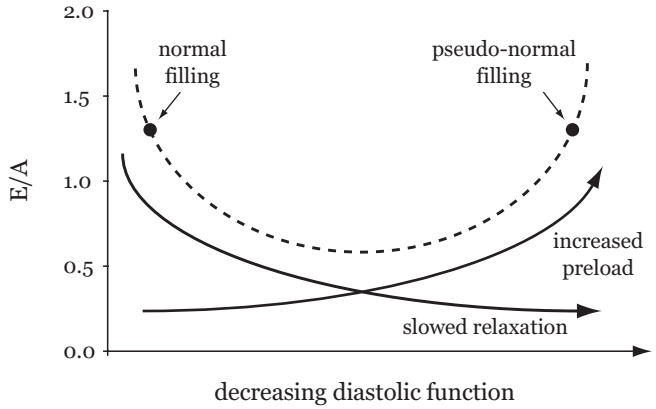

Figure 5-12: Stratification of diastolic abnormalities based on the E/A ratio. The pseudo-normal filling pattern is similar to the normal pattern due to counterbalancing effects of relaxation and LAP (adapted from [107]).

5.4.2.4 Estimating filling pressure

Filling pressure is often expressed by LAP. Yet, in clinical practice *pulmonary capillary wedge pressure* (PCWP) is often used as a surrogate for LAP. This wedge pressure can also be used to estimate end-diastolic pressure (EDP), a measure of ventricular preload. PCWP is measured by advancing a balloon-tipped catheter from a peripheral vein into the RA, the RV and finally into a branch of the pulmonary artery. The balloon is then inflated to occlude the branch of the pulmonary artery. The obtained pressure is very similar to LAP because the occluded vessel, along with its distal branches which eventually form the pulmonary veins, acts as a long catheter which measures the blood pressure within the pulmonary veins.

Even though filling pressure, either expressed by LAP or PCWP, provides *no* indication of *intrinsic* diastolic function, estimating filling pressure is essential for diastolic function assessment, because an elevated filling pressure ultimately leads to *dyspnoea* and *pulmonary oedema* [363].

A number of transmitral flow-based approaches to estimate LAP or PCWP have been introduced [5, 226], e.g., PCWP = 17 + (5 · E/A) – (0.11 · IVRT). They have shown to be very useful in patients with a *depressed EF*. However, in the setting of DHF with *preserved EF*, their accuracy is significantly reduced [226].

5.4.3 Pulmonary venous flow

Additional information about diastolic function may be obtained by incorporating pulmonary venous flow measurements with PW Doppler. Pulmonary venous flow measurements are feasible in about 80% of patients during a routine echocardiographic examination [258]. Images are taken from the apical four-chamber view. The 3-4 mm sample volume is placed 1-3 cm deep within the pulmonary vein.

The pulmonary vein flow profile is characterized by three distinct waves (figure 5-11C). The *first antegrade wave* (PV_s) occurs during ventricular systole, when the LA relaxes and the atrioventricular plane moves towards the apex. The *second antegrade wave* (PV_d) coincides with the early diastolic filling wave, and is the result of the pressure difference between the pulmonary veins and the LA in early diastole. The *last wave* (PV_a), a small *retrograde* flow wave back into the pulmonary veins, coincides with LA systole because of the absence of a valve between the LA and the pulmonary veins.

If LAP is normal, blood enters the LA predominantly during systole. In early stages of diastolic dysfunction (evidenced by a low E/A ratio), antegrade systolic flow decreases, and the contribution during diastole will be relatively larger. However, PV_s is also influenced by LAP, such that an increased LAP will tend to blunt the PV_s and reduce $PV_s/PV_d < 1.0$ [176]. Therefore, similar to the velocities of the E- and A-wave in the transmitral flow pattern, the pulmonary venous PV_s/PV_d ratio also exhibits a non-linear relation to progressive diastolic dysfunction [221].

The peak value and the duration of PV_a have shown to provide information about filling pressure. A peak value > 35 cm/s and a duration of > 30 ms, or longer than the duration of the transmitral A-wave, is predictive of an LAP > 15 mmHg [270].

5.4.4 Conclusion

It appears that the indices derived from transmitral and pulmonary venous flow Doppler measurements present a parabolic or U-shaped pattern during progression from normal to advanced diastolic dysfunction, because of the interfering LAP (figure 5-12) [200]. It is therefore difficult to determine whether a given Doppler pattern corresponds to the left or right side of the parabola, unless invasive or additional non-invasive information about intrinsic diastolic function is available. Novel echocardiographic tools aim to provide this kind of information.

5.5 New non-invasive technologies

5.5.1 Introduction

To overcome the limitations of transmitral and pulmonary flow indices, more advanced echocardiographic imaging modalities have been introduced aiming for a

more direct and reliable quantification of the diastolic properties of the LV itself. In the following paragraphs, we highlight four of these new technologies. They can be classified into two groups, those that focus on *intraventricular haemodynamics* (analysis of wave propagation and intraventricular pressure differences), and those that focus on *longitudinal and circumferential myocardial wall motion* (mitral annular motion and ventricular torsion). Basic knowledge about *fluid dynamics* and *ventricular wall mechanics* is required to make an adequate interpretation of the recorded and/or post-processed parametric images, and to understand the shortcomings of the methods. The techniques described in the remainder of this chapter aim specifically at assessing *global diastolic function*. Other well advanced techniques that seek to assess *regional diastolic function* (such as strain and strain rate imaging) also exist [320]. They are briefly described in paragraph 5.7.4.

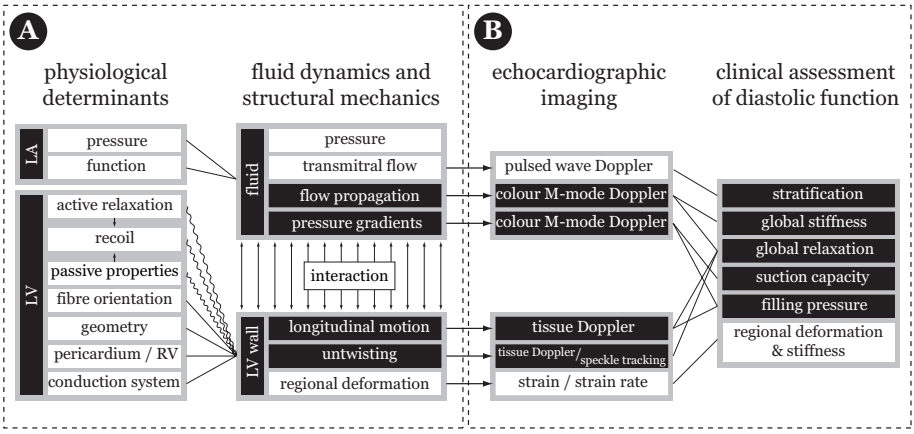

Figure 5-13: A: Schematic overview of the physiologic determinants of the structural mechanical and haemodynamic events observed during diastole. Zigzagged lines are used when the determinants are modulated by age. There is an inherent continuous interaction between the LV wall and the blood pool; B: A list of novel echocardiographic imaging modalities used to quantify these events, and the information that can be derived from the (parametric) images. The topics shown with a black background are currently of specific interest for assessing global diastolic function and are therefore reviewed in detail.

Figure 5-13 is the key figure for the remainder of this chapter. It visually presents the *haemodynamic* (fluid dynamics) and *mechanical* (structural mechanics) events (figure 5-13A) that can be assessed with the new echocardiographic techniques, and summarizes their major physiological determinants. As diastolic heart failure is often called a disease of the elderly, *age dependence* of relaxation and passive properties and, hence, recoil has to be accounted for, so that diseased states can be separated from a normal state in healthy elderly people. It is furthermore essential to realize that, throughout the whole diastole, there is a continuous interaction between the blood pool and the wall. Figure 5-13B shows which echocardiographic tools are well suited to non-invasively assess the haemodynamic and mechanical events, and displays what type of information they can provide when used alone or in combination with standard PW Doppler tools.

5.5.2 Model studies versus clinical studies

The explanation of diastolic events is primarily based on the results of a number of biomedical engineering model studies (numerical and physical) and clinical studies. Each of these studies has undoubtedly proven useful, although their results may sometimes appear contradictory. The major advantages and limitations of both types of studies are summarized in table 5-2. They should be kept in mind throughout the text.

Table 5-2: Differences between model studies and clinical studies.

Model studies (numerical and physical)	
+	Possibility to study the effects of isolated changes of one variable
-	Simplified geometry (three-dimensional axisymmetry)
-	Simplified wall properties
-	Blood-wall interaction difficult to implement (numerical models)
-	Focus either on fluid dynamics or on wall mechanics
-	Relevance greatly depends on the model assumptions (boundary conditions)
Clinical studies	
+	Real-life anatomy and physiology
+	Blood-wall interaction inherently present
-	Inter- and intra-observed variability in measurements
-	Isolated changes in parameters are virtually impossible
-	Measurements may be modulated by a number of unknown factors
-	Statistical correlations do not reveal causality

5.5.3 Fluid-structure interaction

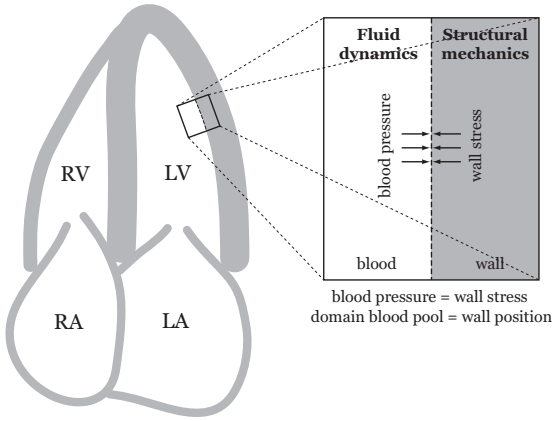

Figure 5-14: Basic principles of fluid-structure interaction between the LV wall and the blood pool. Throughout the whole cardiac cycle, the local blood pressure is seen by the wall as a perpendicular load. At the same time, the displacements of this interface determine the geometric boundaries of the blood pool. This principle is of paramount importance for implementation in numerical models of the heart. The Navier-Stokes equations govern intraventricular haemodynamics, while advanced constitutive material laws determine wall stresses and strains.

There is a continuous *interaction* between LV wall stress and displacements on one hand, and intraventricular fluid dynamics on the other hand. While this interaction is inherently present in the real ventricle and in physical models, it is a prerequisite to implement this principle in numerical models in order to obtain accurate and physically relevant results that explain the peculiarities of diastolic function. From a modelling point of view, it means that the geometric boundaries of the blood pool determine the endocardial wall displacements, and that the intraventricular blood pressure equals the stress perpendicular to the endocardial wall (figure 5-14). The fluid dynamics are governed by the *Navier-Stokes equations*, while wall motion and deformation are governed by appropriately chosen *constitutive wall material laws* [138].

5.6 Intraventricular fluid dynamics

5.6.1 Conservation laws for mass and momentum

Intraventricular fluid dynamics is governed by the *Navier-Stokes equation* and the *continuity equation*. The Navier-Stokes equation (equation 5-4) is a partial differential equation which expresses the conservation of momentum (Newton's second law), leading to the intimate relation between *pressure gradients*, *flow velocity fields* and the *properties of blood*. Analytically, it states that the pressure gradient counterbalances the sum of blood acceleration, viscous losses and hydrostatic forces:

$$\nabla P = -\rho \cdot (\underbrace{\frac{\partial \bar{v}}{\partial t} + \bar{v} \cdot \nabla \bar{v}}_{\text{acceleration}}) + \underbrace{\mu \cdot \nabla^2 \bar{v}}_{\text{viscous}} + \underbrace{\rho \cdot g}_{\text{hydrostatic}} \quad (5\text{-}4)$$

with ρ the density and μ the dynamic viscosity of blood. The continuity equation (equation 5-5) expresses the principle of conservation of mass.

$$\frac{\partial \rho}{\partial t} + \nabla(\rho \cdot \bar{v}) = 0 \quad (5\text{-}5)$$

Even though intraventricular pressure and flow cannot be uncoupled from each other from a theoretical point of view, analyses of both pressure gradients and flow velocities have independently proven useful in assessing diastolic function. In the following paragraphs, we intentionally discuss wave propagation before pressure imaging, since pressure imaging is derived from wave propagation data.

5.6.2 Wave propagation

5.6.2.1 Fluid dynamics

The propagation of blood flow and the ensuing vortex formation during LV filling represent two intriguing aspects of LV fluid dynamics, and explain the existence of many physical [23, 74] and numerical [15, 191, 231, 344, 345] studies in this field.

Intraventricular flow is generally described in three phases. After opening of the mitral valve, blood moves almost simultaneously at all levels towards the apex as a single *quasi-incompressible blood column* (*phase I*). This phenomenon was described by Steen and Steen [298] in a physical model with a rubber balloon ventricle. The underlying principle is comparable to that of *pressure wave* propagation inside a tube with a compliance equal to that of the LV. The pressure wave travels considerably faster than the fastest blood particles themselves, and its velocity can be approximated analytically using the Moens-Korteweg formula [173]:

$$c = \sqrt{\frac{E \cdot h}{2 \cdot \rho \cdot r}} \quad (5\text{-}6)$$

with c the wave speed, E the Young modulus of the wall, h the wall thickness, ρ the density of blood, and r the tube radius.

The *second* and *third* phase constitute the propagation and simultaneous *redistribution* of blood particles within the whole cavity during early (*phase II*) and late (*phase III*) filling as a response to intraventricular pressure differences between base and apex (see paragraph 5.6.3). *Vortex* formation (i.e., a fluid structure that possesses a swirling or circular motion) is the most accepted type of flow redistribution. It has been recognized by several investigators using simplified numerical or physical models, and flow visualization techniques (MRI and colour Doppler) in real ventricles [15, 23, 74, 166, 298, 344, 345].

The results of the three-dimensional – yet axisymmetric – numerical model of Vierendeels et al. [345] revealed that vortex formation was initiated during acceleration of transmitral flow and that this vortex is amplified during deceleration, resulting in

one large vortex between the E-wave and the A-wave. Later, a second vortex is seen at the base, directed opposite to the first one. During acceleration of the A-wave, the second vortex grows and a third one is formed, comparable to the first one. Despite some differences in modelling assumptions, similar vortex patterns were seen in the model of Baccani et al. [14, 15].

The onset of vortex formation and the vortex travel path in numerical models may differ from what is found in clinical in vivo measurements (using echocardiography and MRI), because a real LV is not axisymmetric. Numerical models, moreover, rely on a *simplified* and *idealized geometry* (such as a truncated prolate ellipsoid), do not include *trabeculae* nor *papillary muscles*, use simplified models of the *mitral valve leaflets*, and often implement a *prescribed wall motion*, corresponding to a predefined left ventricular volume with a temporal law chosen on the basis of clinical data. Notwithstanding the relative simplicity of these models, they do provide useful insight in intraventricular fluid dynamics features and clarify several phenomena observed during clinical practice.

Using MRI velocity mapping, Kim et al. [167] showed that an anterior vortex develops immediately after the mid-diastolic closure of the anterior mitral valve leaflet, and that this vortex reappears at the time of final mitral valve closure. Colour Doppler experimental studies by Rodevand et al. [266] have demonstrated a large vortex behind the anterior leaflet, and a smaller vortex behind the posterior leaflet. Kilner et al. [166] confirmed these results and reported that mitral inflow gives rise to recirculating flows beneath the valve leaflets, the dominant direction being under the free edge of the anterior mitral leaflet.

Although vortex travelling was suggested to be a mechanism for early valve closure at end-diastole [23] and was shown to be an important feature to decrease residence cellular time in the apical region [285], cardiologists and echocardiographers are not directly interested in vortex formation as an index of diastolic function, as such. They mainly focus on the so-called *wave propagation velocity* (WPV), which mirrors the velocity by which the maximum blood velocity *propagates* from the LV base to the apex. Experimental studies of the flow in a skeletal muscle LV by Henry et al. [135] denoted that WPV corresponds to the *travelling speed of the vortices*. Steen and Steen [298] found that the travelling speed of these vortices could therefore be associated with WPV as seen on a colour M-mode Doppler (CMD) image (figure 5-15). This knowledge was later supported by the results from the numerical study from Vierendeels et al [345]. Because the individual blood particle is rotating within the vortex ring, it should be stressed that WPV does *not* represent the velocity of the individual fluid particle [19].

5.6.2.2 Instrumentation and image acquisition

In a clinical setting the spatiotemporal information on a CMD image is used to determine the WPV. A CMD image displays colour-coded blood velocities as a function of time on the horizontal axis and depth along a scanline on the vertical axis (see paragraph 3.2.3.5). It typically has a temporal resolution of 5 ms, a spatial resolution of 0.3 mm and a velocity resolution of 3 cm/s [75]. Acquisition is normally made transthoracically, in the four-chamber apical view, by placing the M-mode scanline along the long-axis within the mitral inflow volume (figure 5-16A). A normal

CMD image is characterized by its three 'flames', corresponding to the three phases (I, II and III) mentioned before (figure 5-15A).

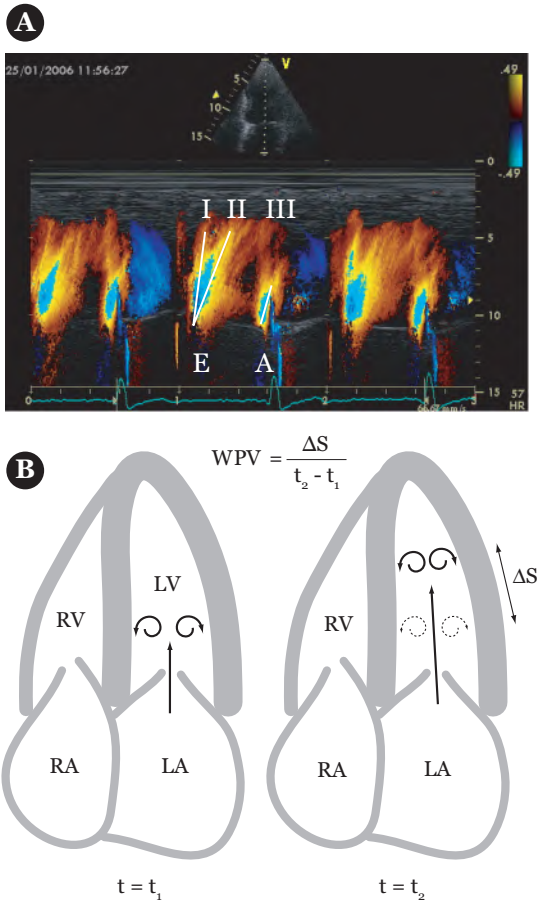

Figure 5-15: A: Representative example of a colour M-mode Doppler image showing three 'flames' during LV filling. Phase I and II correspond with the early diastolic E-wave, while phase III is the result of the late diastolic A-wave. The (artificially) determined slope of the second flame (Phase II) determines the wave propagation velocity (WPV_E); B: Phase II is associated with the vortex travelling velocity from base to apex.

The wave propagation corresponding with *phase II* (WPV_E) has gained the most interest as an index of LV relaxation. Several methods have been developed to measure WPV_E (Brun et al. [41], Duval-Moulin-Garcia et al. [84, 107], Stugaard et al. [306], Takatsuji et al. [324] and Greenberg et al. [305]) and have been meticulously reviewed in [70, 75]. Whereas Stugaard's method is the most *straightforward* technique to find the position of the maximum velocity along the LV base-apex axis, in most of recent work the method of Duval-Moulin-Garcia is applied because of its relatively high *reproducibility* compared to other methods [75], and because it does not require dedicated software. In this method, WPV_E corresponds to the slope of the *isovelocity*

contour of 50% of the maximum velocity, considered from the mitral valve to 4 cm further into the LV. It should be stressed, however, that all methods to determine WPV_E appear somewhat artificial.

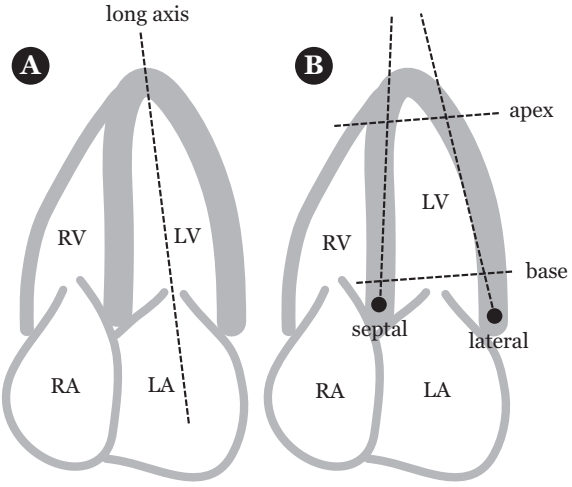

Figure 5-16: A: The ultrasound probe is positioned along a scanline from apex to base (central long-axis) to acquire a spatiotemporal velocity map. The velocity data is used to calculate the wave propagation velocity and the pressure gradients; B: Scanlines and cursor placements used for assessing mitral annular motion (septal and lateral site). Torsion imaging requires a two-dimensional short-axis cross-section at the base and at the apex.

5.6.2.3 Wave propagation velocity in early diastole

A very close correlation between WPV_E and the constant of isovolumic relaxation τ was shown by Brun et al. [41] in 9 patients with end-stage dilated cardiomyopathy (DCM), a disease that is known to alter relaxation. In the study, they also found a significant decrease in WPV_E compared to normals in other diseases that alter relaxation, such as ischaemic cardiomyopathy, systemic hypertension, hypertrophic cardiomyopathy and aortic valve disease. This close correlation between relaxation and wave propagation, which was later confirmed by others [84, 106], suggested that a rapid relaxation (short τ) would promote a faster propagation of blood into the ventricle.

Similar to other indices of relaxation, WPV_E decreases with age [41, 210]. According to Garcia et al. [107], cut-off values for WPV_E indicating impaired relaxation should be set at 55 cm/s and 45 cm/s in young (age < 30 years) and middle-aged (age ≥ 30 years) adults, respectively. Values of WPV_E corresponding with the various stages of diastolic heart failure are shown in figure 5-4.

In contrast to transmitral Doppler indices, WPV_E is considered relatively *independent* of filling pressure, and thus allows distinguishing a *pseudo-normal* from a *normal* mitral inflow profile [104, 324]. Several authors have therefore proposed E/WPV_E as a measure of filling pressure, because the amplitude of the E-wave is directly related to filling pressure and inversely related to τ, whereas WPV_E has shown to be inversely

related to τ [96, 104]. In most studies, filling pressure can be predicted from a linear expression with a general form $P = \alpha \cdot E/WPV_E + \beta$. Significant variations in the coefficients α and β have been reported [75], so there is no generally applicable regression equation. $E/WPV_E > 2$ is associated with PCWP > 15 mmHg in patients [104]. Others stated that in normal volunteers $E/WPV_E > 1.5$ is associated with LAP > 12 mmHg [96].

Barbier et al. [18] showed in an unselected patient cohort that *LV geometry*, *systolic function* (assessed as EF) and *mechanical incoordination (or dyssynchrony)* during relaxation, but not LVC, are important determinants of WPV_E. The relation between LV relaxation and WPV_E is modulated by geometry in particular in case of small ventricles with an elongated shape, as seen in hypertrophic cardiomyopathy [70]. In those conditions, the ability for flow redistribution by means of vortex formation is limited and the WPV will approximate the fastest particles. Consequently, an apparently normal, or *pseudo-normal* WPV_E will be recorded, even though these patients are known to have a *prolonged relaxation* [18, 201]. Mechanical *incoordination,* one of the important determinants of relaxation [194], is the result of mechanical contraction dyssynchrony. An increase in incoordination results in force imbalance and slows the rate of LV isovolumic pressure fall. The relation between systolic function, incoordination and WPV_E is therefore not unexpected, given the integration of relaxation in the contraction-relaxation cycle [45].

Based on experiments with a physical LV membrane model, De Mey et al. [74] showed that WPV_E is *not* completely independent of LAP. They attributed the apparent filling pressure independence as seen in the majority of the in vivo studies to the combination of two *counterbalancing* effects, which normally occur together in normal ventricles with an exponential passive P-V relationship: the *increase in loading* which causes in increase in WPV_E, and the *decrease in LVC* which decreases WPV_E.

5.6.2.4 Wave propagation velocity: a useful index?

In our opinion, the ability of WPV_E to detect LV diastolic mechanical abnormalities remains somewhat controversial, because many potential factors other than relaxation (e.g., geometry, systolic function or mechanical incoordination) can influence intraventricular flow dynamics and, hence, alter WPV_E. Its usefulness is furthermore limited by the existence of diverse measurement methods that are not interchangeable and have a mediocre reproducibility [75]. Impaired relaxation can therefore be left undetected.

Duval-Moulin-Garcia's method has also been recently applied to measure the wave propagation velocity during the A-wave (WPV_A). WPV_A was related to the *force of LA contraction*, and was suggested as a novel index for *LV distensibility* [75, 247, 249, 353]. However, its physical determinants are currently poorly understood from a mechanical point of view and thus require further investigation.

5.6.3 Pressure gradients

5.6.3.1 Fluid dynamics

The existence of an *intraventricular pressure difference* (IVPD) between the LV base and apex has been demonstrated in experimental studies using invasive pressure measurements [62, 97, 196, 234] and was, moreover, reproduced in a number of numerical studies [231, 345].

A typical time course of apical and basal LVP is shown in figure 5-17A. Minimal LVP is first obtained at the apex. Consequently, LVP begins to increase first near the apex and last near the base. Regional IVPD were also recorded during LA systole. However, in contrast to early diastole, the initial upstroke of LVP was noted first near the base and later near the apex [61, 345].

Whereas IVPD during both the E-wave and the A-wave are acknowledged, the majority of experimental and clinical research studies have been focusing on the early diastolic maximum IVPD as a measure of *"diastolic suction",* a property of the LV by which it tends to *refill itself* during early diastole, independent of any force from the LA. Suction has been defined in a number of different ways throughout history, although they actually refer to a *similar phenomenon*. Already in 1930, Katz [158] observed that LVP continued to decline during early diastole despite rapid filling, and thus concluded that normal relaxation caused active suction in the LV, similar to an *aspirating pump*. The actual presence of an IVPD was first demonstrated by Ling et al. [196] and Falsetti et al. [89], and later confirmed by Courtois et al. [61, 62].

Courtois et al. [62] hypothesized that the early diastolic IVPD might be causally related to the release of *elastic energy* stored during the preceding systole (i.e., recoil), which generates suction and contributes to normal filling. They also showed that, due to acutely induced mechanical systolic dysfunction (abrupt coronary artery occlusion), IVPD could be attenuated, lost entirely, or even reversed. They attributed the reduced elastic recoil to a diminished amount of contractile myocardium and demonstrated a strong relationship between diastolic IVPD and systolic function [62].

Nikolic et al. [234] confirmed the relationship between IVPD and the elastic restoring forces and found that IVPD are related to the heterogeneous myocardial stress during IVR and early filling that results in ventricular shape changes and intraventricular redistribution of chamber volume. These shape changes cause local accelerations of blood and the associated pressure differences. The role of elastic recoil assumes greater importance at smaller ESV, leading to greater shape changes and greater IVPD. Firstenberg et al. [97] demonstrated that improvements in diastolic and systolic function, through operative myocardial revascularization and remodelling, result in increases in IVPD, thus complementing previous studies of Courtois et al.

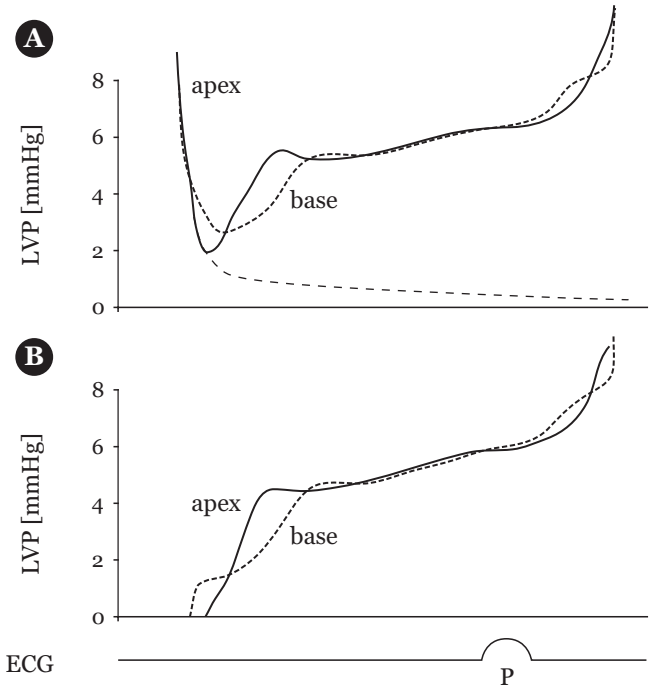

Figure 5-17: A: Typical example of the time course of basal and apical LVP during LV filling. In early diastole, the steep rise in pressure is first observed at the apex, whereas during late diastole, the first increase in pressure is noted at the base; B: Apical and basal pressure with non-filling relaxation pressure as the reference pressure. Both during early and late diastole, filling occurs passively (adapted from [345]).

Vierendeels et al. [345], on the other hand, showed in their axisymmetric numerical LV model that recoil is *not* a prerequisite for the existence of IVPD. They explained the observed IVPD as follows: the pressure recorded at any given location in the LV is the *superposition* of a homogeneously decaying pressure due to LV relaxation and a travelling compression wave which starts at the base, reflects at the apex and then returns to the base [184]. Because the influence of relaxation is initially too strong, the increase in pressure due to the pressure wave is first noticed at the apex and only later at the base (figure 5-17A). Both the E-wave and the A-wave can therefore be considered as *passive filling waves* that are superposed to the decreasing pressure due to relaxation (figure 5-17B).

In our opinion, IVPD is the consequence of *active relaxation*, in agreement with Vierendeels et al. [345], and not due to elastic recoil. However, in a normal LV recoil always accompanies active relaxation, provided ESV < V_{eq}. The relationships found between recoil and IVPD are therefore not unexpected.

5.6.3.2 Data acquisition and processing

Despite the apparent importance of diastolic IVPD, invasive pressure measurements are rarely performed in the clinical setting because the use of multiple

micromanometer catheters is technically and economically very demanding and, hence, unsuitable for everyday clinical practice. A non-invasive approach, based on *fluid dynamics principles*, has therefore been developed which fully exploits the *numerical velocity data* in the CMD image and which may greatly expand the application of this technique.

Pressure gradients can be calculated for the flow velocity field by neglecting the *viscous* [357] and *hydrostatic* terms in the Navier-Stokes equations (see equation 5-4):

$$\nabla P = -\rho \cdot (\underbrace{\frac{\partial \vec{v}}{\partial t} + \vec{v} \cdot \nabla \vec{v}}_{\text{acceleration}}) \tag{5-7}$$

When applying this equation along a streamline, the *differential Euler equation* is obtained (equation 5-8), which expresses the pressure gradient along a streamline as a function of *inertial* and *convective* acceleration (figure 5-18). Note that the term "*pressure gradient*" is reserved to describe the change in pressure per unit distance along a streamline, while a "*pressure difference*" refers to the difference in pressure between two discrete points on the same streamline.

$$\text{pressure gradient} = \frac{\partial P}{\partial s} = -\rho \cdot (\underbrace{\frac{\partial v}{\partial t}}_{\text{inertia}} + \underbrace{v \cdot \frac{\partial v}{\partial s}}_{\text{convection}}) \tag{5-8}$$

With s the line coordinate. The *inertial* component indicates the change in velocity through time at a given position, while the *convective* component refers to the change in velocity through space at a given instant [248, 328]. The minus sign in equation 5-8 indicates that the blood particle has a positive acceleration when it moves from a region of higher to lower pressure. The pressure difference between any two intraventricular points along a streamline can be obtained by spatial integration of the Euler equation, yielding the *non-steady Bernoulli equation* [123]:

$$IVPD = \Delta P = LVP_{base} - LVP_{apex} = -\rho \cdot \int_{apex}^{base} (\underbrace{\frac{\partial v}{\partial t}}_{\text{inertia}} + \underbrace{v \cdot \frac{\partial v}{\partial s}}_{\text{convection}}) ds \tag{5-9}$$

Using this equation, both inertial and convective pressure differences can be calculated from the spatiotemporal velocity map in the CMD image [124]. The abovementioned theoretical principles were validated by several research groups. Significant correlations between invasively and non-invasively obtained IVPD were found in animals [123] and humans [358, 359].

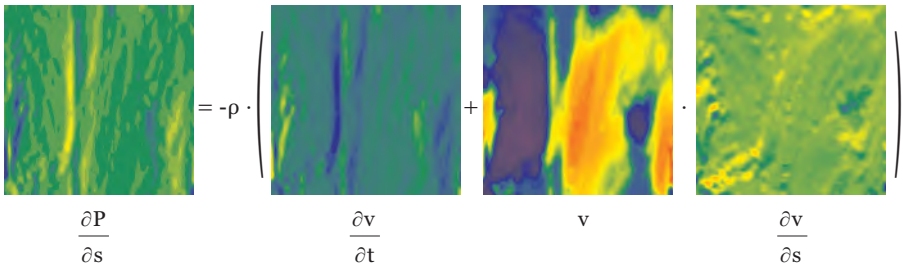

Figure 5-18: Theoretical principles of calculating pressure gradients by post-processing the spatiotemporal velocity information on the colour M-mode Doppler image, using the Euler differential equation. Spatial integration of the pressure gradients is required to obtain the intraventricular pressure difference (IVPD) between the apex and the base.

In this methodology it is assumed that the scanline coincides perfectly with the streamline, a condition unlikely to be fulfilled in practice. However, Greenberg et al. [123] showed in a numerical analysis that a very precise alignment of the scanline is not required: the error in calculating the IVPD was small (mean squared error <0.26 mmHg) if the scanline was misaligned to up to 20° and even if it was displaced from centreline to more than halfway to the edge of the mitral valve.

5.6.3.3 Clinical applications

In the majority of recent publications the abovementioned non-invasive approach has been applied to determine the *peak IVPD* in early diastole. This index has proven valuable for assessing diastolic function and understanding the (patho-)physiological link between systole and early diastole [328].

Rovner et al. [272] proved IVPD a useful indicator of diastolic function improvement in patients with hypertrophic obstructive cardiomyopathy (HOCM), a disorder associated with significant morbidity and mortality. Even though HOCM presents a worst case scenario for application of the Euler equation (because of the impact that altered geometry may have on mitral inflow), they were able to show that IVPD almost doubled after percutaneous septal ablation, a non-surgical reduction of the interventricular septum.

Later, the same group provided evidence for a strong relationship between the ability to augment diastolic suction and maximum oxygen consumption ($Vo_{2,max}$) in heart failure patients [271]. Their study demonstrated that in heart failure patients, the decreased ability to augment diastolic suction is responsible for the inability to accommodate the increase in preload during exercise, resulting in higher filling pressures.

Yotti et al. [358] showed an abnormally low diastolic suction and a blunted capacity to recruit suction with stress in patients with dilated cardiomyopathy (DCM). They used the non-steady Bernoulli equation to find out which mechanisms are causing the significant reduction in IVPD, resulting in exercise-induced dyspnoea. They showed that the overall reduction in IVPD could be ascribed to (i) the *lowered inertial flow acceleration*, due to reduced elastic recoil, and (ii) to the *higher deleterious*

convective deceleration, due to the large disproportion between ventricular and annular dimensions in the dilated ventricle.

5.6.3.4 IVPD is a promising tool

As previously outlined by several investigators, there is no simple relationship between LV diastolic function and intraventricular haemodynamics. Even though IVPD is able to provide valuable information about diastolic suction, it is not unlikely that this index is affected by the same physical factors as is WPV (e.g., LV geometry), because they are both derived from the same source data, being the spatiotemporal velocity map. Moreover, the effect of an elevated filling pressure upon IVPD should be investigated. We are, nonetheless, convinced that an analysis of the *entire* time course of IVPD, instead of merely its peak value,

- may offer more information than a single slope representing WPV, because the IVPD calculation relies on all velocity data in the CMD image, in contrast to WPV, and
- could provide physically more relevant results, as it is more obvious what is actually being measured from an analytical point of view.

The non-invasive determination of IVPD can therefore be regarded as a promising concept that should be pursued vigorously.

5.7 Wall motion and deformation

5.7.1 Components of motion and deformation

Ventricular motion and deformation are fundamentally related to *fibre organization* in the ventricular wall. An accurate description of this complex fibre organization and its relation with ventricular myocardial function remains the subject of many ongoing studies (see paragraph 1.6.3). The myocardium is often considered as a *tri-layered structure*, with circumferentially oriented fibres in the mid-wall, and oblique fibres in the inner (sub-endocardial) and outer (sub-epicardial) wall [303]. This unique fibre alignment allows for three main vectors of deformation: *longitudinal*, *radial* and *circumferential* (figure 5-19).

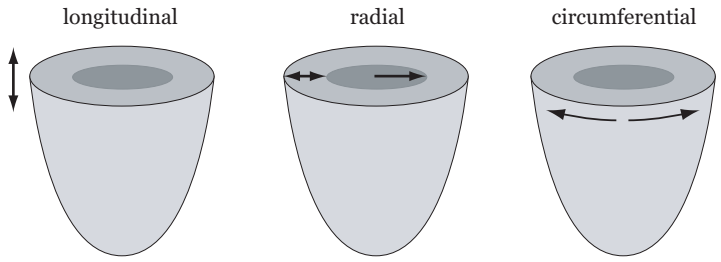

Figure 5-19: Three components of left ventricular deformation: longitudinal, radial (wall thickness and internal diameter change) and circumferential.

5.7.2 Mitral annular motion

5.7.2.1 Mechanical aspects

LV *longitudinal motion* shows a descent of the base towards the apex during systole and a biphasic reverse movement during early and late filling. The apex, on the other hand, remains virtually *stationary* throughout the heart cycle. Consequently, the LV longitudinal velocities range from zero at the apex to a maximum at the base of the LV [302].

The motion of the *mitral annulus* (i.e., the ring-like structure in the atrioventricular plane that supports the mitral valve) represents the sum of the displacements in longitudinal direction of the fibres in the LV wall. Even though the velocity profile of the basal part of the myocardial wall could equally be used to describe longitudinal motion, it appears less common in global diastolic function assessment. Similar to transmitral flow, the mitral annulus shows a *biphasic* velocity profile (figure 5-20). The two velocity waves are referred to as the E'-wave and the A'-wave, corresponding with the early (E) and late (A) transmitral filling waves.

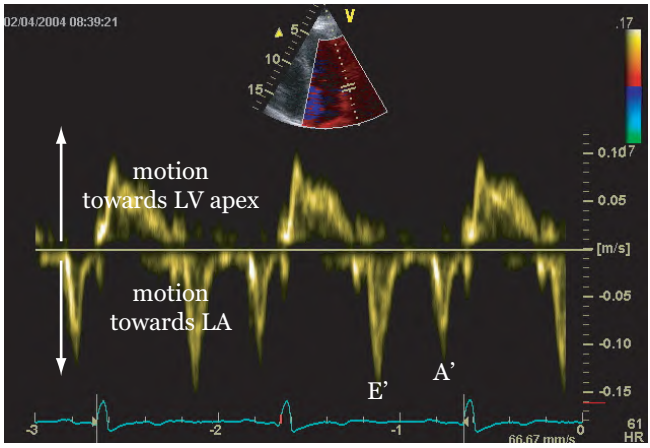

Figure 5-20: Typical biphasic tissue velocity profile during diastole recorded at the mitral annulus with tissue Doppler imaging (TDI). The tissue E'- and A'-waves correspond with the early and late transmitral flow velocities.

The concordance observed between the diastolic mitral annular velocities and transmitral flow patterns can be disrupted in various disease states. In a healthy LV, the onset of early diastolic motion is virtually *simultaneous* with the onset of mitral inflow, but its peak velocity *precedes* the peak velocity of transmitral flow [105, 115, 268]. This finding supports the concept that the upward annular motion (expansion) is not because of a passive response to the incoming blood, but that it is the result of the *elastic recoil* and promotes the flow across the mitral valve. As the blood mass needs to be accelerated, the inertial forces are responsible for the observed time delay between both peaks [105]. In normal subjects, it was also observed that mitral inflow

continues beyond mitral annular motion [143, 290], which indicates that there must be a continuing *circumferential distension* beyond ventricular lengthening [268, 290].

The annulus stays almost stationary during diastasis and moves away from the apex during LA systole, because of two different mechanisms, namely the *additional lengthening* due to ventricular passive filling, and *retraction of the atrioventricular plane* away from the apex as a result of LA contraction [115, 302].

It should be remembered that measuring mitral annular velocities does not reveal *local* ventricular wall velocities, but merely integrates all longitudinal velocities from apex to base. Using *strain rate imaging*, it was shown that the longitudinal diastolic expansion of the LV does *not* occur homogeneously over the wall. This intriguing topic is discussed in paragraph 5.7.4.

5.7.2.2 Instrumentation and image acquisition

The direction and the velocity of the mitral annulus used to be interrogated with greyscale two-dimensional and M-mode echocardiography. Nowadays, *tissue Doppler imaging* (TDI) is common, due to its high feasibility, high reproducibility and ease of application in the clinical setting. TDI allows for quantifying the velocity of the moving tissue instead of blood cells by altering the filter settings of the Doppler system (see paragraph 3.2.4). The PW Doppler modality is the preferred technique for routine assessment of diastolic function in the clinical setting [221].

TDI measurements are usually performed from the apical four-chamber view, with the sample volume situated in the septal or lateral corner of the mitral annulus (figure 5-16B) [252]. The position of the sample volumes needs to be reported in every investigation, because the septal and lateral corners of the mitral annulus move with different velocities [297]. The lateral E'-velocity may be preferred over the other because of its superior reproducibility and because it is not affected by RV diastolic function [164]. In case of local hypokinesis, possibly leading to an underestimation of global diastolic function, it is recommended to determine the *average* E'-velocity from multiple interrogated annular sites [221].

A typical diastolic biphasic TDI velocity profile, showing the E'- and A'-wave, is depicted in figure 5-20. Before the E'-wave, mono- or biphasic velocity waves can be observed, thought to be caused by LV untwisting and rapid LV shape changes [107, 320]. The amplitude of the E'- and A'-wave, as well the time delay between the onsets of the transmitral E-wave and the E'-wave can provide information about global diastolic function and filling pressures.

5.7.2.3 Amplitude of the E'- and A'-wave

Cut-off values for E' and A' corresponding with various stages of diastolic dysfunction are shown in figure 5-11. In normals, A' is nearly always *lower* than E'. Concordant with other indices of relaxation, E' gradually decreases with age [1, 268, 331].

The peak amplitude of the E'-wave (either of the mitral annulus or the myocardial basal wall) has proven to be a valid marker of LV *relaxation*, as it is closely related with τ [241-243] and $(dP/dt)_{min}$ [230].

Unlike the amplitude of the transmitral E-wave, E' is relatively *independent* of filling pressure, and, as such, tends to decrease with decreasing diastolic relaxation without showing pseudo-normalization [90, 228, 230]. The *ratio* between mitral inflow and annular velocity during early diastole (E/E') has therefore become a popular index for estimating filling pressures [227-229, 243, 265]. Based on TDI measurements on the annular septal site, Ommen et al. [243] showed that a ratio E/E' > 15 is highly specific for an elevated LAP, while a value less than 8 is indicative of LAP < 15 mmHg. E/E' ratios between 8 and 15 have been reported to be less reliable for estimating LAP. Nagueh et al. [228] demonstrated that E/E' > 10, with E' measured at the annular lateral site, reliably predicts an elevated PCWP > 12 mmHg. The use of E/E' was shown to apply well in patients with preserved EF, as well as in patients with sinus tachycardia [229], atrial fibrillation [225] and hypertrophic cardiomyopathy [224]. However, it has been observed that E' is *load-dependent* in healthy subjects with normal LV relaxation [95, 105, 230], and in patients undergoing haemodialysis [82]. E/E' cannot warrant accurate estimates of filling pressure in those conditions.

5.7.2.4 Time delay between the onsets of the E- and E'-waves

Apart from its peak amplitude, the *onset* of early mitral annular motion relative to the *onset* of early transmitral flow ($T_{E'-E}$) has been recently proposed by Rivas-Gotz et al. [265] as a novel index of relaxation. $T_{E'-E}$ is calculated by measuring the time from the QRS-peak on the ECG to the onset of the E'-wave on the TDI image, and from QRS-peak to the onset of the E-wave on the transmitral flow Doppler image, and subtracting one from the other (figure 5-21). The rationale of this concept was based on the previous observations that the peak of the E'-wave is delayed with respect to the peak of the E-wave in case of delayed relaxation [105, 129].

In an experimental animal model, $T_{E'-E}$ correlated significantly with τ [265]. Moreover, when entered into a previously reported equation $PCWP = ESV \cdot e^{-IVRT/\tau}$ [326], $T_{E'-E}$ provided a good estimate of PCWP in human subjects. This complex relationship between $T_{E'-E}$ and LAP was simplified by the same authors for use in clinical practice: $IVRT/T_{E'-E} < 2$ allowed to identify patients with LAP > 15 mmHg. The relation between relaxation and $T_{E'-E}$ was later confirmed in a study of Ruan et al. [273] which showed a considerably longer $T_{E'-E}$ is patients with impaired relaxation compared to normals.

The *clinical usefulness* of this new index has been seriously questioned in a another study by Sohn et al. [291], which was originally designed to validate the concept. In that study, no correlation between τ and $T_{E'-E}$ could be found, despite the wide range of τ. Surprisingly, in the patient with the highest τ, a simultaneous onset of the E'- and E-wave was observed. Their observations were in agreement with the results of Rodriguez et al. [268] who demonstrated that the onset of the E'-wave coincided with the onset of the E-wave in normals as well as in patients with LV hypertrophy. Therefore, Sohn et al. concluded that $IVRT/T_{E'-E}$ should not be used to estimate filling pressure because of a possible zero or negative denominator.

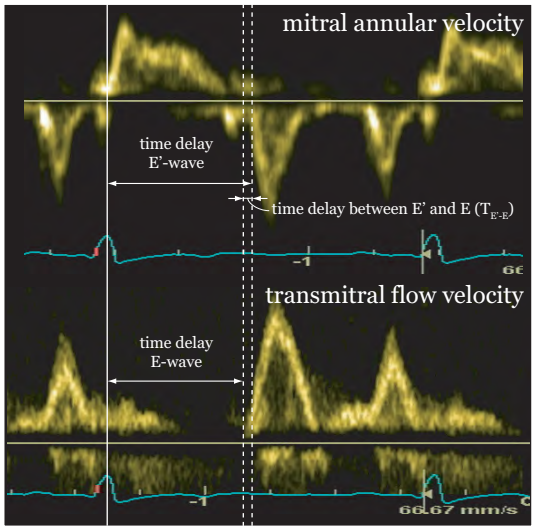

Figure 5-21: Calculation of the time delay between the onsets of the E- and the E'-wave, a potential index for LV relaxation and LA filling pressure.

The *contradictory* results convincingly show that this new index requires further study and validation before being used in a clinical setting. The reason for this significant discrepancy between the two study results may be related to the limited time resolution for detecting small time delays, and the existing variation in time delays in normal subjects.

5.7.2.5 Need for advanced numerical models

Measuring the peak amplitude of the E'-wave is one of the most *straightforward* non-invasive ultrasound-based methods for assessing relaxation, and permits detection of mechanical relaxation abnormalities with a high sensitivity. Notwithstanding its proven clinical usefulness, the precise mechanisms and timing of the longitudinal tissue velocities, in particular in relation to the timing of transmitral flow velocity waves, are still not fully understood.

Advanced numerical models that (i) incorporate fluid-structure interaction, and (ii) account for the anatomical fibre organization and the active and passive myocardial properties, would enable us to improve our insights in the relationship between left ventricular filling and tissue motion. Unfortunately, none of the currently available numerical models meet all of the abovementioned requirements.

5.7.3 Torsion imaging

5.7.3.1 Mechanical aspects

During *systole*, the LV apex rotates *anticlockwise* when viewed from the apex, whereas the base rotates *clockwise* (figure 5-22A). The untwisting begins during early relaxation, continues rapidly during IVR, and ends at the end of the transmitral E-

wave (figure 5-22A-B and figure 5-24A). The transition zone lying at about one third from the base to the apex shows virtually *no rotation* during the entire cycle and is therefore called the *equatorial* cross-section. Similar to the longitudinal elongation, the rapid untwist produces a *suction* effect that augments the LV pressure gradients, promotes early diastolic filling and, hence, contributes to diastolic function [79, 114, 220, 247].

In cardiac mechanics literature, the twisting motion of the LV about its longitudinal axis is often indicated with terms like "*rotation*", "*torsion*" or "*twist*". Although these words are interrelated, they should not be used interchangeably. Both *rotation* and *twist* are used to describe the angle of rotation of a particular cross-section (short-axis view of the myocardium), e.g., the base or the apex, during the cardiac cycle. *Torsion*, on the other hand, usually refers to the *difference* in the angles of rotation between two cross-sections. This *net rotation* or *net twist* is thus calculated as $\text{rotation}_{\text{apex}}$ - $\text{rotation}_{\text{base}}$ and is expressed in degrees (°). However, sometimes the term torsion is *also* used to refer to the net rotation *normalized* for the distance between the two cross-sections. It is then expressed in degrees per unit distance (°/mm).

The *mechanisms* behind ventricular twisting (systole) and untwisting (diastole) basically lie in the *helical myocardial fibre organization*, which shows a anticlockwise gradually varying fibre orientation from the epicardium to the endocardium, such that the transmural angle gradient spans -60° to +60° (see paragraph 1.6.3.1). This way, the spirally aligned myofibres in the wall convert *one-dimensional* fibre deformation into *global torsional deformation* [10]. It has been suggested that torsion facilitates homogeneous distribution of fibre shortening across the LV wall [9, 28]. Torsion has furthermore been proposed to be an energy-minimizing mechanism by which the LV reduces wall stress and oxygen demand [29].

Twisting and untwisting result from the *interaction* of *two counter-rotating torques* [132, 237, 267]. These torques with *opposite* sense originate from the forces developed by shortening of epicardial and endocardial myofibres. Since myofibres in the epicardial layer have a *longer lever arm* (i.e., the distance between the muscle fibre and the longitudinal central axis) to produce a *greater moment*, and since more fibres are present in an epicardial volume shell, the epicardial layer is supposed to *control* the torsion [142]. The epicardium also plays a major role in the rapid untwisting during early diastole (i.e., *torsional recoil*). Because the titin-based stiffness increases from endo- to epicardium, and because fibre shortening is distributed almost homogeneously across the wall, there is a greater restoring force in the epicardium [10].

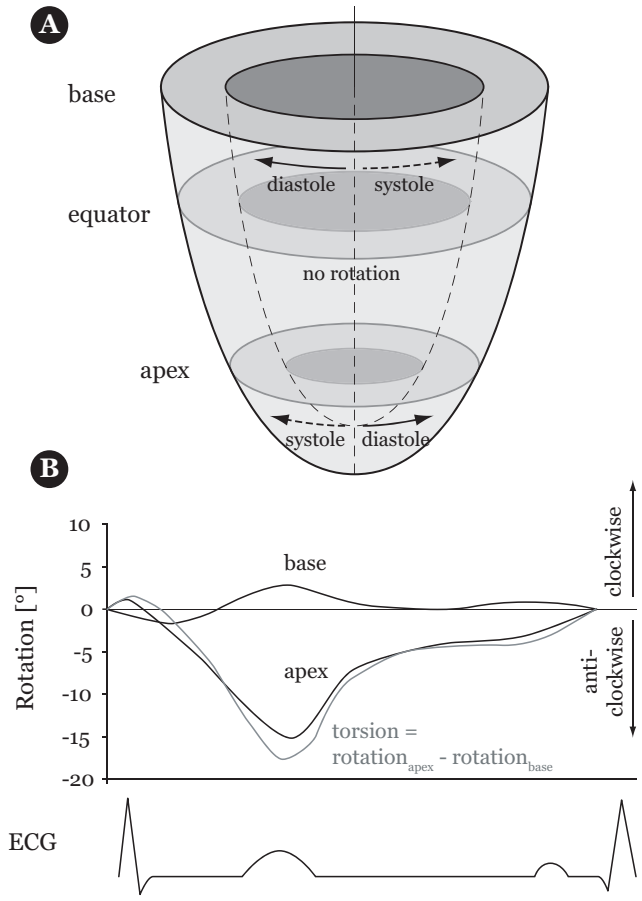

Figure 5-22: A: Visualization of basal and apical rotation during systole and diastole. The rotation at the equatorial level is virtually zero; B: Time course of basal and apical rotation (seen from the apex). Torsion is calculated as the difference between apical and basal rotation (adapted from [132]).

5.7.3.2 Data acquisition and processing

LV twisting has been previously quantified by tracking anatomic landmarks (e.g., the papillary muscle) using *two-dimensional echocardiography* [216], or by radiographic tracking of surgically implanted *myocardial markers* [141, 142]. *Sonomicrometry* (see paragraph 2.3.2) and *magnetic resonance imaging* (MRI) are now frequently used as reference techniques. Unfortunately, the former technique is limited by its invasive nature and the latter is hampered by its complexity, cost and mediocre temporal resolution, thereby precluding their use in clinical practice. *MRI tagging* is a non-invasive technique in which *tags* (i.e., non-invasive markers) are imprinted on the myocardium. These tags, usually positioned in a radial or rectangular grid, are fixed on the myocardium during systolic contraction and diastolic relaxation. The distortion of the grid combined with the displacement of the grid-crossing points reveals the deformation and displacement of the underlying myocardium [244, 360].

Currently two new non-invasive techniques, based on *tissue Doppler imaging* (TDI) and *speckle tracking imaging* (STI), permit quantification of the rotation and the rotational velocity (v_{rot}, expressed in °/s) of a LV *cross-section* over time (figure 5-23) [132, 237, 239].

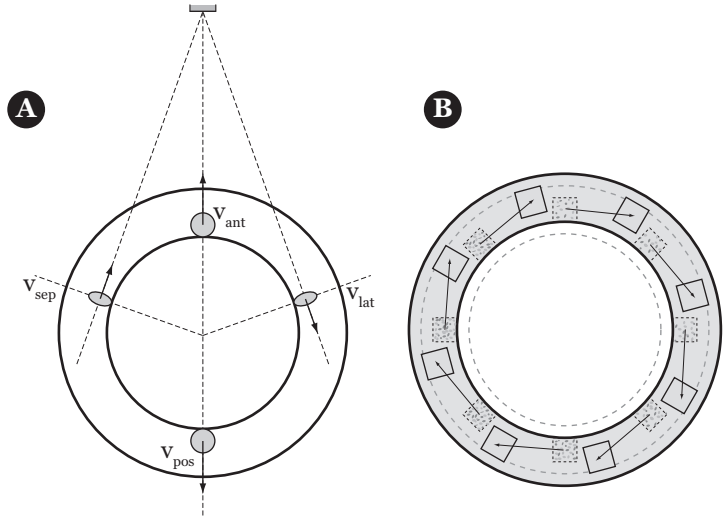

Figure 5-23: Principles of assessing ventricular rotation and torsion using tissue Doppler imaging (A) and speckle tracking imaging (B). During early diastole, the basal cross-section is expanding and rotating clockwise seen from the apex. The principles are explained in the text (v_{sep}, v_{ant}, v_{lat} and v_{pos}: septal, anterior, lateral and posterior velocity) (adapted from [237, 239]).

Notomi et al. [239] introduced the TDI velocity-based method which estimates the average rotational velocity (v_{rot}) of a cross-section by dividing the *tangential velocities* sampled at the lateral (v_{lat}) and septal (v_{sep}) wall by the time-varying *radius* of the cross-section obtained by integrating radial velocities of the anterior (v_{ant}) and posterior (v_{pos}) wall:

$$v_{rot}(t) = (v_{lat} - v_{sep})/2 \cdot r(t) \tag{5-10}$$

with

$$r(t) = r_o + \left\{ \int_o^t (v_{ant} - v_{pos})dt \right\}/2 \tag{5-11}$$

with r_o the end-diastolic radius. *Rotation* of a cross-section is obtained by temporal integration of the rotational velocity (figure 5-23A):

$$\text{rotation} = \int_o^t v_{rot}(t)dt \tag{5-12}$$

Torsion is defined as the net difference between apical and basal LV rotation:

$$\text{LV torsion} = \text{rotation}_{\text{apex}} - \text{rotation}_{\text{base}} \quad (5\text{-}13)$$

This technique has been validated in humans with MRI as the reference method [239].

Speckle tracking imaging (STI) is an alternative way to assess LV rotation using ultrasound. STI is, in contrast to TDI, *not* a Doppler application [132, 237], but instead relies on the analysis of the displacement of *speckle patterns* in the greyscale image. Speckles originate from constructive and destructive interference of ultrasound back-scattered signals from structures smaller than the wavelength of sound. These speckle formations function as *tissue markers* that are tracked from one frame to another throughout the cardiac cycle. The actual LV rotation is calculated as the average rotation of a number of selected regions of interest in the mid-myocardium (figure 5-23B). STI was shown to correlate well with TDI measurements and MRI tagging in humans [237]. Helle-Valle et al. [132] validated the principle of STI with sonomicrometry in animals and with MRI tagging in humans and found good agreements as well.

STI has the advantage over TDI that it is angle-independent. It is, however, very dependent on the greyscale image quality. Another disadvantage of STI is that *de-correlation* may occur, because of speckles disappearing from one frame to the next, as the result of *through-plane motion* [237]. Through-plane motion is most pronounced at the LV base, because this region experiences the highest longitudinal displacement.

5.7.3.3 Future clinical implications

Torsional recoil was shown to be altered in myocardial ischaemia [175, 330], cardiomyopathy [329] and aortic stenosis [10, 223, 277], suggesting its importance in normal diastolic function. Indeed, using MRI tagging, Dong et al. [79] found that the peak *velocity of torsional recoil* is closely and reproducibly related to the time constant of isovolumic relaxation and suggested that it may provide a more physiological and direct non-invasive method for quantifying relaxation than other new echocardiographic measurements. Diastolic untwisting occurs largely (40%) during IVR [239, 259], *before* the opening of the mitral valve, whereas e.g., wave propagation and mitral annular velocity measurements are performed after the opening of the mitral valve, when most of the relaxation process has already been completed. Wave propagation and mitral annular velocity measurements are thus *less sensitive* for *relaxation* and may experience some *influence of load*. More importantly, the demonstrated *preload independence* of the peak recoil velocity [79, 259] suggests that this index may not be subject to *pseudo-normalization* in situations where LAP is increased.

Neither experimental nor clinical studies aiming to find a relation between *invasive early diastolic indices* and *torsion indices* derived from the recently introduced TDI- and STI-based methods have been conducted so far. Nonetheless, both approaches sound very promising and will likely provide incremental value towards early diastolic function.

Recently, Notomi et al. [238] applied TDI-based torsion imaging, combined with CMD imaging and PW Doppler imaging to gain insights into the quantitative and temporal relation between LV torsion, IVPD and transmitral flow velocities. They found that

the peak recoil velocity precedes the peak IVPD, which itself precedes the peak E-wave (figure 5-24), and proposed a quantitative relation between the peak IVPD and peak recoil velocity. More importantly, they described the relation between the amount of *systolic LV torsion* and *IPVD*, thereby once again revealing the mechanistic connection between *systolic* events and *diastolic* (dys)function.

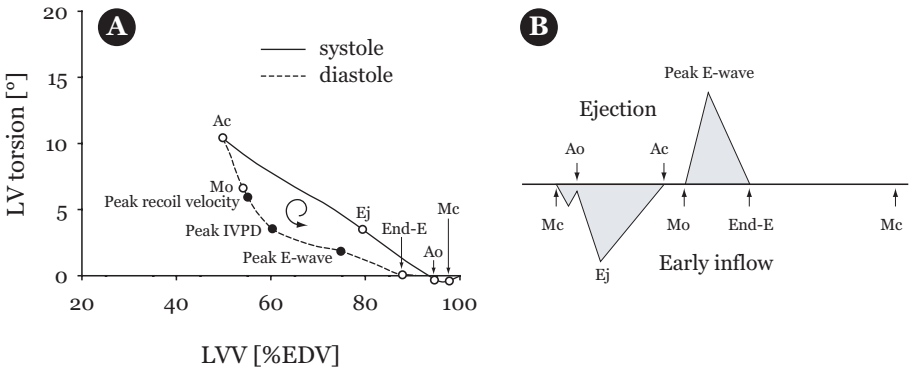

Figure 5-24: A: LV torsion-volume relation during systole and early diastole. The relation between torsion and volume during systole is virtually linear, the diastolic relation is curvilinear; B: Aortic ejection and early mitral inflow (Mo and Mc: mitral valve opening and closure, Ao and Ac: aortic valve opening and closure, Ej: peak aortic flow velocity) (adapted from [238]).

5.7.4 Strain rate imaging

Strain rate imaging (SRI) depicts the rate of myocardial deformation and enables quantification of regional myocardial function with high temporal resolution, compared to other non-invasive imaging modalities, including MR (see paragraph 3.2.4.2). Its high frame rate (> 100 FPS) makes SRI suitable for interrogating the short-lived and/or complex myocardial deformation patterns during diastole.

The main diastolic deformation of the LV occurs parallel with the early and late filling phases. Using SRI analyses, Støylen et al. [301] and Voigt et al. [346] showed that during both phases the initial lengthening of the wall starts at the base, and successively propagates as a *stretch wave* towards the more apical parts in an ordered sequence [115, 302]. The propagation velocity of this tissue elongation wave can be determined from the slope in the strain rate image, as shown in figure 5-25A. Due to quasi-incompressibility of myocardial tissue, the elongation of LV is accompanied with simultaneous *wall thinning* and an *increase in cavity diameter* (figure 5-25B) [302]. As a result, the peak velocity of the mitral annulus, measured with TDI, is determined not only by the *rate of deformation* (i.e., the local strain rate), but also by the *propagation velocity* of the stretch wave. Stated differently, when stretching of the different parts of the LV occurs less simultaneously, the peak velocity of the mitral annulus will be reduced. It was also found that the peak strain rate and propagation velocity of stretching are reduced in diastolic dysfunction [302]. These findings may add valuable information about the physiology and pathophysiology of diastole from

a mechanical point of view [302]. It should be noted, though, that TDI measurements are quicker and more practical in clinical practice.

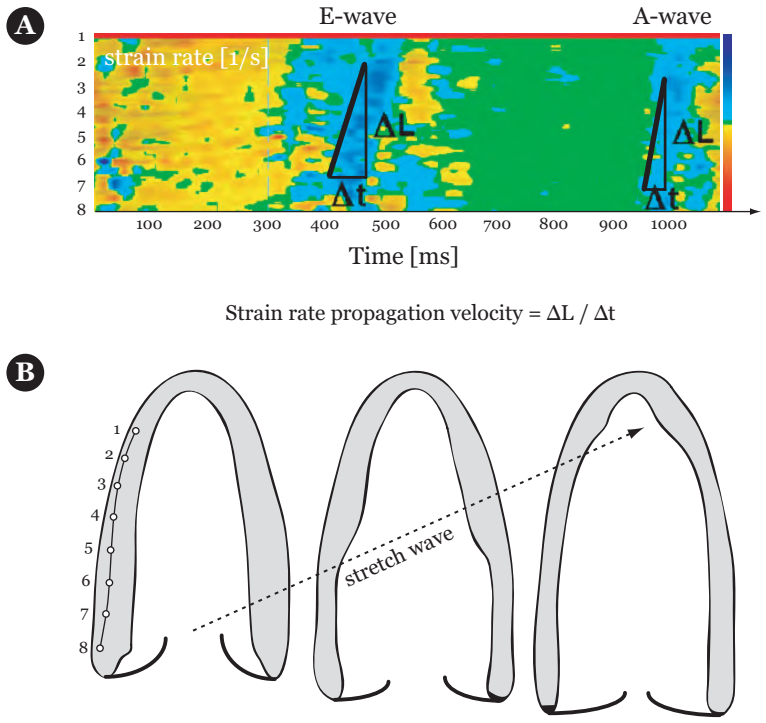

Figure 5-25: A: Yellow to red colours indicate negative strain rate (shortening during systole); blue to cyan colours correspond to positive strain rate (lengthening during diastole). The numbers to the left refer to the numbers on the two-dimensional image. The strain rate propagation velocity during early and late filling is defined as ΔL/Δt; B: The velocity profile of the mitral annulus is the result of a propagating stretch wave (adapted from [301]).

5.8 Final considerations

Diastolic function is as an important determinant of cardiac performance as is systolic function, because the LV must not only be able to *empty* but also to *fill* without a compensatory increase in LAP.

Four relatively new echocardiographic imaging modalities have been presented that offer the possibility to quantify specific *haemodynamic* and *mechanical* diastolic events, and provide incremental value to existing transmitral flow Doppler indices. All measurements are feasible with the new generation of ultrasound systems.

The usefulness of *wave propagation velocity*, derived from the spatiotemporal velocity map, is somewhat hampered by its mediocre reproducibility and by a number of possible influencing factors of which the effects remain poorly understood. Wave propagation velocity may therefore not be considered a simple index of diastolic function, but rather a composite function of more factors.

Mitral annular motion, in contrast, is much easier to interpret and has been shown to be very sensitive for diastolic relaxation abnormalities.

Non-invasive visualization of *pressure gradients* and *rotational deformation* are two relatively unexplored, but nonetheless very promising techniques. They are the latest in a long line of echocardiographic advances and will probably expand the diagnostic value of echocardiography. To exploit the knowledge about the relation between echocardiography-based indices and diastolic function, online or offline tools should be developed that allow for automatic calculation of pressure gradients and visualization of torsion [328].

It should be noted, however, that even these novel echocardiographic tools are potentially affected by a number of variables of which the mechanical impact is inadequately understood. Their contribution to the understanding of disturbances of intrinsic diastolic dysfunction can still be improved, for instance with the help of (computationally intensive) numerical LV models.

All indices are influenced to some extent by the principles of *elastic recoil*, which shows that *systolic function* is an important determinant of early diastolic events. It should also be stressed that the new techniques appear considerably *less* affected by LAP, than do the transmitral flow velocities, and thus bring us a step closer to the assessment of *intrinsic diastolic function*.

In the near future, it is likely that with the advent of real-time three-dimensional echocardiography (RT3DE), *three-dimensional counterparts* of the existing diastolic indices will be introduced and/or *new concepts* will be proposed that hold promise for multiple clinical applications. RT3DE will undeniably extend the current knowledge which is mostly obtained from interpretation and quantitative analysis of two-dimensional images acquired in specific cross-sectional planes.

At this moment, however, we consider one simple index of LV diastolic function as elusive and probably beyond the capabilities of any echocardiography-based technology.

6

Chapter 6

Modelling Myocardial Resistance: Implications for the Assessment of Fractional Flow Reserve

The contents of this chapter were published in

Biomechanics and Modeling in Mechanobiology
2004 Sep; 3(1): 48-55
Influence of Zero-Flow Pressure on Fractional Flow Reserve
Claessens TE, Van Herck PL, Matthys KS, Segers P, Vrints CJ and Verdonck PR.

6.1 Introduction

Whereas all of the previous chapters dealt with the mechanical characteristics of the heart muscle, the present chapter is about the blood vessels that nourish the heart muscle in order to fulfil its pump function: the *coronary circulation*.

First, a brief overview is provided of the basic coronary haemodynamic principles and the consequences of coronary artery disease upon blood flow to the myocardium. It permits to understand how the functional severity of a coronary artery stenosis, i.e., a local narrowing in a coronary artery, can be assessed in a catheterization laboratory using pressure and/or flow measurements. Special attention was paid to the pressure-based index *fractional flow reserve* (FFR), which expresses to what extent coronary flow is limited due to the presence of a coronary artery stenosis.

The focus of this chapter, however, lies on our simplified hydraulic model of the coronary circulation, in which we aimed to assess the influence of elevated back-pressures and varying aortic pressures upon FFR.

6.2 Coronary haemodynamics

6.2.1 Blood flow to the heart

Blood is transported to the heart via the *coronary arteries*. The large arteries that lie on the surface of the heart are called the *epicardial coronary arteries* (diameter 2 to 4 mm), while the *intramyocardial coronary arteries* lie within the myocardium (see paragraph 1.3.3 and figure 1-3).

The human heart receives about 5% of the cardiac output (or about 0.25 l/min) under baseline conditions [92]. In a healthy subject, blood flow can raise three- to fourfold when oxygen demand is increased (e.g., during exercise) [163]. Such a large increase in blood flow, accomplished by *vasodilation* of the resistance vessels, is mandatory because, unlike other muscles, oxygen extraction from blood to the heart is already *close to maximum* in baseline conditions, and thus not able to rise much further. Indeed, since oxygen consumption of an organ is equal to the product of blood flow and oxygen extraction from the blood, the only practical way to increase oxygen consumption for the heart is then to *increase blood flow* (Fick's law).

6.2.2 Phasic pressure and flow

Despite many intensive studies, the physical forces that are responsible for instantaneous coronary pressure and flow are still not fully understood [69]. The pressure-flow relation in the whole coronary circulation has shown to be extremely complex, mainly because of the *spatially inhomogeneous* and *non-linear mechanical properties of the coronary vessels*, the *smooth muscle tone* in the vessel walls, the time-varying proximal (upstream) and distal (downstream) *blood pressure*, and the temporal and transmural variation in *extravascular compressive forces* upon the intramyocardial vessels [136].

Unlike all other organs, coronary blood flow is *phasic* in nature, and occurs *predominantly in diastole*, in particular in the coronary arteries supplying the left ventricle (LV). The flow impediment to coronary flow during systole is generally thought to be the effect of myocardial contraction, during which the intramyocardial vessels are partially compressed by extravascular compressive forces, which are larger in the endocardium than in the epicardium [92]. In the coronary arteries supplying the right ventricle (RV), blood flow tends to be sustained during systole and diastole, because the intramyocardial pressure is lower (figure 6-1). In the LV, this phenomenon is generally known as *systolic flow impediment* [288], first proposed by Scaramucci in 1695 [279]. The impact of myocardial contraction upon coronary blood flow has since then been explained by means of a *systolic vascular waterfall* [80, 351], an *intramyocardial pump model* [294], and the *time-varying elastance model* (see paragraph 2.4.4) [174]. Very recently, the phasic coronary flow profile was also explained using *wave intensity analysis* [69].

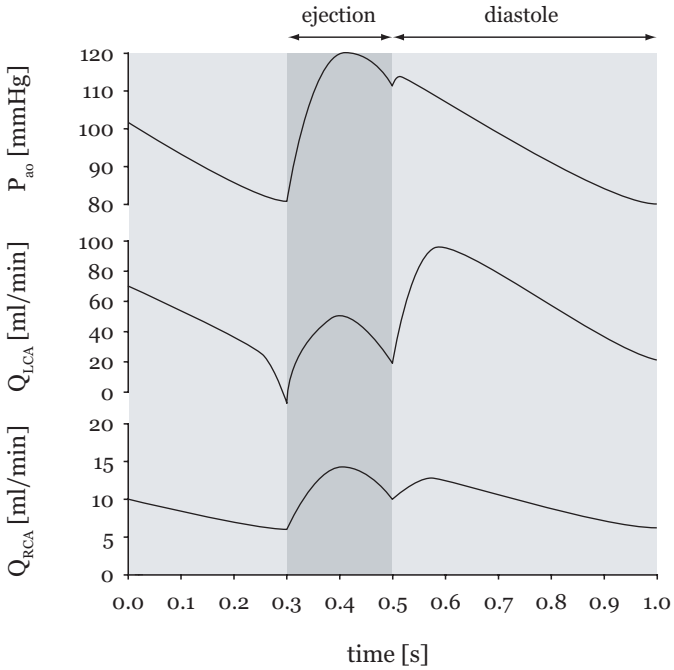

Figure 6-1: Aortic pressure (P_{ao}) and coronary flow in the left (LCA) and right (RCA) coronary arteries. Particularly in the LCA, the flow is impeded due to systolic contraction. In the RCA, blood remains sustained during systole and diastole (adapted from [25]).

While complex analyses are required to elucidate the temporal variation in coronary pressure and flow, the relation between *time-averaged* pressure and flow can be much more easily explained by the *Poiseuille equation* (equation 6-1). It states that the average flow (Q) is determined by the mean pressure at the inlet (P_i) and outlet (P_o) of the coronary circulation, and by the mean resistance of the microvascular bed (R_{myo}):

$$Q = \frac{P_i - P_o}{R_{myo}} \qquad (6\text{-}1)$$

The resistance of the epicardial coronary part, especially of the Left Anterior Descending (LAD), is considered relatively small compared to the microvascular resistance and is generally neglected. The inlet pressure in the coronary circulation is assumed to be the mean aortic pressure P_{ao}. The outlet pressure approximates central venous pressure P_v. A schematic representation of the "time-averaged" coronary artery and its depending microvascular bed is depicted in figure 6-2.

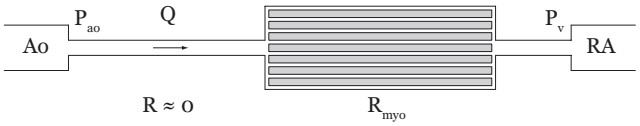

Figure 6-2: Schematic representation of an epicardial coronary artery and its depending microvascular bed (P_{ao}: aortic pressure, P_v: venous pressure, Ao: aorta, RA: right atrium, Q: coronary flow, R_{myo}: myocardial resistance, R: resistance of epicardial coronary artery).

6.2.3 Metabolic and autoregulation

The resistance vessels (less than 350 µm in diameter) of the coronary circulation are responsible for two important physiological phenomena: *metabolic regulation* and *autoregulation* (figure 6-3) [64]. Although metabolic regulation and autoregulation are defined separately, both are probably the result of the same feedback mechanism [195].

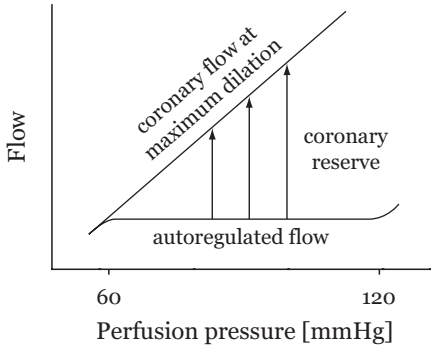

Figure 6-3: The sigmoid line (resting coronary blood flow) characterizes the autoregulatory capacity of the coronary circulation between 60 and 120 mmHg. The solid line represents the maximum achievable flow as a linear function of perfusion pressure. The ratio between maximum achievable flow and resting flow is referred to as coronary reserve (adapted from [64]).

Autoregulation describes a phenomenon that is common to many organs: it is the intrinsic tendency of an organ to *maintain virtually constant blood flow* (and oxygen delivery) despite *changes in arterial perfusion pressure* [136]. It is accomplished by adjusting *vascular resistance* appropriately to match blood flow needs. For example,

at a given level of cardiac work, a reduction in perfusion pressure is counterbalanced by a decrease in resistance, thereby maintaining blood flow. Conversely, if perfusion pressure increases, resistance increases to maintain relatively constant coronary blood flow. This autoregulatory "*plateau*" occurs between approximately 60 and 120 mmHg perfusion pressure. Autoregulation can be studied in all organs, except in the LV, by raising P_{ao} and then measuring flow. In the LV, an increase in P_{ao} increases LV work, which causes myocardial blood flow to increase. If one wants to assess the autoregulating capacity of the coronary circulation, the coronary artery must be *cannulated* so that perfusion pressure can be varied while P_{ao} remains constant [136].

Metabolic regulation refers to the variation in coronary blood flow with metabolic demand of the myocardium and is also accomplished by the resistance vessels. During maximal exercise or after administration of pharmacological agents, such as papaverine or adenosine, the resistance vessels will fully dilate, so that blood flow maximizes and becomes linearly dependent on perfusion pressure. This condition is also referred to as *hyperaemic flow*. The ratio between hyperaemic and resting blood flow is called the *coronary flow reserve*.

6.3 Coronary artery disease

6.3.1 Coronary artery stenosis

The most common cause of coronary artery disease is *atherosclerosis,* one of the leading causes of illness and death in most Western countries [165]. Atherosclerosis is a chronic, progressive disease of the epicardial arteries in which *plaques,* made up of fatty substances, cholesterol, cellular wastes, calcium and the blood-clotting protein fibrin, develop on the inner lining of the arteries. These plaques cause a gradual, progressive narrowing of the lumen of the artery, and make blood flow through the artery more difficult. A *local* deposit of plaque is referred to as a *coronary artery stenosis*.

One of the first symptoms of coronary artery disease is *angina (pectoris),* an intense pain felt behind the breastbone, caused by an imbalance between oxygen demand and oxygen supply. The latter condition, also referred to as *ischaemia*, is the result of a reduced blood flow to the heart (see infra). *Stable* angina occurs when the pain is brought on by a predictable amount of work and stops when there is reduced demand on the heart. With *unstable* angina, however, the pain can come without a specific reason, and it may leave just as unpredictably.

A *myocardial infarction*, or "*heart attack"*, caused by a sudden rupture of an atherosclerotic plaque and subsequent blocking of the coronary artery, leads to death of cardiac muscle. The consequences of a myocardial infarction depend largely on how much cardiac muscle has become necrotic.

6.3.2 Haemodynamic effect of a stenosis

Several fundamental principles of the haemodynamic effects of a coronary stenosis need to be explained to understand the rationale behind the functional indices outlined paragraph 6.4.2.

A coronary artery stenosis causes an *additional resistance* to flow in series with the microvascular resistance so that *perfusion pressure* to the myocardium is lowered. The stenosis resistance is directly related to the morphologic features of the stenosis. In order to maintain blood flow at a level that is sufficient for myocardial oxygen demand in resting conditions, the distal resistance vessels will dilate, thanks to the autoregulating capacity of the coronary circulation. However, in this setting, maximum achievable blood flow (e.g., during exercise) will be limited because the distal vessels are already using part of their vasodilatory capacity in resting conditions. We then say that *coronary reserve*, defined as the capacity of the coronary vasculature to increase blood flow in response to hyperemic stimulation, is *reduced* because of the presence of a stenosis. The narrower the lesion, the lower the coronary reserve, because the ability of the resistance vessels to dilate is further limited [162].

Collateral vessels, i.e., pre-existing vessels that normally have little or no blood flow, can play a significant role in supplying oxygen to the heart, particularly when oxygen supply is limited due to a stenosis or occlusion of epicardial arteries. Collateral vessels allow blood to flow around the stenosed artery to another artery nearby or to the same artery past the stenosis, protecting the cardiac tissue from injury.

6.3.3 Treating coronary artery disease

Coronary artery disease can be controlled with a combination of *changes in lifestyle* and various *drugs*, which either dilate the blood vessels, lower blood pressure, or slow down the heart rhythm.

However, *surgical* and *non-surgical interventions* exist to effectively unblock the coronary artery and improve blood flow to the heart. This can be accomplished by *percutaneous transluminal coronary angioplasty* (PTCA), *stenting*, *atherectomy* or *coronary artery bypass grafting* (CABG). In PTCA, a small balloon attached to a catheter is inserted in the coronary artery and inflated in the narrowed section to open up the blockage. The catheter is removed when the lumen area is restored. Coronary stenting is a procedure that usually follows a balloon angioplasty. During stenting, a wire mesh tube is placed in the coronary artery to keep the artery expanded. Some stents are drug-coated (drug-eluting stents) to avoid restenosis of the coronary artery. Atherectomy is a technique which mechanically removes plaque from the arteries either by pushing a cutting device against the blockage or by grinding the material blocking the artery. One may also perform a CABG, a surgical operation during which one or more narrowed or closed coronary arteries are bypassed using the left or right thoracic internal artery, the great saphenous vein from the leg, or the radial artery from the forearm. It is performed in particular in cases of severe angina that do not respond to other treatment.

6.4 Assessment of stenosis severity

6.4.1 Imaging

To assess the severity and extent of coronary artery disease, patients are often referred for *coronary angiography*. Coronary angiography is a procedure in which a

radiopaque dye that can be seen using *x-ray* equipment is injected into one of the coronary arteries. The obtained x-ray motion pictures, called *angiograms* (figure 6-4A), allow the angiographer to view the exact site of the narrowing and to estimate its severity, and allow the surgeon to locate where treatment should be performed [4]. However, because angiography only depicts the complex coronary cross-sectional anatomy from a *planar two-dimensional image* of the contrast-filled vessel lumen, its capability to assess the *haemodynamic effect* on coronary blood flow is limited, in particular in case of complex plaque morphology, lesion eccentricity and irregularities of the segment adjacent to the lesion [126]. These well-recognized limitations have been documented repeatedly by intravascular ultrasound (IVUS) imaging and ischaemia stress testing [2, 333]. Additionally, it only has a mediocre spatial resolution, which renders structural features smaller than about 0.2 mm invisible to the angiographer.

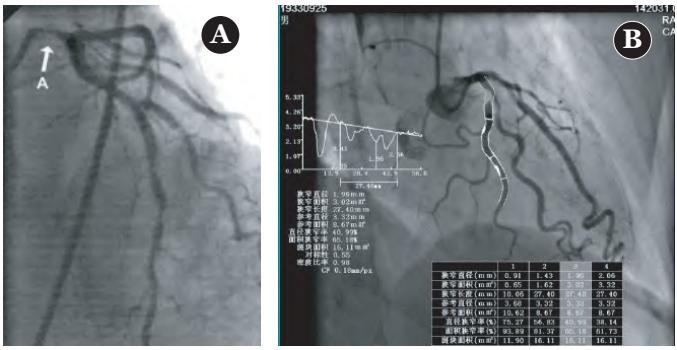

Figure 6-4: A: Coronary angiograph showing a critically severe stenosis in the left main coronary artery; B: Automated assessment of stenosis severity using quantitative coronary angiography (QCA).

Quantitative coronary angiography (QCA), originally described by Brown et al. [40], was intended to replace the "eyeball" interpretation of the angiogram with a technique that permits objective and automated detection of the boundaries of the stenosis, interpolation of the expected dimensions of the coronary vessel at the point of obstruction, and angiographically derived estimation of atheromatous plaque size (figure 6-4B) [86]. Even though QCA is more unbiased and reproducible than “visual” coronary angiography, QCA possesses virtually all of the other limitations of conventional interpretation methods.

6.4.2 Functional indices

6.4.2.1 Functional stenosis severity

While coronary angiography presently remains the *cornerstone* of the assessment of coronary stenoses [195], visual appreciation of intermediate coronary lesions does not always reflect their *functional severity* (i.e., the extent to which the stenosis affects the myocardial pressure-flow relation) for reasons outlined in the previous paragraph. A stenosis is considered *functionally significant* if it is able to limit

maximum achievable blood flow to such a degree that ischaemia of myocardial tissue supplied by that particular stenotic artery can be induced if the patient is sufficiently stressed [255].

To complement coronary angiography, two indices have been proposed that more objectively reflect the haemodynamic impact of the epicardial stenosis upon the myocardial blood flow: *coronary flow reserve* (CFR) and *fractional flow reserve* (FFR). Within the last few years, technology has advanced such that, in patients undergoing coronary angiography, these indices can be safely measured using intracoronary wires carrying Doppler and pressure transducers [64, 162]. To measure CFR and FFR, maximum coronary blood flow must be obtained without performing physical exercise. This condition can be achieved with pharmacological agents, such as intracoronary or intravenous adenosine, or intracoronary papaverine [163].

6.4.2.2 Coronary flow reserve

In 1974, Gould et al. [122] introduced the concept of *coronary flow reserve* (CFR) to assess the functional severity of a coronary artery stenosis. CFR is calculated as the ratio of *hyperaemic flow* to *resting flow* for a given coronary artery (figure 6-5):

$$\mathrm{CFR} = \frac{\text{hyperaemic flow}}{\text{resting flow}} \tag{6-2}$$

It follows from 6.3.2 that CFR will decrease when stenosis severity increases. Later, in 1990, he used Doppler ultrasound scanning techniques to measure intracoronary flow velocities (which were assumed proportional to flow) to introduce *coronary flow velocity reserve* (CVR) as a surrogate index for CFR. A cut-off value of 2.0 was found to define a functionally significant stenosis [215].

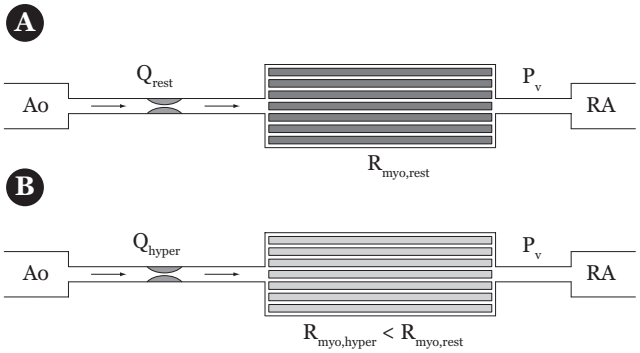

Figure 6-5: Schematic representation of a stenosed coronary artery in series with its dependent microvasculature to explain the rationale behind the concept of coronary flow velocity reserve (CVR). A: Resting (basal) flow; B: In hyperaemic conditions, flow increases because of the reduced microvascular resistance.

Unfortunately, as CVR reflects the haemodynamic impact of both the *epicardial stenosis* and the *microvascular resistance* on limiting hyperaemic blood flow, an abnormal CVR cannot differentiate which of the two components is responsible for

flow impairment (figure 6-5). This can be an issue in conditions that are known to affect microvascular resistance independent of the stenosis resistance, such as age, LV hypertrophy, diabetes mellitus, and myocardial infarction [209]. Note also that CFR can be altered by changes in either basal or hyperaemic flow, which are influenced by physiological changes in heart rate, blood pressure and contractility often occurring during coronary catheterization [163, 256]. In this sense, CVR should not be regarded as a stenosis-specific index [256, 269].

To eliminate the impact of these confounding factors, another index has been proposed, the *relative coronary flow velocity reserve* (rCVR), which scales the CVR of the interrogated vessel to an adjacent angiographically normal reference vessel [121]. It is defined as

$$\mathrm{rCVR} = \frac{\mathrm{CVR}_{\text{stenosed vessel}}}{\mathrm{CVR}_{\text{normal vessel}}} \tag{6-3}$$

The normal range for rCVR is 0.8 to 1.0 [20, 85]. From a theoretical point of view, rCVR should provide a more stenosis-specific quantification of flow impairment [121]. However, rCVR cannot be used in patients with three-vessel coronary disease who have no suitable nondiseased reference vessel. Moreover, its assessment requires that the haemodynamic and microcirculatory abnormalities affect the different regions of the myocardium to the same degree. This condition is not fulfilled in case of myocardial infarction or LV regional dysfunction, where the assumption of a uniform microvascular circulatory response does not apply. rCVR has therefore not enjoyed widespread use [163].

6.4.2.3 Fractional flow reserve

In the early 1990's, Pijls and de Bruyne et al. [71, 72, 255, 256] introduced *fractional flow reserve* (FFR) as a novel and stenosis-specific index of stenosis severity. The concept of FFR was based on the idea of Young et al. [361], who suggested that the severity of a stenosis should be defined in terms of its effect on *maximal flow*.

FFR is defined as the *fraction* of hyperaemic flow to the myocardium in the presence of a stenosis (Q_S) to the *theoretical normal hyperaemic flow* in the same myocardial bed without a stenosis (Q_N):

$$\mathrm{FFR} = \frac{Q_S}{Q_N} \tag{6-4}$$

It thus represents the fraction of the normal maximal myocardial flow that can be achieved despite the presence of a coronary artery stenosis. For example, if FFR equals 0.6 as a result of a stenosis, maximum myocardial flow is only 60% of what it could be without the stenosis [163]. The range of FFR is from approximately 0.25 (total occlusion) to 1.0 (completely normal artery).

Using a *simplified model* of a stenosed coronary artery and myocardial vascular bed (figure 6-6), it was shown that FFR can be estimated from pressure measurements in the aorta (P_{ao}) and distal to the stenosis (P_{dis}), measured in hyperaemic conditions [256]. Assuming that the resistance (R_{myo}) against blood flow caused by the myocardium is *linear* and *minimal* during hyperaemia, and that venous pressure (P_v)

equals the *back-pressure* opposing coronary flow, the flow through the hypothetical healthy coronary artery (Q_N) and the flow through the stenosed artery (Q_S) can be expressed as:

$$Q_N = \frac{P_{ao} - P_v}{R_{myo,N}} \text{ and } Q_S = \frac{P_{dis} - P_v}{R_{myo,S}} \tag{6-5}$$

where $R_{myo,S}$ and $R_{myo,N}$ represent the myocardial resistances in the stenosed and healthy microvascular bed, respectively. Provided that $R_{myo,S}$ and $R_{myo,N}$ are equal, equation 6-4 yields

$$FFR = \frac{Q_S}{Q_N} = \frac{\frac{P_{ao} - P_v}{R_{myo,S}}}{\frac{P_{dis} - P_v}{R_{myo,N}}} = \frac{P_{dis} - P_v}{P_{ao} - P_v} \tag{6-6}$$

Further assuming that P_v is small compared to P_{dis} and P_{ao}, FFR can be simply estimated as

$$FFR \approx \frac{P_{dis}}{P_{ao}} \tag{6-7}$$

So, under several assumptions, it appears that FFR can be easily estimated during maximal vasodilation from the ratio of the *mean coronary artery pressure distal to the stenosis* (P_{dis}), and the *mean aortic pressure* (P_{ao}), both during diagnostic and interventional procedures.

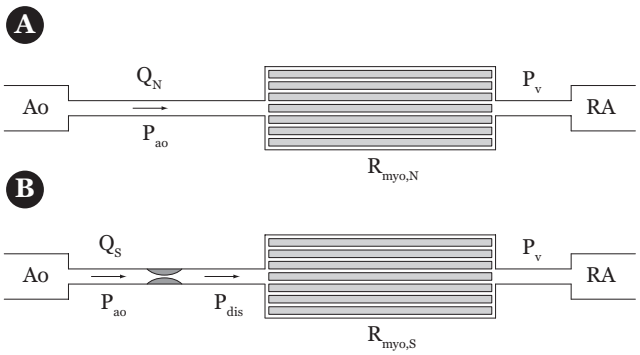

Figure 6-6: Schematic representation of a stenosed coronary artery in series with its dependent microvasculature to explain the rationale behind the concept of fractional flow reserve (FFR). A: Coronary flow in the hypothetical healthy artery; B: Coronary flow in the actual stenotic artery.

Pijls et al. [256] validated the pressure-derived FFR (equation 6-7) against the flow-derived FFR (equation 6-4) in a dog model using a Doppler ultrasound scanning flow probe, and reported close correlations. Later, a landmark study demonstrated that FFR < 0.75 correlated with *non-invasively defined ischaemia* (i.e., indicated by positive results on dobutamine echocardiography, thallium scintigraphy or bicycle

exercise testing) in patients with stable angina and single-vessel disease [253]. The established cut-off value of 0.75 implies that the stenosis is considered significant when P_{dis} < 75% of P_{ao} during maximum hyperaemia. A clinical example of an FFR assessment using pressure measurements is shown in figure 6-7.

The reproducibility of FFR with moderate haemodynamic manipulations was found to be robust in patients with single-vessel coronary artery disease and normal ventricles [72]. FFR was therefore considered a *very stenosis-specific* index, *independent of baseline haemodynamics*, *microvascular resistance*, and with an unequivocal *normal value of 1* [72]. Because of these advantages, FFR rapidly developed into a frequently used index to identify clinically relevant stenoses and to serve as a basis for evaluating the success of coronary interventions [91, 207].

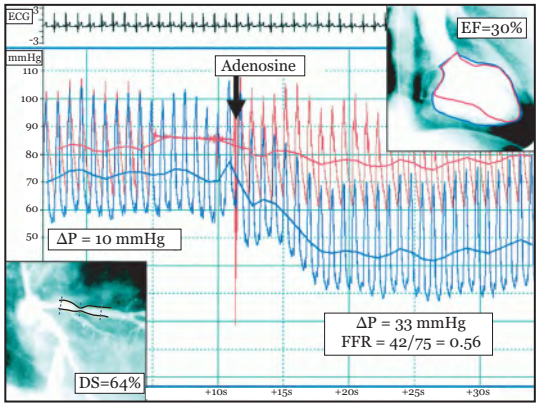

Figure 6-7: Example of a FFR measurement in the catheterization laboratory. After infusion of adenosine, the true functional severity of the coronary artery stenosis is revealed. FFR is simply quantified as the ratio of P_{dis} to P_{ao} (adapted from [73]).

Despite the proven clinical usefulness of FFR, the back-pressure opposing coronary flow that is used in the formula for FFR remains subject of debate. If P_v is the actual back-pressure in the coronary circulation, it can indeed be neglected. However, it has been argued that a so-called *zero-flow pressure*, P_{zf}, which is considerably higher than P_v, should be accounted for. By disregarding P_{zf}, one would *underestimate* the actual impediment to flow that a stenosis and its microvasculature present. The influence of P_{zf} on FFR is analyzed in detail using a *simplified hydraulic model of the coronary circulation* in paragraph 6.6.

The existence of a positive P_{zf} is not the only potential limitation of FFR. Critics have argued that FFR cannot be a stenosis-specific index from a theoretical point of view, and stated that a full understanding of the patient's coronary artery stenosis severity still requires the definition of *both epicardial stenosis* and *myocardial resistance* to flow [213, 214, 287]. Indeed, as the stenosis pressure drop depends on flow across a stenosis, which is determined by both the myocardial and epicardial stenosis resistance, FFR is also influenced by the myocardial resistance.

6.5 Zero-flow pressure

6.5.1 Pressure-flow relations in collapsible tubes

In a classic Poiseuille flow, an increase in flow through a *rigid tube* is accompanied by a proportional increase in pressure drop between the *inlet* (P_i) and *outlet* pressure (P_o). However, the relation between pressure and flow becomes more complex in case of *collapsible tubes* where *surrounding pressure* (P_S) may become higher than P_o (figure 6-8).

As long as P_i is below P_S, there will be no flow (Q = 0) because the whole tube collapses along its length. When P_S is below P_o, the collapsible tube acts like a rigid tube in which Poiseuille's law is applicable (figure 6-8A). If, on the other hand, P_S is higher than P_i but lower than P_o, pressure close to the end of the tube would be lower than P_S, and the vessel must close with cessation of flow. If flow ceases, the pressure inside the tube must rise above P_S, and the vessel must open. Yet, if the tube opens, the pressure towards the end of the tube must be close to P_o, which is again below P_S.

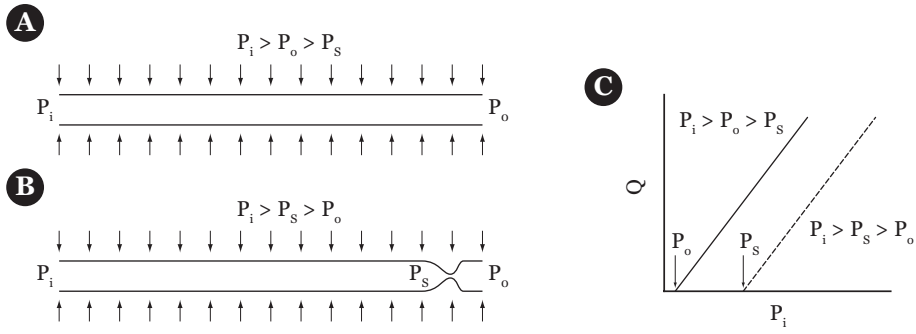

Figure 6-8: Schematic representation of a typical waterfall phenomenon. A: Collapsible tube when surrounding pressure P_S is lower than outflow pressure (P_o): no waterfall will occur; B: Surrounding pressure is above P_o, such that a local collapse occurs and flow is regulated by inflow (P_i) and surrounding pressure; C: Pressure-flow diagrams corresponding with conditions A and B.

This paradox was already described in 1912 by Knowlton and Starling [170]. What actually happens in this configuration is that the tube will collapse *locally* so that the pressure inside the tube just proximal to the collapse equals P_S (figure 6-8B). Under these circumstances, Q is determined by the tube resistance R, and the pressure difference between P_i and P_S. Hence, Q will become *unrelated* to P_o. These pressure-flow characteristics led to the use of the analogy with a *waterfall*: changes of pressure (water level) below a waterfall do not affect the flow of water over the fall. The pressure drop across the local collapse is then referred to as the *height* of the waterfall. To summarize, there are *three possible flow conditions* in collapsible tubes [136]:

- $Q = 0$ for $P_S > P_i > P_o$ (no flow)
- $Q = (P_i - P_o)/R$ for $P_i > P_o > P_S$ (Poiseuille flow)
- $Q = (P_i - P_S)/R$ for $P_i > P_S > P_o$ (hydraulic waterfall)

Note that in the third equation, R is the resistance of the *fully open tube segment*, which is only slightly shorter than the tube itself. So the Poiseuille equation still holds for flow through the tube up to the location of the vascular waterfall, provided that the proper driving pressure is applied, i.e., P_i-P_S instead of P_i-P_o [251]. The pressure-flow relation in the tube is thus shifted to the right (figure 6-8C), showing an intercept P_S with the pressure-axis. The effect of the narrowed portion of the tube, which is small compared to the total length of the tube, is accounted for by substituting P_S for P_o, so that it acts as a *back-pressure* for flow in the tube.

6.5.2 The vascular waterfall

The existence of vascular waterfalls (in series as well as in parallel) as described in the previous paragraph has been reported in many body parts, such as the lungs, the brain and the liver [136]. The mechanism behind vascular waterfalls was originally explained in 1954 by Burton et al. [49], who stated that partial closure of arterioles by *active smooth muscle tone* would cause cessation of flow when transmural pressure dropped below a *critical closing pressure*. However, several arguments against vessel closure due to tone were reported [136].

In 1978, Bellamy [22] performed coronary pressure-flow measurements in *dilated* arteries during *prolonged diastoles*, when tissue pressures are relatively low and unchanging. He was interested in particular in the shape of the pressure-flow relations and their intercepts with the pressure-axis, and found that coronary flow *ceases* even if P_{ao} is higher than P_v. The reported zero-flow pressure P_{zf} has been interpreted as a *back-pressure* to flow that could represent the existence of a *vascular waterfall*, caused by *extravascular tissue pressure* (P_S) working on the outside of collapsible vessels during diastole.

From a mechanical point of view, the effect of active smooth muscle tone and extravascular tissue pressure is comparable, as shown by Permut and Riley [251]. Both phenomena can be modelled by a pressure-flow relation at the end of a collapsible vessel as in figure 6-8C when the inward-acting pressure, whether due to external forces or active tone, is greater than the outflow pressure [251].

A number of *other potential mechanisms* have been suggested in literature that may explain flow cessation even when P_{ao} is well above P_v. They will be briefly touched upon in paragraph 6.6.5.

6.6 Impact of P_{zf} on fractional flow reserve

6.6.1 Introduction

Pijls and De Bruyne [257] suggested that FFR could be relatively easily estimated using mean aortic pressure (P_{ao}) and mean pressure distal to a stenosis (P_{dis}) during hyperaemia, under the assumption that the negligible venous pressure P_v is the back-pressure in the coronary circulation (equation 6-7). However, for several reasons outlined in the previous paragraph, it would be more appropriate to use the zero-flow pressure P_{zf} in the formula for FFR, irrespective of the actual mechanism behind it. The correct expression for the pressure-derived FFR would then be

$$FFR_c = \frac{P_{dis} - P_{zf}}{P_{ao} - P_{zf}} \quad (6\text{-}8)$$

In recent years, we have used a hydraulic bench model of the epicardial coronary vessels to study (epicardial) coronary haemodynamics in general and FFR in particular [281]. We used this type of model first to validate the concept of FFR, and later to demonstrate the insensitivity of FFR to detect suboptimal stent deployment, a finding that has been confirmed in clinical studies [91, 207, 281]. Although the latter model incorporated the phasic character of coronary blood flow (i.e., myocardial perfusion primarily occurring in diastole), the myocardial resistance model was still simple and the measured epicardial pressure-flow relationships did not take into account the existence of a P_{zf}.

In this investigation, we first presented a modification of our hydraulic bench resistance model that allows us to incorporate an easily adjustable P_{zf}, yielding coronary pressure-flow relations better matching coronary physiology. To achieve this, we applied the concept of the waterfall model (see paragraph 6.6.2). Secondly, in analogy with a mathematical study by Siebes et al. [287], which was conducted at the same time as we did our hydraulic study, it was studied to what extent disregarding P_{zf} overestimates P_{dis}/P_{ao} and how this relates to the level of P_{ao} (see paragraph 6.6.3).

6.6.2 Experimental validation of the waterfall effect

6.6.2.1 Model description

The constructed model of the *myocardial microcirculation* (figure 6-9A) represents a vessel path in an *average layer* in the myocardial wall. Basically, it was made of a *silicon tube* (diameter 2 mm, total length of 45 cm) embedded in a Plexiglas chamber containing *four separate compartments*. All compartments were sealed and connected to *external water columns* generating surrounding pressures (P_S) to mimic extravascular tissue pressures in the myocardium. The myocardial resistance model (c) was supplied from an *upstream reservoir* (a) at a constant, but adjustable level (range 0 mmHg - 70 mmHg) to generate different flow levels (figure 6-9B). The *outflow pressure* equalled atmospheric pressure (d). In each compartment, different surrounding pressures were applied, further referred to as P_{S1} - P_{S4}.

Ten different *surrounding pressure configurations* (C_1 - C_{10}) were studied (table 6-1). In the first configuration, C_1, there were *no* surrounding pressures. In configurations C_2 - C_4, we assumed a *homogeneous* P_S over the whole vessel path. Accordingly, the water level in each of the water columns was identical. Configurations C_5 - C_7 were similar to the previous three configurations, except for the most downstream region, where no surrounding pressure is used. In the last three configurations (C_8 - C_{10}), we used a low P_{S4} in the most downstream region. P_{S1}, P_{S2} and P_{S3} were chosen arbitrarily.

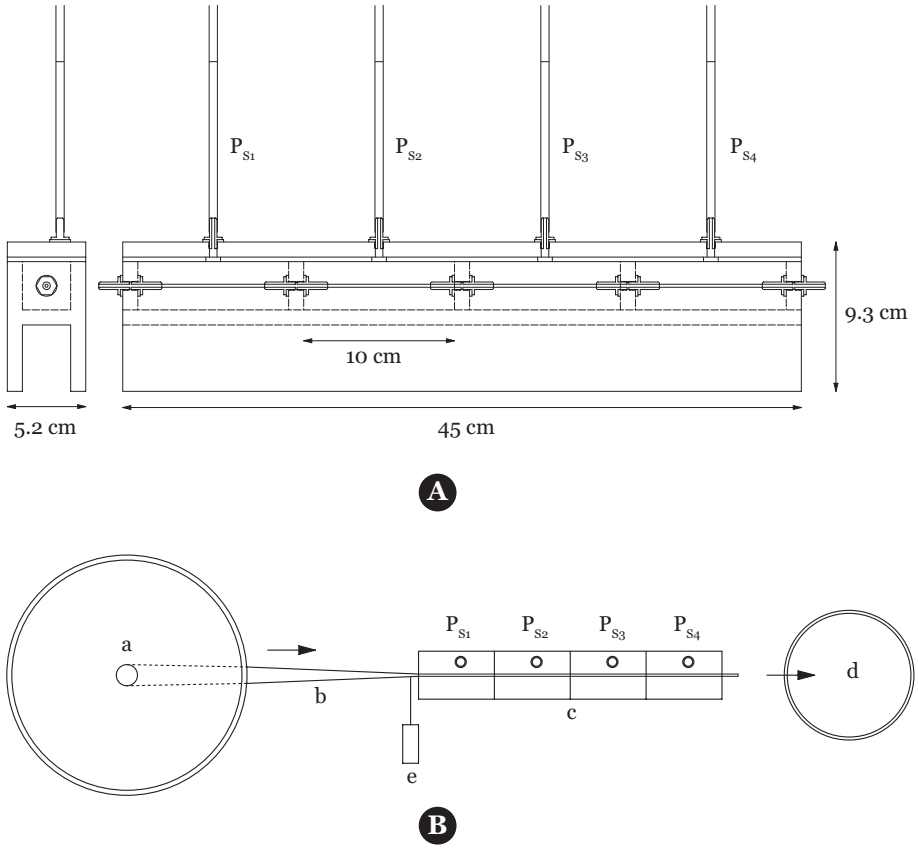

Figure 6-9: A: Myocardial resistance model representing a vessel path in an average layer in the myocardial wall. The model consists of four small diameter (2 mm) silicon tubes embedded in four different Perspex compartments in which surrounding pressures (P_S) can be created by means of external water columns; B: Schematic representation of the first experimental setup to assess the hydraulic characteristics of the myocardial resistance model (c). The model is supplied by water originating from a reservoir at a constant pressure level (a) by means of a tube (b). Outflow pressure is atmospheric pressure (d). Driving pressure is measured proximal to the model with a pressure sensor (e). Ten different surrounding pressure configurations were tested. A configuration is a specific combination of four pressures, P_{S1} - P_{S4}, imposed by means of water columns connected to the four compartments of the resistance model.

6.6.2.2 Measurement protocol

Pressures were measured 3 cm proximal (P_{ao}) to the model of the microcirculation using epidural catheters (e) directly connected to a piezoelectric transducer (Datex-Ohmeda, Helsinki, Finland). The signal was sampled at 200 Hz during 5 s using a custom-written acquisition program in Labview (National Instruments, Austin, TX, USA). Flow was measured in a volumetric way at the distal end of the system (d). In these experiments, the generated flow conditions were steady state.

Table 6-1: Surrounding pressure configurations and measured P_{zf}-values.

Configuration	P_{S1}	P_{S2}	P_{S3}	P_{S4}	P_{zf}
	mmHg				
C_1	0	0	0	0	0
C_2	18	18	18	18	17
C_3	37	37	37	37	34
C_4	55	55	55	55	53
C_5	18	18	18	0	17
C_6	37	37	37	0	34
C_7	55	55	55	0	49
C_8	18	37	37	18	34
C_9	37	37	37	18	34
C_{10}	18	37	55	18	49

P_{S1} - P_{S4} are the surrounding pressures in the respective compartments. The configurations are referred to as C_1 - C_{10}. The measured P_{zf}-values are shown in the last column.

6.6.2.3 Evaluation of the resistance model

The pressure-flow relations measured in the myocardial resistance model in steady state conditions are displayed in figure 6-10. In appendix 6.8, it is shown stepwise in a theoretical model how one can calculate pressure and flow and find out why and where hydraulic waterfalls occur. Measured P_{zf}-values for the 10 combinations are shown in the last column of table 6-1. In all surrounding pressure configurations, the intercept with the pressure-axis (P_{zf}) slightly underestimated the highest P_S in the compartments. The difference between the pressure intercept (P_{zf}) and the value of P_S can be explained by the fact that the used silicon tubes, which have a very low bending stiffness, sustain a possible collapse in case of a small positive transmural pressure. The curves were linear in a large interval, but the resistance started to decrease at relatively low flows. The observed non-linearity in the pressure-flow relations is probably due to the narrow passageways between two compartments, acting like flow obstructing stenoses. According to Poiseuille's law, the resistance of the silicon tube would theoretically be

$$R = \frac{8 \cdot \mu \cdot L}{\pi \cdot r^4} = 0.143\,\text{mmHg/ml/min} \qquad (6\text{-}9)$$

with dynamic viscosity μ = 1.002 mPa.s, tube length L = 450 mm, tube radius r = 1 mm.

Given the observation that P_{zf} is only determined by the absolute value of the highest surrounding pressure applied — and not by the position where this pressure was exerted — it is justified to use only one compartment for mimicking the extravascular pressures for the second part of the study (see paragraph 6.6.3). The second

compartment will be used for this purpose. Also, in order to reduce the resistance distal to the waterfall site (and to allow us to simulate realistic flow levels for normal levels of P_{ao}), the diameter of the silicon tube in compartments 3 and 4 will be increased to 3.5 mm.

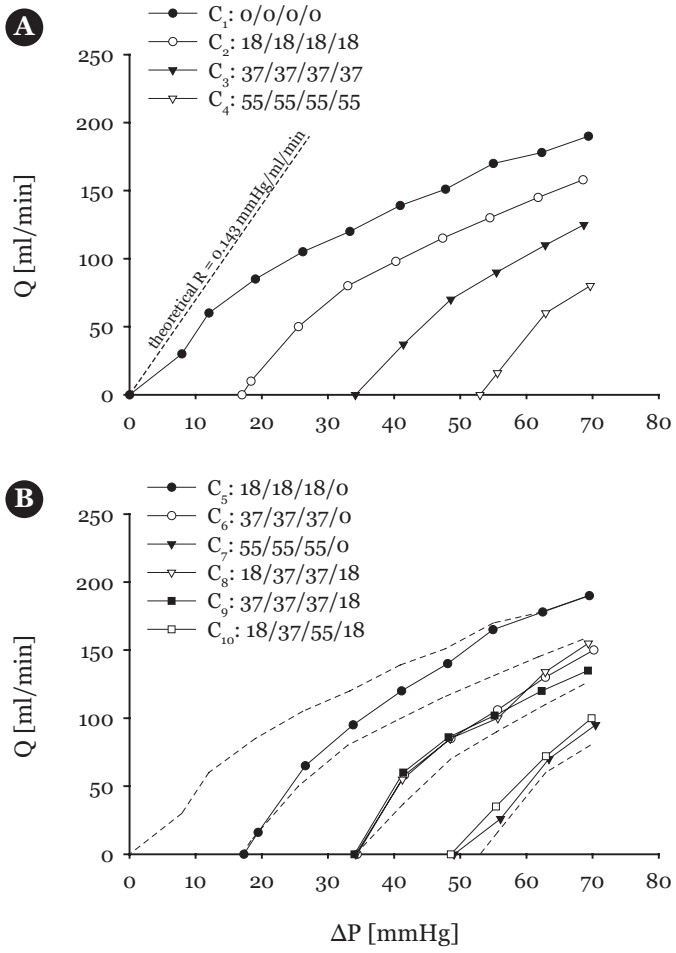

Figure 6-10: A: Measured myocardial pressure–flow relations under surrounding pressure configurations C_1 - C_4. Values of P_{zf} are nearly identical to the applied P_S. The resistance of the model is not constant, but increases with flow, probably due to the flow obstructing passageways between the compartments. The dashed line represents the ideal Poiseuille relation; B: Pressure–flow relations for configurations C_5 - C_{10}. C_1 - C_4 are shown as dashed lines. P_{zf} is determined by the greatest P_S in one of the compartments.

6.6.3 Influence of P_{zf} on FFR: hydraulic bench model

6.6.3.1 Description of the experimental setup

The experimental setup is shown schematically in figure 6-11. Pulsatile flow was generated by a model of the human left heart (d), which basically consists of two

(instead of four) pulmonary veins (c), the LA and LV and the aortic arch [341]. The elastic properties of the aorta were simulated by installing an air chamber (Windkessel element) (e). Distal to the Windkessel, most of the test fluid (30% glycerine and 70% water; ρ = 1060 kg/m³ and μ = 3.5 mPa.s at room temperature, thus comparable to blood) flows towards the global systemic resistance (f), while only a smaller quantity (coronary flow) perfuses the myocardial resistance model (l). Distal to the resistance model, an overflow reservoir (n) is installed to avoid air being sucked into the tubes at any time. Another reservoir (o) receives flow from the peripheral resistance and the overflow reservoir. The test fluid is then again elevated to the preload level (b) using a pump (a).

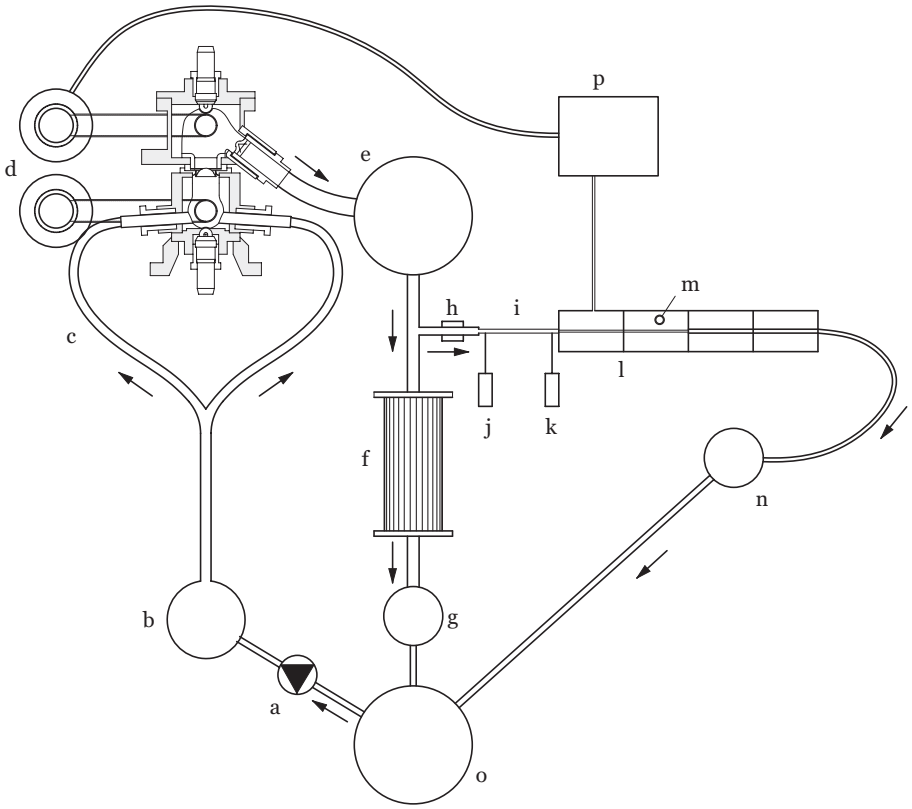

Figure 6-11: Schematic representation of the main hydraulic setup. The myocardial resistance model (l) and the peripheral resistance (f) are perfused by a water-glycerine mixture (70%/30%) under physiological pressures generated by a cardiovascular simulator (d), fed by two (instead of four) pulmonary veins (c). The compliance of the aorta is adjusted by a Windkessel (e). Zero-flow pressures in the coronary resistance are controlled by an external adjustable water column (m). The effect of systolic compression is simulated by a pneumatic unit (p). Pressure is measured proximal (j) and distal (k) to the coronary artery (i). Flow is measured proximal to the coronary artery (h). A pump (a) brings the test fluid from reservoirs (n), (g) and (o) to a reservoir on preload level (b), in order to close the hydraulic loop.

Compared to the myocardial resistance model validation experiments (see paragraph 6.6.2.3), the model was modified in three ways. Firstly, we connected compartment 1 to the pneumatic unit (p) also actuating our model of the LV. This way, compartment 1 is compressed in phase with LV contraction, simulating the effect of LV contraction on systolic flow (systolic flow impediment) [207]. Secondly, to allow for a simple control of P_{zf} during diastole, a (constant) surrounding pressure was applied only in compartment 2. Thirdly, in order to realize hyperaemic coronary flow values within a physiological range, we used tubes with a larger diameter (diameter 3.5 mm) in compartments 3 and 4. As such, the first two compartments of the model include all "active" resistance components, i.e., the systolic flow impediment and non-zero P_{zf}. This active part was then further connected to a passive peripheral resistance element (f), composed of a porous material embedded in a water-filled reservoir, of which the resistance level is changed by increasing the pressure in the water reservoir and thus compressing the porous material inside. This passive resistance was controlled to an appropriate value and kept constant throughout the whole experiment.

Note that our model reflects *hyperaemic conditions*, as FFR is always measured during hyperaemia. As such, the model does not contain the autoregulating properties of the coronary circulation.

6.6.3.2 Experimental protocol

Flow was measured proximal (h) to the epicardial coronary artery using an ultrasonic flow meter (Transonic, Ithaca, NY, USA). Pressures were registered in the proximal (j) and distal (k) part of the coronary artery. Mean P_{ao} was set to 70, 90 and 110 mmHg by adjusting the pneumatic actuating pressure (enhancing cardiac contractility). For each level of P_{ao}, the value of P_{zf} was varied between 0 and 30 mmHg in steps of 5 mmHg. Data were recorded during 5 seconds, and time averaged to obtain P_{ao}, P_{dis} and Q. Experiments were first done using a *healthy* (control) silicon phantom (diameter 3 mm, length 10 cm) of the *left anterior descending* (LAD) and then repeated using a *diseased* coronary artery phantom with a 89% area stenosis (i). They were mounted proximal to our model of the microcirculation.

6.6.3.3 Data analysis

The analysis consisted of comparing the following three formulas for fractional flow reserve:

- conventional pressure-derived $FFR = P_{dis}/P_{ao}$;
- flow-derived $FFR_Q = Q_S/Q_N$;
- corrected pressure-derived $FFR_C = (P_{dis}-P_{zf})/(P_{ao}-P_{zf})$.

The different methods for calculating fractional flow reserve were compared using a Bland-Altman analysis [32], with FFR_Q as the golden standard. Analysis of variance (ANOVA) with a post hoc Scheffé test was used to assess the difference between the methods. The level of significance was set at a p-value of 0.05. All values were expressed as mean ± SD. Statistics were performed using Statview 5 (Cary, NC, USA).

6.6.4 Results

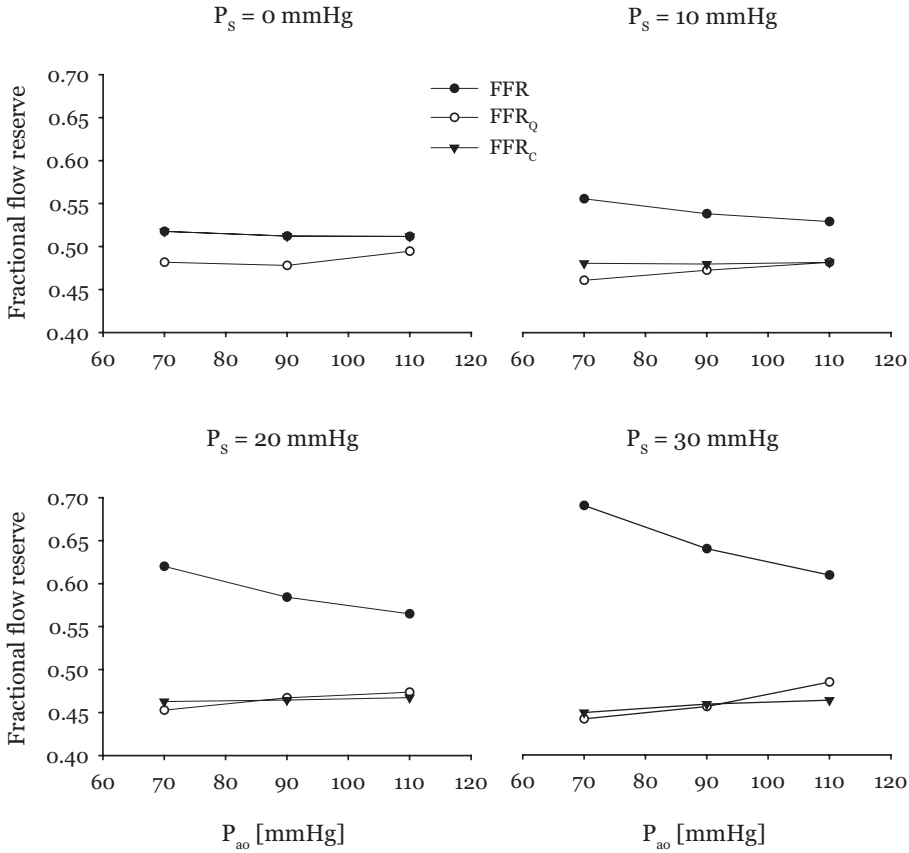

Figure 6-12: Relation between pressure-derived FFR = P_{dis}/P_{ao}, corrected pressure-derived $FFR_C = (P_{dis}-P_{zf})/(P_{ao}-P_{zf})$ and flow-derived $FFR_Q = Q_S/Q_N$ in a 89% area stenosis for various levels of surrounding pressures (P_S) and aortic pressure (P_{ao}). FFR_Q and FFR_C correlate well. FFR consistently overestimates FFR_Q and FFR_C, except when P_S = 0 mmHg.

The effect of various levels of P_{zf} and P_{ao} on FFR, FFR_C and FFR_Q (reference method) is shown in figure 6-12 for a 89% area stenosis. We found a good agreement between FFR_Q and FFR_C for each value of P_S, except for P_S = 0 mmHg, where FFR is equal to FFR_C and both overestimate FFR_Q. The mean difference between FFR_Q and FFR was -0.101 ± 0.067 ($p < 0.001$), while the mean difference between FFR_Q and FFR_C was -0.011 ± 0.011 ($p = 0.77$) (figure 6-13).

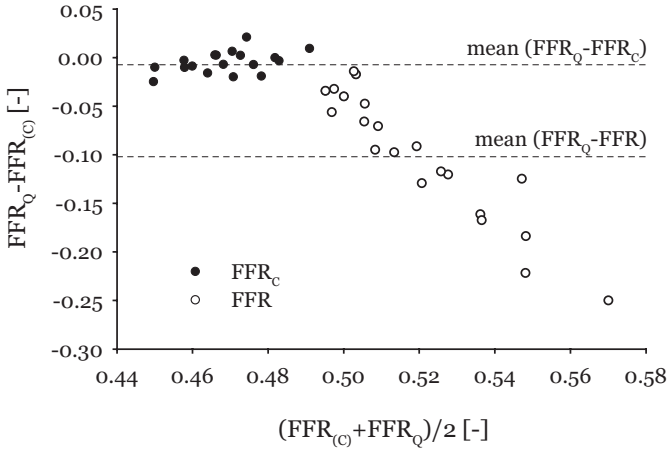

Figure 6-13: Bland-Altman description of the relation between FFR_Q and $FFR_{(C)}$. FFR clearly overestimates FFR_Q, while FFR_C matches FFR_Q very well.

The extent to which FFR overestimates FFR_Q increased with decreasing P_{ao} and increasing P_S, as shown in figure 6-14. The overestimation varied between 2.84% (for P_S = 5 mmHg en P_{ao} = 110 mmHg) and 56.18% (for P_S = 30 mmHg and P_{ao} = 70 mmHg).

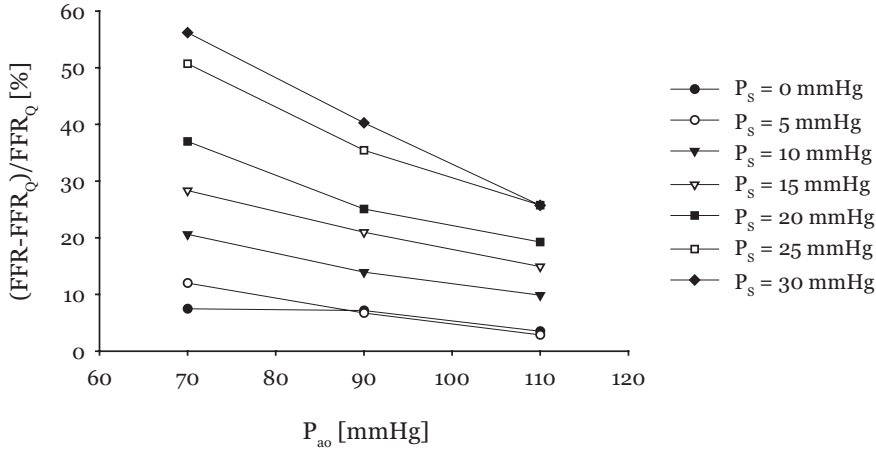

Figure 6-14: The amount of overestimation of pressure-derived FFR compared to flow-derived FFR_Q increases with increasing P_S and decreasing P_{ao}. Maximum overestimation is 56.18% (for P_S = 30 mmHg and P_{ao} = 70 mmHg).

6.6.5 Discussion

This study showed that applying the waterfall principle to a hydraulic myocardial resistance model yields an experimental setup that allows for generating epicardial pressure and flow data incorporating *biphasic flow patterns* and *easily controllable*

levels of P_{zf}. This experimental setup further enabled us to demonstrate that the pressure-derived fractional flow reserve corrected for a P_{zf} (FFR_C) agrees well with the flow-based FFR_Q, while the conventional FFR overestimates FFR_Q. The degree of overestimation was directly related to P_{zf}. As a consequence, it would be more accurate to assess the severity of a stenosis with the corrected FFR_C from a physiological point of view. Currently, this back-pressure is commonly neglected and FFR is simply calculated as a ratio of mean distal to mean aortic pressure (P_{dis}/P_{ao}).

Segers et al. [281] previously made use of a hydraulic bench model of the coronary artery and microcirculation to validate the basic concept of FFR. Later, Matthys et al. [207] further elaborated this model by implementing the effect of ventricular contraction during systole on flow. In the present study, we simulated coronary pressure-flow relations in a more physiological way with the incorporation of an adjustable P_{zf}. This was achieved by directly simulating the *waterfall principle* via compression of a silicon collapsible tube.

Various explanations have been given for the physics behind P_{zf}, the most important one being the *waterfall concept*, the effect of *intramyocardial capacitance* [169, 251, 293] and the existence of the *collateral arteries* [212]. To the best of our knowledge, however, an exact clarification has not been given up to date. Our main objective with the hydraulic bench model was to design a myocardial resistance model that allows generating appropriate pressure-flow curves showing a positive P_{zf} in our integrated hydraulic bench model. The applied waterfall model fulfils this criterion, demonstrated by the steady state measurements on the resistance model itself. We assessed the hydrodynamic properties of the myocardial resistance model in a first series of experiments. In the absence of a surrounding pressure, the pressure-flow relation is virtually linear and passes through the origin. When increasing the surrounding pressure P_S, the pressure-flow relation shifts to the right, resulting in a positive P_{zf} (figure 6-10).

We subsequently assessed the effect of variable P_{ao} and P_S on FFR in our model. The data showed that FFR overestimates the reference FFR_Q, while FFR corrected for P_{zf} (FFR_C) is an excellent estimate for FFR_Q. The overestimation increased with increasing P_{zf} and decreasing P_{ao} and it was more than 50% if P_{ao} = 70 mmHg and P_{zf} = 30 mmHg (figure 6-14). As some patients may have high P_{zf} (e.g., in case of severe hypertrophy), FFR could therefore be a too optimistic evaluation of the stenosis severity. This conceptually important issue was recently also addressed by Siebes et al. [287] in a mathematical parametric study, in which the effects of elevated back-pressures and variable P_{ao} were investigated. They showed that the pressure-derived FFR equals FFR_Q when P_{zf} is included in the formula and that FFR exceeds FFR_Q when P_{zf} is not accounted for. This was true for all levels of P_{ao}, stenosis resistance and microvascular resistance. Our hydraulic bench study results are thus in perfect agreement with their theoretical considerations.

Although it is clear that neglecting P_{zf} (or even P_v) in FFR will overestimate FFR_Q, the question remains whether this consideration is relevant in a clinical setting, especially given the difficulties in estimating P_{zf}. In humans, P_{zf} is usually determined by *extrapolation* of the pressure-flow relation to the pressure-axis during diastole. Using this method, some studies indeed have shown rather high values for P_{zf} in humans during hyperaemia: P_{zf} = 37.9 ± 9.8 mmHg according to Dole et al. [78], and

P_{zf} = 36.9 ± 16 mmHg according to Meneveau et al. [211]. In dog studies, P_{zf}-values of 10 to 15 mmHg have been reported in a normal beating heart [22], but in LV hypertrophy values as high as 40 mmHg during total coronary occlusion were observed by Duncker et al. [83]. The range of studied surrounding pressures in this study is thus realistic. If the measured P_{zf} represents a correct estimate of the back-pressure in the coronary circulation, FFR can be overestimated considerably (figure 6-14).

On the other hand, the conventionally calculated FFR has shown to be very valuable in clinical practice and has been proved to correlate well with non-invasive studies [71, 254, 255]. According to these studies, mainly performed in *selected patients* (single vessel disease and no prior myocardial infarction), a cut-off value of FFR < 0.75 showed a sensitivity of 88% and specificity of 100% for scintigraphic evidence of myocardial ischaemia [254]. More recently, a similar study was carried out in a heterogeneous group of consecutive patients, but still resulted in high sensitivity and specificity values of 79% and 73%, respectively [355]. We agree that correcting FFR for P_{zf} will not lead to major changes for a stenosis with an FFR in the threshold region of 0.75 or higher. The effect will mainly be apparent for stenoses in the lower FFR range, where the haemodynamic severity of the stenosis is obvious. Nevertheless, from a *conceptual* point of view, it should be clear that measuring P_{zf} and implementing it in the formula of FFR_C, is a more accurate way of assessing coronary stenosis severity, in particular in patients with a high P_{zf}.

6.6.6 Study limitations

Although the use of an in vitro model may be superior to animal and human studies in several aspects, a number of potential shortcomings need to be addressed:

(i) In nature, the pressure compressing the coronary bed is *dynamic*, which means that it is high during systole (systolic flow impediment) and low during diastole (generating P_{zf}). In our model, the mechanisms inducing systolic flow impediment and P_{zf} generation are spatially *uncoupled*. Systolic flow impediment is generated by applying pneumatic pressure (which was also used for compressing the LV) to the first compartment of the myocardial resistance model, while P_{zf} is created by applying a constant surrounding pressure on the second compartment.

(ii) Also, we did not account for *collateral flow*. Collateral flow from other arteries has the same effect on FFR as an elevated P_{zf}. Messina et al. [212] explained that if collateral flow enters for example the distal LAD, the inflow into the proximal LAD will be reduced by the amount of collateral flow so that total flow through the LAD's microvascular bed is what it would have been in the absence of collateral flow. Flow measured at the origin of the LAD will reach zero at a higher pressure when there is collateral flow. Both result in an overestimation of the FFR in comparison with the flow ratio in the real coronary circulation [256, 287]. Nonetheless, absence of collateral circulation in our model does not influence the validity of our results, since we aimed to investigate the effect of P_{zf} only.

(iii) Furthermore, we did not specifically quantify the effect of *epicardial* and *intramyocardial capacitance* on instantaneous phasic pressure-flow relations. However, we are convinced that this would not affect our study results, since the concepts of pressure- and flow-derived fractional flow reserve rely on the mean values of coronary pressure and flow, and potential capacitance effects *cancel out* over diastole and systole [256]. We therefore believe that the effects of capacitance do not need to be accounted for in our hydraulic model.

(iv) The coronary microvasculature was modelled with only one "*average*" elastic tube. This way, regional and temporal differences in extravascular tissue pressure [136] could not be simulated. To do so, it would be more realistic to use multiple parallel tubes to mimic several *parallel* layers in the myocardium, each of them being exposed to a different P_{zf} (with the highest extravascular pressure near the endocardial layer). An electric analogue of such a model has been previously developed by Downey and Kirk [80].

(v) Finally, we performed our experiments with only *one stenosis* with an area reduction of 89%. The relation between stenosis severity and percentage overestimation between FFR and FFR_Q has therefore not been studied. The general nature of our findings, however, warrants applicability for other stenosis levels. Yet, the effect magnitude will likely be related to the functional severity of the stenosis.

6.6.7 Conclusions

In a simplified hydraulic model of the coronary circulation, we were able to show that the presence of a zero-flow pressure P_{zf} requires a modification of the traditional formula $FFR = P_{dis}/P_{ao}$ in order to accurately assess the flow-limiting effect of a coronary artery stenosis. Since the P_{zf} will mainly affect FFR values that, even after correction, leave no doubt about the indication for treatment, this finding may not have a large impact on clinical decision making. Still, the used model is a good representation of our current understanding of the diseased coronary circulation.

6.7 Do we need better functional indices?

Even though the *superiority* of functional indices CVR and FFR over coronary angiography for decision making has been repeatedly demonstrated, Spaan et al. [295] recently argued that they hold *limited promise* for further advancement in clinical applications because they are theoretically unable to differentiate between the haemodynamic effect of *stenosis resistance* and *microvascular resistance*. Likewise, this further implies that neither FFR nor CVR can be considered as a *stenosis-specific* index. Moreover, it can be shown that CVR and FFR are affected by R_{myo} in *opposite* directions. From the schematic representation of the coronary circulation, depicted in figure 6-5, it is relatively easily appreciated that CVR decreases when myocardial resistance R_{myo} increases, which is a well known limitation of the concept of CVR. Even though FFR (either or not corrected for P_{zf}) was initially considered *independent* of *microvascular resistance* R_{myo} [72], the *quadratic* relation between the

stenosis pressure drop and coronary flow (equation 6-10) is hardly compatible with such an assumption [113, 361]. This is explained as follows. The transstenotic pressure drop ΔP can be written as

$$\Delta P = a_1 \cdot Q + a_2 \cdot Q^2 \qquad (6\text{-}10)$$

where a_1 is the coefficient for *viscous frictional losses* along the stenosis, and a_2 is the coefficient for *inertial pressure losses* at the exit of the stenosis [195]. This equation is solidly based on fluid dynamic theory and has been extensively validated with stenosis models in tubes and arteries [120, 204, 361]. As expected, our 89% area stenosis model also showed a quadratic pressure drop-flow relation (figure 6-15).

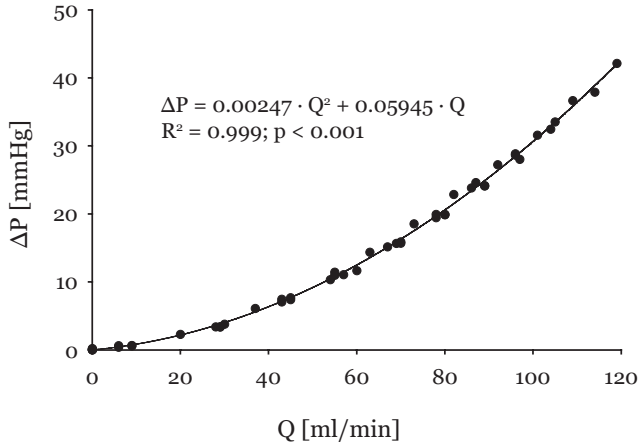

Figure 6-15: Quadratic relation between flow (Q) and stenosis pressure drop (ΔP) in the 89% area stenosis used in the hydraulic experiments.

The stenosis resistance, R_S, calculated as the slope of the pressure-drop flow relation, therefore increases with flow:

$$R_S = \frac{d(\Delta P)}{dQ} = a_1 + 2 \cdot a_2 \cdot Q \qquad (6\text{-}11)$$

FFR can also be expressed as

$$FFR = \frac{Q_S}{Q_N} = \frac{R_{myo}}{R_S + R_{myo}} = \frac{R_{myo}}{a_1 + 2 \cdot a_2 \cdot Q + R_{myo}} \qquad (6\text{-}12)$$

It follows from equation 6-12 that FFR will increase when flow decreases, which in turn can be the result of a decrease in P_{ao} or an increase in R_{myo}.

It was therefore not surprising that Meuwissen et al. [213] reported a relatively large percentage of *conflicting outcomes* (27%) in patients with an intermediate coronary stenosis between FFR and CVR, based on their respective cut-off values for clinical decision-making [213]. The same group later introduced the *hyperaemic stenosis*

resistance (HSR) index, defined as the ratio of *hyperaemic stenosis pressure drop* (ΔP) to *hyperaemic average peak flow velocity* (v)*:*

$$HSR = \Delta P / v \tag{6-13}$$

The best cut-off value was determined as 0.8 mmHg/cm/s. Like FFR, HSR has an unequivocal normal reference value HSR = 0, and is independent of basal (haemodynamic) conditions. This novel index was shown more accurate in identifying functionally significant coronary stenoses (as determined by SPECT) than the traditional haemodynamic parameters based on either flow velocity (CVR) or pressure measurements (FFR) alone, because HSR is based on a *combination* of intracoronary pressure and flow velocity signals [214]. The gain in accuracy was predominantly achieved in patients of intermediate lesions with *conflicting* predictive outcomes between FFR and CVR [295].

HSR is, by definition, also flow-dependent. However, it is less sensitive to changes in maximal flow, caused by an insufficient amount of adenosine or because of microvascular dysfunction, because stenosis pressure drop and velocity are affected in the *same* direction. The effect of changes in R_{myo} on stenosis resistance therefore partially cancels out, which is an advantage over FFR and CVR.

The application of HSR may currently be hampered as it requires sequential use of two sensor-equipped wires to avoid worsening the haemodynamic severity of the stenosis. Nevertheless, once combined pressure and Doppler flow wires are widely available, HSR has a high potential to improve clinical decision-making in the catheterization laboratory [163].

6.8 Appendix: serial waterfalls explained

The hydraulic waterfall phenomenon and the corresponding pressure-flow relations are explained stepwise by means of an example in which two serial waterfalls are created (figure 6-16).

Initially, the configuration without any surrounding pressures is assumed (figure 6-16A). In this condition, pressure-flow relations are governed by Poiseuille's Law: $Q = \Delta P/R$. For simplicity, consider Q = 200 ml/min and ΔP = 70 mmHg, such that total resistance equals 70 mmHg/200 ml/min = 0.35 mmHg/ml/min. This resistance value is in the same range as the measured resistance in the myocardial resistance model (figure 6-10). The outflow pressure (P_o) is kept constant at 0 mmHg. With P_i = 70 mmHg, pressures inside the tubes at the end of each chamber are 52.5 mmHg, 35 mmHg, 17.5 mmHg, and 0 mmHg, respectively.

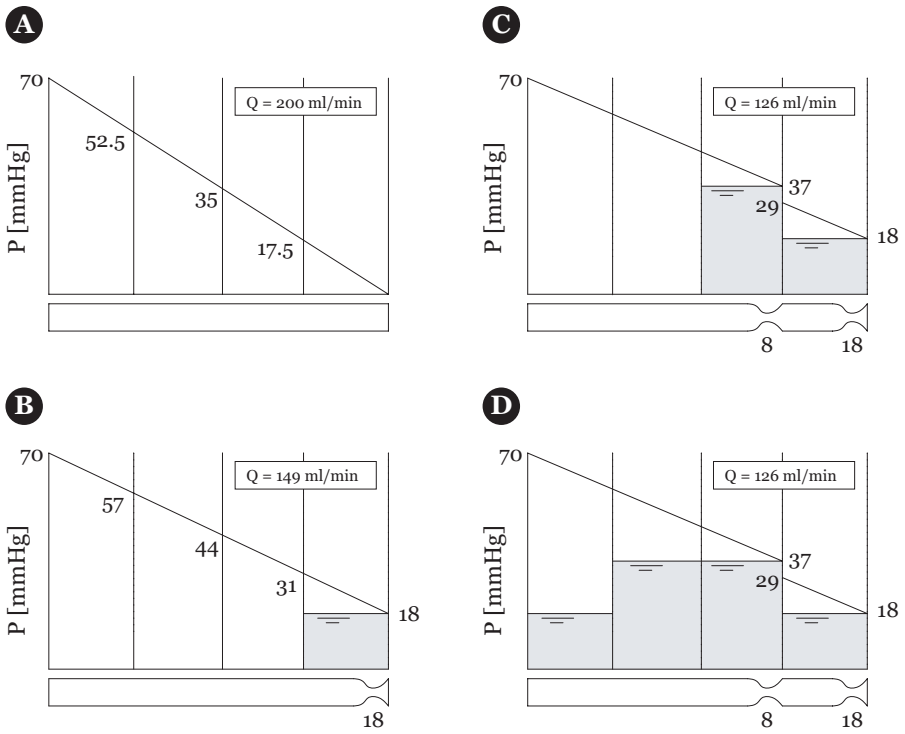

Figure 6-16: Example of a theoretical resistance model with hydraulic waterfalls. Inflow pressure P_i = 70 mmHg. Outflow pressure P_o = 0 mmHg. Waterfalls are shown under each graph. A: With P_S = 0 pressure decreases linearly from 70 to 0 mmHg and no waterfall exists; B: If P_{S4} > 0, a waterfall will originate at the distal end of the model. $P_{zf} = P_{S4}$ becomes the back-pressure causing a flow reduction; C: A second waterfall is created in the third compartment because P_{S3} is higher than the internal pressure in the third compartment. P_{zf} increases to P_{S3} and resistance decreases to 3/4 of its original value. Flow decreases even though resistance decreases; D: Surrounding pressures in compartments 1 and 2 have no influence on pressure and flow as long as they are lower than internal pressure.

In the following three steps, it is shown how pressure and flow in the vessel are obtained, when applying the same surrounding pressures as in configuration C_8 (18/37/37/18 mmHg). First, raise P_{S4} to 18 mmHg (figure 6-16B). Because $P_{S4} > P_o$, one would think that the vessel collapses due to the positive transmural pressure and that flow will stopas a result. Yet, if flow stops, there is no pressure gradient between the inflow pressure and the pressure in the last compartment, which means that pressure in the last compartment would increase to 70 mmHg (hydrostatic situation) and the vessel reopens. What actually happens is that the vessel partially collapses at the end of the fourth compartment, thereby creating a local pressure drop, called a *hydraulic waterfall*. Under these circumstances, there is a perfect equilibrium between the inner and surrounding pressure. The magnitude of this pressure drop is exactly 18 mmHg. Hence, pressure proximal to this narrowing must be 18 mmHg too since P_o = 0 mmHg. Because P_i = 70 mmHg and the back-pressure to flow is 18 mmHg, the driving pressure is only 52 mmHg instead of 70 mmHg. As a result, flow decreases to Q = (70 - 18)/0.35 = 149 ml/min.

If, in addition, P_{S3} is augmented to 37 mmHg, another waterfall will originate because the internal pressure at the end of the third compartment (31 mmHg) is lower than 37 mmHg. Driving pressure is only 70 - 37 = 33 mmHg now, while the resistance is reduced to 3/4 of its initial value (0.35 mmHg/ml/min). Flow is then $33/(3/4 \cdot 0.35)) = 126$ ml/min. As flow is constant along the vessel path, pressure at the proximal end of the last compartment is $18 + 126 \cdot (1/4) \cdot 0.35 = 29$ mmHg. The magnitude of the *second waterfall* is then 37 - 29 = 8 mmHg (figure 6-16C).

When increasing P_{S1} and P_{S2} to 18 and 37 mmHg respectively, no waterfall will be added because the internal pressure is greater than the surrounding pressures (figure 6-16D). Pressure and flow are therefore identical to the previous situation.

This theoretical example explained how two hydraulic waterfalls originated in the given configuration of surrounding pressures: the first one at the end of compartment 4 and the second one between compartments 3 and 4. For every P_i, P_o and surrounding pressure configuration, pressure and flow can be calculated in an analogous way.

7

Chapter 7

Conclusions and Future Prospects

7.1 Conclusion

Within this thesis, we have critically evaluated a number of theoretical concepts and models that are used to quantify left ventricular (LV) systolic and diastolic mechanics. We additionally studied how LV wall mechanics affects coronary pressure and flow.

Chapter 1 covered the basic anatomy and physiology of the cardiovascular system, and explained that the LV chamber properties are determined by the contraction and relaxation properties of the constituent muscle fibres and the connective tissue network in which they are supported.

In *chapter 2* we meticulously analyzed pressure-volume (P-V) signals in the mouse obtained with a miniaturized combined pressure-conductance catheter, and focused on the applicability of the linear time-varying elastance concept. It was found that this concept, which has become very popular in the field of cardiovascular modelling, does not hold well in the mouse LV, because the intercept of the end-systolic P-V relationship (ESPVR) with the volume-axis varies considerably with time, and because the isochrones (i.e., curves that connect P-V data points occurring at the same time instant after the onset of systole) are non-linear. The conventional linear time-varying elastance function should therefore not be applied in the mouse to accurately model the time course of increasing and decreasing stiffness, even though this function can be easily calculated when P-V data are available.

In the remaining chapters of this thesis, the systolic and diastolic mechanical LV properties were investigated using echocardiography, a non-invasive ultrasound-based imaging modality.

The physical background of ultrasound and the principles underlying greyscale and Doppler echocardiography were explained in the first part of *chapter 3*. In this chapter we also validated a new method for determining two-dimensional myocardial strains in a phantom model and in open-chest sheep. The proposed technique solves the angle dependence of current strain imaging and will likely accelerate the use of strain and strain rate imaging in clinical practice.

End-systolic elastance (E_{es}), the slope of the linear assumed ESPVR, is considered the gold standard for assessing changes in global ventricular contractility in the research environment. In *chapter 4* we applied an existing method to determine E_{es} non-invasively from echocardiography and brachial blood pressure measurements in the Asklepios data set. Using this data set, we demonstrated the intrinsic dependence of E_{es} on LV geometry. We proposed a novel population-specific method for converting E_{es} into an index that reflects the intrinsic myocardial contractile state of a given LV (contractility of a "volume unit"), and compared this index with three previously suggested myocardial contractility indices. Considerable inconsistencies between all indices were observed when analyzing age- and gender-related differences in myocardial contractility. However, regardless of the index that was used, it was found that myocardial contractility increases consistently in women with age, while in men it seems to reach a plateau value at the age of 51-55. This remarkable finding definitely deserves further investigation.

In *chapter 5* we shifted from systolic function indices towards echocardiography-based indices of relaxation and diastolic function. In clinical practice, diastolic function is often assessed in terms of LV relaxation and compliance (LVC). Using a hydraulic model of the LV during early diastole, we were first able to show that end-systolic pressure (ESP) had the largest impact upon isovolumic relaxation rate, followed by LVC and the rate of inactivation. In the second part of this chapter, an extensive review was provided of four relatively new echocardiographic approaches (wave propagation velocity, mitral annular velocity, intraventricular pressure differences and torsion) for gaining additional insights in relaxation and diastolic function. Even though most of these new diastolic indices are well capable of detecting abnormalities, their relationship with underlying myocardial mechanics is not fully understood. Additional studies using also physical and numerical models of the LV are mandatory to further elucidate the relation between diastolic indices and intrinsic diastolic mechanics in the LV.

In the *last chapter* we investigated the influence of an increased zero-flow pressure (P_{zf}, back-pressure to flow in the coronary circulation) on fractional flow reserve (FFR), an index that is nowadays frequently used in the catheterization laboratory to assess the functional severity of a coronary artery stenosis. FFR equals the ratio of hyperaemic myocardial flow through the stenosed coronary segment (Q_S) to hyperaemic flow through the same segment in the hypothetical case that there would be no stenosis (Q_N). In practice, however, FFR is measured using pressure wires and calculated as the mean pressure distal to the stenosis divided by the mean aortic pressure (P_{dis}/P_{ao}). A simplified hydraulic model of a stenosed coronary artery and its depending microvascular bed was developed. This model easily allows for changing P_{zf} using the principle of the hydraulic waterfall and is, moreover, capable of mimicking the effect of systolic flow impediment. The results showed that FFR should be calculated as $(P_{dis}-P_{zf})/(P_{ao}-P_{zf})$ instead of (P_{dis}/P_{ao}) in order not to underestimate the functional severity of the stenosis. The discrepancy between the two measures becomes higher at lower P_{ao}. Unfortunately, the clinical feasibility of this improved index is seriously hampered due to difficulties in measuring P_{zf}.

7.2 Future prospects

The findings of this thesis can be used as a starting point for further research topics. Some of the interesting ones are listed below. Several suggestions for improving the techniques and methodologies applied in this research are also outlined below.

The original time-varying elastance model (*chapter 2*) did not appear to be appropriate for representing time-varying stiffness in the murine ventricle. In more recent literature, alternative models have been presented that more accurately reflect natural cardiac pressure and volume variations. These models do not only include elastance, but also incorporate a resistive component, which accounts for the relation between pressure and aortic outflow, and a (usually negligible) inertial component. Additional analyses are required to assess the contribution of such resistive and inertial components in the murine ventricular function model and, hence, to determine which model best predicts ventricular pressure. One could also try a very different approach and build a mathematical (instead of a semi-phenomenological)

elastance model, derived from theoretical P-V loops (and corresponding isochrones). Theoretical P-V data can in turn be reconstructed from numerical simulations incorporating (i) appropriate murine cardiomyocyte models (with physiological force-length and force-velocity relationships), (ii) appropriate constitutive material laws of extracellular tissue, and (iii) a number of assumptions with respect to spatial and temporal inhomogeneities in ventricular structure.

The two-dimensional strain imaging method (*chapter 3*) has a large potential for clinical practice. However, some aspects of this methodology need to be investigated, e.g., the influence of out-of-plane motion upon strain estimation in the in vivo setting. Moreover, a comparison between the current method, based on a one-dimensional kernel, and tracking using a two-dimensional kernel, as presented by, for example, Kaluzynski et al. [150], is left for future work. The current method can also be extended towards three-dimensional strain imaging when three-dimensional ultrasound imaging is available at a sufficient frame rate.

It would be worthwhile to see whether the proposed methods for converting E_{es} into a measure of myocardial contractility (*chapter 4*) can be fine-tuned further by accounting for the ratio between the long-axis and the short-axis distance. Once an appropriate normalization method is established, it could provide valuable insights in the mechanisms underlying geometric remodelling (concentric remodelling, eccentric hypertrophy and concentric hypertrophy).

The hydraulic model of the LV (*chapter 5*) can be improved in many ways, e.g., (i) by adding a freely-moving atrioventricular plane instead of keeping the ventricular base fixed, (ii) by using pathological mitral valves, (iii) by implementing a contractile left atrial chamber to simulate the second phase of ventricular filling, (iv) by introducing papillary muscles and chordae tendineae, or (v) by accounting for an anatomically accurate fibre orientation to model early diastolic untwisting. One of the major limitations inherent to all of the current physical models is that they are passive models which require external pressure to simulate the effect of the contraction-relaxation cycle. As a result, buckling may occur when the model is at its end-systolic configuration. To tackle this type of problem, alternative materials should be looked for, which are capable of actively developing stress and strain induced by electrical activation and, hence, do not require external pressure. Initial experiments have been performed using a dielectric active polymer. However, up to date, this strategy was not successful for modelling the LV. Yet, once a model has been developed which acceptably mimics diastolic wall mechanics, its potential as a research tool for echocardiography-based diastology will be greatly increased.

Even though our model of the coronary circulation (*chapter 6*) was shown appropriate for explaining the effect of an elevated P_{zf} upon FFR, it can still be modified in various aspects to obtain pressure-flow curves that better resemble coronary pressure and flow in conscious humans. Therefore, compliance of the epicardial and intramyocardial vessels needs to be accounted for. It would furthermore be valuable to make use of several tubes in parallel for mimicking myocardial resistance. Each of these tubes would then be subjected to different surrounding pressures, depending on its relative position in the myocardial wall. One may also improve its physiological realism by adding collateral flow to the model in order to quantify its potential contribution to the measured P_{zf}. It would also be

interesting to use this model to investigate the sensitivity of the hyperaemic stenosis resistance index (HSR) to changes in haemodynamics. Lastly, in order to improve the overall applicability of this model, an additional variable resistance should be incorporated to mimic the autoregulating properties of a normal coronary circulation.

References

[1] Alam M, Wardell J, Andersson E, Samad BA and Nordlander R. *Characteristics of mitral and tricuspid annular velocities determined by pulsed wave Doppler tissue imaging in healthy subjects*. J Am Soc Echocardiogr 12: 618-628, 1999.

[2] Alfonso F, Macaya C, Goicolea J, Iniguez A, Hernandez R, Zamorano J, Perez-Vizcayne MJ and Zarco P. *Intravascular ultrasound imaging of angiographically normal coronary segments in patients with coronary artery disease*. Am Heart J 127: 536-544, 1994.

[3] Applegate RJ, Cheng CP and Little WC. *Simultaneous conductance catheter and dimension assessment of left ventricle volume in the intact animal*. Circulation 81: 638-648, 1990.

[4] Applegate RJ, Herrington DM and Little WC. *Coronary angiography: more than meets the eye*. Circulation 87: 1399-1401, 1993.

[5] Appleton CP, Galloway JM, Gonzalez MS, Gaballa M and Basnight MA. *Estimation of left ventricular filling pressures using two-dimensional and Doppler echocardiography in adult patients with cardiac disease. Additional value of analyzing left atrial size, left atrial ejection fraction and the difference in duration of pulmonary venous and mitral flow velocity at atrial contraction*. J Am Coll Cardiol 22: 1972-1982, 1993.

[6] Arts T, Bovendeerd P, Delhaas T and Prinzen F. *Modeling the relation between cardiac pump function and myofiber mechanics*. J Biomech 36: 731-736, 2003.

[7] Arts T, Bovendeerd PH, Prinzen FW and Reneman RS. *Relation between left ventricular cavity pressure and volume and systolic fiber stress and strain in the wall*. Biophys J 59: 93-102, 1991.

[8] Arts T, Bovendeerd PHM, Prinzen FW and Reneman RS. *Relation between Left-Ventricular Cavity Pressure and Volume and Systolic Fiber Stress and Strain in the Wall*. Biophysical Journal 59: 93-102, 1991.

[9] Arts T, Veenstra PC and Reneman RS. *Epicardial deformation and left ventricular wall mechanisms during ejection in the dog*. Am J Physiol 243: H379-390, 1982.

[10] Ashikaga H, Criscione JC, Omens JH, Covell JW and Ingels NB, Jr. *Transmural left ventricular mechanics underlying torsional recoil during relaxation*. Am J Physiol Heart Circ Physiol 286: H640-647, 2004.

[11] Baan J, Jong TT, Kerkhof PL, Moene RJ, van Dijk AD, van der Velde ET and Koops J. *Continuous stroke volume and cardiac output from intra-ventricular dimensions obtained with impedance catheter*. Cardiovasc Res 15: 328-334, 1981.

[12] Baan J and Van der Velde ET. *Sensitivity of left ventricular end-systolic pressure-volume relation to type of loading intervention in dogs*. Circ Res 62: 1247-1258, 1988.

[13] Baan J, van der Velde ET, de Bruin HG, Smeenk GJ, Koops J, van Dijk AD, Temmerman D, Senden J and Buis B. *Continuous measurement of left ventricular volume in animals and humans by conductance catheter*. Circulation 70: 812-823, 1984.

[14] Baccani B, Domenichini F and Pedrizzetti G. *Vortex dynamics in a model left ventricle during filling*. European Journal of Mechanics B-Fluids 21: 527-543, 2002.

[15] Baccani B, Domenichini F, Pedrizzetti G and Tonti G. *Fluid dynamics of the left ventricular filling in dilated cardiomyopathy*. J Biomech 35: 665-671, 2002.

[16] Baicu CF, Zile MR, Aurigemma GP and Gaasch WH. *Left ventricular systolic performance, function, and contractility in patients with diastolic heart failure*. Circulation 111: 2306-2312, 2005.

[17] Barbee RW, Perry BD, Re RN and Murgo JP. *Microsphere and dilution techniques for the determination of blood flows and volumes in conscious mice*. Am J Physiol 263: R728-733, 1992.

[18] Barbier P, Grimaldi A, Alimento M, Berna G and Guazzi MD. *Echocardiographic determinants of mitral early flow propagation velocity*. Am J Cardiol 90: 613-619, 2002.

[19] Batchelor G. *An Introduction to Fluid Dynamics*. London: Cambridge University Press, 1967.

[20] Baumgart D, Haude M, Goerge G, Ge J, Vetter S, Dagres N, Heusch G and Erbel R. *Improved assessment of coronary stenosis severity using the relative flow velocity reserve*. Circulation 98: 40-46, 1998.

[21] Belcher P, Boerboom LE and Olinger GN. *Standardization of end-systolic pressure-volume relation in the dog*. Am J Physiol 249: H547-553, 1985.

[22] Bellamy RF. *Diastolic coronary artery pressure-flow relations in the dog*. Circ Res 43: 92-101., 1978.

[23] Bellhouse BJ. *Fluid mechanics of a model mitral valve and left ventricle*. Cardiovasc Res 6: 199-210, 1972.

[24] Beneken JEW and DeWit B. *A physical approach to hemodynamic aspects of the human cardiovascular system*. In: *Physical bases of circulatory transport: Regulation and exchange*, edited by Reeve EB, and Guyton AC. Philadelphia, PA: W.B. Saunders, 1967, p. 1-45.

[25] Berne RM and Levy MN. *Cardiovascular Physiology, 3rd edition*. St. Louis: Mosby, 1977.

[26] Bernstein SE. *Physiological Characteristics*. In: *Biology of the Laboratory Mouse*, edited by Hill M. New York: 1966, p. 337-350.

[27] Beyar R and Sideman S. *A computer study of the left ventricular performance based on fiber structure, sarcomere dynamics, and transmural electrical propagation velocity*. Circ Res 55: 358-375, 1984.

[28] Beyar R and Sideman S. *The dynamic twisting of the left ventricle: a computer study*. Ann Biomed Eng 14: 547-562, 1986.

[29] Beyar R and Sideman S. *Left ventricular mechanics related to the local distribution of oxygen demand throughout the wall*. Circ Res 58: 664-677, 1986.

[30] Beyar R and Sideman S. *Relating left ventricular dimension to maximum elastance by fiber mechanics*. Am J Physiol 251: R627-635, 1986.

[31] Bittner V. *Menopause and cardiovascular risk cause or consequence?* J Am Coll Cardiol 47: 1984-1986, 2006.

[32] Bland JM and Altman DG. *Statistical methods for assessing agreement between two methods of clinical measurement*. Lancet 1: 307-310., 1986.

[33] Boltwood CM, Jr., Appleyard RF and Glantz SA. *Left ventricular volume measurement by conductance catheter in intact dogs. Parallel conductance volume depends on left ventricular size*. Circulation 80: 1360-1377, 1989.

[34] Bombardini T. *Myocardial contractility in the echo lab: molecular, cellular and pathophysiological basis*. Cardiovasc Ultrasound 3: 27, 2005.

[35] Bonow RO and Udelson JE. *Left ventricular diastolic dysfunction as a cause of congestive heart failure. Mechanisms and management*. Ann Intern Med 117: 502-510, 1992.

[36] Bovendeerd PH, Arts T, Delhaas T, Huyghe JM, van Campen DH and Reneman RS. *Regional wall mechanics in the ischemic left ventricle: numerical modeling and dog experiments*. Am J Physiol 270: H398-410, 1996.

[37] Brady AJ. *Mechanical properties of isolated cardiac myocytes*. Physiol Rev 71: 413-428, 1991.

[38] Braunwald E. *Heart Disease: A Textbook of Cardiovascular Disease. 3rd ed.* Philadelphia: WB Saunders, 1988, p. 449–470.

[39] Brennan EG and O'Hare NJ. *Calibration and assessment of a fluid-filled catheter-transducer system for the measurement of ventricular diastolic pressures*. Physiol Meas 19: 405-412, 1998.

[40] Brown BG, Bolson E, Frimer M and Dodge HT. *Quantitative coronary arteriography: estimation of dimensions, hemodynamic resistance, and atheroma mass of coronary artery lesions using the arteriogram and digital computation*. Circulation 55: 329-337, 1977.

[41] Brun P, Tribouilloy C, Duval AM, Iserin L, Meguira A, Pelle G and Dubois-Rande JL. *Left ventricular flow propagation during early filling is related to wall relaxation: a color M-mode Doppler analysis*. J Am Coll Cardiol 20: 420-432, 1992.

[42] Brutsaert DL, Housmans PR and Goethals MA. *Dual control of relaxation. Its role in the ventricular function in the mammalian heart*. Circ Res 47: 637-652, 1980.

[43] Brutsaert DL, Rademakers FE and Sys SU. *Triple control of relaxation: implications in cardiac disease*. Circulation 69: 190-196, 1984.

[44] Brutsaert DL and Sonnenblick EH. *Force-velocity-length-time relations of the contractile elements in heart muscle of the cat*. Circ Res 24: 137-149, 1969.

[45] Brutsaert DL and Sys SU. *Relaxation and diastole of the heart*. Physiol Rev 69: 1228-1315, 1989.

[46] Burkhoff D, Mirsky I and Suga H. *Assessment of systolic and diastolic ventricular properties via pressure-volume analysis: a guide for clinical, translational, and basic researchers*. Am J Physiol Heart Circ Physiol 289: H501-512, 2005.

[47] Burkhoff D, Sugiura S, Yue DT and Sagawa K. *Contractility-dependent curvilinearity of end-systolic pressure-volume relations*. Am J Physiol 252: H1218-1227, 1987.

[48] Burkhoff D, van der Velde E, Kass D, Baan J, Maughan WL and Sagawa K. *Accuracy of volume measurement by conductance catheter in isolated, ejecting canine hearts*. Circulation 72: 440-447, 1985.

[49] Burton AC. *Relation of Structure to Function of Walls of Bloods Vessels*. Physiology Review 34: 619-652, 1954.

[50] Capasso JM, Remily RM, Smith RH and Sonnenblick EH. *Sex differences in myocardial contractility in the rat*. Basic Res Cardiol 78: 156-171, 1983.

[51] Carabello BA. *Evolution of the study of left ventricular function: everything old is new again*. Circulation 105: 2701-2703, 2002.

[52] Carabello BA and Spann JF. *The uses and limitations of end-systolic indexes of left ventricular function*. Circulation 69: 1058-1064, 1984.

[53] Castro PL, Greenberg NL, Drinko J, Garcia MJ and Thomas JD. *Potential pitfalls of strain rate imaging: angle dependency*. Biomed Sci Instrum 36: 197-202, 2000.

[54] Cazorla O, Freiburg A, Helmes M, Centner T, McNabb M, Wu Y, Trombitas K, Labeit S and Granzier H. *Differential expression of cardiac titin isoforms and modulation of cellular stiffness*. Circ Res 86: 59-67, 2000.

[55] Celentano A, Palmieri V, Arezzi E, Mureddu GF, Sabatella M, Di Minno G and De Simone G. *Gender differences in left ventricular chamber and midwall systolic function in normotensive and hypertensive adults*. J Hypertens 21: 1415-1423, 2003.

[56] Chemla D, Coirault C, Hebert JL and Lecarpentier Y. *Mechanics of Relaxation of the Human Heart*. News Physiol Sci 15: 78-83, 2000.

[57] Chen CH, Fetics B, Nevo E, Rochitte CE, Chiou KR, Ding PA, Kawaguchi M and Kass DA. *Noninvasive single-beat determination of left ventricular end-systolic elastance in humans*. J Am Coll Cardiol 38: 2028-2034, 2001.

[58] Claessens TE, Georgakopoulos D, Afanasyeva M, Vermeersch SJ, Millar HD, Stergiopoulos N, Westerhof N, Verdonck PR and Segers P. *Non-linear isochrones in murine left ventricular pressure-volume loops: how well does the time-varying elastance concept hold?* Am J Physiol Heart Circ Physiol 2005.

[59] Cohen BJ. *Medical Terminology: An Illustrated Guide (4th edition)*. Lippincott Williams & Wilkins, 2003, p. 584.

[60] Costa KD, Takayama Y, McCulloch AD and Covell JW. *Laminar fiber architecture and three-dimensional systolic mechanics in canine ventricular myocardium*. Am J Physiol 276: H595-607, 1999.

[61] Courtois M, Kovacs SJ, Jr. and Ludbrook PA. *Transmitral pressure-flow velocity relation. Importance of regional pressure gradients in the left ventricle during diastole*. Circulation 78: 661-671, 1988.

[62] Courtois M, Kovacs SJ and Ludbrook PA. *Physiological early diastolic intraventricular pressure gradient is lost during acute myocardial ischemia*. Circulation 81: 1688-1696, 1990.

[63] Criscione JC, Rodriguez F and Miller DC. *The myocardial band: simplicity can be a weakness*. Eur J Cardiothorac Surg 28: 363-364; author reply 364-367, 2005.

[64] Crossman DC. *The pathophysiology of myocardial ischaemia*. Heart 90: 576-580, 2004.

[65] D'Hooge J, Bijnens B, Thoen J, Van de Werf F, Sutherland GR and Suetens P. *Echocardiographic strain and strain-rate imaging: a new tool to study regional myocardial function*. IEEE Trans Med Imaging 21: 1022-1030, 2002.

[66] D'Hooge J, Heimdal A, Jamal F, Kukulski T, Bijnens B, Rademakers F, Hatle L, Suetens P and Sutherland GR. *Regional strain and strain rate measurements by cardiac ultrasound: principles, implementation and limitations*. Eur J Echocardiogr 1: 154-170, 2000.

[67] D'Hooge J, Konofagou E, Jamal F, Heimdal A, Barrios L, Bijnens B, Thoen J, Van de Werf F, Sutherland G and Suetens P. *Two-dimensional ultrasonic strain rate measurement of the human heart in vivo*. IEEE Trans Ultrason Ferroelectr Freq Control 49: 281-286, 2002.

[68] Danton MH, Greil GF, Byrne JG, Hsin M, Cohn L and Maier SE. *Right ventricular volume measurement by conductance catheter*. Am J Physiol Heart Circ Physiol 285: H1774-1785, 2003.

[69] Davies JE, Whinnett ZI, Francis DP, Manisty CH, Aguado-Sierra J, Willson K, Foale RA, Malik IS, Hughes AD, Parker KH and Mayet J. *Evidence of a dominant backward-propagating "suction" wave responsible for diastolic coronary filling in humans, attenuated in left ventricular hypertrophy*. Circulation 113: 1768-1778, 2006.

[70] De Boeck BW, Oh JK, Vandervoort PM, Vierendeels JA, van der Aa RP and Cramer MJ. *Colour M-mode velocity propagation: a glance at intra-ventricular pressure gradients and early diastolic ventricular performance*. Eur J Heart Fail 7: 19-28, 2005.

[71] De Bruyne B, Bartunek J, Sys SU and Heyndrickx GR. *Relation between myocardial fractional flow reserve calculated from coronary pressure measurements and exercise-induced myocardial ischemia*. Circulation 92: 39-46., 1995.

[72] de Bruyne B, Bartunek J, Sys SU, Pijls NH, Heyndrickx GR and Wijns W. *Simultaneous coronary pressure and flow velocity measurements in humans. Feasibility, reproducibility, and hemodynamic dependence of coronary flow velocity reserve, hyperemic flow versus pressure slope index, and fractional flow reserve*. Circulation 94: 1842-1849, 1996.

[73] De Bruyne B, Pijls NH, Bartunek J, Kulecki K, Bech JW, De Winter H, Van Crombrugge P, Heyndrickx GR and Wijns W. *Fractional flow reserve in patients with prior myocardial infarction*. Circulation 104: 157-162, 2001.

[74] De Mey S, De Sutter J, Vandervoort P, De Buyzere M and Verdonck P. *Assesment of LV diastolic filling using color M-mode Doppler echocardiography: validation in new hydoraulic model*. Biomech Model Mechanobiol 2: 127-138, 2004.

[75] De Mey S, De Sutter J, Vierendeels J and Verdonck P. *Diastolic filling and pressure imaging: taking advantage of the information in a colour M-mode Doppler image*. Eur J Echocardiogr 2: 219-233, 2001.

[76] Despopoulos A and Silbernagl S. *Color atlas of physiology*. Stuttgart: Georg Thieme Verlag, 2003, p. 436.

[77] Devereux RB, Alonso DR, Lutas EM, Gottlieb GJ, Campo E, Sachs I and Reichek N. *Echocardiographic assessment of left ventricular hypertrophy: comparison to necropsy findings*. Am J Cardiol 57: 450-458, 1986.

[78] Dole WP, Richards KL, Hartley CJ, Alexander GM, Campbell AB and Bishop VS. *Diastolic coronary artery pressure-flow velocity relationships in conscious man*. Cardiovasc Res 18: 548-554., 1984.

[79] Dong SJ, Hees PS, Siu CO, Weiss JL and Shapiro EP. *MRI assessment of LV relaxation by untwisting rate: a new isovolumic phase measure of tau*. Am J Physiol Heart Circ Physiol 281: H2002-2009, 2001.

[80] Downey JM and Kirk ES. *Inhibition of coronary blood flow by a vascular waterfall mechanism*. Circ Res 36: 753-760., 1975.

[81] Drzewiecki GM, Karam E and Welkowitz W. *Physiological basis for mechanical time-variance in the heart: special consideration of non-linear function*. J Theor Biol 139: 465-486, 1989.

[82] Dumesnil JG, Gaudreault G, Honos GN and Kingma JG, Jr. *Use of Valsalva maneuver to unmask left ventricular diastolic function abnormalities by Doppler echocardiography in patients with coronary artery disease or systemic hypertension*. Am J Cardiol 68: 515-519, 1991.

[83] Duncker DJ, Zhang J, Pavek TJ, Crampton MJ and Bache RJ. *Effect of exercise on coronary pressure-flow relationship in hypertrophied left ventricle*. Am J Physiol 269: H271-281, 1995.

[84] Duval-Moulin AM, Dupouy P, Brun P, Zhuang F, Pelle G, Perez Y, Teiger E, Castaigne A, Gueret P and Dubois-Rande JL. *Alteration of left ventricular diastolic function during coronary angioplasty-induced ischemia: a color M-mode Doppler study*. J Am Coll Cardiol 29: 1246-1255, 1997.

[85] El-Shafei A, Chiravuri R, Stikovac MM, El-Badry MA, Donohue TJ, Bach RG, Aguirre FV, Caracciolo EA, Bitar S, Wolford TL, Miller DD and Kern MJ. *Comparison of relative coronary Doppler flow velocity reserve to stress myocardial perfusion imaging in patients with coronary artery disease*. Catheter Cardiovasc Interv 53: 193-201, 2001.

[86] Escaned J, Baptista J, Di Mario C, Haase J, Ozaki Y, Linker DT, de Feyter PJ, Roelandt JR and Serruys PW. *Significance of automated stenosis detection during quantitative angiography. Insights gained from intracoronary ultrasound imaging*. Circulation 94: 966-972, 1996.

[87] Esposito G, Santana LF, Dilly K, Cruz JD, Mao L, Lederer WJ and Rockman HA. *Cellular and functional defects in a mouse model of heart failure*. Am J Physiol Heart Circ Physiol 279: H3101-3112, 2000.

[88] Faller A and Schuenke M. *The Human Body: An Introduction to Structure and Function*. Georg Thieme Verlag, 2004, p. 708.

[89] Falsetti HL, Verani MS, Chen CJ and Cramer JA. *Regional pressure differences in the left ventricle*. Cathet Cardiovasc Diagn 6: 123-134, 1980.

[90] Farias CA, Rodriguez L, Garcia MJ, Sun JP, Klein AL and Thomas JD. *Assessment of diastolic function by tissue Doppler echocardiography: comparison with standard transmitral and pulmonary venous flow*. J Am Soc Echocardiogr 12: 609-617, 1999.

[91] Fearon WF, Luna J, Samady H, Powers ER, Feldman T, Dib N, Tuzcu EM, Cleman MW, Chou TM, Cohen DJ, Ragosta M, Takagi A, Jeremias A, Fitzgerald PJ, Yeung AC, Kern MJ and Yock PG. *Fractional flow reserve compared with intravascular ultrasound guidance for optimizing stent deployment*. Circulation 104: 1917-1922, 2001.

[92] Feigl EO. *Coronary physiology*. Physiol Rev 63: 1-205, 1983.

[93] Feldman MD, Erikson JM, Mao Y, Korcarz CE, Lang RM and Freeman GL. *Validation of a mouse conductance system to determine LV volume: comparison to echocardiography and crystals*. Am J Physiol Heart Circ Physiol 279: H1698-1707, 2000.

[94] Feldman MD, Mao Y, Valvano JW, Pearce JA and Freeman GL. *Development of a multifrequency conductance catheter-based system to determine LV function in mice*. Am J Physiol Heart Circ Physiol 279: H1411-1420, 2000.

[95] Firstenberg MS, Greenberg NL, Main ML, Drinko JK, Odabashian JA, Thomas JD and Garcia MJ. *Determinants of diastolic myocardial tissue Doppler velocities: influences of relaxation and preload*. J Appl Physiol 90: 299-307, 2001.

[96] Firstenberg MS, Levine BD, Garcia MJ, Greenberg NL, Cardon L, Morehead AJ, Zuckerman J and Thomas JD. *Relationship of echocardiographic indices to pulmonary capillary wedge pressures in healthy volunteers*. J Am Coll Cardiol 36: 1664-1669, 2000.

[97] Firstenberg MS, Smedira NG, Greenberg NL, Prior DL, McCarthy PM, Garcia MJ and Thomas JD. *Relationship between early diastolic intraventricular pressure gradients, an index of elastic recoil, and improvements in systolic and diastolic function*. Circulation 104: I330-335, 2001.

[98] Frank O. *Zur Dynamik des Herzmuskels*. Z Biol 37: 370-447, 1895.

[99] Fromageau J, Brusseau E, Vray D, Gimenez G and Delachartre P. *Characterization of PVA cryogel for intravascular ultrasound elasticity imaging*. IEEE Trans Ultrason Ferroelectr Freq Control 50: 1318-1324, 2003.

[100] Gaasch WH. *Diagnosis and treatment of heart failure based on left ventricular systolic or diastolic dysfunction*. Jama 271: 1276-1280, 1994.

[101] Gaasch WH, Blaustein AS, Andrias CW, Donahue RP and Avitall B. *Myocardial relaxation. II. Hemodynamic determinants of rate of left ventricular isovolumic pressure decline*. Am J Physiol 239: H1-6, 1980.

[102] Gaasch WH and Zile MR. *Left ventricular diastolic dysfunction and diastolic heart failure*. Annu Rev Med 55: 373-394, 2004.

[103] Gaasch WH, Zile MR, Hoshino PK, Apstein CS and Blaustein AS. *Stress-shortening relations and myocardial blood flow in compensated and failing canine hearts with pressure-overload hypertrophy*. Circulation 79: 872-883, 1989.

[104] Garcia MJ, Ares MA, Asher C, Rodriguez L, Vandervoort P and Thomas JD. *An index of early left ventricular filling that combined with pulsed Doppler peak E velocity may estimate capillary wedge pressure*. J Am Coll Cardiol 29: 448-454, 1997.

[105] Garcia MJ, Rodriguez L, Ares M, Griffin BP, Thomas JD and Klein AL. *Differentiation of constrictive pericarditis from restrictive cardiomyopathy: assessment of left ventricular diastolic velocities in longitudinal axis by Doppler tissue imaging*. J Am Coll Cardiol 27: 108-114, 1996.

[106] Garcia MJ, Smedira NG, Greenberg NL, Main M, Firstenberg MS, Odabashian J and Thomas JD. *Color M-mode Doppler flow propagation velocity is a preload insensitive index of left ventricular relaxation: animal and human validation*. J Am Coll Cardiol 35: 201-208, 2000.

[107] Garcia MJ, Thomas JD and Klein AL. *New Doppler echocardiographic applications for the study of diastolic function*. J Am Coll Cardiol 32: 865-875, 1998.

[108] Garot J, Pascal O, Diebold B, Derumeaux G, Gerber BL, Dubois-Rande JL, Lima JA and Gueret P. *Alterations of systolic left ventricular twist after acute myocardial infarction*. Am J Physiol Heart Circ Physiol 282: H357-362, 2002.

[109] Georgakopoulos D and Kass D. *Assessment of Cardiovascular Function in the Mouse Using Pressure-Volume Relationships*. Acta Cardiol Sin 101-112, 2002.

[110] Georgakopoulos D and Kass D. *Minimal force-frequency modulation of inotropy and relaxation of in situ murine heart*. J Physiol 534: 535-545, 2001.

[111] Georgakopoulos D and Kass DA. *Estimation of parallel conductance by dual-frequency conductance catheter in mice*. Am J Physiol Heart Circ Physiol 279: H443-450, 2000.

[112] Georgakopoulos D, Mitzner WA, Chen CH, Byrne BJ, Millar HD, Hare JM and Kass DA. *In vivo murine left ventricular pressure-volume relations by miniaturized conductance micromanometry*. Am J Physiol 274: H1416-1422, 1998.

[113] Gewirtz H. *Fractional flow reserve*. Circulation 94: 2306-2307, 1996.

[114] Gibbons Kroeker CA, Tyberg JV and Beyar R. *Effects of load manipulations, heart rate, and contractility on left ventricular apical rotation. An experimental study in anesthetized dogs*. Circulation 92: 130-141, 1995.

[115] Gibson DG and Francis DP. *Clinical assessment of left ventricular diastolic function.* Heart 89: 231-238, 2003.

[116] Gilbert JC and Glantz SA. *Determinants of left ventricular filling and of the diastolic pressure-volume relation.* Circ Res 64: 827-852, 1989.

[117] Gillebert TC, Leite-Moreira AF and De Hert SG. *Relaxation-systolic pressure relation. A load-independent assessment of left ventricular contractility.* Circulation 95: 745-752, 1997.

[118] Gopakumaran B, Petre JH, Sturm B, White RD and Murray PA. *Estimation of current leakage in left and right ventricular conductance volumetry using a dynamic finite element model.* IEEE Trans Biomed Eng 47: 1476-1486, 2000.

[119] Gordon AM, Huxley AF and Julian FJ. *The variation in isometric tension with sarcomere length in vertebrate muscle fibres.* J Physiol 184: 170-192, 1966.

[120] Gould KL. *Pressure-flow characteristics of coronary stenoses in unsedated dogs at rest and during coronary vasodilation.* Circ Res 43: 242-253, 1978.

[121] Gould KL, Kirkeeide RL and Buchi M. *Coronary flow reserve as a physiologic measure of stenosis severity.* J Am Coll Cardiol 15: 459-474, 1990.

[122] Gould KL, Lipscomb K and Hamilton GW. *Physiologic basis for assessing critical coronary stenosis. Instantaneous flow response and regional distribution during coronary hyperemia as measures of coronary flow reserve.* Am J Cardiol 33: 87-94, 1974.

[123] Greenberg NL, Vandervoort PM, Firstenberg MS, Garcia MJ and Thomas JD. *Estimation of diastolic intraventricular pressure gradients by Doppler M-mode echocardiography.* Am J Physiol Heart Circ Physiol 280: H2507-2515, 2001.

[124] Greenberg NL, Vandervoort PM and Thomas JD. *Instantaneous diastolic transmitral pressure differences from color Doppler M mode echocardiography.* Am J Physiol 271: H1267-1276, 1996.

[125] Grossman W, Braunwald E, Mann T, McLaurin LP and Green LH. *Contractile state of the left ventricle in man as evaluated from end-systolic pressure-volume relations.* Circulation 56: 845-852, 1977.

[126] Gruberg L, Mintz GS, Satler LF, Kent KM, Pichard AD and Leon MB. *Intravascular imaging and physiologic lesion assessment to define critical coronary stenoses.* Ann Thorac Surg 68: 1547-1551, 1999.

[127] Guccione JM, Costa KD and McCulloch AD. *Finite element stress analysis of left ventricular mechanics in the beating dog heart.* J Biomech 28: 1167-1177, 1995.

[128] Guyton AC. *Textbook of medical physiology (7th ed.).* Philadelphia: W. B. Suanders Company, 1986, p. 150-164.

[129] Hasegawa H, Little WC, Ohno M, Brucks S, Morimoto A, Cheng HJ and Cheng CP. *Diastolic mitral annular velocity during the development of heart failure.* J Am Coll Cardiol 41: 1590-1597, 2003.

[130] Hayward CS, Kalnins WV and Kelly RP. *Gender-related differences in left ventricular chamber function.* Cardiovasc Res 49: 340-350, 2001.

[131] Heimdal A, Stoylen A, Torp H and Skjaerpe T. *Real-time strain rate imaging of the left ventricle by ultrasound.* J Am Soc Echocardiogr 11: 1013-1019, 1998.

[132] Helle-Valle T, Crosby J, Edvardsen T, Lyseggen E, Amundsen BH, Smith HJ, Rosen BD, Lima JA, Torp H, Ihlen H and Smiseth OA. *New noninvasive method for assessment of left ventricular rotation: speckle tracking echocardiography.* Circulation 112: 3149-3156, 2005.

[133] Hellyer PW. *Use of a conductance catheter to assess the effect of endotoxemia on left ventricular end-systolic pressure-volume relationships in anesthetized swine.* Am J Vet Res 55: 458-464, 1994.

[134] Helmes M, Lim CC, Liao R, Bharti A, Cui L and Sawyer DB. *Titin determines the Frank-Starling relation in early diastole.* J Gen Physiol 121: 97-110, 2003.

[135] Henry FS, Shortland AP, Iudicello F, Black RA, Jarvis JC, Collins MW and Salmons S. *Flow in a simple model skeletal muscle ventricle: comparison between numerical and physical simulations.* J Biomech Eng 119: 13-19, 1997.

[136] Hoffman JI and Spaan JA. *Pressure-flow relations in coronary circulation*. Physiol Rev 70: 331-390., 1990.

[137] Hunter P and Arts T. *Tissue remodeling with micro-structurally based material laws*. Adv Exp Med Biol 430: 215-225, 1997.

[138] Hunter PJ, Pullan AJ and Smaill BH. *Modeling total heart function*. Annu Rev Biomed Eng 5: 147-177, 2003.

[139] Hurrell DG, Nishimura RA, Ilstrup DM and Appleton CP. *Utility of preload alteration in assessment of left ventricular filling pressure by Doppler echocardiography: a simultaneous catheterization and Doppler echocardiographic study*. J Am Coll Cardiol 30: 459-467, 1997.

[140] Igarashi Y and Suga H. *Assessment of slope of end-systolic pressure-volume line of in situ dog heart*. Am J Physiol 250: H685-692, 1986.

[141] Ingels NB, Jr., Daughters GT, 2nd, Stinson EB and Alderman EL. *Measurement of midwall myocardial dynamics in intact man by radiography of surgically implanted markers*. Circulation 52: 859-867, 1975.

[142] Ingels NB, Jr., Hansen DE, Daughters GT, 2nd, Stinson EB, Alderman EL and Miller DC. *Relation between longitudinal, circumferential, and oblique shortening and torsional deformation in the left ventricle of the transplanted human heart*. Circ Res 64: 915-927, 1989.

[143] Isaaz K, Munoz del Romeral L, Lee E and Schiller NB. *Quantitation of the motion of the cardiac base in normal subjects by Doppler echocardiography*. J Am Soc Echocardiogr 6: 166-176, 1993.

[144] Jamal F, Strotmann J, Weidemann F, Kukulski T, D'Hooge J, Bijnens B, Van de Werf F, De Scheerder I and Sutherland GR. *Noninvasive quantification of the contractile reserve of stunned myocardium by ultrasonic strain rate and strain*. Circulation 104: 1059-1065, 2001.

[145] Jamal F, Szilard M, Kukulski T, Liu XS, D'Hooge J, Bijnens B, Rademakers F, Hatle L, Descheerder I and Sutherland GR. *Changes in systolic and postsystolic wall thickening during acute coronary occlusion and reperfusion in closed-chest pigs: Implications for the assessment of regional myocardial function*. J Am Soc Echocardiogr 14: 691-697, 2001.

[146] James JF, Hewett TE and Robbins J. *Cardiac physiology in transgenic mice*. Circ Res 82: 407-415, 1998.

[147] Jensen JA. *Estimation of Blood Velocities Using Ultrasound*. Cambridge, UK: Cambridge Univ. Press, 1996.

[148] Jerri AJ. *Shannon Sampling Theorem - Its Various Extensions and Applications - Tutorial Review*. Proceedings of the Ieee 65: 1565-1596, 1977.

[149] Jessup M and Brozena S. *Heart failure*. N Engl J Med 348: 2007-2018, 2003.

[150] Kaluzynski K, Chen X, Emelianov SY, Skovoroda AR and O'Donnell M. *Strain rate imaging using two-dimensional speckle tracking*. IEEE Trans Ultrason Ferroelectr Freq Control 48: 1111-1123, 2001.

[151] Kameyama T, Chen Z, Bell SP, Fabian J and LeWinter MM. *Mechanoenergetic studies in isolated mouse hearts*. Am J Physiol 274: H366-374, 1998.

[152] Karliner JS, LeWinter MM, Mahler F, Engler R and O'Rourke RA. *Pharmacologic and hemodynamic influences on the rate of isovolumic left ventricular relaxation in the normal conscious dog*. J Clin Invest 60: 511-521, 1977.

[153] Kasai C, Namekawa K, Koyano A and Omoto R. *Real-Time Two-Dimensional Blood-Flow Imaging Using an Auto-Correlation Technique*. Ieee Transactions on Sonics and Ultrasonics 32: 458-464, 1985.

[154] Kass DA, Beyar R, Lankford E, Heard M, Maughan WL and Sagawa K. *Influence of contractile state on curvilinearity of in situ end-systolic pressure-volume relations*. Circulation 79: 167-178, 1989.

[155] Kass DA, Hare JM and Georgakopoulos D. *Murine cardiac function: a cautionary tail*. Circ Res 82: 519-522, 1998.

[156] Kass DA and Maughan WL. *From 'Emax' to pressure-volume relations: a broader view*. Circulation 77: 1203-1212, 1988.

[157] Katz AM and Zile MR. *New molecular mechanism in diastolic heart failure*. Circulation 113: 1922-1925, 2006.

[158] Katz LN. *The role played by the ventricular relaxation process in filling the ventricle*. Am J Physiol Heart Circ Physiol 95: 542-553, 1930.

[159] Katz MA. *Physiology of the heart*. Lippincot Williams & Wilkins, 2000.

[160] Kawaguchi O, Pae WE, Daily WB, Sapirstein JS and Pierce WS. *Left ventricular mechanoenergetics during asynchronous left atrial-to-aortic bypass. Effects of pumping rate on cardiac workload and myocardial oxygen consumption*. J Thorac Cardiovasc Surg 110: 793-799, 1995.

[161] Kelly RP, Ting CT, Yang TM, Liu CP, Maughan WL, Chang MS and Kass DA. *Effective arterial elastance as index of arterial vascular load in humans*. Circulation 86: 513-521, 1992.

[162] Kern MJ. *Coronary physiology revisited : practical insights from the cardiac catheterization laboratory*. Circulation 101: 1344-1351, 2000.

[163] Kern MJ, Lerman A, Bech JW, De Bruyne B, Eeckhout E, Fearon WF, Higano ST, Lim MJ, Meuwissen M, Piek JJ, Pijls NH, Siebes M and Spaan JA. *Physiological assessment of coronary artery disease in the cardiac catheterization laboratory: a scientific statement from the American Heart Association Committee on Diagnostic and Interventional Cardiac Catheterization, Council on Clinical Cardiology*. Circulation 114: 1321-1341, 2006.

[164] Khouri SJ, Maly GT, Suh DD and Walsh TE. *A practical approach to the echocardiographic evaluation of diastolic function*. J Am Soc Echocardiogr 17: 290-297, 2004.

[165] Kiechl S and Willeit J. *The natural course of atherosclerosis. Part I: incidence and progression*. Arterioscler Thromb Vasc Biol 19: 1484-1490, 1999.

[166] Kilner PJ, Yang GZ, Wilkes AJ, Mohiaddin RH, Firmin DN and Yacoub MH. *Asymmetric redirection of flow through the heart*. Nature 404: 759-761, 2000.

[167] Kim WY, Walker PG, Pedersen EM, Poulsen PK, Oyre S, Houlind K and Yoganathan AP. *Left-Ventricular Blood-Flow Patterns in Normal Subjects - a Quantitative-Analysis by 3-Dimensional Magnetic-Resonance Velocity Mapping*. J Am Coll Cardiol 26: 224-238, 1995.

[168] Kjorstad KE, Korvald C and Myrmel T. *Pressure-volume-based single-beat estimations cannot predict left ventricular contractility in vivo*. Am J Physiol Heart Circ Physiol 282: H1739-1750, 2002.

[169] Klocke FJ, Mates RE, Canty JM, Jr. and Ellis AK. *Coronary pressure-flow relationships. Controversial issues and probable implications*. Circ Res 56: 310-323., 1985.

[170] Knowlton FP and Starling EH. *The influence of variations in temperature and blood-pressure on the performance of the isolated mammalian heart*. J Physiol Lond 44: 206-219, 1912.

[171] Kocica MJ, Corno AF, Carreras-Costa F, Ballester-Rodes M, Moghbel MC, Cueva CN, Lackovic V, Kanjuh VI and Torrent-Guasp F. *The helical ventricular myocardial band: global, three-dimensional, functional architecture of the ventricular myocardium*. Eur J Cardiothorac Surg 29 Suppl 1: S21-40, 2006.

[172] Kornet L, Schreuder JJ, van der Velde ET, Baan J and Jansen JR. *A new approach to determine parallel conductance for left ventricular volume measurements*. Cardiovasc Res 48: 455-463, 2000.

[173] Korteweg DJ. *Uber die Fortpflanzungsgeschwindigkeit des Schalles in Elastichen Rohren*. Ann Phys Chem 5: 525–537, 1879.

[174] Krams R, Sipkema P and Westerhof N. *Varying elastance concept may explain coronary systolic flow impediment*. Am J Physiol 257: H1471-1479, 1989.

[175] Kroeker CA, Tyberg JV and Beyar R. *Effects of ischemia on left ventricular apex rotation. An experimental study in anesthetized dogs*. Circulation 92: 3539-3548, 1995.

[176] Kuecherer HF, Muhiudeen IA, Kusumoto FM, Lee E, Moulinier LE, Cahalan MK and Schiller NB. *Estimation of mean left atrial pressure from transesophageal pulsed Doppler echocardiography of pulmonary venous flow*. Circulation 82: 1127-1139, 1990.

[177] Kutner MH, Nachtsheim CJ, Neter J and Li W. *Applied linear statistical models (5th ed.)*. Mc Graw Hill College, 2005, p. 76.

[178] Labeit S and Kolmerer B. *Titins: giant proteins in charge of muscle ultrastructure and elasticity*. Science 270: 293-296, 1995.

[179] Lang RM, Bierig M, Devereux RB, Flachskampf FA, Foster E, Pellikka PA, Picard MH, Roman MJ, Seward J, Shanewise J, Solomon S, Spencer KT, St John Sutton M and Stewart W. *Recommendations for chamber quantification*. Eur J Echocardiogr 7: 79-108, 2006.

[180] Langeland S, D'Hooge J, Claessens T, Claus P, Verdonck P, Suetens P, Sutherland GR and Bijnens B. *RF-based two-dimensional cardiac strain estimation: a validation study in a tissue-mimicking phantom*. IEEE Trans Ultrason Ferroelectr Freq Control 51: 1537-1546, 2004.

[181] Langeland S, D'Hooge J, Torp H, Bijnens B and Suetens P. *Comparison of time-domain displacement estimators for two-dimensional RF tracking*. Ultrasound Med Biol 29: 1177-1186, 2003.

[182] Langeland S, D'Hooge J, Wouters PF, Leather HA, Claus P, Bijnens B and Sutherland GR. *Experimental validation of a new ultrasound method for the simultaneous assessment of radial and longitudinal myocardial deformation independent of insonation angle*. Circulation 112: 2157-2162, 2005.

[183] Lankford EB, Kass DA, Maughan WL and Shoukas AA. *Does volume catheter parallel conductance vary during a cardiac cycle?* Am J Physiol 258: H1933-1942, 1990.

[184] Lanoye LL, Vierendeels JA, Segers P and Verdonck PR. *Wave intensity analysis of left ventricular filling*. J Biomech Eng 127: 862-867, 2005.

[185] Leblanc N, Chartier D, Gosselin H and Rouleau JL. *Age and gender differences in excitation-contraction coupling of the rat ventricle*. J Physiol 511 (Pt 2): 533-548, 1998.

[186] Lee S, Ohga Y, Tachibana H, Syuu Y, Ito H, Harada M, Suga H and Takaki M. *Effects of myosin isozyme shift on curvilinearity of the left ventricular end-systolic pressure-volume relation of In situ rat hearts*. Jpn J Physiol 48: 445-455, 1998.

[187] Legrice IJ, Hunter PJ and Smaill BH. *Laminar structure of the heart: a mathematical model*. Am J Physiol 272: H2466-2476, 1997.

[188] LeGrice IJ, Smaill BH, Chai LZ, Edgar SG, Gavin JB and Hunter PJ. *Laminar structure of the heart: ventricular myocyte arrangement and connective tissue architecture in the dog*. Am J Physiol 269: H571-582, 1995.

[189] Leinwand LA. *Sex is a potent modifier of the cardiovascular system*. J Clin Invest 112: 302-307, 2003.

[190] Leite-Moreira AF. *Current perspectives in diastolic dysfunction and diastolic heart failure*. Heart 92: 712-718, 2006.

[191] Lemmon JD and Yoganathan AP. *Three-dimensional computational model of left heart diastolic function with fluid-structure interaction*. J Biomech Eng 122: 109-117, 2000.

[192] Lenther C. *Geigy scientific tables*. Basel: Ciba Geigy Limited, 1990.

[193] Levick JR. *An Introduction to Cardiovascular Physiology, 2nd edition*. Oxford: Butterworth-Heinemann, 1995, p. 326.

[194] Lew WY and Rasmussen CM. *Influence of nonuniformity on rate of left ventricular pressure fall in the dog*. Am J Physiol 256: H222-232, 1989.

[195] Lim MJ and Kern MJ. *Coronary pathophysiology in the cardiac catheterization laboratory*. Curr Probl Cardiol 31: 493-550, 2006.

[196] Ling D, Rankin JS, Edwards CH, 2nd, McHale PA and Anderson RW. *Regional diastolic mechanics of the left ventricle in the conscious dog*. Am J Physiol 236: H323-330, 1979.

[197] Lips DJ, van der Nagel T, Steendijk P, Palmen M, Janssen BJ, van Dantzig JM, de Windt LJ and Doevendans PA. *Left ventricular pressure-volume measurements in mice: comparison of closed-chest versus open-chest approach*. Basic Res Cardiol 99: 351-359, 2004.

[198] Little WC. *Diastolic dysfunction beyond distensibility: adverse effects of ventricular dilatation*. Circulation 112: 2888-2890, 2005.

[199] Little WC and Freeman GL. *Description of LV pressure-volume relations by time-varying elastance and source resistance*. Am J Physiol 253: H83-90, 1987.

[200] Little WC, Ohno M, Kitzman DW, Thomas JD and Cheng CP. *Determination of left ventricular chamber stiffness from the time for deceleration of early left ventricular filling*. Circulation 92: 1933-1939, 1995.

[201] Lorell BH, Paulus WJ, Grossman W, Wynne J and Cohn PF. *Modification of abnormal left ventricular diastolic properties by nifedipine in patients with hypertrophic cardiomyopathy*. Circulation 65: 499-507, 1982.

[202] Lunkenheimer PP, Redmann K and Anderson RH. *The architecture of the ventricular mass and its functional implications for organ-preserving surgery*. Eur J Cardiothorac Surg 27: 183-190, 2005.

[203] Massie BM and Shah NB. *Evolving trends in the epidemiologic factors of heart failure: rationale for preventive strategies and comprehensive disease management*. Am Heart J 133: 703-712, 1997.

[204] Mates RE, Gupta RL, Bell AC and Klocke FJ. *Fluid dynamics of coronary artery stenosis*. Circ Res 42: 152-162, 1978.

[205] Matsubara H, Takaki M, Yasuhara S, Araki J and Suga H. *Logistic time constant of isovolumic relaxation pressure-time curve in the canine left ventricle. Better alternative to exponential time constant*. Circulation 92: 2318-2326, 1995.

[206] Matsuda Y, Toma Y, Moritani K, Ogawa H, Kohno M, Miura T, Matsuda M, Matsuzaki M, Fujii H and Kusukawa R. *Assessment of left atrial function in patients with hypertensive heart disease*. Hypertension 8: 779-785, 1986.

[207] Matthys K, Carlier S, Segers P, Ligthart J, Sianos G, Serrano P, Verdonck PR and Serruys PW. *In vitro study of FFR, QCA, and IVUS for the assessment of optimal stent deployment*. Catheter Cardiovasc Interv 54: 363-375., 2001.

[208] Maughan WL, Sunagawa K and Sagawa K. *Effects of arterial input impedance on mean ventricular pressure-flow relation*. Am J Physiol 247: H978-983, 1984.

[209] McGinn AL, White CW and Wilson RF. *Interstudy variability of coronary flow reserve. Influence of heart rate, arterial pressure, and ventricular preload*. Circulation 81: 1319-1330, 1990.

[210] Mego DM, DeGeare VS, Nottestad SY, Lamanna VP, Oneschuk LC, Rubal BJ and Zabalgoitia M. *Variation of flow propagation velocity with age*. J Am Soc Echocardiogr 11: 20-25, 1998.

[211] Meneveau N, Di Mario C, Gil R, de Jaegere P, de Feyter PJ, Roelandt J and Serruys PW. *Instantaneous pressure-velocity relationship of the coronary flow, alternative to coronary reserve measurement: a feasibility study and reproducibility of the method*. Arch Mal Coeur Vaiss 86: 975-985., 1993.

[212] Messina LM, Hanley FL, Uhlig PN, Baer RW, Grattan MT and Hoffman JI. *Effects of pressure gradients between branches of the left coronary artery on the pressure axis intercept and the shape of steady state circumflex pressure-flow relations in dogs*. Circ Res 56: 11-19, 1985.

[213] Meuwissen M, Chamuleau SA, Siebes M, Schotborgh CE, Koch KT, de Winter RJ, Bax M, de Jong A, Spaan JA and Piek JJ. *Role of variability in microvascular resistance on fractional flow reserve and coronary blood flow velocity reserve in intermediate coronary lesions*. Circulation 103: 184-187, 2001.

[214] Meuwissen M, Siebes M, Chamuleau SA, van Eck-Smit BL, Koch KT, de Winter RJ, Tijssen JG, Spaan JA and Piek JJ. *Hyperemic stenosis resistance index for evaluation of functional coronary lesion severity*. Circulation 106: 441-446, 2002.

[215] Miller DD, Donohue TJ, Younis LT, Bach RG, Aguirre FV, Wittry MD, Goodgold HM, Chaitman BR and Kern MJ. *Correlation of pharmacological 99mTc-sestamibi myocardial perfusion imaging with poststenotic coronary flow reserve in patients with angiographically intermediate coronary artery stenoses*. Circulation 89: 2150-2160, 1994.

[216] Mirro MJ, Rogers EW, Weyman AE and Feigenbaum H. *Angular displacement of the papillary muscles during the cardiac cycle*. Circulation 60: 327-333, 1979.

[217] Mirsky I. *Left ventricular stresses in the intact human heart*. Biophys J 9: 189-208, 1969.

[218] Mirsky I, Tajimi T and Peterson KL. *The development of the entire end-systolic pressure-volume and ejection fraction-afterload relations: a new concept of systolic myocardial stiffness*. Circulation 76: 343-356, 1987.

[219] Miyatake K, Okamoto M, Kinoshita N, Owa M, Nakasone I, Sakakibara H and Nimura Y. *Augmentation of atrial contribution to left ventricular inflow with aging as assessed by intracardiac Doppler flowmetry*. Am J Cardiol 53: 586-589, 1984.

[220] Moon MR, Ingels NB, Jr., Daughters GT, 2nd, Stinson EB, Hansen DE and Miller DC. *Alterations in left ventricular twist mechanics with inotropic stimulation and volume loading in human subjects*. Circulation 89: 142-150, 1994.

[221] Mottram PM and Marwick TH. *Assessment of diastolic function: what the general cardiologist needs to know*. Heart 91: 681-695, 2005.

[222] Mur G and Baan J. *Computation of the input impedances of a catheter for cardiac volumetry*. IEEE Trans Biomed Eng 31: 448-453, 1984.

[223] Nagel E, Stuber M, Burkhard B, Fischer SE, Scheidegger MB, Boesiger P and Hess OM. *Cardiac rotation and relaxation in patients with aortic valve stenosis*. Eur Heart J 21: 582-589, 2000.

[224] Nagueh SF, Bachinski LL, Meyer D, Hill R, Zoghbi WA, Tam JW, Quinones MA, Roberts R and Marian AJ. *Tissue Doppler imaging consistently detects myocardial abnormalities in patients with hypertrophic cardiomyopathy and provides a novel means for an early diagnosis before and independently of hypertrophy*. Circulation 104: 128-130, 2001.

[225] Nagueh SF, Kopelen HA and Quinones MA. *Assessment of left ventricular filling pressures by Doppler in the presence of atrial fibrillation*. Circulation 94: 2138-2145, 1996.

[226] Nagueh SF, Kopelen HA and Zoghbi WA. *Feasibility and accuracy of Doppler echocardiographic estimation of pulmonary artery occlusive pressure in the intensive care unit*. Am J Cardiol 75: 1256-1262, 1995.

[227] Nagueh SF, Lakkis NM, Middleton KJ, Spencer WH, 3rd, Zoghbi WA and Quinones MA. *Doppler estimation of left ventricular filling pressures in patients with hypertrophic cardiomyopathy*. Circulation 99: 254-261, 1999.

[228] Nagueh SF, Middleton KJ, Kopelen HA, Zoghbi WA and Quinones MA. *Doppler tissue imaging: a noninvasive technique for evaluation of left ventricular relaxation and estimation of filling pressures*. J Am Coll Cardiol 30: 1527-1533, 1997.

[229] Nagueh SF, Mikati I, Kopelen HA, Middleton KJ, Quinones MA and Zoghbi WA. *Doppler estimation of left ventricular filling pressure in sinus tachycardia. A new application of tissue doppler imaging*. Circulation 98: 1644-1650, 1998.

[230] Nagueh SF, Sun H, Kopelen HA, Middleton KJ and Khoury DS. *Hemodynamic determinants of the mitral annulus diastolic velocities by tissue Doppler*. J Am Coll Cardiol 37: 278-285, 2001.

[231] Nakamura M, Wada S, Mikami T, Kitabatake A and Karino T. *Computational study on the evolution of an intraventricular vortical flow during early diastole for the interpretation of color M-mode Doppler echocardiograms*. Biomech Model Mechanobiol 2: 59-72, 2003.

[232] Nakamura T, Kimura T, Arai S, Motomiya M and Suzuki N. *Left ventricular function of concentric hypertrophied heart after chronic pressure overload as studied in the isolated canine heart preparation*. Jpn J Physiol 34: 613-628, 1984.

[233] Nikolic S, Yellin EL, Tamura K, Vetter H, Tamura T, Meisner JS and Frater RW. *Passive properties of canine left ventricle: diastolic stiffness and restoring forces*. Circ Res 62: 1210-1222, 1988.

[234] Nikolic SD, Feneley MP, Pajaro OE, Rankin JS and Yellin EL. *Origin of regional pressure gradients in the left ventricle during early diastole*. Am J Physiol 268: H550-557, 1995.

[235] Nishimura RA, Housmans PR, Hatle LK and Tajik AJ. *Assessment of diastolic function of the heart: background and current applications of Doppler echocardiography. Part I. Physiologic and pathophysiologic features*. Mayo Clin Proc 64: 71-81, 1989.

[236] Nishimura RA and Tajik AJ. *Evaluation of diastolic filling of left ventricle in health and disease: Doppler echocardiography is the clinician's Rosetta Stone*. J Am Coll Cardiol 30: 8-18, 1997.

[237] Notomi Y, Lysyansky P, Setser RM, Shiota T, Popovic ZB, Martin-Miklovic MG, Weaver JA, Oryszak SJ, Greenberg NL, White RD and Thomas JD. *Measurement of ventricular torsion by two-dimensional ultrasound speckle tracking imaging*. J Am Coll Cardiol 45: 2034-2041, 2005.

[238] Notomi Y, Martin-Miklovic MG, Oryszak SJ, Shiota T, Deserranno D, Popovic ZB, Garcia MJ, Greenberg NL and Thomas JD. *Enhanced ventricular untwisting during exercise: a mechanistic manifestation of elastic recoil described by Doppler tissue imaging*. Circulation 113: 2524-2533, 2006.

[239] Notomi Y, Setser RM, Shiota T, Martin-Miklovic MG, Weaver JA, Popovic ZB, Yamada H, Greenberg NL, White RD and Thomas JD. *Assessment of left ventricular torsional deformation by Doppler tissue imaging: validation study with tagged magnetic resonance imaging*. Circulation 111: 1141-1147, 2005.

[240] Oh JK, Seward JB and Tajik AJ. *The Echo Manual. Second edition*. Philadelphia, Pa: Lippincott Williams & Wilkins, 1999.

[241] Oki T, Tabata T, Yamada H, Wakatsuki T, Mishiro Y, Abe M, Onose Y, Iuchi A and Ito S. *Left ventricular diastolic properties of hypertensive patients measured by pulsed tissue Doppler imaging*. J Am Soc Echocardiogr 11: 1106-1112, 1998.

[242] Oki T, Tabata T, Yamada H, Wakatsuki T, Shinohara H, Nishikado A, Iuchi A, Fukuda N and Ito S. *Clinical application of pulsed Doppler tissue imaging for assessing abnormal left ventricular relaxation*. Am J Cardiol 79: 921-928, 1997.

[243] Ommen SR, Nishimura RA, Appleton CP, Miller FA, Oh JK, Redfield MM and Tajik AJ. *Clinical utility of Doppler echocardiography and tissue Doppler imaging in the estimation of left ventricular filling pressures: A comparative simultaneous Doppler-catheterization study*. Circulation 102: 1788-1794, 2000.

[244] Osman NF, Kerwin WS, McVeigh ER and Prince JL. *Cardiac motion tracking using CINE harmonic phase (HARP) magnetic resonance imaging*. Magn Reson Med 42: 1048-1060, 1999.

[245] Owan TE and Redfield MM. *Epidemiology of diastolic heart failure*. Prog Cardiovasc Dis 47: 320-332, 2005.

[246] Parmley WW and Sonnenblick EH. *Relation between mechanics of contraction and relaxation in mammalian cardiac muscle*. Am J Physiol 216: 1084-1091, 1969.

[247] Parthenakis FI, Patrianakos AP, Tzerakis PG, Kambouraki DM, Chrysostomakis SI and Vardas PE. *Late left ventricular diastolic flow propagation velocity determined by color M-mode Doppler in the assessment of diastolic dysfunction*. J Am Soc Echocardiogr 17: 139-145, 2004.

[248] Pasipoularides A. *Clinical assessment of ventricular ejection dynamics with and without outflow obstruction*. J Am Coll Cardiol 15: 859-882, 1990.

[249] Patrianakos AP, Parthenakis FI, Mavrakis HE, Zacharis EA and Vardas PE. *Late left ventricular color M-mode Doppler in the assessment of diastolic dysfunction in patients with dilated cardiomyopathy*. J Am Soc Echocardiogr 18: 979, 2005.

[250] Paulus WJ. *How to diagnose diastolic heart failure. European Study Group on Diastolic Heart Failure*. Eur Heart J 19: 990-1003, 1998.

[251] Permut S and Riley RL. *Hemodynamics of Collapsible Vessels With Tone: the Vascular Waterfall*. J Appl Physiol 18: 924-932, 1963.

[252] Peverill RE, Gelman JS, Mottram PM, Moir S, Jankelowitz C, Bain JL and Donelan L. *Factors associated with mitral annular systolic and diastolic velocities in healthy adults*. J Am Soc Echocardiogr 17: 1146-1154, 2004.

[253] Pijls NH, De Bruyne B, Peels K, Van Der Voort PH, Bonnier HJ, Bartunek JKJJ and Koolen JJ. *Measurement of fractional flow reserve to assess the functional severity of coronary-artery stenoses*. N Engl J Med 334: 1703-1708, 1996.

[254] Pijls NH, De Bruyne B, Peels K, Van Der Voort PH, Bonnier HJ, Bartunek JKJJ and Koolen JJ. *Measurement of fractional flow reserve to assess the functional severity of coronary-artery stenoses*. N Engl J Med 334: 1703-1708., 1996.

[255] Pijls NH, Van Gelder B, Van der Voort P, Peels K, Bracke FA, Bonnier HJ and el Gamal MI. *Fractional flow reserve. A useful index to evaluate the influence of an epicardial coronary stenosis on myocardial blood flow*. Circulation 92: 3183-3193, 1995.

[256] Pijls NH, van Son JA, Kirkeeide RL, De Bruyne B and Gould KL. *Experimental basis of determining maximum coronary, myocardial, and collateral blood flow by pressure measurements for assessing functional stenosis severity before and after percutaneous transluminal coronary angioplasty*. Circulation 87: 1354-1367, 1993.

[257] Pijls NHJ and de Bruyne B. *Coronary Pressure*. Dordrecht: Kluwer Academic Publishers, 1997.

[258] Quinones MA. *Assessment of diastolic function*. Prog Cardiovasc Dis 47: 340-355, 2005.

[259] Rademakers FE, Buchalter MB, Rogers WJ, Zerhouni EA, Weisfeldt ML, Weiss JL and Shapiro EP. *Dissociation between left ventricular untwisting and filling. Accentuation by catecholamines*. Circulation 85: 1572-1581, 1992.

[260] Redfield MM, Jacobsen SJ, Borlaug BA, Rodeheffer RJ and Kass DA. *Age- and gender-related ventricular-vascular stiffening: a community-based study*. Circulation 112: 2254-2262, 2005.

[261] Redfield MM, Jacobsen SJ, Burnett JC, Jr., Mahoney DW, Bailey KR and Rodeheffer RJ. *Burden of systolic and diastolic ventricular dysfunction in the community: appreciating the scope of the heart failure epidemic*. Jama 289: 194-202, 2003.

[262] Reyes M, Freeman GL, Escobedo D, Lee S, Steinhelper ME and Feldman MD. *Enhancement of contractility with sustained afterload in the intact murine heart: blunting of length-dependent activation*. Circulation 107: 2962-2968, 2003.

[263] Rhoades RA and Tanner JV. *Medical Physiology*. Lippincott Williams and Wilkins, 2003.

[264] Rietzschel ER, De Buyzere ML, Bekaert S, Segers P, De Bacquer D, Cooman L, Van Damme P, Cassiman P, Langlois M, van Oostveldt P, Verdonck P, De Backer G and Gillebert TC. *Rationale, Design, Methods and Baseline Characteristics of the Asklepios Study*. Department of Cardiovascular Diseases, Ghent University Hospital, De Pintelaan 185, B-9000 Ghent, 2006.

[265] Rivas-Gotz C, Khoury DS, Manolios M, Rao L, Kopelen HA and Nagueh SF. *Time interval between onset of mitral inflow and onset of early diastolic velocity by tissue Doppler: a novel index of left ventricular relaxation: experimental studies and clinical application*. J Am Coll Cardiol 42: 1463-1470, 2003.

[266] Rodevand O, Bjornerheim R, Edvardsen T, Smiseth OA and Ihlen H. *Diastolic flow pattern in the normal left ventricle*. J Am Soc Echocardiogr 12: 500-507, 1999.

[267] Rodriguez EK, Hunter WC, Royce MJ, Leppo MK, Douglas AS and Weisman HF. *A method to reconstruct myocardial sarcomere lengths and orientations at transmural sites in beating canine hearts*. Am J Physiol 263: H293-306, 1992.

[268] Rodriguez L, Garcia M, Ares M, Griffin BP, Nakatani S and Thomas JD. *Assessment of mitral annular dynamics during diastole by Doppler tissue imaging: comparison with mitral Doppler inflow in subjects without heart disease and in patients with left ventricular hypertrophy*. Am Heart J 131: 982-987, 1996.

[269] Rossen JD and Winniford MD. *Effect of increases in heart rate and arterial pressure on coronary flow reserve in humans*. J Am Coll Cardiol 21: 343-348, 1993.

[270] Rossvoll O and Hatle LK. *Pulmonary venous flow velocities recorded by transthoracic Doppler ultrasound: relation to left ventricular diastolic pressures*. J Am Coll Cardiol 21: 1687-1696, 1993.

[271] Rovner A, Greenberg NL, Thomas JD and Garcia MJ. *Relationship of diastolic intraventricular pressure gradients and aerobic capacity in patients with diastolic heart failure*. Am J Physiol Heart Circ Physiol 289: H2081-2088, 2005.

[272] Rovner A, Smith R, Greenberg NL, Tuzcu EM, Smedira N, Lever HM, Thomas JD and Garcia MJ. *Improvement in diastolic intraventricular pressure gradients in patients with HOCM after ethanol septal reduction*. Am J Physiol Heart Circ Physiol 285: H2492-2499, 2003.

[273] Ruan Q, Rao L, Middleton KJ, Khoury DS and Nagueh SF. *Assessment of left ventricular diastolic function by early diastolic mitral annulus peak acceleration rate: experimental studies and clinical application*. J Appl Physiol 100: 679-684, 2006.

[274] Sagawa K. *The end-systolic pressure-volume relation of the ventricle: definition, modifications and clinical use*. Circulation 63: 1223-1227, 1981.

[275] Sagawa K. *The ventricular pressure-volume diagram revisited*. Circ Res 43: 677-687, 1978.

[276] Salo RW, Wallner TG and Pederson BD. *Measurement of ventricular volume by intracardiac impedance: theoretical and empirical approaches*. IEEE Trans Biomed Eng 33: 189-195, 1986.

[277] Sandstede JJ, Johnson T, Harre K, Beer M, Hofmann S, Pabst T, Kenn W, Voelker W, Neubauer S and Hahn D. *Cardiac systolic rotation and contraction before and after valve replacement for aortic stenosis: a myocardial tagging study using MR imaging*. AJR Am J Roentgenol 178: 953-958, 2002.

[278] Sato T, Shishido T, Kawada T, Miyano H, Miyashita H, Inagaki M, Sugimachi M and Sunagawa K. *ESPVR of in situ rat left ventricle shows contractility-dependent curvilinearity*. Am J Physiol 274: H1429-1434, 1998.

[279] Scaramucci J. *Theoremata familiaria viros eruditos consulentia de variis physico-medicis lucubrationibus juxta leges mecanicas*. Apud Joannem Baptistam Bustum 70–81, 1696.

[280] Schmid P, Jaermann T, Boesiger P, Niederer PF, Lunkenheimer PP, Cryer CW and Anderson RH. *Ventricular myocardial architecture as visualised in postmortem swine hearts using magnetic resonance diffusion tensor imaging*. Eur J Cardiothorac Surg 27: 468-472, 2005.

[281] Segers P, Fostier G, Neckebroeck J and Verdonck P. *Assessing coronary artery stenosis severity: in vitro validation of the concept of fractional flow reserve*. Catheter Cardiovasc Interv 46: 375-379., 1999.

[282] Segers P, Georgakopoulos D, Afanasyeva M, Champion HC, Judge DP, Millar HD, Verdonck P, Kass DA, Stergiopulos N and Westerhof N. *Conductance catheter-based assessment of arterial input impedance, arterial function, and ventricular-vascular interaction in mice*. Am J Physiol Heart Circ Physiol 288: H1157-1164, 2005.

[283] Senzaki H, Chen CH and Kass DA. *Single-beat estimation of end-systolic pressure-volume relation in humans. A new method with the potential for noninvasive application*. Circulation 94: 2497-2506, 1996.

[284] Shishido T, Hayashi K, Shigemi K, Sato T, Sugimachi M and Sunagawa K. *Single-beat estimation of end-systolic elastance using bilinearly approximated time-varying elastance curve*. Circulation 102: 1983-1989, 2000.

[285] Shortland AP, Black RA, Jarvis JC, Henry FS, Iudicello F, Collins MW and Salmons S. *Formation and travel of vortices in model ventricles: application to the design of skeletal muscle ventricles*. J Biomech 29: 503-511, 1996.

[286] Shung KK. *Diagnostic Ultrasound: Imaging and Blood Flow Measurements*. Boca Raton: Taylor & Francis Group, 2006, p. 215.

[287] Siebes M, Chamuleau SA, Meuwissen M, Piek JJ and Spaan JA. *Influence of hemodynamic conditions on fractional flow reserve: parametric analysis of underlying model*. Am J Physiol Heart Circ Physiol 283: H1462-1470., 2002.

[288] Smith NP. *A computational study of the interaction between coronary blood flow and myocardial mechanics*. Physiol Meas 25: 863-877, 2004.

[289] Sodums MT, Badke FR, Starling MR, Little WC and O'Rourke RA. *Evaluation of left ventricular contractile performance utilizing end-systolic pressure-volume relationships in conscious dogs*. Circ Res 54: 731-739, 1984.

[290] Sohn DW, Chai IH, Lee DJ, Kim HC, Kim HS, Oh BH, Lee MM, Park YB, Choi YS, Seo JD and Lee YW. *Assessment of mitral annulus velocity by Doppler tissue imaging in the evaluation of left ventricular diastolic function*. J Am Coll Cardiol 30: 474-480, 1997.

[291] Sohn DW, Kim YJ, Park YB and Choi YS. *Clinical validity of measuring time difference between onset of mitral inflow and onset of early diastolic mitral annulus velocity in the evaluation of left ventricular diastolic function*. J Am Coll Cardiol 43: 2097-2101, 2004.

[292] Solomon SB, Nikolic SD, Frater RW and Yellin EL. *Contraction-relaxation coupling: determination of the onset of diastole*. Am J Physiol 277: H23-27, 1999.

[293] Spaan JA. *Coronary diastolic pressure-flow relation and zero flow pressure explained on the basis of intramyocardial compliance*. Circ Res 56: 293-309., 1985.

[294] Spaan JA, Breuls NP and Laird JD. *Diastolic-systolic coronary flow differences are caused by intramyocardial pump action in the anesthetized dog*. Circ Res 49: 584-593, 1981.

[295] Spaan JA, Piek JJ, Hoffman JI and Siebes M. *Physiological basis of clinically used coronary hemodynamic indices*. Circulation 113: 446-455, 2006.

[296] Spotnitz HM. *Macro design, structure, and mechanics of the left ventricle*. J Thorac Cardiovasc Surg 119: 1053-1077, 2000.

[297] Srivastava PM, Burrell LM and Calafiore P. *Lateral vs medial mitral annular tissue Doppler in the echocardiographic assessment of diastolic function and filling pressures: which should we use?* Eur J Echocardiogr 6: 97-106, 2005.

[298] Steen T and Steen S. *Filling of a model left ventricle studied by colour M mode Doppler*. Cardiovasc Res 28: 1821-1827, 1994.

[299] Steendijk P, Tulner SA, Schreuder JJ, Bax JJ, van Erven L, van der Wall EE, Dion RA, Schalij MJ and Baan J. *Quantification of left ventricular mechanical dyssynchrony by conductance catheter in heart failure patients*. Am J Physiol Heart Circ Physiol 286: H723-730, 2004.

[300] Stevens C, Remme E, LeGrice I and Hunter P. *Ventricular mechanics in diastole: material parameter sensitivity*. J Biomech 36: 737-748, 2003.

[301] Stoylen A, Skjelvan G and Skjaerpe T. *Flow propagation velocity is not a simple index of diastolic function in early filling. A comparative study of early diastolic strain rate and strain rate propagation, flow and flow propagation in normal and reduced diastolic function*. Cardiovasc Ultrasound 1: 3, 2003.

[302] Stoylen A, Slordahl S, Skjelvan GK, Heimdal A and Skjaerpe T. *Strain rate imaging in normal and reduced diastolic function: comparison with pulsed Doppler tissue imaging of the mitral annulus*. J Am Soc Echocardiogr 14: 264-274, 2001.

[303] Strackee J and Westerhof N. *The Physics of Heart and Circulation*. Institute of Physics Publishing Bristol and Philadelphia, 1993, p. 502.

[304] Streeter DD, Jr., Spotnitz HM, Patel DP, Ross J, Jr. and Sonnenblick EH. *Fiber orientation in the canine left ventricle during diastole and systole*. Circ Res 24: 339-347, 1969.

[305] Stugaard M, Greenberg NL, Vandervoort PM, Christian RL, FouadTarazi F and Thomas JD. *Automatic quantification of color Doppler M-mode filling patterns of the left ventricle*. J Am Coll Cardiol 29: 7023-7023, 1997.

[306] Stugaard M, Smiseth OA, Risoe C and Ihlen H. *Intraventricular early diastolic filling during acute myocardial ischemia, assessment by multigated color m-mode Doppler echocardiography*. Circulation 88: 2705-2713, 1993.

[307] Stull LB, Leppo MK, Marban E and Janssen PM. *Physiological determinants of contractile force generation and calcium handling in mouse myocardium*. J Mol Cell Cardiol 34: 1367-1376, 2002.

[308] Su JB and Crozatier B. *Preload-induced curvilinearity of left ventricular end-systolic pressure-volume relations. Effects on derived indexes in closed-chest dogs*. Circulation 79: 431-440, 1989.

[309] Suga H. *Cardiac energetics: from E(max) to pressure-volume area.* Clin Exp Pharmacol Physiol 30: 580-585, 2003.

[310] Suga H. *Total mechanical energy of a ventricle model and cardiac oxygen consumption*. Am J Physiol 236: H498-505, 1979.

[311] Suga H. *Ventricular energetics*. Physiol Rev 70: 247-277, 1990.

[312] Suga H, Hayashi T and Shirahata M. *Ventricular systolic pressure-volume area as predictor of cardiac oxygen consumption*. Am J Physiol 240: H39-44, 1981.

[313] Suga H, Hisano R, Goto Y, Yamada O and Igarashi Y. *Effect of positive inotropic agents on the relation between oxygen consumption and systolic pressure volume area in canine left ventricle*. Circ Res 53: 306-318, 1983.

[314] Suga H and Sagawa K. *Instantaneous pressure-volume relationships and their ratio in the excised, supported canine left ventricle*. Circ Res 35: 117-126, 1974.

[315] Suga H and Sagawa K. *Mathematical interrelationship between instantaneous ventricular pressure-volume ratio and myocardial force-velocity relation*. Ann Biomed Eng 1: 160-181, 1972.

[316] Suga H, Sagawa K and Shoukas AA. *Load independence of the instantaneous pressure-volume ratio of the canine left ventricle and effects of epinephrine and heart rate on the ratio*. Circ Res 32: 314-322, 1973.

[317] Suga H, Yamada O, Goto Y and Igarashi Y. *Peak isovolumic pressure-volume relation of puppy left ventricle*. Am J Physiol 250: H167-172, 1986.

[318] Sunagawa K, Maughan WL, Burkhoff D and Sagawa K. *Left ventricular interaction with arterial load studied in isolated canine ventricle*. Am J Physiol 245: H773-780, 1983.

[319] Sutherland GR, Di Salvo G, Claus P, D'Hooge J and Bijnens B. *Strain and strain rate imaging: a new clinical approach to quantifying regional myocardial function.* J Am Soc Echocardiogr 17: 788-802, 2004.

[320] Sutherland GR, Hatle L, Claus P, D'hooge J and Bijnens BH. *Doppler Myocardial Imaging: A textbook*. 2005, p. 210.

[321] Szwarc RS, Laurent D, Allegrini PR and Ball HA. *Conductance catheter measurement of left ventricular volume: evidence for nonlinearity within cardiac cycle*. Am J Physiol 268: H1490-1498, 1995.

[322] Szwarc RS, Mickleborough LL, Mizuno S, Wilson GJ, Liu P and Mohamed S. *Conductance catheter measurements of left ventricular volume in the intact dog: parallel conductance is independent of left ventricular size*. Cardiovasc Res 28: 252-258, 1994.

[323] Takaoka H, Esposito G, Mao L, Suga H and Rockman HA. *Heart size-independent analysis of myocardial function in murine pressure overload hypertrophy*. Am J Physiol Heart Circ Physiol 282: H2190-2197, 2002.

[324] Takatsuji H, Mikami T, Urasawa K, Teranishi J, Onozuka H, Takagi C, Makita Y, Matsuo H, Kusuoka H and Kitabatake A. *A new approach for evaluation of left ventricular diastolic function: spatial and temporal analysis of left ventricular filling flow propagation by color M-mode Doppler echocardiography*. J Am Coll Cardiol 27: 365-371, 1996.

[325] Teichholz LE, Kreulen T, Herman MV and Gorlin R. *Problems in echocardiographic volume determinations: echocardiographic-angiographic correlations in the presence of absence of asynergy*. Am J Cardiol 37: 7-11, 1976.

[326] Thomas JD, Flachskampf FA, Chen C, Guererro JL, Picard MH, Levine RA and Weyman AE. *Isovolumic relaxation time varies predictably with its time constant and aortic and left atrial pressures: implications for the noninvasive evaluation of ventricular relaxation*. Am Heart J 124: 1305-1313, 1992.

[327] Thomas JD, Newell JB, Choong CY and Weyman AE. *Physical and physiological determinants of transmitral velocity: numerical analysis*. Am J Physiol 260: H1718-1731, 1991.

[328] Thomas JD and Popovic ZB. *Intraventricular pressure differences: a new window into cardiac function*. Circulation 112: 1684-1686, 2005.

[329] Tibayan FA, Lai DT, Timek TA, Dagum P, Liang D, Daughters GT, Ingels NB and Miller DC. *Alterations in left ventricular torsion in tachycardia-induced dilated cardiomyopathy*. J Thorac Cardiovasc Surg 124: 43-49, 2002.

[330] Tibayan FA, Rodriguez F, Langer F, Zasio MK, Bailey L, Liang D, Daughters GT, Ingels NB, Jr. and Miller DC. *Alterations in left ventricular torsion and diastolic recoil after myocardial infarction with and without chronic ischemic mitral regurgitation*. Circulation 110: II109-114, 2004.

[331] Tighe DA, Vinch CS, Hill JC, Meyer TE, Goldberg RJ and Aurigemma GP. *Influence of age on assessment of diastolic function by Doppler tissue imaging*. Am J Cardiol 91: 254-257, 2003.

[332] Tobita K and Keller BB. *End-systolic myocardial stiffness is a load-independent index of contractility in stage 24 chick embryonic heart*. Am J Physiol 276: H2102-2108, 1999.

[333] Topol EJ and Nissen SE. *Our preoccupation with coronary luminology. The dissociation between clinical and angiographic findings in ischemic heart disease*. Circulation 92: 2333-2342., 1995.

[334] Torrent-Guasp F, Ballester M, Buckberg GD, Carreras F, Flotats A, Carrio I, Ferreira A, Samuels LE and Narula J. *Spatial orientation of the ventricular muscle band: physiologic contribution and surgical implications*. J Thorac Cardiovasc Surg 122: 389-392, 2001.

[335] Torrent-Guasp F, Kocica MJ, Corno A, Komeda M, Cox J, Flotats A, Ballester-Rodes M and Carreras-Costa F. *Systolic ventricular filling*. Eur J Cardiothorac Surg 25: 376-386, 2004.

[336] Torrent-Guasp F, Kocica MJ, Corno AF, Komeda M, Carreras-Costa F, Flotats A, Cosin-Aguillar J and Wen H. *Towards new understanding of the heart structure and function*. Eur J Cardiothorac Surg 27: 191-201, 2005.

[337] Tsutsui H, Uematsu M, Shimizu H, Yamagishi M, Tanaka N, Matsuda H and Miyatake K. *Comparative usefulness of myocardial velocity gradient in detecting ischemic myocardium by a dobutamine challenge*. J Am Coll Cardiol 31: 89-93, 1998.

[338] van der Velde ET, Burkhoff D, Steendijk P, Karsdon J, Sagawa K and Baan J. *Nonlinearity and load sensitivity of end-systolic pressure-volume relation of canine left ventricle in vivo*. Circulation 83: 315-327, 1991.

[339] Vasan RS and Levy D. *Defining diastolic heart failure: a call for standardized diagnostic criteria*. Circulation 101: 2118-2121, 2000.

[340] Vendelin M, Bovendeerd PH, Engelbrecht J and Arts T. *Optimizing ventricular fibers: uniform strain or stress, but not ATP consumption, leads to high efficiency*. Am J Physiol Heart Circ Physiol 283: H1072-1081, 2002.

[341] Verdonck P, Kleven A, Verhoeven R, Angelsen B and Vandenbogaerde J. *Computer-controlled in vitro model of the human left heart*. Med Biol Eng Comput 30: 656-659., 1992.

[342] Vetter FJ and McCulloch AD. *Three-dimensional analysis of regional cardiac function: a model of rabbit ventricular anatomy*. Prog Biophys Mol Biol 69: 157-183, 1998.

[343] Vetter FJ and McCulloch AD. *Three-dimensional stress and strain in passive rabbit left ventricle: a model study*. Ann Biomed Eng 28: 781-792, 2000.

[344] Vierendeels JA, Dick E and Verdonck PR. *Hydrodynamics of color M-mode Doppler flow wave propagation velocity V(p): a computer study*. J Am Soc Echocardiogr 15: 219-224, 2002.

[345] Vierendeels JA, Riemslagh K, Dick E and Verdonck PR. *Computer simulation of intraventricular flow and pressure gradients during diastole*. J Biomech Eng 122: 667-674, 2000.

[346] Voigt JU, Lindenmeier G, Werner D, Flachskampf FA, Nixdorff U, Hatle L, Sutherland GR and Daniel WG. *Strain rate imaging for the assessment of preload-dependent changes in regional left ventricular diastolic longitudinal function*. J Am Soc Echocardiogr 15: 13-19, 2002.

[347] Weidemann F, Dommke C, Bijnens B, Claus P, D'Hooge J, Mertens P, Verbeken E, Maes A, Van de Werf F, De Scheerder I and Sutherland GR. *Defining the transmurality of a chronic myocardial infarction by ultrasonic strain-rate imaging: implications for identifying intramural viability: an experimental study*. Circulation 107: 883-888, 2003.

[348] Weidemann F, Jamal F, Kowalski M, Kukulski T, D'Hooge J, Bijnens B, Hatle L, De Scheerder I and Sutherland GR. *Can strain rate and strain quantify changes in regional systolic function during dobutamine infusion, B-blockade, and atrial pacing--implications for quantitative stress echocardiography*. J Am Soc Echocardiogr 15: 416-424, 2002.

[349] Weisfeldt ML, Scully HE, Frederiksen J, Rubenstein JJ, Pohost GM, Beierholm E, Bello AG and Daggett WM. *Hemodynamic determinants of maximum negative dP-dt and periods of diastole*. Am J Physiol 227: 613-621, 1974.

[350] Weiss JL, Frederiksen JW and Weisfeldt ML. *Hemodynamic determinants of the time-course of fall in canine left ventricular pressure*. J Clin Invest 58: 751-760, 1976.

[351] Westerhof N, Sipkema P and Van Huis GA. *Coronary pressure-flow relations and the vascular waterfall*. Cardiovasc Res 17: 162-169., 1983.

[352] White PA, Brookes CI, Ravn H, Hjortdal V, Chaturvedi RR and Redington AN. *Validation and utility of novel volume reduction technique for determination of parallel conductance*. Am J Physiol Heart Circ Physiol 280: H475-482, 2001.

[353] Wierzbowska K, Kasprzak JD, Drozdz J, Wejner-Mik P and Krzeminska-Pakula M. *The assessment of mitral inflow propagation velocity in the diagnosis of advanced left ventricular diastolic dysfunction*. Kardiol Pol 59: 224-234, 2003.

[354] Wiggers CJ. *Studies on the consecutive phase of the cardiac cycle. I. The duration of the consecutive phases of the cardiac cycle and the criteria for their precise determination*. Am J Physiol 56: 415, 1921.

[355] Yanagisawa H, Chikamori T, Tanaka N, Hatano T, Morishima T, Hida S, Iino H, Amaya K, Takazawa K and Yamashina A. *Correlation between thallium-201 myocardial perfusion defects and the functional severity of coronary artery stenosis as assessed by pressure- derived myocardial fractional flow reserve*. Circ J 66: 1105-1109., 2002.

[356] Yang XP, Liu YH, Rhaleb NE, Kurihara N, Kim HE and Carretero OA. *Echocardiographic assessment of cardiac function in conscious and anesthetized mice*. Am J Physiol 277: H1967-1974, 1999.

[357] Yellin EL, Nikolic S and Frater RW. *Left ventricular filling dynamics and diastolic function*. Prog Cardiovasc Dis 32: 247-271, 1990.

[358] Yotti R, Bermejo J, Antoranz JC, Desco MM, Cortina C, Rojo-Alvarez JL, Allue C, Martin L, Moreno M, Serrano JA, Munoz R and Garcia-Fernandez MA. *A noninvasive method for assessing impaired diastolic suction in patients with dilated cardiomyopathy*. Circulation 112: 2921-2929, 2005.

[359] Yotti R, Bermejo J, Antoranz JC, Rojo-Alvarez JL, Allue C, Silva J, Desco MM, Moreno M and Garcia-Fernandez MA. *Noninvasive assessment of ejection intraventricular pressure gradients*. J Am Coll Cardiol 43: 1654-1662, 2004.

[360] Young AA, Imai H, Chang CN and Axel L. *Two-dimensional left ventricular deformation during systole using magnetic resonance imaging with spatial modulation of magnetization*. Circulation 89: 740-752, 1994.

[361] Young DF, Cholvin NR, Kirkeeide RL and Roth AC. *Hemodynamics of arterial stenoses at elevated flow rates*. Circ Res 41: 99-107, 1977.

[362] Yturralde RF and Gaasch WH. *Diagnostic criteria for diastolic heart failure*. Prog Cardiovasc Dis 47: 314-319, 2005.

[363] Zile MR, Baicu CF and Gaasch WH. *Diastolic heart failure--abnormalities in active relaxation and passive stiffness of the left ventricle*. N Engl J Med 350: 1953-1959, 2004.

[364] Zile MR and Brutsaert DL. *New concepts in diastolic dysfunction and diastolic heart failure: Part I: diagnosis, prognosis, and measurements of diastolic function*. Circulation 105: 1387-1393, 2002.

[365] Zile MR, Gaasch WH, Carroll JD, Feldman MD, Aurigemma GP, Schaer GL, Ghali JK and Liebson PR. *Heart failure with a normal ejection fraction: is measurement of diastolic function necessary to make the diagnosis of diastolic heart failure?* Circulation 104: 779-782, 2001.

Symbols and Abbreviations

Abbreviations

A	atrial contraction
ANOVA	analysis of variance
Ao	aorta
ADP	adenosine diphosphate
ATP	adenosine triphosphate
AV	atrioventricular
BL	baseline
BM	basal metabolism
BPM	beats per minute
BSA	body surface area
CABG	coronary artery bypass grafting
CFR	coronary flow reserve
CHF	congestive heart failure
CVR	coronary flow velocity reserve
CMD	colour M-mode Doppler
CO	cardiac output
CT	computed tomography
CV	coefficient of variation
DCM	dilated cardiomyopathy
DHF	diastolic heart failure
DT	deceleration time
E	early filling
ECC	excitation-contraction coupling
ECG	electrocardiogram
ECM	extracellular matrix
EDP	end-diastolic pressure
EDPVR	end-diastolic pressure-volume relationship
EDV	end-diastolic volume
EF	ejection fraction
EI	elastance index
ESP	end-systolic pressure
ESPVR	end-systolic pressure-volume relationship
ESV	end-systolic volume
EW	external work
FFR	fractional flow reserve
FPS	frames per second
GLM	general linear model
HR	heart rate
HSR	hyperaemic stenosis resistance
IMT	intima media thickness
IR	inactivation rate
IVRT	isovolumic relaxation time
IVPD	intraventricular pressure difference
IVPG	intraventricular pressure gradient
LA	left atrium/atrial
LAD	left anterior descending artery
LAP	left atrial pressure

LCA	left coronary artery
LCX	left circumflex artery
LV	left ventricle/ventricular
LVC	left ventricular compliance
LVID	left ventricular internal diameter
LVM	left ventricular mass
LVP	left ventricular pressure
MRI	magnetic resonance imaging
PA	pulmonary artery
PCWP	pulmonary capillary wedge pressure
PE	potential energy
PET	positron emission tomography
PP	pulse pressure
PRF	pulse repetition frequency
PTCA	percutaneous transluminal coronary angioplasty
PV	pulmonary vein velocity
PVA	polyvinylalcohol
PVA	pressure-volume area
PW	pulsed wave
PWT	posterior wall thickness
QCA	quantitative coronary angiography
RA	right atrium/atrial
RA	regression algorithm
RCA	right coronary artery
rCVR	relative CVR
RMSe	root mean square error
RV	right ventricle/ventricular
RWT	relative wall thickness
SA	sinoatrial
SD	standard deviation
SE(M)	standard error (on the mean)
SHF	systolic heart failure
SM	sonomicrometry
SPECT	single photon emission computed tomography
SRI	strain rate imaging
STI	speckle tracking imaging
SV	stroke volume
SW	stroke work
SWT	septal wall thickness
TDI	tissue Doppler imaging
US	ultrasound
VCO	vena cava occlusion
WPV	wave propagation velocity

Symbols

a	parameter
a	acceleration
A	velocity of late diastolic filling wave

A	area
b	parameter
c	wave propagation velocity
c	parameter
Ca	calcium
d	depth
e	Euler constant
E	velocity of early diastolic filling wave
E	Young's modulus
E(t)	time-varying elastance
E_{es}	end-systolic elastance
E_{max}	maximum elastance
E_N	normalized time-varying elastance
f	frequency
F	female
g	gravity constant
G	conductance
i	count
k	count
L	length
M	male
n	count
P	phosphate
P	pressure
Q	flow
R	Pearson's correlation coefficient
R	resistance
R^2	coefficient of determination
s	line coordinate
t	time
V	volume
V_o	intercept of ESPVR
V_d	dead volume
V_{eq}	equilibrium volume

Greek Symbols

α	gain factor
α	parameter
β	parameter
γ	parameter
δ	parameter
ε	error
ε	strain
μ	dynamic viscosity
φ	phase
π	pi
θ	angle
ρ	density

σ	stress
τ	time constant of isovolumic relaxation

Subscripts

∞	asymptotic
adj	adjusted
ant	anterior
ao	aorta/aortic
ax	axial
az	azimuthal
b	blood
c	corrected
c	circumferential
d	diastolic
d	distal
d	Doppler
dis	distal
eq	equilibrium
es	end-systolic
est	estimated
f	fibre
i	inlet
lat	lateral
lin	linear
L	logistic
log	logarithmic
max	maximum
meas	measured
min	minimum
myo	myocardial
N	normal
Nyq	Nyquist
o	outlet
o	at time zero
p	parallel
post	posterior
quad	quadratic
r	received
r	radial
rot	rotational
s	systolic
sept	septal
S	stenotic
S	surrounding
t	transmitted
tot	total
v	venous
x	distance

zf	zero-flow

Operators

$\partial/\partial x$	partial derivative with respect to variable x
d/dx	derivative with respect to variable x
Δ	difference
∇	nabla
$\int$	integral operator
$\sum$	summation

Units

m	meter
µm	micrometer
mm	millimeter
cm	centimeter
s	second
ms	millisecond
min	minute
Pa	Pascal
mmHg	millimeter of mercury
g	gram
Hz	Hertz
kHz	kiloHertz
Mhz	megaHertz
S	Siemens